Annual Report 2021

Physik-Department

Lehrstuhl für Funktionelle Materialien

mit dem

Fachgebiet Physik Weicher Materie

Technische Universität München

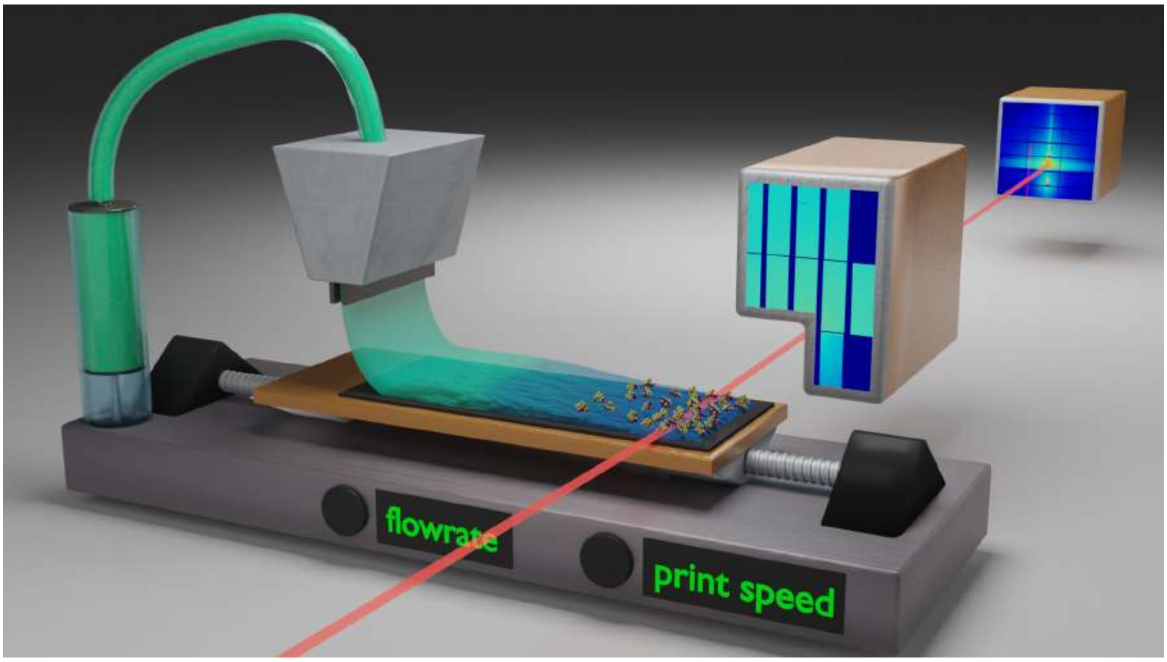

Prof. Peter Müller-Buschbaum, PhD
Chair of Functional Materials
muellerb@ph.tum.de
www.ph.nat.tum.de/functmat

Prof. Christine M. Papadakis, PhD
Soft Matter Physics Group
papadakis@tum.de
www.softmatter.ph.tum.de

Physik-Department
Technische Universität München
James-Franck-Straße 1
85748 Garching

Secretaries/Administration:
Marion Waletzki: marion.waletzki@ph.tum.de
Carola Kappauf: carola.kappauf@ph.tum.de

Tel.: +49(0)89 289-12452
Fax: +49(0)89 289-12473

Cover page picture:

In situ monitoring of thin-film nanoscale morphological and crystalline characteristics during slot-die coating by grazing-incidence small-angle X-ray scattering (GISAXS) and grazing-incidence wide-angle X-ray scattering (GIWAXS). The GIWAXS (near the sample) and GISAXS (further away from the sample) detectors are shown as well. Flow rate and print speed represent externally tunable parameters of the thin-film deposition process.

Editor: Dr. Apostolos Vagias

Preface

It is a great pleasure to present the annual report for the year 2021 in the name of the staff of the Chair of Functional Materials and the Soft Matter Physics Group. It provides an overview of our teaching, research and development activities. Our research activities are focused on functional materials and cover a broad range from soft matter physics to the development of methods and instrumentation. We examine the fundamental physics of material properties using mainly scattering methods (neutron, X-ray and light scattering). The overall goal of our research is to explain the functional characteristics of soft condensed matter from the knowledge of the molecular dynamics and nanostructure as well as their kinetics.

In 2021, the chair activities covered the specific areas of polymer solutions and gels, responsive thin films, functional thin films, photovoltaics, battery materials, real-time characterization and instrumentation and software development. Also in 2021, the Corona pandemic continued to strongly affect the entire life and research activities. The second year in a row, all group activities had to be cancelled, and office and laboratory work was restricted by additional regulations. Conferences and workshops were to a large extent held in online format.

Despite these challenges, the activities in the fields of polymer films for application in photovoltaics and polymer-hybrid systems were successfully continued. With *"TUM.solar"*, the keylab in the network of in the Bavarian Collaborative Research Project *"Solar Technologies go Hybrid"* (SolTec) headed by Prof. Müller-Buschbaum was running in its tenth year of funding. Research activities covered a broad area of next generation solar cells, including organic solar cells, dye-sensitized solar cells, hybrid solar cells, perovskite solar cells and quantum dot solar cells. Moreover, thermoelectric materials and energy storage materials with focus on the lithium ion battery technology were actively researched. In addition, we investigated polymers with complex architectures, novel responsive polymers (also under high pressure), self-assembling polymers in solution, multiresponsive and orthogonally switchable polymers as well as polymers for medical applications. Special focus was on the pathways of structural changes upon application of a change of environment.

The in-house experiments available in the laboratories of the chair were supplemented by many activities at large-scale facilities, comprising synchrotron radiation and neutron scattering experiments, despite challenges imposed by the Corona pandemic. Unfortunately, the in-house X-ray scattering instrument for SAXS/WAXS/GISAXS/GIWAXS broke down in August, and its repair lasted the rest of the year. Importantly, the general renovation of the laboratories including a reorganization of the instrument floorplan continued in its third year.

In 2021, the Chair of Functional Materials and the Soft Matter Physics Group comprised 10 fellows, 59 PhD students, 24 master students, 18 bachelor students, 3 student assistants and 5 administrative and technical staff members. 12 PhD theses were accomplished; moreover, 6 master theses as well as 18 bachelor theses were finished. Due to the Corona pandemic, we had very limited possibilities to host guests from abroad at the chair in person, and interactions were mostly online only.

All members of the chair were very active at virtual conferences and workshops, participating with both, talks and posters. A highlight was the organization of the *"SolTech Conference 2021"* in *"Haus der bayerischen Wirtschaft"* in downtown Munich. It was an in-person event and all participants enjoyed to have a real conference experience. Prof. Papadakis co-organized a conference *"Osmolyte and cosolvent effects in stimuli-responsive soft matter systems"*, which was held as a virtual event, but still was a great success.

Regarding teaching activities of the chair, we offered the lectures *"Materials Science"* and *"Introduction to Condensed Matter Physics"* (Papadakis). Specialized lectures comprised *"Polymer physics"* (Müller-Buschbaum), *"Nanostructured soft materials"* (Papadakis) and *"Measurement and Sensor Technology"* (Müller-Buschbaum). Prof. Papadakis acted again as a deputy women's representative of the Physics Department. Moreover, Prof. Müller-Buschbaum headed the activities in the *"Network Renewable Energies (NRG)"* in the MSE.

As a service to the community, Prof. Papadakis acted as one of the Editors-in-Chief of *"Colloid and Polymer Science"* and Prof. Müller-Buschbaum served as Associate Editor at *"ACS Applied Materials & Interfaces"*.

This annual report comprises a selection of the different research topics and projects carried out in the individual groups of the chair. It highlights the dedicated and successful research activities and collaborations with other groups and large-scale facilities. We wish all chair members a fruitful continuation and a very successful year 2022.

Peter Müller-Buschbaum and Christine M. Papadakis March 2022

Contents

1 Polymer solutions and gels

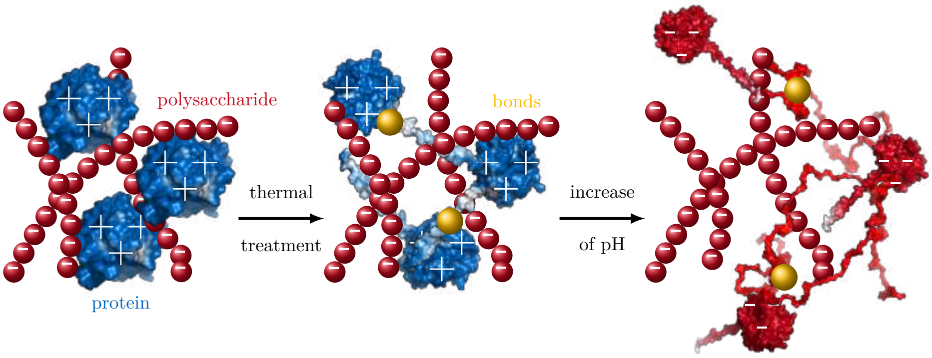

1.1 Pressure-dependence of water dynamics in concentrated aqueous PNIPAM solutions with a methanol cosolvent

B.-J. Niebuur, W. Lohstroh[1], M.-S. Appavou[2], A. Schulte[3], C. M. Papadakis

[1] MLZ, Technical University of Munich, Germany
[2] JCNS at MLZ, Garching, Germany
[3] University of Central Florida, U. S. A.

Cosolvents are essential in many contexts, including the preparation of pharmaceutical formulations and in biological systems. In solutions of thermoresponsive polymers, addition of a cosolvent may lead to a strong reduction of the cloud point and re-entrant behavior. These features have been termed co-non-solvency. A prototype responsive polymer in this respect is poly(*N*-isopropylacrylamide) (PNIPAM). At atmospheric pressure, PNIPAM exhibits a cloud point at 30 °C in purely aqueous solutions, and its solubility is governed by the temperature-dependent hydration of hydrophilic and hydrophobic groups. In the presence of a cosolvent, e.g. methanol, the cloud point is significantly reduced. The application of pressure has a dramatic effect on the co-non-solvency effect: While the coexistence line in the temperature-pressure frame adopts a convex-upward shape, in the presence of a cosolvent its maximum is shifted to significantly higher pressures as well as to higher temperatures (Fig. 1.1a).

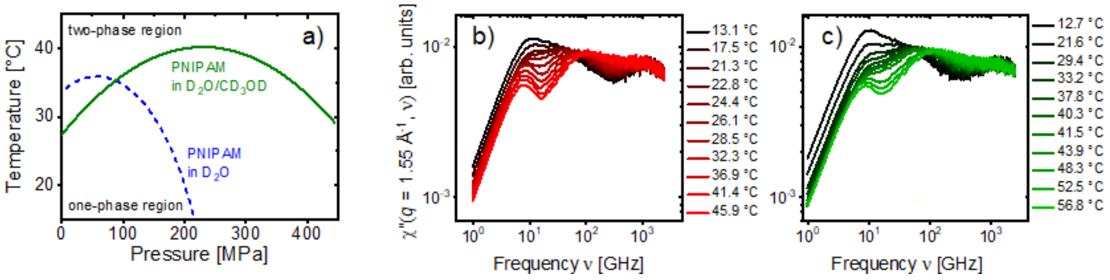

Figure 1.1:
(a) Coexistence lines of 3 wt% PNIPAM solutions in 80:20 v/v D_2O/CD_3OD (olive full line) and in neat D_2O (blue dashed line), as determined using turbidimetry [2,3]. (b, c) Imaginary part of the dynamic susceptibility of the 25 wt% PNIPAM solution in 80:20 v/v H_2O/CD_3OD obtained at a momentum transfer $q = 1.55$ Å^{-1} at 0.1 MPa (b) and 200 MPa (c) at the temperatures indicated. The curves just below and just above the respective cloud point are highlighted in bold. From [1].

In purely aqueous solutions, application of pressure enhances the hydrophobic hydration. As a result, the polymer chains stay hydrated in the two-phase region, even though the chains collapse. Mechanisms that reduce the total volume of the system may favor the reversal of the co-non-solvency effect at high pressure, because these facilitate a more efficient packing of the small water molecules on the chain. Since the volume of a monomer solvated with a cosolvent is relatively large, the cosolvent is released. It was predicted that the interactions of the two solvents with the polymer and with each other, both on the chain and in the bulk solvent mixture, play a role. Here, we use quasi-elastic neutron scattering (QENS) to simultaneously characterize the dynamics of both bulk and hydration water and to discern the scattering signal of water by using perdeuterated methanol, CD_3OD, in a concentrated PNIPAM solution in an H_2O/CD_3OD mixture [1].
PNIPAM with a molar mass 36 kg/mol was dissolved at a concentration of 25 wt% in an 80:20 v/v H_2O/CD_3OD mixture. QENS measurements were conducted at the spectrometer TOFTOF (MLZ, Garching) using neutrons having a wavelength of 6.0 Å and a rotation speed of the chopper system of 14,000 rpm. The samples were mounted in a custom-made aluminum pressure

cell. Measurements were performed during heating between 13 and 57 °C at 0.1 and 200 MPa across the respective cloud point. The measuring time at each temperature was 120 min. The signal was recorded in an angular range of 7.5° to 140°. The spectra were normalized to the incoming neutron flux and to a vanadium standard measurement. An empty pressure cell spectrum was subtracted from the data. The dynamic structure factors were transformed into the imaginary part of the dynamic susceptibility, $\chi''(q,\nu)$ (Fig. 1.1b and c).
The susceptibility spectra at low temperatures, i.e. in the one-phase region, show strong contributions at low (ca. 10 GHz) and high frequencies (ca. 1000 GHz), that are present at both pressures. The contribution at low frequencies is due to the relaxation of hydration water, i.e. water molecules that are associated with the polymer chains. The high-frequency contributions are due to dynamic processes in the bulk solvent. At atmospheric pressure, the coil-to-globule transition at the cloud point temperature goes along with an abrupt release of polymer-bound water (Fig. 1.2a).

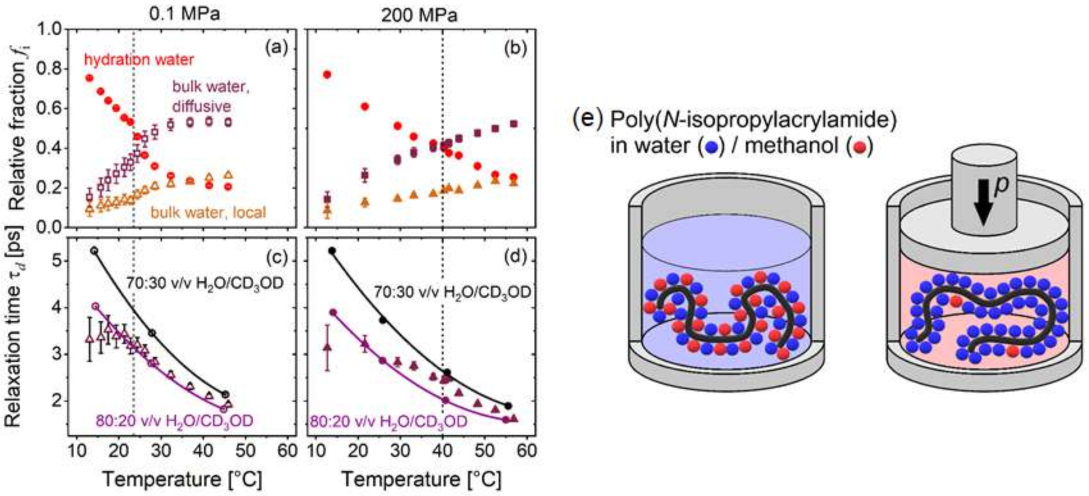

Figure 1.2:
(a, b) Relative populations of different water species and (c, d) relaxation times τ_d of the bulk diffusive mode (bottom) as a function of temperature in a 25 wt% PNIPAM solution at ambient (open symbols) and high pressure (full symbols). Full lines indicate τ_d in 80:20 and 70:30 v/v H_2O/CD_3OD mixtures without the polymer. Open and full triangles refer to τ_d in a 25 wt% PNIPAM solvent mixture. (e) Resulting picture of the water and methanol adsorption on the chain. All from [1].

In contrast, at high pressure, the fraction f_H of bound water decreases gradually with increasing temperature (Fig. 1.2b). The relaxation time τ_d of the bulk diffusive mode in the polymer solution is compared with that in the neat 80:20 and 70:30 v/v H_2O/CD_3OD solvent mixtures in Fig. 1.2c and d). We conclude that, at a pressure of 200 MPa, water replaces the majority of methanol adsorbed on the chains altering the effective solvent composition. Preferential water adsorption and the hydrophobic interaction thus play a major for the breakdown of the co-non-solvency effect at high pressures (Fig. 1.2e). The results demonstrate that QENS is a powerful approach to gain molecular insight into the interplay of co-non-solvency and water dynamics.

[1] B.-J. Niebuur, W. Lohstroh, C.-H. Ko, M.-S. Appavou, A. Schulte, C. M. Papadakis, *Macromolecules* **54**, 4387-4400 (2021)

[2] B.-J. Niebuur, L. Chiappisi, X. Zhang, F. Jung, A. Schulte, C. M. Papadakis, *ACS Macro Lett.* **7**, 1155-1160 (2018)

[3] B.-J. Niebuur, C.-H. Ko, X. Zhang, K.-L. Claude, L. Chiappisi, A. Schulte, C. M. Papadakis, *Macromolecules* **53**, 3946-3955 (2020)

1.2 A thermoresponsive poly(2-oxazoline)-based molecular brush in aqueous solution: effect of a cosolvent

B. Yazdanshenas, C. Spies, C. Sachse[1], S. Da Vela[2], R. Jordan[1], C. M. Papadakis

[1] Fakultät Chemie und Lebensmittelchemie, Technische Universität Dresden, Germany

[2] European Molecular Biology Laboratory, c/o DESY, Hamburg, Germany

Unusual polymeric architectures can lead to novel and potentially useful properties. Molecular brush polymers are a type of graft polymers with polymeric side chains attached to each repeat unit of a linear polymer backbone. The high grafting density gives the molecular brushes a rather compact structure, that affects their physical properties. For example, when the side arms are thermoresponsive in aqueous solution, the cloud point T_{CP} of the molecular brush is shifted with respect to the linear analogues [1].

Here, we investigate a thermoresponsive poly(2-oxazoline)-based molecular brush, P*i*POx$_{100}$-*g*-PEtOx$_{17}$, with poly(2-ethyl-2-oxazoline) (PEtOx) side chains and a poly(2-isopropenyl-2-oxazoline) (P*i*POx) backbone. Poly(2-alkyl-2-oxazoline)s are well-known for their tunable thermoresponsivity, which strongly depends on the alkyl substituent, the polymeric architecture, and concentration [2]. When the alkyl substituent is an ethyl group, the linear polymer in aqueous solution exhibits lower critical solution temperature (LCST) behavior with cloud points of typically 60 °C. We previously found that T_{CP} of the P*i*POx$_{100}$-*g*-PEtOx$_{17}$ molecular brush in pure water is suppressed to 45 and 40 °C, for concentrations of 10 and 30 g L^{-1}, respectively [1,3]. Moreover, a temperature-dependent small-angle neutron scattering (SANS) study of 30 g L^{-1} of this brush in D_2O showed that, from room temperature to T_{CP}, the backbone of the molecular brushes stretches due to dehydration of the side arms [1]. At temperatures above T_{CP}, the brushes collapse and form compact aggregates.

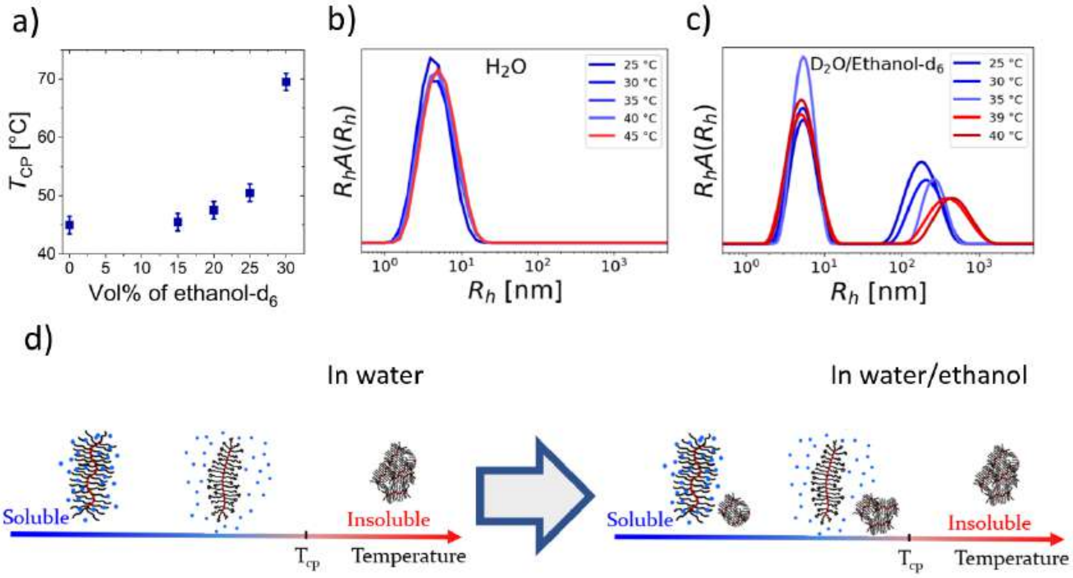

Figure 1.3:
Effect of the cosolvent ethanol-d$_6$ on a 10 g L^{-1} aqueous solution of P*i*POx$_{100}$-*g*-PEtOx$_{17}$. a) T_{CP} as a function of ethanol-d$_6$ volume fraction. b) and c) Temperature-dependent DLS of solutions in pure H_2O [3] and in an 80:20 D_2O/ethanol-d$_6$ v/v solvent mixture, respectively. d) Schematic representation of solubility behavior of the molecular brush in pure H_2O (left) compared with the one in an 80:20 D_2O/ethanol-d$_6$ v/v solvent mixture (right).

In this work, we study the effect of the cosolvent ethanol on the solubility of this molecular brush. Water-ethanol solvent mixtures are known to exhibit abnormal mixing properties and were demonstrated to result in increase of solubility for several types of poly(2-oxazoline)s [4]. We investigate solutions of 10 g L^{-1} in deuterated solvents, to compare with future SANS experiments. Turbidimetry revealed a drastic increase of T_{CP} with increasing ethanol-d_6 fraction (Fig. 1.3a). Previously, dynamic light scattering (DLS) showed that in pure water (H_2O) all brushes dissolve individually, at concentration of 10 g L^{-1} (Fig. 1.3b,[3]). However, our results show that in presence of 20 vol % ethanol-d_6, aggregates of a size of a few hundred nm appear already below T_{CP}, in coexistence with individually dissolved molecular brushes (Fig. 1.3c).
In addition, a morphological study was performed by synchrotron small-angle X-ray scattering (SAXS), in hydrogenated solvent mixtures. Fig. 1.4a shows the SAXS data at 40 °C (i.e. below T_{CP}) as a function of ethanol volume fraction. The mid-q range, reflecting scattering from the individually dissolved brushes, was modeled by a Guinier-Porod function (black solid line).

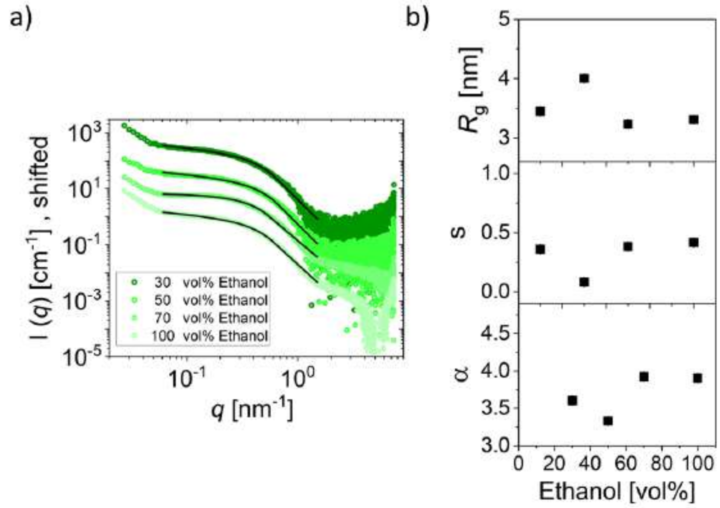

Figure 1.4:
a) Symbols: SAXS data of 10 g L^{-1} P*i*POx100-*g*-PEtOx$_{17}$ at 40 °C in aqueous solutions with different ethanol volume fractions, as indicated in the graph. Black solid lines show the SAXS model fits. b) Structural parameters resulting from model fitting. From top to bottom: radius of gyration, R_g, dimensionality parameter, s, and Porod exponent, α.

The resulting fitting parameters are presented in Fig. 1.4b. The radius of gyration, R_g, decreases with increasing ethanol volume fraction. Moreover, the dimensionality parameter, s, is close to zero, which indicates a rather spherical and, therefore, compact shape of the brushes. This is consistent with the very small R_g-value compared with the calculated largest possible length of the fully stretched brush in longitudinal direction (37 nm [1]). Furthermore, the increase of the Porod exponent, α from ca. 3 to 4 with increasing ethanol volume fraction suggests a transition from a rough to a smooth surface of the compact brushes.

In summary, addition of ethanol as co-solvent to aqueous solutions of the investigated thermoresponsive PEtOx-based molecular brush not only introduces a drastic increase of T_{CP}, but also a different solubility mechanism, compared with a purely aqueous solution, which deserves further investigations.

[1] J.-J. Kang , K. Shehu, C. Sachse, F. Jung, C.-H. Ko, L. Barnsley, R. Jordan, C. M. Papadakis, *Colloid. Polym. Sci.* **299**, 193-203 (2021)

[2] R. Hoogenboom, *Angew. Chem. Int. Ed.* **48**, 7978-7994 (2009)

[3] K. Shehu, Master Thesis, Technical University of Munich (2018)

[4] H. M. L. Lambermont-Thijs, H. P. C. v. Kuringen, J. P. W. v. d. Put, U. S. Schubert, R. Hoogenboom, *Polymers* **2**, 188-199 (2010)

1.3 Stimuli-responsive micelles from amphiphilic triblock terpolymers

Y. Li, C.-H. Ko, A. Skandalis [1], D. S. Molodenskiy[2], S. Pispas[1], C. M. Papadakis

[1] Theoretical and Physical Chemistry Institute, NHRF, Athens, Greece
[2] DESY, Hamburg, Germany

Stimuli-sensitive core-shell micelles from triblock terpolymers having a hydrophobic, a hydrophilic, and a responsive block offer many possibilities for biomedical applications. In the present work, we investigate poly(2-(dimethylamino) ethyl methacrylate)-*b*-poly(lauryl methacrylate)-*b*-poly((oligo ethylene glycol)methacrylate) ($PDMAEMA_{89}$-*b*-$PLMA_{38}$-*b*-$POEGMA_{48}$) (Figure 0.1a [1]). The PDMAEMA block features tertiary amino groups and is a weak cationic polyelectrolyte, which is thermo-responsive at high pH-values. The PLMA block is permanently hydrophobic and ensures micelle formation. The POEGMA block is a permanently hydrophilic block and was chosen to ensure the solubility of micelles, even when the PDMAEMA block is collapsed. In the present work, we investigate the concentration dependence of the micellar structures in aqueous micellar solutions of $PDMAEMA_{89}$-*b*-$PLMA_{38}$-*b*-$POEGMA_{48}$ at pH 7.8 and 25 °C. It may be expected that the shell of the micelle consists of two layers, where the inner layer contains both PDMAEMA and POEGMA, while the outer one consists of PDMAEMA only. All three blocks are biocompatible, which qualifies the micelles for biomedical applications, e.g. for the delivery of genes when the micellar shell is positively charged. For characterization, synchrotron small-angle X-ray scattering was used.

For the sample preparation, the triblock terpolymer was dissolved in a tetrahydrofuran/D_2O mixture. A 24 mg/mL solution was obtained by evaporating the tetrahydrofuran using a rotary evaporator. 3 and 10 mg/mL polymer solutions were prepared by dilution with D_2O. Synchrotron SAXS measurements were performed at the BioSAXS beamline at EMBL, DESY, using a wavelength of 0.124 nm and a sample detector distance of 3.0 m. The background from the solvent and the sample holder was subtracted using the software ATSAS. Model fits were carried out using the software SasView 4.04.

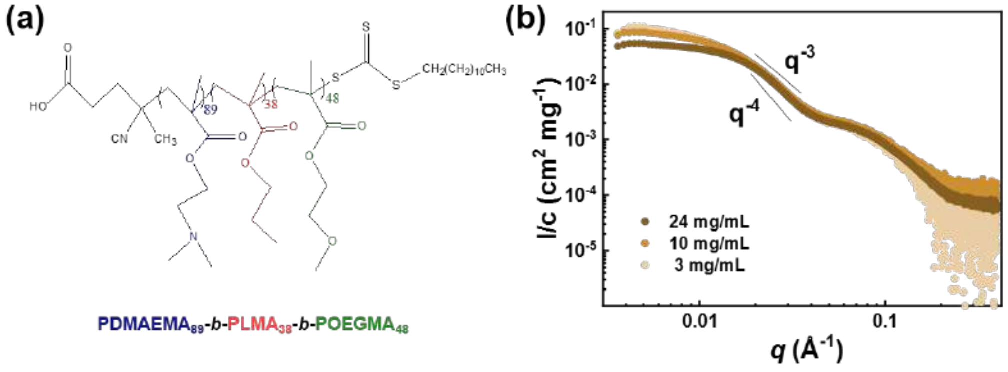

Figure 1.5:
(a) Chemical structure of the $PDMAEMA_{89}$-*b*-$PLMA_{38}$-*b*-$POEGMA_{48}$. (b) SAXS data of the $PDMAEMA_{89}$-*b*-$PLMA_{38}$-*b*-$POEGMA_{48}$ solutions in D_2O normalized by the concentrations given in the graph. The parameter q denotes the momentum transfer.

In Fig. 1.5 (b), the SAXS data are shown for the three concentrations investigated. They feature two decays that hint to the presence of micelles. The normalization by polymer concentration shows that the curves overlap over the entire q-range, only the forward scattering at low momentum transfers q becomes flatter, when the concentration increases from 3 to 24 mg/mL.

Moreover, there are differences in the slope at high q-values, which may reflect local changes, possibly in the shell.

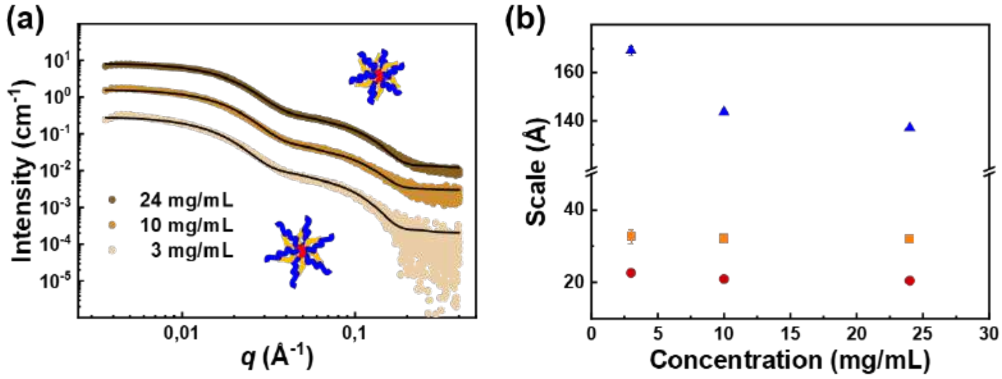

Figure 1.6:
Structural parameters of the micelles in dependence on the polymer concentration. (a) Similar representation as in Fig. 1.5 (b), but the SAXS scattering curves are shifted vertically by factors of 2 and 6, respectively. Symbols represent the experimental data, black solid lines the model fits. (b) Core radius (red circles) and thickness of the inner shell layer (orange squares) and the outer shell layer (blue triangles).

Model fitting was carried out using a model for spherical micelles featuring a core and a shell that consists of two layers. Fig. 1.6 (a) shows the scattering curves and the respective fits. Fig. 1.6 (b) shows the resulting structural parameters of the micelles. With concentration increasing from 3 to 24 mg/mL, the radius of the micellar core and the thickness of the inner shell layer stay unchanged at ca. 20 and 32 Å. In contrast, the thickness of the outer shell layer decreases from 170 Å for the 3 mg/mL solution to 140 Å at 24 mg/mL. As observed in the most dilute solution, the sum of the shell thicknesses is only slightly lower than the contour length of the PDMAEMA block (223 Å), i.e. it is rather stretched. The decreasing thickness of the outer shell layer is attributed to interactions between the micelles. While the thickness of the inner shell layer is significantly lower than the contour length of the POEGMA block (120 Å), the core radius is larger than the end-to-end distance of PLMA in Gaussian conformation (15 Å). Thus, we conclude that the micellar core not only consists of PLMA, but also includes a certain fraction of the PDMAEMA blocks. This may be due to the attractive interaction between the methacrylate backbones.

We conclude that the increasing concentration of polymer solution reduces the thickness of the micellar shell due to the interactions between the outer layers of the micelles. As expected, increasing the polymer concentration does not affect the inner parts of the micellar structure.

[1] A. Skandalis, S. Pispas, *Polym. Chem.* **8**, 4538-4547 (2017)

1.4 Effect of pH on the structure of thermoresponsive telechelic polyelectrolyte networks

C.-H. Ko, F. A. Jung, M. M. S. Lencina[1], R. Schweins[2], C. Patrickios[3], C. Tsitsilianis[1], C. M. Papadakis

[1] University of Patras, Greece
[2] ILL, Grenoble, France
[3] University of Cyprus, Nicosia

In aqueous environment, triblock copolymers from a hydrophilic middle block and hydrophobic endblocks form self-assembled micellar hydrogels. Their rheological response depends strongly on the exchange dynamics of the endblocks. These can be tuned by chosing end blocks that are thermoresponsive polymers. In our previous work, we used triblock copolymers with end blocks from poly(tri-ethylene glycol methyl ether methacrylate/*n*-butyl methacrylate) (P(TEGMA-*co*-*n*BuMA)) random copolymers and the pH-responsive weak polyelectrolyte poly(2-dimethylamino ethyl methacrylate) (PDMAEMA) as the midblock [1]. In this system, the control of the exchange dynamics of the stickers was achieved by varying temperature. The system behaved as a viscoelastic complex fluid (dynamic network) at low temperatures, while an elastic hydrogel was formed (”frozen” network) at higher temperatures, which was mainly attributed to the reduction of the endblock exchange.

In the present work, we explore the effect of pH, that affects the ionization degree of the PDMAEMA midblock and thus the conformation of the bridging chains and their intermolecular interactions on the dynamics and the network structure [2]. Small-angle neutron scattering (SANS) is employed to monitor structural changes of the hydrogels.

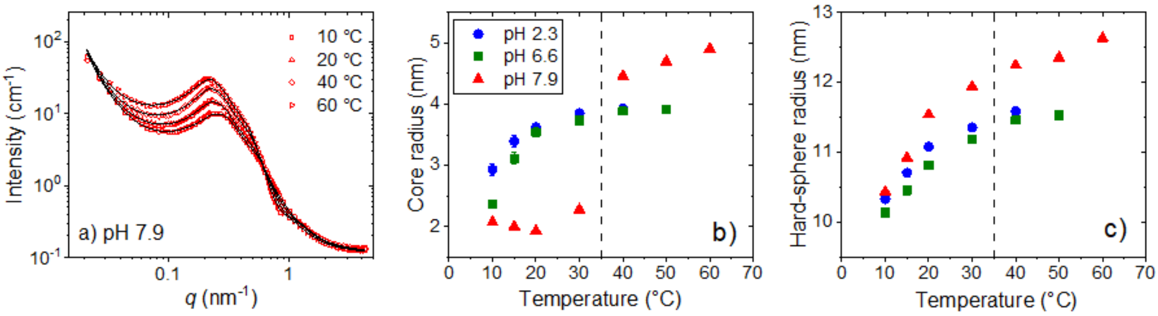

Figure 1.7:
(a) Representative SANS data at pH 7.9 at the temperatures given. Symbols: experimental data; lines: model fits. For clarity, only every second data point is shown. (b) Resulting core radius and (c) hard-sphere radius in dependence on temperature for the 3 pH values studied. All from [2].

Hydrogels were prepared by dissolving the P(nBuMA$_{18}$-*co*-TEGMA$_{15}$)-*b*-(PDMAEMA)$_{159}$-*b*-P(nBuMA$_{18}$-*co*-TEGMA$_{15}$) triblock terpolymer in D_2O at a concentration of 4 wt%, adjusting the pH by adding HCl or NaOH, and by centrifuging.

Rheological experiments revealed that the relaxation time is maximum at pH 6. SANS experiments were carried out at pH values of 2.3 (where PDMAEMA is highly ionized), 6.6 (where the relaxation time is maximum) and at 7.9 (where PDMAEMA is nearly non-ionized and thermoresponsive). As an example, the curves at pH 7.9 are shown in dependence on temperature in Fig. 1.7a. They feature a maximum at momentum transfers q = 0.21-0.25 nm^{-1}. At 0.3-1 nm^{-1}, a shoulder appears which reflects the form factor of the micelles. The smooth decay at

$q > 1\ \mathrm{nm}^{-1}$ is mainly due to concentration fluctuations in the micellar shell. The forward scattering at $q < 0.1\ \mathrm{nm}^{-1}$ is due to large-scale inhomogeneities of the network or large clusters. A model was fitted, that comprises the form factor of spherical core-shell micelles, which are correlated by a hard-sphere structure factor. These terms are combined with the Ornstein-Zernike term describing the concentration fluctuations in the micellar shell and in the matrix between the cores, and a Porod term reflecting large-scale inhomogeneities.

At pH 2.3 and 6.6, the core radius increases up to 30 °C and then becomes constant (Fig. 1.7b). This increase might be explained by an increase of the aggregation number and/or the transformation of the TEGMA moieties from hydrophilic to hydrophobic. In contrast, at pH 7.9, the core radius stays constant at a lower value (2 nm) up to 30 °C, then increases sharply to 4.5 nm at 40 °C and further to 4.8 nm at 60 °C. This increase points to an increase of the aggregation number of the micelles due to an increased hydrophobicity of the endblocks at 35 °C, which we attribute to the transition temperature of the P(TEGMA-*co*-*n*BuMA) endblocks. At pH 2.3 and 6.6, the hard-sphere radius, which is related to the average distance between those micelles, that are correlated with each other (either by bridging or via the hard-sphere potential), increases up to 35 °C and becomes constant above 35 °C (Fig. 1.7c). At pH 7.9, the hard-sphere radius is larger than at the lower pH values and keeps increasing in the entire temperature range.

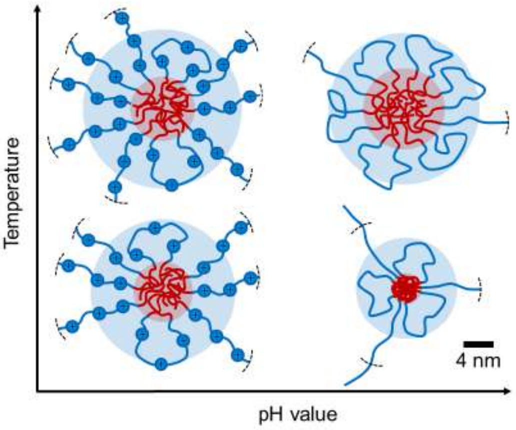

Figure 1.8:
Schematic structures of the micelles forming the network in dependence on pH value and temperature [2]. Shaded circles indicate the core (red) and the entire micelle (blue). Blue plusses indicate positive charges on the PDMAEMA block. Intermicellar bridges which connect micelles in the micellar network are indicated with dashed lines. The scale bar gives the length scale.

The resulting micellar structures, which are the building blocks of the network, are schematically shown in dependence on pH and temperature, in Fig. 1.8. While at pH 2.3 and 6.6, the temperature-dependent structural properties of the micelles are similar, a strong temperature dependence is observed at pH 7.9. Therefore, the observed maximum of the terminal relaxation times at pH 6.6 may be ascribed to two opposite effects. Firstly, the increase of pH above 6.0 induces an improvement of the network connectivity due to the weakening of the repulsive interactions among the micelles. Secondly, at pH 7.9, the drastic decrease of the degree of ionization of the bridging chains induces remarkable changes in the network structure. The connectivity of the network is substantially decreased, and the core distances are higher. The PDMAEMA midblock is much less hydrophilic at pH 7.9, which affects the temperature dependent hydrophobic/hydrophilic balance of the terpolymer and leads to a sharp variation of the characteristic sizes of the micelles with temperature at this pH value. We conclude that the present system is both temperature- and pH-responsive, enabling tailoring the rheological properties of the thermoresponsive telechelic polyelectrolyte hydrogels.

[1] C. Tsitsilianis, G. Serras, C.-H. Ko, F. Jung, C. M. Papadakis, M. Rikkou-Kalourkoti, C. S. Patrickios, R. Schweins, C. Chassenieux, *Macromolecules* **51**, 2169-2179 (2018)

[2] M. M. S. Lencina, C.-H. Ko, F. A. Jung, R. Schweins, M. Rikkou-Kalourkoti, C. S. Patrickios, C. M. Papadakis, C. Tsitsilianis, *ACS Appl. Polym. Mater.* **3**, 819–829 (2021)

1.5 Effect of co-solvent on the rheological properties and self-assembled structures from telechelic polyampholytes

M. A. Dyakonova, Y. Li, I. N. Besiri[1], Z. Di[2], C. Tsitsilianis[1], C. M. Papadakis

[1] University of Patras, Greece
[2] JCNS at MLZ, Garching, Germany

Telechelic polymers form self-assembled hydrogels with the hydrophobic endblocks forming micelles, that are bridged by the hydrophilic blocks. Using polyelectrolytes as the middle blocks, hydrogels which are responsive to pH and ionic strength have been designed. Using a polyampholyte middle block has the advantage of an even stronger pH response. However, non-equilibrium states cannot be excluded, especially for long and strongly hydrophobic blocks. We investigated previously a telechelic polyampholyte, namely PMMA$_{86}$-*b*-P(DEA$_{190}$-*co*-MAA$_{96}$)-*b*-PMMA$_{86}$ (Fig. 1.9a), where PMMA stands for poly(methyl methacrylate) and P(DEA-*co*-MAA) for poly(2-(diethylamino)ethyl methacrylate-*co*-methacrylic acid) [1]. While the endblocks are permanently hydrophobic and form “frozen” micelles, the middle block changes from being positively charged at low pH values to being negatively charged at high pH values. This is reflected in both, the dynamic mechanical properties and the structure of the micellar hydrogel. At pH 3, a a freestanding gel is formed at a polymer concentration of 3 wt%, which features small micelles from PMMA, that are connected by a low number of stretched P(DEA-*co*-MAA) blocks (bridges), forming loosely packed, large aggregates.

In the present work, we alter the nature of the solvent by using water/acetone mixtures. This is expected to have two effects: First, the dielectric permittivity is reduced compared to the one of neat water, enhancing the electrostatic interactions between the charges in the polyampholyte middle block. Second, acetone is a good solvent for PMMA and thus, the mobility of the PMMA endblocks is enhanced, enabling exchange of the PMMA blocks between different micellar cores. Thus, we expect a rearrangement of the network structure, as the acetone content is increased. Besides, acetone is a good solvent for P(DEA-*co*-MAA). To investigate the mesoscopic structures, we use small-angle neutron scattering (SANS) on solutions with polymer concentrations of 0.5 wt% prepared in perdeuterated solvents.

Samples were prepared by dissolving the polymer in $D_2O/(CD_3)_2CO$ mixtures at room temperature to achieve a polymer concentration of 0.5 wt%. The pH was adjusted to a value of 3.0 by adding HCl. The solutions were left to shake and were centrifuged. Samples containing 0-10 wt% of $(CD_3)_2CO$ were gels, whereas those with 15-30 wt% were liquids. SANS measurements were carried out at the instrument KWS-1 (JCNS at MLZ). The neutron wavelength was chosen at 0.47 nm. The exposure times were 10-45 min at sample-detector distances of 1.17-19.67 m. The samples were mounted in 1 mm quartz glass cuvettes and were measured at 26 °C. The scattering of the D_2O filled cell was subtracted from the sample scattering.

The SANS data at different $(CD_3)_2CO$ contents are presented in Fig. 1.9b. The curve of the solution in pure D_2O and the ones of solutions with $(CD_3)_2CO$ contents in the solvent mixture up to 10 wt% have a similar shape, namely a shallow maximum. In contrast, the curves between 15 and 25 wt% feature forward scattering, which may be attributed to finite clusters of micelles. Moreover, the above mentioned maximum becomes more pronounced and moves to higher momentum transfers q, and the scattering at high q-values changes shape. At 30 wt% of $(CD_3)_2CO$, the curve shape is significantly different: The forward scattering is strong, the maximum is very weak and shifted to a high q-value, and a broad shoulder is present. The data were modeled by a form factor for polydisperse spheres to describe the cores, a hard-sphere structure factor to characterize their correlation, a modified Porod law to describe the forward scattering related to finite clusters of micelles and an Ornstein-Zernike structure to describe the scattering from the matrix blocks. Good agreement with the data is achieved.

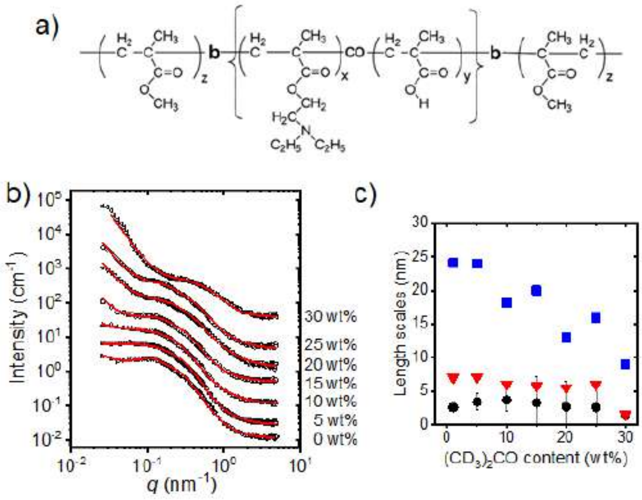

Figure 1.9:
(a) Chemical structure of PMMA$_{86}$-*b*-P(DEA$_{190}$-*co*-MAA$_{96}$)-*b*-PMMA$_{86}$. Reprinted with permission from [3]. (b) SANS curves of 0.5 wt% solutions in mixtures of D$_2$O/(CD$_3$)$_2$CO at the (CD$_3$)$_2$CO contents in the solvent mixture given in the graph. The symbols represent the data, and the solid lines the model fits. The curves are shifted vertically. (c) Resulting length scales: black circles: average sphere radius, blue squares: hard-sphere radius, red triangles down: correlation length. All from [2].

In neat D$_2$O, the resulting sphere radius is 2.6 nm (Fig. 1.9c). We assume that these radii correspond to the PMMA cores along with the inner dense part of the shell formed by the middle blocks. The hard-sphere radius, i.e half the distance between the correlated micelles, is 24.2 nm. At the pH value chosen, a large fraction of DEA segments is protonated, which leads to repulsive electrostatic interactions between similarly charged units along the polyampholyte middle block. As a result, the middle block adopts a stretched conformation and can bridge distant neighboring micelles. The correlation length of the concentration fluctuations of the middle blocks is found at 7 nm. With the (CD$_3$)$_2$CO content in the solvent mixture increasing to 25 wt%, the sphere radius and the correlation length are rather unchanged, but the distance between the spheres decreases steadily to 16 nm at 25 wt%. At 5-10 wt%, (CD$_3$)$_2$CO lowers the dielectric permittivity of the medium by 5-6 units; thus, the strength of the repulsive electrostatic interactions between the charged DEA units in the bridging polyampholytic blocks is altered. As a consequence, the middle blocks are more flexible than in neat D$_2$O, resulting in a lower degree of bridging. However, the PMMA blocks are still not mobile enough to allow for disruption of the micellar networks. This is corroborated by the fact that the forward scattering is weak. At 15-25 wt%, the strong forward scattering shows that the micellar clusters are of finite size. Presumably, the larger clusters are disrupted, when the middle blocks become more flexible, enabling a bridge-to-loop transition. Significant differences are observed at 30 wt% of (CD$_3$)$_2$CO: The sphere radius has decreased to 1.4 nm, suggesting that the micelles are now very small and consist of very few PMMA end blocks, i.e. the micellar network has transformed into random network-like clusters. These clusters are smaller than at lower (CD$_3$)$_2$CO contents. The correlation length and the hard-sphere radius have also decreased significantly. We suppose, that the dielectric permittivity of the medium is so low, that the strength of repulsive interactions along the polyampholytic blocks is strongly reduced, which leads to a severe shrinkage of the bridging chains. Moreover, the PMMA end blocks lose their hydrophobicity, and they become highly mobile. We conclude that addition of a cosolvent is a route for the manipulation of the network architecture and thus of the mechanical properties.

[1] M. A. Dyakonova, G. Gotzamanis, B.-J. Niebuur, N. S. Vishnevetskaya, K. N. Raftopoulos, Z. Di, S. K. Filippov, C. Tsitsilianis, C. M. Papadakis, *Soft Matter* **13**, 3568-3579 (2017)

[2] M. A. Dyakonova, Y. Li, I. N. Besiri, Z. Di, I. Grillo, C. Tsitsilianis, C. M. Papadakis, *Colloid Polym. Sci.* **299**, 419-428 (2021)

[3] G. Gotzamanis, K. Papadimitriou, C. Tsitsilianis, *Polym. Chem.* **7**, 2121-2129 (2016)

1.6 Protein-polysaccharide nanoparticles: effect of thermal treatment

J. Allwang, Y. Li, S. Da Vela[1], D. Salianitis[2], A. Chroni[2], A. Papagiannopoulos[2],
C. M. Papadakis

[1] EMBL, DESY, Hamburg, Germany
[2] Theoretical and Physical Chemistry Institute, National Hellenic Research Foundation, Athens, Greece

Complexation of proteins with polysaccharides results in nanoparticles (NPs), which are biocompatible and have a vast array of potential applications as carriers of drugs or nutrients. The complexes are formed at a low pH-value, where the net charges of the protein and the polysaccharide are of opposite sign. Thermal treatment, during which, typically, disulfide bonds between the protein molecules are formed, was previously used to stabilize the NPs against disintegration at higher pH-values [1]. In previous studies, very dilute dispersions were used to characterize the NPs by static and dynamic light scattering in order to assess their stability [1]. In the present work, we investigate NPs from the proteolytic enzyme trypsin (TRY) and the polysaccharide hyaluronic acid (HA). Different from other proteins, TRY has the ability to hydrolyze proteins, and it has a high isoelectric point, namely ~ 10.5. At pH 4, the TRY molecules have a net positive charge, while HA is negatively charged. Thus, this pH value is chosen for NP preparation and thermal treatment. The effect of thermal treatment as well as their behavior at higher pH values are investigated. Modulated 3D cross-correlation light scattering (3D-DLS) [2] is used to determine the overall size of the NPs and thus their stability, while synchrotron small-angle X-ray scattering (SAXS) elucidates the changes of their inner structures.

Aqueous dispersions with concentrations of TRY and HA of 1 g/L and 0.12 g/L were prepared, and the final pH-value was adjusted to ~ 4 by adding small amounts of citric acid. Thermal treatment was applied by heating to $60\ ^\circ\mathrm{C}$ for 10 min. Afterwards, the pH-value was set to 7 or 12 by adding small amounts of NaOH to the heat-treated dispersion. 3D-DLS measurements were carried out using an LS Spectrometer from LS Instruments with a wavelength of 660 nm. Angle-dependent measurements were carried out, measuring at least 10 times for 30 s each time. The CONTIN algorithm was used to determine the distributions of relaxation times and the average values of hydrodynamic radii R_H.SAXS was performed at beamline P12 at the European Molecular Biology Laboratory (EMBL) at DESY, Hamburg using a sample-detector distance of 3.0 m and a wavelength of 0.124 nm.

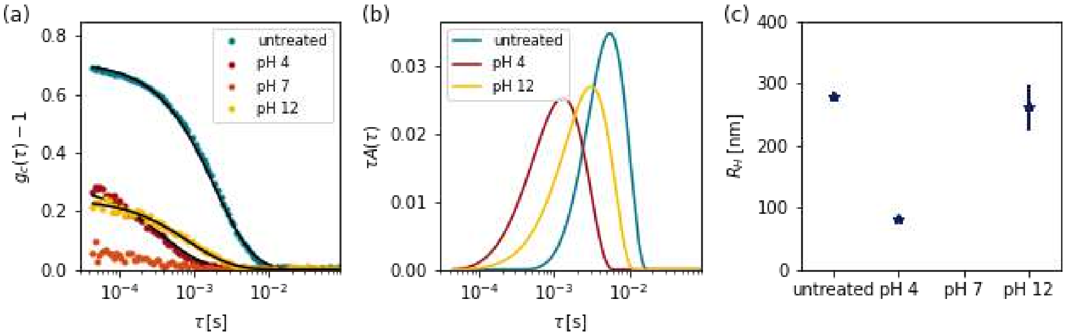

Figure 1.10:
(a) Cross-correlation curves and (b) corresponding distributions of relaxation times for the dispersions given in the graphs. (c) Resulting hydrodynamic radii.

Fig. 1.10a shows the cross-correlation curves of the untreated and the heat-treated dispersions at different pH-values. All curves feature a single decay at different relaxation times and with different intercepts. The lower intercept values after thermal treatment imply a higher fraction of multiple scattering. At pH 7, the intercept of the cross-correlation curve is very low, which may be due to strong multiple scattering caused by a significant fraction of larger particles, presumably aggregates. This hampers further analysis. The relaxation time distributions (Fig. 1.10b) feature single peaks. The resulting R_H-values show that thermal treatment results in a decrease of R_H from $\sim$ 280 to $\sim$ 80 nm (Fig. 1.10c). We conclude that, during the thermal treatment, the NPs break down into smaller fragments before the disulfide bonds are formed. Increasing the pH-value causes the hydrodynamic radius of the treated samples to increase to $\sim$ 260 nm, which may be attributed to swelling rather than aggregation because of the high overall charge of the NPs at pH 12.

SAXS results of the identical dispersions are given in Fig. 1.11. The curves feature a decay at low momentum transfer q (forward scattering), that is due to scattering from the entire NPs (Fig. 1.11a). Moreover, a shoulder is present at high q-values, that reflects the internal structure. The Porod approximation is used to describe the forward scattering with the exponent m_F that relates to the surface roughness of the NPs. A modified Ornstein-Zernike structure factor describes the shoulder at high q-values, giving information about the correlation length of local concentration fluctuations, ξ, and the fractal dimension n of the corresponding structure. These parameters indicate the conformation of the building blocks within the NPs.

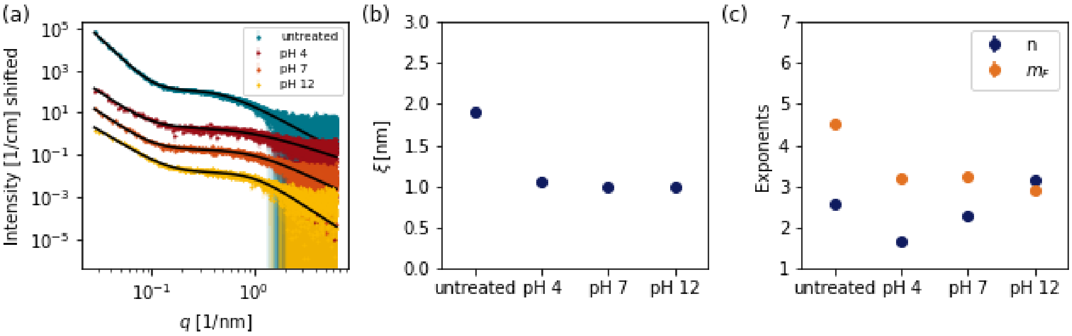

Figure 1.11:
(a) SAXS data (symbols, shifted vertically) with model fits (lines) for the dispersions given in the graph; (b, c) Resulting structural parameters: (b) correlation lengths ξ and (c) exponents n and m_F.

Fig. 1.11b shows that ξ decreases strongly upon thermal treatment, while further increase of the pH-value has negligible effect. The exponent m_F (Fig. 1.11c) is above 4 for the untreated dispersion, and at $\sim$ 3 for the heat-treated dispersions, hinting at a rougher surface after thermal treatment. Analysis of the exponent n reveals a change from $\sim$ 2.8 for the untreated dispersion to $\sim$ 1.5 after thermal treatment, indicating a transition from partially unfolded to fully unfolded proteins. With increasing pH, n increases to $\sim$ 3.2. This implies a compaction of the internal structure of the NPs, which is in contrast to the swelling of the entire NPs found by 3D-DLS and suggests a reorganization of the internal structure.

To summarize, we created biocompatible nanocarriers and characterized their overall size, surface morphology and internal structure. The changes of the size and internal structure upon increase of pH show that they are responsive, enabling controlled release applications.

[1] A. Papagiannopoulos, E. Vlassi, *Food Hydrocoll.* **87**, 602-610 (2019)

[2] I. D. Block, F. Scheffold, *Rev. Sci. Instrum.* **81**, 123107 (2010)

2 Responsive thin films

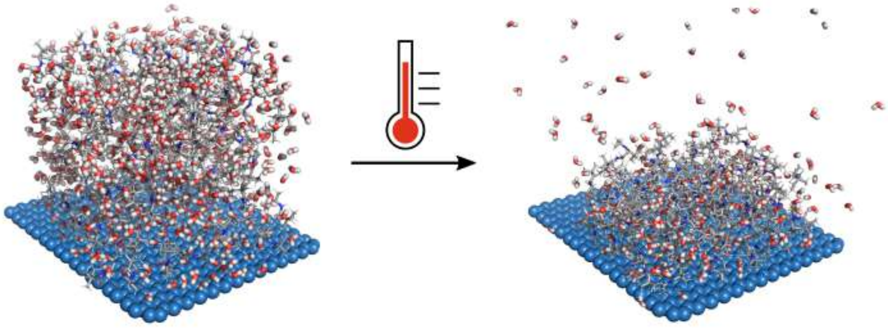

2.1 Influence of NaI on PNIPAM thin film swelling behavior in co-nonsolvency conditions

C. Geiger, R. Cubitt[1], P. Müller-Buschbaum

[1] ILL, Grenoble, France

Responsive polymers, as switchable materials, enable a large number of applications. They are used, for example, in drug delivery systems, shape memory gels and actuators, or moisture permeability regulating fabrics. External stimuli triggering the switching process can include changes in temperature, pressure, or pH value. In case multiple stimuli are known to induce a strong response, the polymer is categorized as 'multiresponsive' [1]. For PNIPAM (poly(N-isopropylacrylamide)), both the co-nonsolvency effect in water/methanol mixtures and anions of the Hofmeister series are individually known to strongly influence the solvation of the PNIPAM chain and thus the responsive behavior in solutions and thin films. Since a preferential absorption mechanism of methanol to the PNIPAM chain, as well as a direct binding mechanism of NaI to the amide group have been proposed [2,3], both effects are expected to impact the polymer solvation behavior, especially at low solvent content. Therefore, we examine the influence of NaI on the swelling of PNIPAM in co-nonsolvency conditions in the polymer-rich side of the phase diagram by performing thin film swelling experiments in vapor atmosphere.

For the experiment, first a salt-free PNIPAM thin film reference, then a NaI doped PNIPAM thin film sample were mounted in a custom-made sample environment, and subsequently dried in a N_2 flow (step I), then swollen in mixed water/methanol (D_2O/CH_3OH) vapor (step II), until the swollen equilibrium state (step III) was reached. Static and kinetic (time-resolved) Time-of-Flight neutron reflectometry (ToF-NR) was used to record the evolving film thickness and solvent distribution along the film's normal direction. The reflectivity curves obtained during the static measurements, and the time-resolved data corresponding to the swelling process of the NaI doped sample are shown in Fig. 2.1.

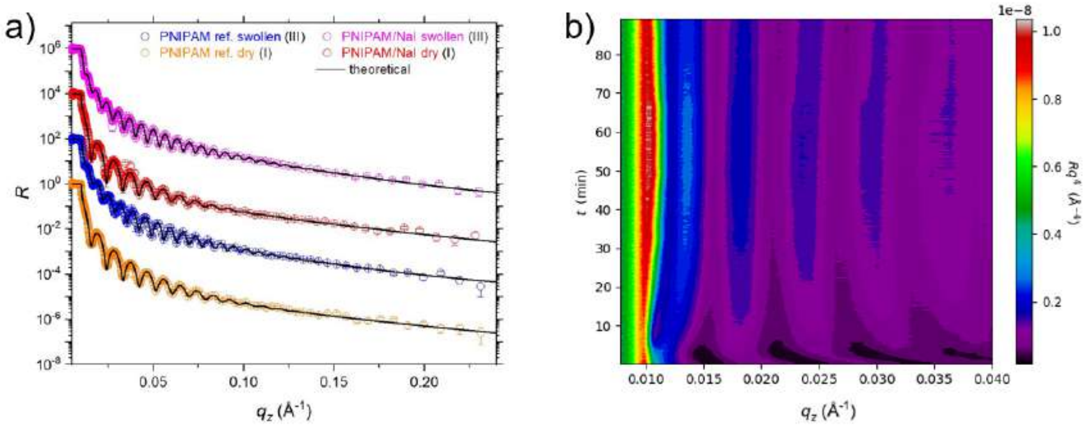

Figure 2.1:
a) Static specular reflectivity $R(q_z)$ obtained with ToF-NR (vertically shifted) for the PNIPAM reference during dry (I, orange) and D_2O/CH_3OH swollen (III, blue) states, as well as for the PNIPAM/NaI doped thin film during dry (I, red) and D_2O/CH_3OH swollen (III, magenta) states. Fits of the reflectivity are depicted as black solid lines. b) Time-resolved specular reflectivity recorded for the swelling process of the PNIPAM/NaI doped sample in mixed D_2O/CH_3OH vapor.

SLD profiles during the dry and swollen equilibrium states corresponding to the fits of the static ToF-NR data are shown in Fig. 2.2 a), while the film thickness evolution extracted from the kinetic data of both samples is depicted in Fig. 2.2 b).

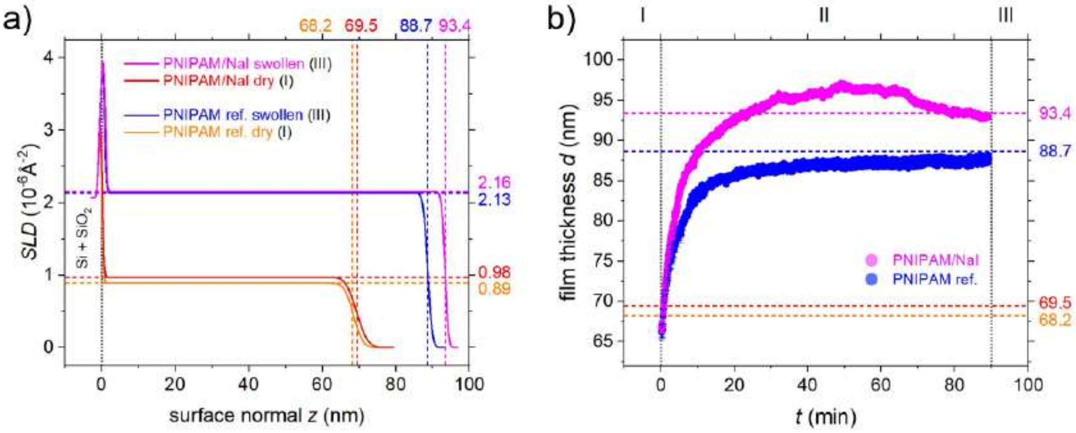

Figure 2.2:
a) SLD profiles obtained from fits of the static reflectivity Rq_z of the PNIPAM reference in the dry (I, orange) and swollen (III, blue) equilibrium states, and the PNIPAM/NaI doped sample during the dry (I, red) and D_2O/CH_3OH swollen (III, magenta) equilibrium states. Dashed lines mark the equilibrium film thicknesses (vertical) and SLD of the polymer bulk layer (horizontal). b) Film thickness evolution obtained from time-resolved ToF-NR during the swelling process (II) for the PNIPAM reference (blue) and PNIPAM/NaI doped thin film (magenta). Dashed horizontal lines mark the polymer thicknesses in dry and swollen equilibrium (I, III).

Regarding the equilibrium states, while the dried films are of similar initial thickness when compared to the PNIPAM reference, the NaI doped PNIPAM film reaches a higher swelling ratio in the swollen equilibrium. The bulk polymer layer SLD in swollen equilibrium is very similar, suggesting only a minor difference in water/methanol ratio within the absorbed solvent content. From the kinetic data, it is evident, that while the swelling of the reference is a continuous single-step process, the NaI doped film thickness reaches an intermediate maximum, before decreasing again.

This data suggests that the addition of NaI facilitates solvent uptake, even during swelling in co-nonsolvency conditions. To understand how the solvation processes at local functional groups relate to this observed mesoscopic swelling behavior, *in situ* FTIR spectroscopy measurements will be conducted, to build onto our research with poly(acrylamides) in co-nonsolvency conditions [4,5].

[1] M. Hruby, P. Štěpánek, J. Pánek, C. M. Papadakis, *Colloid Polym. Sci.* **297**, 1383-1401 (2019)

[2] F. Tanaka, T. Koga, H. Kojima, N. Xue, F. M. Winnik, *Macromolecules* **44**, 2978-2989 (2011)

[3] Y. Zhang, S. Furyk, D. E. Bergbreiter, P. S. Cremer, *J. Am. Chem. Soc.* **127**, 14505-14510 (2005)

[4] C. Geiger, J. Reitenbach, L. P. Kreuzer, T. Widmann, P. Wang, R. Cubitt, C. Henschel, A. Laschewsky, C. M. Papadakis, P. Müller-Buschbaum, *Macromolecules* **54**, 3517-3530 (2021)

[5] C. Geiger, J. Reitenbach, C. Henschel, L. P. Kreuzer, T. Widmann, P. Wang, G. Mangiapia, J.-F. Moulin, C. M. Papadakis, A. Laschewsky, P. Müller-Buschbaum, *Adv. Eng. Mater.* **23**, 2100191 (2021)

2.2 Water swelling behavior and subsequent co-nonsolvency-triggered film contraction of poly(sulfobetaine)-based diblock copolymer thin films

P. Wang, R. Cubitt[1], A. Laschewsky[2], C. M. Papadakis, P. Müller-Buschbaum

[1] ILL, Grenoble, France
[2] Universität Potsdam, Potsdam-Golm, Germany

The co-nonsolvency of PNIPAM has been subject to many experimental and theoretical studies, such as homopolymer solutions, cross-linked microgels, grafted polymer brushes and thin films [1,2]. However, the co-nonsolvency behavior of diblock copolymer (DBC) thin films, containing an nonionic thermo-responsive poly(*N*-isopropylmethacrylamide) (PNIPMAM) block and a zwitterionic poly(sulfobetaine)s (PSBs) block, in mixed water/acetone vapors is newly touched. The chemical structure of the investigated DBC is shown in Fig. 2.3a. The concept of the two performed experiments (H_2O swelling followed by acetone-d6 addition and D_2O swelling followed by acetone-d6 addition) is shown in Fig. 2.3b as experiments A and B respectively. The dried PSBP-*b*-PNIPMAM thin film is exposed to H_2O/D_2O vapor, then the atmosphere is changed to an acetone-d6 mixed vapor.

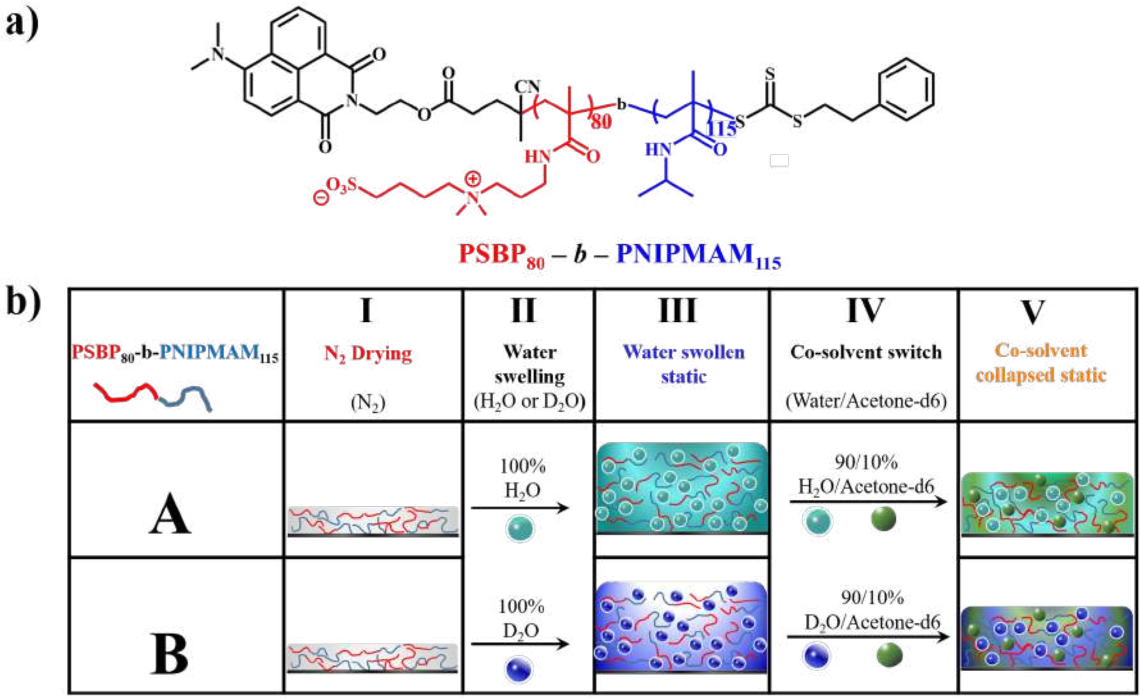

Figure 2.3:
a) Chemical structure of the studied DBC. The PSBP block is labeled in red and the PNIPMAM block is labeled in blue. b) Diagram of the experimental design applied for ToF-NR, SR. The two experiments, (H_2O swelling followed by acetone-d6 addition) and (D_2O swelling followed by acetone-d6 addition), are marked as A and B respectively.

In situ Time-of-Flight neutron reflectometry (ToF-NR) measurements are applied to monitor the kinetic processes in both protocols, water swelling (state II) and cosolvent switch (state IV), with a time resolution of 5 s. The kinetic data is acquired over a time of 180 min. Thickness and SLD values for the kinetic processes are determined from fits to the ToF-NR data and plotted in Fig. 2.4 together with the SR data. After hydration (state III) and cosolvent switch processes (state IV), the swelling ratio and SLD show agree well with the values determined from the static ToF-NR data and during the entire protocol a very good agreement between the SR data and the ToF-NR thicknesses is seen.

The kinetics of cosolvent switch (Fig. 2.4a and Fig. 2.4c) shows a similar two-step collapse in the swelling ratio and SLD for both experiments. A similar final equilibrium swelling ratio is reached after the cosolvent switch, despite having different (isotope-sensitive) swelling ratios after swelling. Looking into the two-step collapse in more detail, first a weak collapse occurs almost at the time as the films are exposed to the mixed water/cosolvent vapor. After a brief equilibration phase, a second stronger collapse happens and then the films shrink slowly over a longer time span until the final equilibrium is reached. In general, the studied

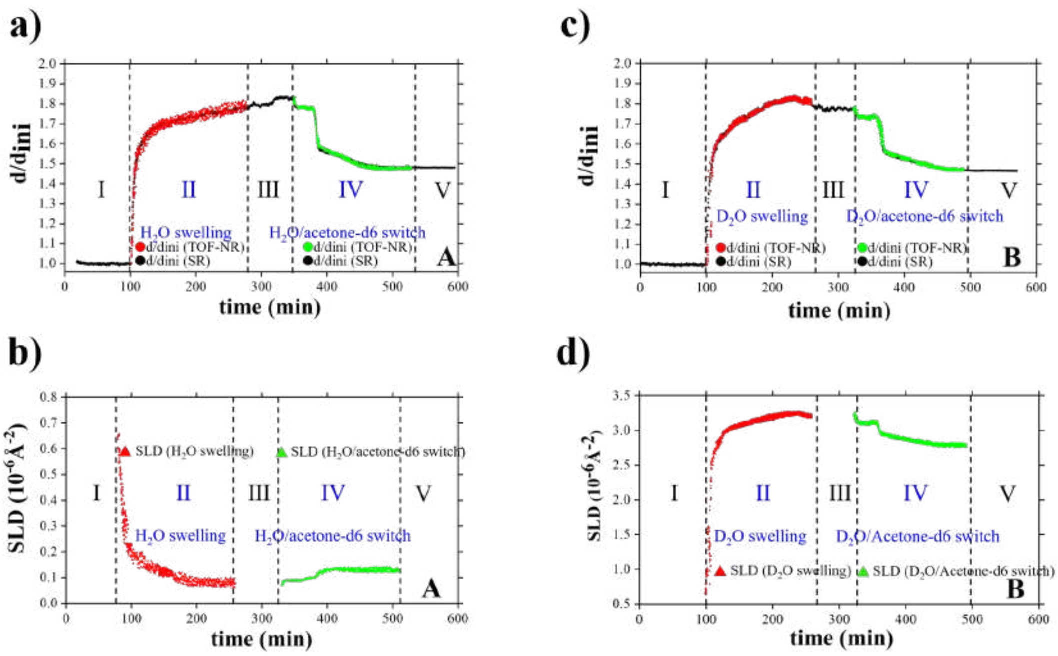

Figure 2.4:
Panels (a, b): Swelling ratio d/d_{ini}; panels (c,d): bulk SLD values, as a function of time with indicated states I-V. State V indicates the collapsed static state with the cosolvent. The live SR data is plotted as black dots. Swelling ratio and bulk SLD is plotted as red dots for water swelling and green dots for the cosolvent switch respectively. The two experiments, (H_2O swelling followed by acetone-d6 addition) and (D_2O swelling followed by acetone-d6 addition), are marked in all panels (a-d) as A and B respectively.

DBC achieves three different and stable static thicknesses upon swelling and co-nonsolvency effect. The two blocks of the DBC show a separate, but interlinked co-nonsolvency behavior in water/acetone-d6 atmosphere due to cooperative hydration effects. At the same time, besides studying an affinity of the DBC thin film towards water or its isotopes, also the sensitivity and stability of the formed hydration shell exposed to mixed water/acetone-d6 atmosphere is revealed.

[1] C. Geiger, J. Reitenbach, L. P. Kreuzer, T. Widmann, P. Wang, R. Cubitt, C. Henschel, A. Laschewsky, C. M. Papadakis, P. Müller-Buschbaum, *Macromolecules* **54**, 3517-3530 (2021)

[2] L. P. Kreuzer, C. Geiger, T. Widmann, P. Wang, R. Cubitt, V. Hildebrand, A. Laschewsky, C. M. Papadakis, P. Müller-Buschbaum, *Macromolecules* **54**, 7147-7159 (2021)

2.3 Salt-dependent swelling and phase transition kinetics of orthogonally dual thermoresponsive polymer thin films

L. P. Kreuzer, C. Geiger, T. Widmann, P. Wang, A. Vagias[1], J. E. Heger, M. Haese[2], V. Hildebrand[3], A. Laschewsky[3], C. M. Papadakis, P. Müller-Buschbaum

[1] MLZ, Garching, Germany
[2] GEMS at MLZ, Garching, Germany
[3] University of Potsdam, Potsdam-Golm, Germany

Orthogonally dual-thermoresponsive diblock copolymers (DBCs) consist of a polymer block that features a lower critical solution temperature (LCST) and a polymer block that exhibits an upper critical solution temperature (UCST). Recently, such DBCs made of an LCST-type poly(*N*-isopropylmethacrylamide) (PNIPMAM) and a UCST-type poly(sulfobetaine) (PSB) block, gained scientific attention due to their self-assembly behavior in solution. The DBCs form core-shell micelles and can invert their structure upon temperature change. This dual stimuli-sensitive behavior is commonly referred to as 'schizophrenic' self-assembly. The structure inversion can be realized via different pathways, which depend on the relative positions of the lower and upper consolute boundaries of the PNIPMAM ($CP_{PNIPMAM}$) and PSB block (CP'_{PSB}), respectively. Recent publications focused on the effect of monovalent salts e.g., NaCl and NaBr on $CP_{PNIPMAM}$ and CP'_{PSB}, and revealed that especially the position of CP'_{PSB} and therefore, the pathway of the structural inversion, strongly depends on the salt concentration [1,2]. In this way, four different phase transitions and aggregation regimes are accessible, which render 'schizophrenic' DBC systems highly attractive in the fields of drug delivery, emulsification, and smart rheology.

'Schizophrenic' DBCs have also been investigated in thin-film geometry, where a pronouncedly different thermal behavior has been found [3]. This is mainly addressed to altered polymer-polymer and polymer-water interactions as compared to solution, which is based on a higher polymer concentration and enlarged interfacial areas. It leads to interface interactions that greatly affect relevant diffusion processes. As a consequence, a shift of $CP_{PNIPMAM}$ and CP'_{PSB}, which in the context of thin films refer rather to a collapse and swelling temperature, was observed. While these studies were conducted in a salt-free environment, the present work addresses the question of how the presence of salt impacts on the swelling and thermal behavior of orthogonally dual-thermoresponsive DBC thin films. Therefore, we prepared thin DBC films of PSB-*b*-PNIPMAM from salt-containing solutions with different NaBr concentrations (0, 2, 10, and 20 mM). By taking into account the polymer composition and concentration in the spin-coating solution, thin films containing 0, 2.9, 14.5, and 29 mol % of NaBr per zwitterionic group were obtained. The initially dried thin films are swollen in D_2O vapor at 15 °C, before the temperature is gradually increased to 60 °C (Fig. 2.5a). After an equilibration time of 2 h, the temperature is gradually reduced back to 15 °C. Time-of-flight neutron reflectometry (ToF-NR) and simultaneous spectral reflectance are used *in situ* to obtain mesoscopic information about the film thickness and incorporated amount of D_2O. Furthermore, *in situ* Fourier transform infrared (FTIR) spectroscopy is applied to monitor changes in the molecular vibrations of the DBC in the thin film.

Increasing the NaBr content within the thin films to 14.5 mol % leads to a maximum D_2O incorporation and swelling process, while a further increase of the NaBr content does not show any further significant effect on the thin film behavior (Fig. 2.5b,c). These results are mainly referred to the salt-sensitive nature of the zwitterionic PSB block and can be seen as a thin-film analogue to the well-known salting-in effect in solution. Upon heating and cooling, and independently of the NaBr content, strong non-monotonic changes in the respective hydration states of the individual polymer blocks are observed (Fig. 2.5b,c). It is revealed that the swelling of the PSB block upon heating occurs at higher temperatures than its collapse upon cooling. This is inline with the described salting-in effect. In contrast, the PNIPMAM block features a collapse during heating, which is barely affected by the NaBr content, while upon cooling no clear transition is detected.

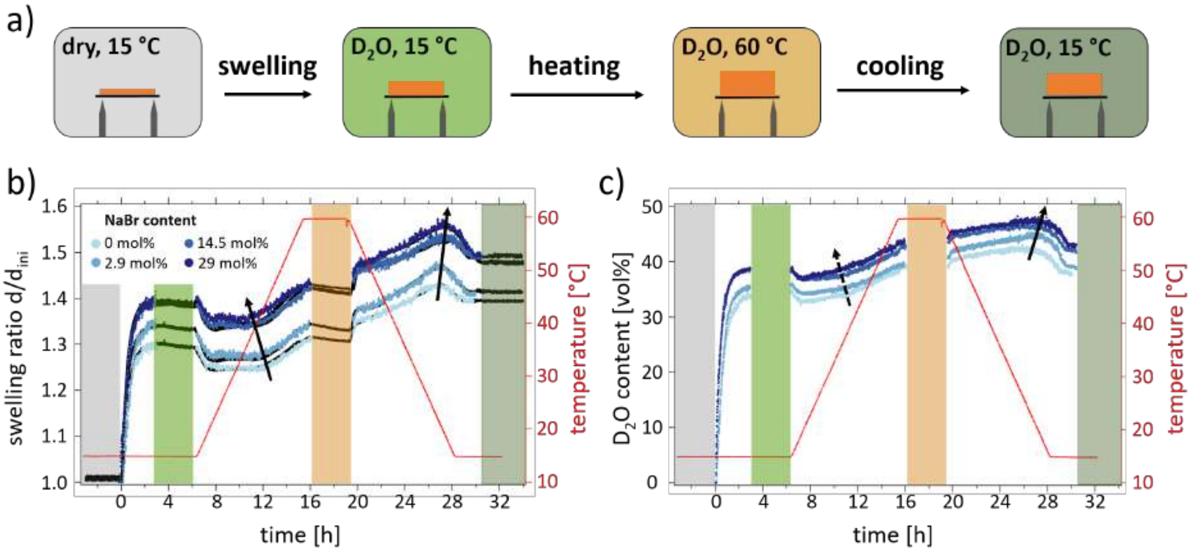

Figure 2.5:
(a) Schematic overview of the performed experiment. (b) Swelling ratio d/d$_{ini}$ and (c) D_2O content as a function of measurement time. The black data points in the left graph represent simultaneous spectral reflectance measurements. The temperature is plotted in red. The black arrows mark the shift of swelling temperature of the PSB block to higher and lower temperatures during heating and cooling, respectively. The colored squares indicate the static states in dry nitrogen at 15 °C (gray) and wet D_2O vapor at 15 (light green), 60 (orange), and again at 15 °C after cooling (dark green).

This might be due to a strong correlation between the hydration states of the PNIPMAM and PSB block. Also still ongoing polymer arrangement processes from the heating process might impact on the thin film behavior upon cooling. FTIR measurements confirm the changing hydration states of both polymer blocks, as well as the shifting swelling temperature of the PSB block with varying NaBr content. A detailed description of this study can be found in our recently published work [4].

In summary, this study reveals the complex interplay between the different external stimuli, temperature and NaBr content, while simultaneously demonstrating the versatility of this thin film system. By careful adjustment of both parameters, multiple distinct thin-film regimes regarding its swelling degree and hydration state can be realized. These results might contribute to the development of multi-functional nanoswitches.

[1] N. S. Vishnevetskaya, V. Hildebrand, N. M. Nizardo, C. H. Ko, Z. Di, A. Radulesco, L. C. Barnsley, P. Müller-Buschbaum, A. Laschewsky, C. M. Papadakis, *Langmuir* **35**, 6441-6452 (2019)

[2] C. M. Papadakis, P. Müller-Buschbaum, A. Laschewsky, *Langmuir* **35**, 9660-9676 (2019)

[3] L. P. Kreuzer, T. Widmann, L. Bießmann, N. Hohn, J. Pantle, R. Märkl, J.-F. Moulin, V. Hildebrand, A. Laschewsky, C. M. Papadakis, P. Müller-Buschbaum, *Macromolecules* **53**, 2841-2855 (2020)

[4] L. P. Kreuzer, T. Widmann, C. Geiger, P. Wang, A. Vagias, J. E. Heger, M. Haese, V. Hildebrand, A. Laschewsky, C. M. Papadakis, P. Müller-Buschbaum, *Langmuir* **37**, 9179-9191 (2021)

2.4 Influence of Hofmeister series salts on the swelling behavior of PNIPMAM thin films exposed to water vapor atmosphere

J. Reitenbach, D. Schanzenbach[1], A. Laschewsky[1], P. Müller-Buschbaum

[1] Universität Potsdam, Potsdam-Golm, Germany

Poly(*N*-isopropyl methacrylamide) (PNIPMAM) is a thermoresponsive polymer, which possess a lower critical solution temperature (LCST) in water at around 44 °C. By dissolving PNIPMAM in water, the amide groups form intermolecular hydrogen bonds with the solvent, thereby building up an organized water shell around the polymer. However, with increasing temperature, the water shell is disrupted leading to preferential polymer-polymer interactions. As a result, this change causes a coil-to-globule transition in solution or a volume phase transition in polymer thin films, as observable by the change in the film thickness. In general, the polymer-solvent interactions can be influenced by several stimuli such as pressure, light or the addition of salts, leading to a change in the LCST. The latter was thoroughly investigated in solution and found to follow a specific trend, depending on the so-called Hofmeister series, which is generally more pronounced for anions than for cations. In the Hofmeister series, the typical order of the anion series is: $CO_3^{2-} > SO_4^{2-} > S_2O_3^{2-} > H_2PO_4^{-} > F^{-} > Cl^{-} > Br^{-} \approx NO_3^{-} > I^{-} > ClO_4^{-} > SCN^{-}$. The species to the left of Cl^{-} are referred to as kosmotropes and those to the right are called chaotropes. Kosmotropes are in general strongly hydrated ions causing a so-called salting-out effect on macromolecules, whereas chaotropes show a reverse behavior. Recent works tried to explain this phenomenon and proposed a hypothesis, that direct ion-macromolecule interactions are the reason for these effects [1]. Depending on the nature of the salt, different interactions between the ion and the polymer were discussed in the literature. First, the ions are able to polarize a hydrogen bonded water molecule at a polar and protic functional group. Second, ions can raise the surface tension of the polymer-water interface, and finally, the ions can bind directly to a polar functional moiety [2]. These interactions are exemplarily shown in Fig. 2.6 for poly(*N*-isopropyl acrylamide) (PNIPAM), which is a structural analogon to PNIPMAM, only differing in a missing methyl group in the polymer backbone.

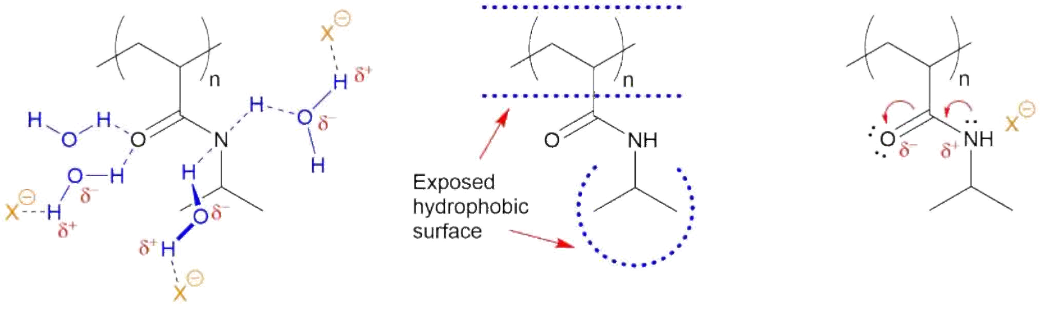

Figure 2.6:
Proposed interactions between anions and PNIPAM in water. Reproduced with permission from ref. [2].

To further elucidate these effects, we investigate thin films of PNIPMAM with different magnesium salts within a water vapor atmosphere at a constant temperature and ambient pressure. The advantage of using thin films compared to polymers in dilute solution or in bulk is that a certain mechanical stability is given with only little loss in responsiveness of the system. However, the complexity of the system is further increased for thin films compared with bulk samples due to the interactions at the interfaces with the substrate and with the surrounding vapor atmosphere. As a first step towards the investigation of the LCST change upon salt addition and in order to gain mechanistic insights, the swelling behavior of PNIPMAM thin films in presence of $Mg(ClO_4)_2$ and $Mg(NO_3)_2$ is investigated in a water vapor atmosphere via spectral reflectance (SR) and time-of-flight neutron reflectometry (ToF-NR) measurements. Both anions are chaotropes, whereas the cation is a divalent kosmotrope. Via SR and ToF-NR measurements it is shown, that the different salts have a huge impact on the swelling behavior of PNIPMAM thin films. It was observed that the swelling ratio is larger for the $Mg(NO_3)_2$ than for the $Mg(ClO_4)_2$ salt. To gain further insights on a molecular level, additional *in situ* Fourier-transform infrared spectroscopy (FTIR) measurements are performed. On the left panel of Fig. 2.7, the FTIR spectra is exemplarily shown from an *in situ* measurement over time of a PNIPMAM thin film containing $Mg(NO_3)_2$ in a certain concentration with the assignment of the most prominent signals to their functional groups. The spectra clearly show that an uptake of D_2O causes changes in the peak area and in the position of the hydrated functional groups. The trend for the peak position of the stretching vibration of the carbonyl group is depicted on the right of Fig. 2.7. The analysis shows that in comparison to the PNIPMAM thin film without salt (black curve), the addition of salt leads to a shift of the peak position to lower wavenumbers (blue and orange curve). This shift indicates a direct contact between the carbonyl group of the PNIPMAM polymer and the magnesium salts. Overall the peak position of the carbonyl group shifts over time to lower wavenumbers, which can be interpreted as hydration of this functional group during the uptake of water (in the present study we used deuterated water D_2O to achieve high contrast in the ToF-NR experiments).

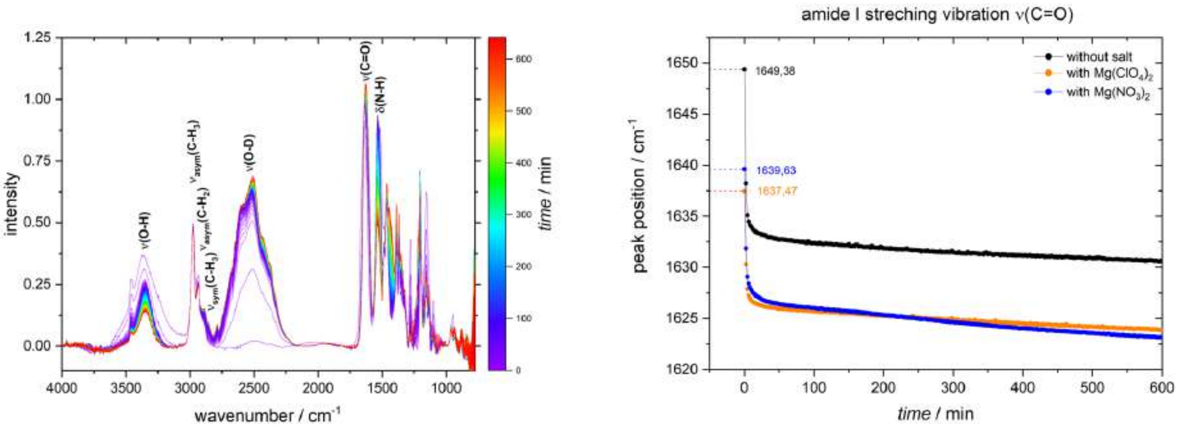

Figure 2.7:
FTIR spectra from an *in situ* measurement over time of a PNIPMAM thin film containing $Mg(NO_3)_2$ with assignment of the most prominent signals to their functional groups (left panel); trend for the peak position of the stretching vibration of the carbonyl group for the PNIPMAM thin film without salt (black), the PNIPMAM thin film containing $Mg(ClO_4)_2$ (orange) and for the PNIPMAM thin film containing $Mg(NO_3)_2$ (blue) (right panel).

With the present investigation, it can be shown that the type of salt highly impacts the hydration around functional groups and therefore the swelling ratio of PNIPMAM thin films exposed to water vapor atmosphere. From the analysis of the ToF-NR data, we will gain further insights into the water distribution inside the thin PNIPMAM films from the associated scattering length density (SLD) profiles. The presence of the salts increases the complexity in the understanding of the SLD profiles due to the presence of multiple species with different SLD contributions.

[1] Y. Zhang, S. Furyk, L. B. Sagle, Y. Cho, D. E. Bergbreiter, P. S. Cremer, *J. Phys. Chem.* **111** (25), 8916-8924 (2007)

[2] Y. Zhang, S. Furyk, D. S. Berbreiter, P. S. Cremer, *J. Am. Chem. Soc.* **127** (41), 14505-14510, (2005)

2.5 Highly tunable thin film nanostructures in a doubly pH-responsive terpolymer

F. A. Jung, M. Schart, L. Bührend, E. Meidinger, H. Amenitsch[1], S. Ariaee[2],
D. Posselt[2], C. Tsitsilianis[3], C. M. Papadakis

[1] ELETTRA, Trieste, Italy
[2] Roskilde University, Denmark
[3] University of Patras, Greece

Thin films from responsive block copolymers self-assemble into a plethora of different structures, which is of interest for, among others, sensor technology. Using multiblock polymers with charged segments extends the range of possible structural behavior further. The demixing behavior of the blocks is altered by the additional electrostatic interactions and the presence of mobile counterions. In the present work, we investigate a pentablock terpolymer with two chemically different, pH-responsive charged blocks and hydrophobic end-blocks. We focus on the influence of the charge state of the polymer on the microphase separation and self-assembly behavior in thin films [1].

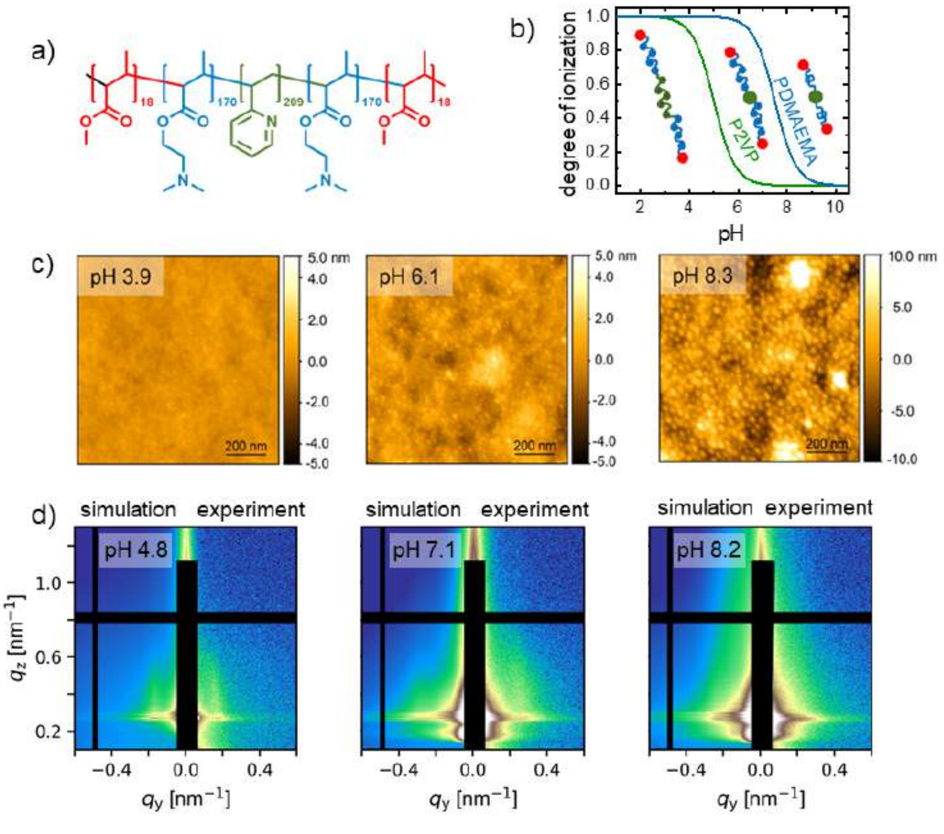

Figure 2.8:
(a) Chemical structure of the non-charged pentablock terpolymer. (b) Calculated degrees of ionization of P2VP (green) and PDMAEMA (blue) as a function of pH. Red: PMMA. (c) AFM height images and (d) simulated (left) and experimental (right) GISAXS maps of films prepared from the pH values given. All from [1].

The pentablock terpolymer under investigation has a symmetric topology of the type $M_{18}D_{170}V_{209}D_{170}M_{18}$ (Fig. 2.8a) with a central poly(2-vinylpyridine) V block and intermediate poly(2-(dimethylamino)ethyl methacrylate) (PDMAEMA) D blocks, which are end-capped by short poly(methyl methacrylate) M blocks. Both P2VP and PDMAEMA are weak cationic polyelectrolytes, i.e. they become positively charged at pH-values below their dissociation constants pK_a of 5.0 and 7.5, respectively (Fig. 2.8b). The PMMA blocks are uncharged and hydrophobic. In aqueous solution, at $\mathrm{pH} < 5$, both P2VP and PDMAEMA are expected to be charged. At $5 < \mathrm{pH} < 8$, i.e. between the pK_a-values, P2VP is rather uncharged, while PDMAEMA is rather charged. Furthermore, P2VP becomes hydrophobic, i.e., the solubility of this block in water is strongly influenced by the pH value. At $\mathrm{pH} > 8$, both P2VP and PDMAEMA are uncharged. Here, we present results on the surface and inner film structures in dependence on the pH-value of the solutions used for film preparation, i.e. the charge state of the blocks. At this, atomic force microscopy (AFM) and grazing-incidence small-angle X-ray scattering (GISAXS) are used.

Thin films on Si wafers were prepared from 3 wt% aqueous solutions having pH-values of 1.8-8.3. An MFP-3D AFM was used. GISAXS experiments were performed at the Austrian SAXS beamline at the Elettra Sincrotrone Trieste (ELETTRA), using an X-ray wavelength of 0.155 nm and a PILATUS3 1M detector at a sample-to-detector distance of 1.95 m. Incident angles were between 0.17 and 0.20°. For modeling of the 2D GISAXS maps, simulations were performed using the software BornAgain 1.16, as detailed in [2].

AFM height images reveal homogeneous surfaces for pH values up to 3.9 (Fig. 2.8c). Between pH 5.1 and pH 7.2, a dot-like nanostructure is found, which is assigned to standing cylinders protruding from the film surface. At a pH value of 8.3, the dots are observed as well, but the dot radius is larger; moreover, large aggregates are present.

At pH 4.1, the 2D GISAXS map features weak Bragg reflections, indicating a microphase-separated structure with a characteristic repeat distance of 35 nm (Fig. 2.8d). At pH 4.8-7.1, a slightly bent Bragg rod is observed, which indicates the presence of standing cylinders, having a repeat distance of 21 nm at pH 7.1. Thus, the repeat distance varies strongly. The diffuse scattering at pH 8.2 is due to large aggregates at the film surface. Modeling the 2D GISAXS maps with an array of standing cylinders results in the nanostructures shown in Fig. 2.9.

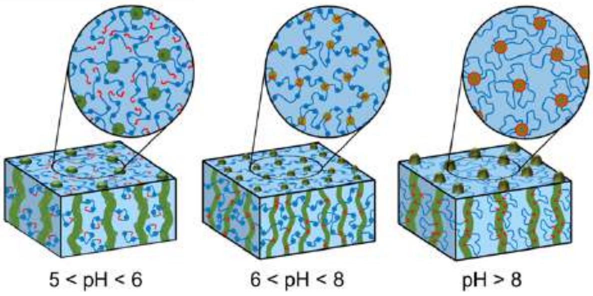

Figure 2.9:
Schematic drawing of the thin film structures depending on the pH-value during film preparation [1]. Red: PMMA, blue: PDMAEMA, green: P2VP. Ionized PDMAEMA and P2VP blocks are indicated with charge symbols. For clarity, counterions are not explicitly drawn

At $\mathrm{pH} < 5$, the films are weakly ordered because of the high degrees of ionization of both P2VP and PDMAEMA, which promotes mixing of all blocks to maximize the counterion entropy. Between pH 5 and pH 6, cylinders from P2VP are formed in a matrix, that is a mixture of PDMAEMA and PMMA blocks. At pH 6-8, the P2VP blocks are fully uncharged and mix with the PMMA blocks, forming cylinders. These are bridged by PDMAEMA blocks, which explains the low repeat distance in this pH range. At $\mathrm{pH} > 8$, the cylinders are formed by mixed P2VP/PMMA blocks, but the PDMAEMA blocks form loops rather than bridges, resulting in a higher repeat distance. Thus, multiblock copolymers with charged blocks allow strong variation of the film nanostructure, especially in the repeat distances.

[1] F. A. Jung, M. Schart, L. Bührend, E. Meidinger, J.-J. Kang, B.-J. Niebuur, S. Ariaee, D. S. Molodenskiy, D. Posselt, H. Amenitsch, C. Tsitsilianis, C. M. Papadakis, *Adv. Funct. Mater.* **31**, 2102905 (2021)

[2] F. A. Jung, D. Posselt, D.-M. Smilgies, P. A. Panteli, C. Tsitsilianis, C. S. Patrickios, C. M. Papadakis, *Macromolecules* **53**, 6255-6266 (2020)

2.6 Co-nonsolvency in PNIPAM thin films under water-methanol mixture exposure

M. Le Dû, C. Geiger, P. Müller-Buschbaum

A key step in the evolution of synthetic materials science is to achieve self-adaptation as in biological systems. Smart materials such as responsive polymers are candidate materials to attempt this aim by having their physical and/or chemical properties modified in response to external stimuli. Poly(*N*-isopropylacrylamide) (PNIPAM) is a promising candidate for this new generation of materials. It undergoes a reversible coil-to-globule transition in water which takes place at 32 °C, known as its Lower Critical Solution Temperature [1]. However, PNIPAM is not only sensitive to temperature, it also shows peculiar properties in solvent mixtures, this phenomenon is known as co-nonsolvency [2]. This co-nonsolvency allows PNIPAM to be part of the class of double-stimuli polymers. The targeted build-up of such a smart material requires a clear understanding of the polymer response mechanisms. Phase behavior of PNIPAM in solutions has been intensively studied in the scientific community, while much less in known in the thin film configuration. This work focuses on the systematic investigation of different driving forces potentially responsible for the co-nonsolvency phenomenon in PNIPAM thin films systems exposed to water-methanol mixtures. PNIPAM thin films have been prepared via conventional spin-coating. Several swelling experiments using different water-methanol mixtures were performed to elucidate the mesoscopic responses of the PNIPAM thin film systems. Then, *in situ* FT-IR spectroscopy allowed to support a hypothesis on the molecular mechanisms behind the PNIPAM co-nonsolvency in films. Starting from a dry state, where no free water molecules were present in the system, the films experienced a swelling process via absorption of the solvent molecules in vapor state. Fig. 2.10 shows the film response, expressed in thickness change, under vapor exposure to different methanol molar fractions in water-methanol co-solvents.

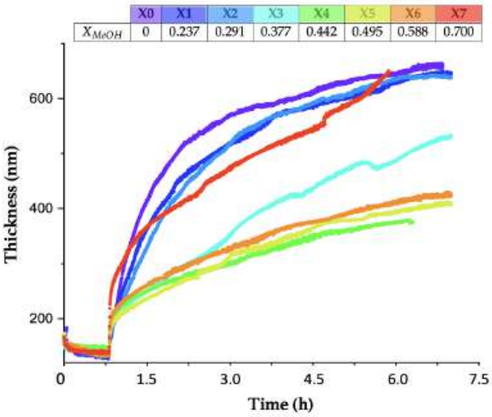

Figure 2.10:
Thickness evolution of the PNIPAM films as a function of time for the different methanol volume fractions in water-methanol co-solvent mixtures.

From Fig. 2.10, insights can be extracted into how the co-nonsolvency effects are expressed. Indeed, a shrinking of the film thickness is observed by addition of methanol to the system. This shrinking ceizes at a peculiar point in time, called in this work as "critical co-nonsolvency point" which represents the greatest collapse conformation of the polymer chains. This feature agrees with results obtained in previous studies concerning PNIPAM behaviour in water-methanol solutions, where a high turbidity is observed over a well-defined range of intermediate methanol molar fractions [3]. In the thin films examined here, this critical point is observed for $X_{MeOH} = 0.442$. Complementary *in situ* FTIR characterization has been performed under vapor exposures with the composition of (i) the critical co-nonsolvency point and of (ii) pure DI water. The obtained spectra have been decomposed and analyzed for each of the characteristic absorption peaks. The main outcome of these analysis was centered on the signals of the amide proton of the PNIPAM polymer. A comparison of the signals responsible for the bending and stretching motions of the N-H bonds has been performed for the two different vapor exposures examined. Fig. 2.11 shows the evolution of the N-H absorption peak shifts and their integrals over the time for stretching and bending modes. Based on the observations from Fig. 2.11, it can seen that the integral curves of the water-methanol mixture at a given time are above the integral of the signals corresponding to DI water vapor exposure. Hence, it seems that the processes involving absorption of solvent mixture is faster than the absorption of pure deionized (DI) water. Furthermore, this leads to think that the PNIPAM thin film absorbs a larger total amount of solvent in presence to water-methanol mixture compared to pure DI water. In previous work about the co-nonsolvency effects in PNIPAM solutions using water-methanol co-solvent mixture, it has been reported that the methanol molecules would have a bridging capacity between the polymer branches [4]. In addition, the behavior of the amide proton is in general representative of the polymer-polymer interactions in the system. As a consequence, the drastic shift of the N-H stretching vibration peaks towards lower wavenumber values would mean a strong absorption of methanol and thus stronger polymer-polymer interactions. Thus, the presence of the methanol greatly enhances interaction between the polymer branches leading to collapse of the coil structure. Indeed, the peak shift in the case of exposure to DI water does not reach this extreme variation as in the co-solvent case. Peak shifts of the bending motion of the amide proton can be attributed to changes in the number of solvent molecules attached to the amide bond. Hence, the higher shift in the mixture absorption case would mean that more methanol molecules form bonds with the amide proton of PNIPAM. The peak position curves of both swelling tests do not converge to the same point, also resulting from a different number of bonds formed between the solvents and the amide proton of the PNIPAM macromolecule. The two panels of Fig. 2.11 show two different vibrational modes for the same chemical group. Indeed, the correlation of the information from the two panels leads to think that the co-nonsolvency phenomenon in PNIPAM thin films involves a competition between solvent molecules which is characterized by a stronger affinity of the methanol molecule to the amide proton.

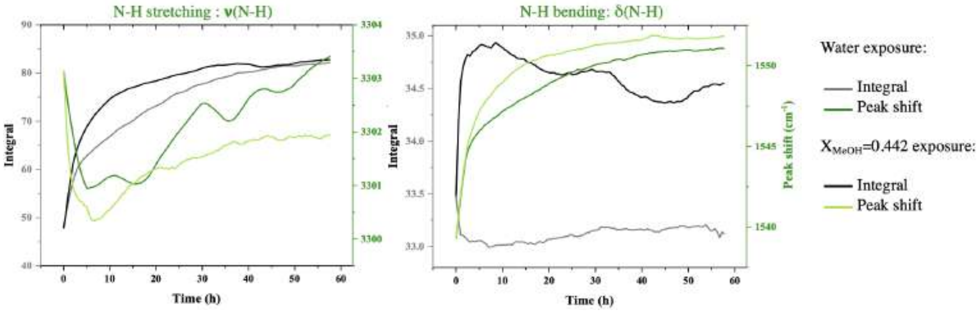

Figure 2.11:
Evolution of the (left) stretching and (right) bending N-H absorption peaks and their integrals under water exposure and water-methanol exposure probed with *in situ* FTIR.

[1] M. Heskins, J. E. Guillet, *J. Macromol. Sci., Chem.* **2**, 1441-1455 (1968)

[2] C. Scherzinger, A. Schwarz, A. Bardow, K. Leonhard, W. Richtering, *Curr. Opin. Colloid Interface Sci.* **19**, 84-94 (2014)

[3] I. Bischofberger, D. C. E. Calzolari, V. Trappe, *Soft Matter* **10**, 8288–8295 (2014)

[4] D. Cahit, F. Rodriguez-Ropero, N. F. A. van der Vegt, *J. Phys. Chem. B* **121**, 7741-7748 (2017)

2.7 Nanoscale hydration effects in grafted polyoxazoline brushes of variable topologies

A. Vagias[1], A. Nelson[2], E. M. Benetti[3,4], P. Wang, C. Geiger, J. Reitenbach, L. P. Kreuzer[1], T. Saerbeck[5], R. Cubitt[5], P. Müller-Buschbaum

[1] MLZ, TUM, Garching, Germany
[2] ANSTO, Sydney, Australia
[3] ETH, Zurich, Switzerland
[4] University of Padova, Padova, Italy
[5] ILL, Grenoble, France

Cyclic macromolecules are found in living organisms such as in the DNA of Escherichia Coli, but also in peptides of mammalian cells [1]. Inspired by nature, the strong advances in polymer chemistry have helped nonlinear polymeric geometries to be successfully achieved [1]. Variabilities in the macromolecular topology have been shown to affect physicochemical characteristics in both bulk states and under confinement. Conformations, interactions and dynamics of ring polymers have attracted the interest in soft condensed matter community. The absence of chain ends leads to significant differences in properties of cyclic polymers compared to linear polymers in the bulk. Ring polymers exhibit smaller melt viscosities and lower viscoelastic relaxation times than linear ones [2]. In the melt state, higher glass transition temperature has been reported for the same (small) molecular weight [1]. In solutions of core-shell micelles, cyclic polymers can enhance the micellar stabilization when present as corona blocks [3]. However, the topological effects and solvent-polymer interactions in grafted brushes at near-wall proximity have been scarcely experimentally investigated. In recent tribological experiments [4], it was shown that upon sliding past SiOx bare surfaces, the cyclic PLL-*g*-PEOXA homologue exhibited significantly smaller friction forces compared to the linear one. However, details of the grafted brush nanostructure remain unexplored. For a thorough characterization, it is intriguing to correlate topology, water uptake capability and water distribution. We use time-of-flight neutron reflectometry (TOF-NR) to probe in-situ the D_2O vapor uptake by monolayers of PLL-*g*-PEOXA block copolymer (BCP) grafted brushes. The BCP brushes are anchored on a titanium oxide (TiO_2) layer that has been pre-sputtered on top of a silicon oxide/silicon (SiO_2/Si) substrate [4].

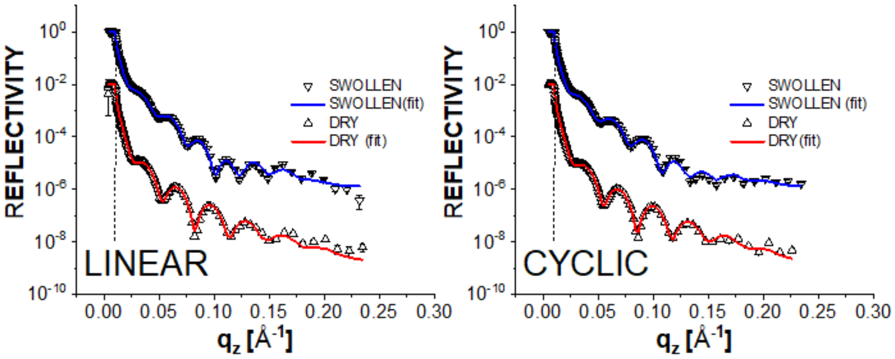

Figure 2.12:
ToF-NR specular reflectivity curves vs. momentum transfer q_z for the linear (left) and cyclic (right) PLL-*g*-PEOXA grafted brushes at a grafting density σ = 0.15 chains/nm^2 with. Solid lines represent the fit in the dry (red) and swollen (blue) state using a four layer slab model.

These BCP have poly-l-lysine (PLL, $M_{w,PLL}$=12 kg /mol) as common anchoring agent and a PEOXA ($D_p \sim 100$) side chain as the polymer block of variable topology [4]. The ToF-NR experiments have been performed at the D17 instrument (ILL) using a wavelength λ band between

λ = 2 Å and λ = 24 Å and a sample-to-detector distance SDD = 3.4m. Fig. 2.12 shows time-of-flight neutron reflectivity (TOF-NR) curves in the dry and fully swollen static state with 45 min acquisition time over a broad q_z range covered by two incident angles (α_i = 0.7° and 4°) for linear and cyclic fully protonated PLL-g-PEOXA grafted brushes with the associated fits. The shift in the minima of Kiessig fringes to lower q_z values upon swelling in Fig. 2.12 suggests a layer thickness increase for both systems. TOF-NR modeling was performed using a four-slab model: air | PLL-g-PEOXA (dry or swollen with D_2O) | TiO_2 | SiO_2 | Si. The sample cell was a home-built controlled humidity chamber connected to a gas-flow setup that allows premixing of different incoming streams of pure nitrogen and D_2O vapor at pre-determined ratios thus enabling tunable relative humidity RH values in the range from RH = 5% to RH = 95% [5]. We also performed TOF-NR experiments during D_2O vapor swelling with continuous acquisition of 2 s 2D ToF-NR frames at α_i = 1.2°. The neutron scattering length density (SLD) profiles during D_2O vapor swelling can reveal the evolution of D_2O distribution within the PLL-g-PEOXA brush layer. Fig. 2.13 depicts neutron SLD profiles obtained from the four-slab component modeling of the kinetic TOF-NR curves during D_2O solvent vapor swelling.

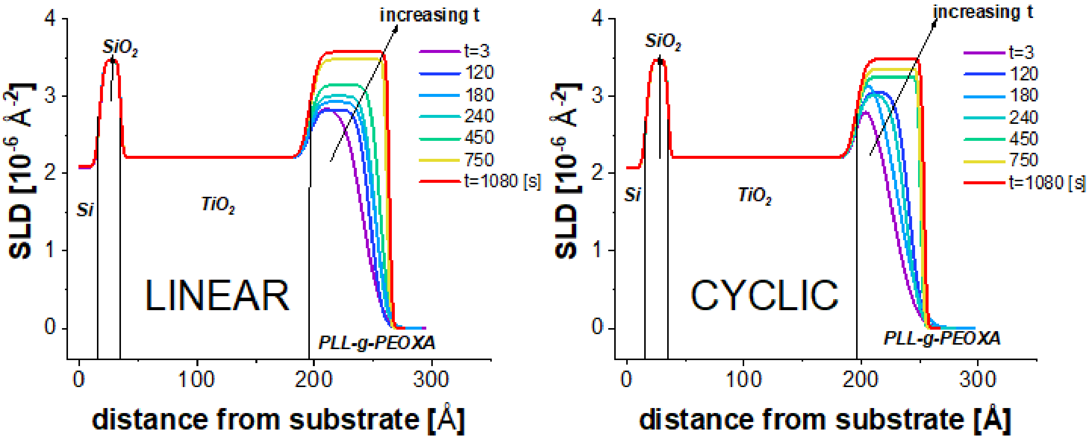

Figure 2.13:
SLD profiles vs. distance from the substrate for the linear (left) and cyclic (right) PLL-g-PEOXA grafted brushes at a grafting density σ = 0.15 chains/nm^2 using a four layer slab model. Color coding represents the evolution from t = 3 s (purple) to t = 1080 s (red).

The neutron SLD profiles suggest kinetic differences in water uptake, thickness and D_2O amount adsorbed from each brush topology. The SLD modelling suggest smaller thickness, rougher air/PLL-g-PEOXA interface and smaller areas under the SLD profile for the cyclic compared to the linear system, suggesting an overall lower amount of absorbed D_2O in the cyclic system. We identify morphological differences during vapor swelling in comb-shaped PLL-g-PEOXA grafted brushes of linear and cyclic PEOXA topology expressed in different absorbed D_2O amount and roughness of PEOXA-air interface. We performed three swelling/drying steps to assess reproducibility. The current analysis focuses on determining aging effects, checking reproducibility in solvent vapor swelling as well as correlating with independent quartz crystal microbalance (QCM) results for fully immersed PLL-g-PEOXA brushes.

[1] F. M. Haque, S. M. Grayson, *Nature* **12**, 433-444 (2020)

[2] M. Kapnistos, M. Lang, D. Vlassopoulos, W. Pyckhout-Hintzen, D. Richter, D. Cho, T. Chang, *Nature Materials* **7**, 997-1002 (2008)

[3] G. Morgese, B. S. Shaghasemi, V. Causin, M. Zenobi-Wong, S. N. Ramakrishna, E. Reimhult, E. M. Benetti, *Angew. Chem., Int. Ed.* **56**, 4507-4511 (2017)

[4] S. N. Ramakrishna, G. Morgese, M. Zenobi-Wong, E. M. Benetti, *Macromolecules* **52**, 1632-1641 (2019)

3 Functional thin films

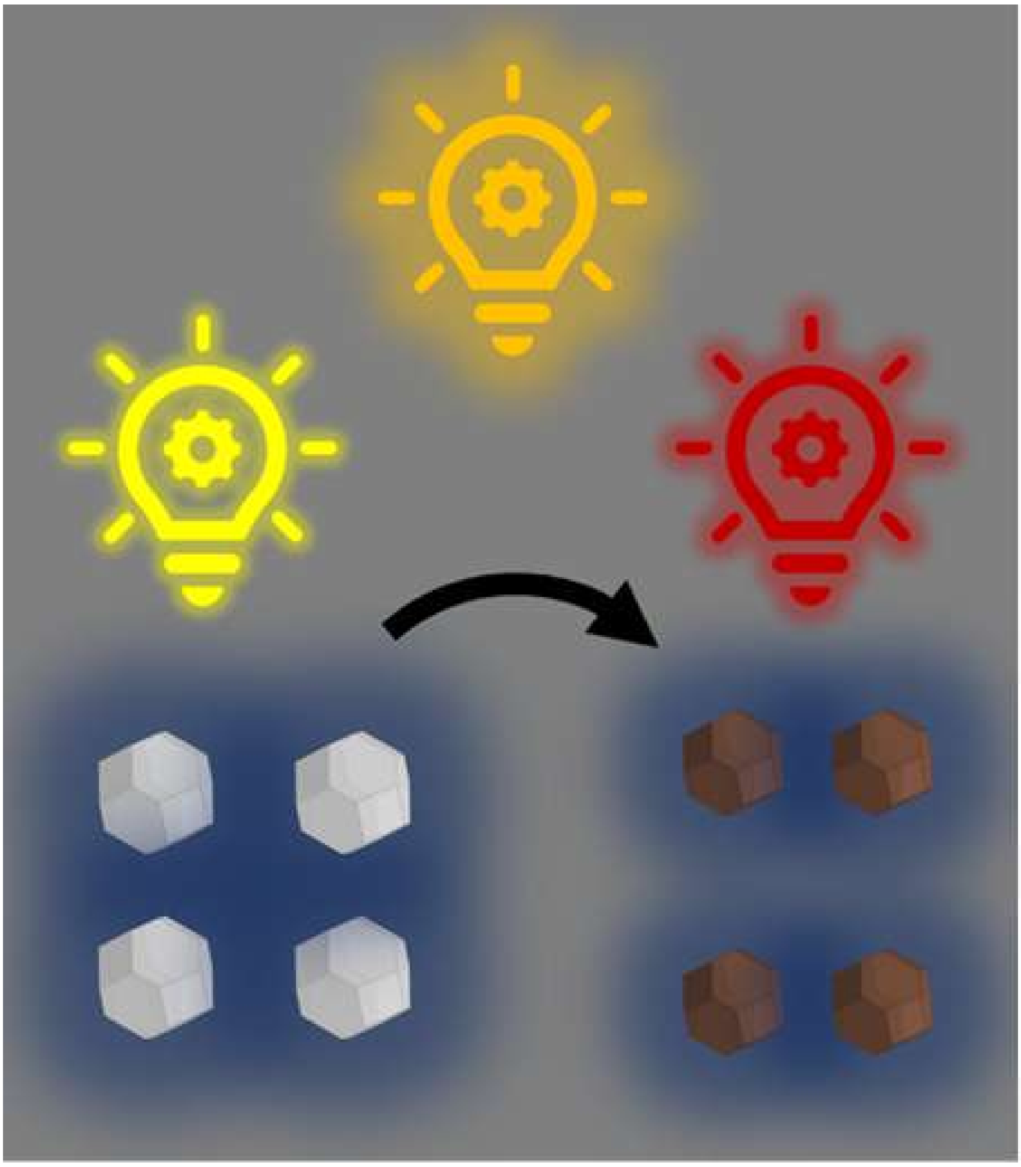

3.1 Improvement of the thermoelectric properties of PEDOT:PSS films via DMSO addition and DMSO/salt post-treatment

S. Tu, T. Tian, A. L. Oechsle, S. Yin, W. Cao, N. Li, M. Reus, L. K. Reb, S. Hou[1],
A. S. Bandarenka[1], M. Schwartzkopf[2], S. V. Roth[2], P. Müller-Buschbaum

[1] ECS, Garching, Germany
[2] DESY, Hamburg, Germany

Thermoelectric (TE) technology is a promising energy harvester towards the re-utilization of ubiquitous waste heat sources and has gathered enormous attention and experienced substantial developments during recent years [1]. The direct and efficient conversion towards pollution-free electricity originates from the concept of the Seebeck effect, which sets the base for electrical power generation. In the present work, the choice of hydrophilic DMSO as a solvent additive and readily available salt in combination with DMSO for a post-treatment allows for a facile engineering of the PEDOT:PSS thin films fabricated via spin-coating.

For our initial measurements, the pristine film presents a quite poor conductivity σ of 1.3 S/cm, which primarily results from the poor charge carrier transport caused by the presence of a large fraction of uncoupled PSS dopant species within the film as known from the literature [2]. Furthermore, the use of only 5% DMSO co-solvent substantially increases σ up to 706 S/cm despite an essentially unchanged S. Remarkably, a subsequent DMSO post-treatment gives rise to a higher σ value of 931 S/cm along with an increased S of 26.3 μV/K, achieving an optimized power factor value of 64.4 WK^{-2}m^{-1} as shown in Fig. 3.1. Such a simultaneous increase in S and σ signifies the effective enhancement of the charge carrier mobility. The improvements induced by DMSO post-treatment can be readily interpreted as a physical PSS de-doping, i.e., the removal of some non-ionized PSS, facilitating the charge transport across the PEDOT chains. By the addition of inorganic salts to DMSO used in the post-treatment, the TE properties are changed. Intriguingly, a higher S is obtained for all DMSO/salt post-treatments in the investigated concentration regime for the two salts $NaHCO_3$ and Na_2SO_3 compared to pure DMSO post-treatment. No dependence on salt concentration for S is seen, which is attributed mainly to the limited capability of chemical de-dopants to reduce the oxidation level of PEDOT chains. At 10% volume fraction of salt, a high σ (beyond 800 S/cm) of the PEDOT:PSS films is maintained. Thus, a maximum power factor value of 105.2 WK^{-2}m^{-1} is obtained for this salt concentration due to the synergistic effect of a physical-chemical de-doping that contributes directly to an enhanced S and a moderately reduced σ during the reduction process.

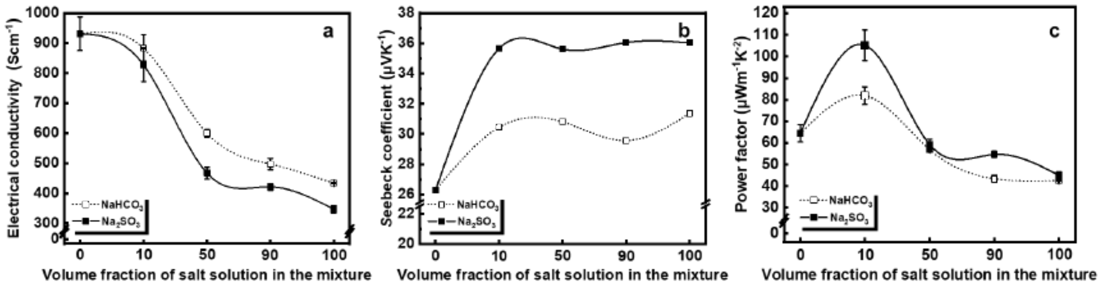

Figure 3.1:
TE properties of PEDOT:PSS thin-films under different treatment conditions in terms of a) electrical conductivity σ, b) Seebeck coefficient S, and c) power factor.

PEDOT:PSS films were characterized with AFM as shown in Fig. 3.2a-e. The contrast observed in AFM micrographs provides further evidence for the phase separation between intrinsically miscible PEDOT and PSS moieties. Not surprisingly, the film surface of the neat PEDOT:PSS film appears to be relatively blurred. This is characteristic of a highly phase-mixed state, which is mainly caused by the capping of the PEDOT chains by the non-conductive PSS layer. Caused by the DMSO and salt addition/post-treatment, all PEDOT:PSS films present a more evident phase separation on the film surface as seen by the brighter granular morphologies.

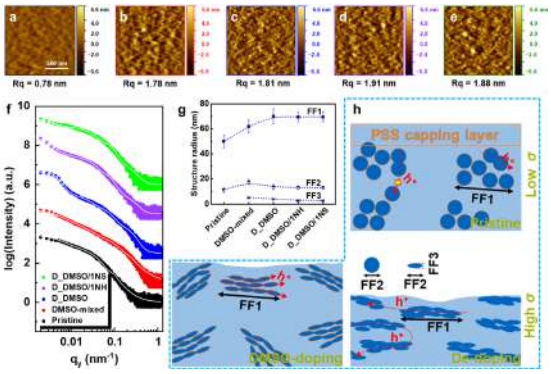

Figure 3.2:
Topographic AFM images of PEDOT:PSS films: (a) Pristine; (b) DMSO-mixed; (c) D_DMSO; (d) D_DMSO/1NH; (e) D_DMSO/1NS. The film doped with 5% DMSO is labeled as DMSO-mixed film and the DMSO-mixed samples followed by post-treatment with DMSO, DMSO/$NaHCO_3$, or DMSO/Na_2SO_3 are labeled as D_DMSO, D_DMSO/1NH and D_DMSO/1NS film, respectively. (f) Horizontal line cuts from 2D GISAXS data (symbols) comparing the different processing conditions together with the GISAXS model fits (lines). Data shifted along the y-axis for clarity. g) Characteristic radii from the GISAXS analysis for the different PEDOT:PSS films. Dotted lines serve as guides to the eye. h) Schematic of morphological models upon different treatments. "h+" represents the PEDOT positive charge carriers.

GISAXS measurements were made to inspect if and how these different treatments altered the inner microstructures. Fig. 3.2f plots the representative horizontal line cuts of the 2D GISAXS data in conjunction with their fits. The scattering objects are assumed to have a spherical shape and the respective radii are plotted in Fig. 3.2g. The largest radius (form factor 1, denoted "FF1") has a value of 50-70 nm. It can be assigned to the network-like structures generated through agglomeration from smaller PEDOT domains, which would provide long conduction pathways for charge carrier transport. DMSO treatments further increase its value, suggesting the loss of PSS and the additional aggregation of the PEDOT domains. The smaller radii (FF2: 11-17 nm and form FF3: 3-5 nm) well match the diameter and thickness respectively of the pancake-like PEDOT domains proposed by others earlier [3]. Thus, PEDOT pancake-shaped domains occur in two different orientations with the long axis parallel and also perpendicular to the film surface. Both characteristic length scales (FF2 and FF3) decrease upon any post-treatment as compared to the DMSO-mixed film, evidencing that PSS is not only selectively removed from the PSS-rich domains but also from the PEDOT-rich domains.
As a result, a significantly improved inter-grain coupling between the PEDOT-rich grains is expected after the de-doping processes. Fig. 3.2h summarizes the morphological changes upon the different treatments. Three distinct states can be differentiated: The pristine state is featured by spherical PEDOT domains. An elongation of the PEDOT domains is introduced by the DMSO-doping. In this state, longer and favorable percolation paths are developed, which would facilitate the connection among individual grains and then achieve high charge carrier mobility. After the de-doping, the PEDOT domains are slightly reduced in size but having less PSS contents enables a more efficient charge carrier transport, thus achieving higher σ values.

[1] S. Tu, T. Tian, A. L. Oechsle, S. Yin, X. Jiang, W. Cao, N. Li, M. A. Scheel, L. K. Reb, S. Hou, A. S. Bandarenka, M. Schwartzkopf, S. V. Roth, P. Müller-Buschbaum, *Chem. Eng. J.* **429**, 132295 (2022)

[2] S. Xu, M. Hong, X. L. Shi, Y. Wang, L. Ge, Y. Bai, L. Wang, M. Dargusch, J. Zou, Z. G. Chen, *Chem. Mater.* **31**, 5238-5244 (2019)

[3] A. M. Nardes, M. Kemerink, R. A. J. Janssen, J. A. M. Bastiaansen, N. M. M. Kiggen, B. M. W. Langeveld, A. J. J. M. Van Breemen, M. M. de Kok, *Adv. Mater.* **19**, 1196-2000 (2007)

3.2 Nanostructure morphology of zwitterionic block copolymer coatings relevant for antibacterial science and microelectronics

A. Vagias[1], T. Manouras[2], L. Koufakis[2], S. Anastasiadis[2,3], M. Vamvakaki[2,3], P. Müller-Buschbaum

[1] MLZ, TUM, Garching, Germany
[2] FORTH, Heraklion, Greece
[3] University of Crete, Heraklion, Greece

The optimization of antibacterial coatings is a long-standing quest in polymer science with direct impact on the polymer manufacturing industry [1,2]. From a materials science standpoint, the antibacterial efficacy can be typically quantified in terms of contact angle energy measurements and microscopy [2]. In order to take advantage of orthogonal solvencies and mechanical stability differences between different polymers, antibacterial coatings can reinforce their performance when copolymers of different hydrophilicity are utilized as building blocks. Poly[2-(dimethylamino)ethyl methacrylate] (PDMAEMA) is a polymer with key role not only in antibacterial efficacy upon quaternization [2], but also as template in miniaturization of electronic devices via photolithography [3]. Although contact angle measurements and microscopy are quite standard techniques to assess the performance of such coatings, the non-destructive exploration of sub-surface nanostructures and self-assembly in PDMAEMA-based block copolymer (BCP) templates when copolymerized with polymer blocks of different hydrophilicity and mechanical stability remains a vastly unexplored territory.

By means of X-ray reflectivity (XRR) and grazing-incidence small-angle X-ray scattering (GISAXS), we focus on the sub-surface characterization in the dry state of templates for BCP lithography, ultrathin spin-coated amphiphilic poly(2-dimethylamino ethyl ethacrylate)-*b*-poly(tetrahydropyranyl methacrylate), PDMAEMA-*b*-PTHPMA copolymers with and without pre-immersion in ethyl lactate as solvent annealing. Our results are corroborated by 2D GISAXS simulations using the software BornAgain [4].

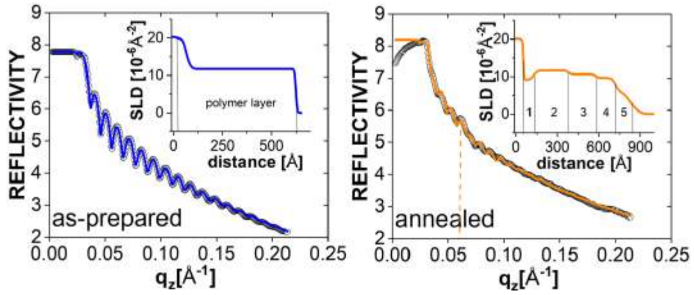

Figure 3.3:
Normalized X-ray reflectivity data (black data points) vs. momentum transfer q_z in Å^{-1} acquired for the as-prepared (left) and annealed (right) PDMAEMA$_{21}$-*b*-PTHPMA$_{29}$ thin films. The corresponding fits are denoted by the solid blue and orange lines respectively. A Bragg reflex is denoted by the vertical dashed line for the annealed sample. Insets: X-ray scattering length density (SLD) profiles vs. distance from the substrate for single (as-prepared) and multiple (annealed) polymer layers.

Fig. 3.3 presents XRR experimental curves for the as-prepared (AP, left) and the annealed (ANN, right) sample. Solid lines represent the respective fits using a slab model consisting of Si and SiO$_2$ layers as substrate for both samples and different number of polymer layers for each sample. The interfacial roughness, thickness and perpendicular profiles of the films have been assessed. For the annealed sample, a larger thickness (D$_{XRR,ANN}$ = 770 Å) was found compared to the as-prepared one (D$_{XRR,AP}$ = 570 Å). The XRR data corroborate mesoscopic observations using optical microscopy (not shown) and those on the nanometric length scale using AFM (not shown). The Kiessig fringes of the as-prepared sample are characterized by strong oscillation minima suggesting a flat and well-defined interface with low RMS roughness. The XRR modeling proposes RMS roughnesses for either sample type are in line with values for classical symmetric BCP systems [5]. For the XRR modeling of the annealed sample, a single polymer layer model failed and a multilayer model had to be used. The XRR curve of the annealed samples does not contain sharp oscillations of constant amplitude. Instead, we identify weaker oscillations and the presence of a single Bragg reflex at q$_z \sim 0.061$ Å^{-1}. This peak translates to a lamellar spacing of $d_{lam} \sim$ 56nm using the Bragg equation [6]. The damped oscillations could imply presence of nanoindentations (islands and/or holes) on top of the annealed film. These indentations are anticipated by post-preparation annealing protocols for thin BCP films. Representative experimental 2D GISAXS patterns are shown in Fig. 3.4 acquired at our in-house SAXS instrument (Ganesha, SAXSLAB) at λ = 1.54 Å and a sample-detector distance SDD = 1466 mm. Along the out-of-plane wavevector q_y, no significant scattering features are present meaning that lateral segregation along the sample's plane is not very pronounced. The GISAXS intensity is modulated along the q_z direction for both as-prepared and annealed samples, but the extend that these two samples manifest these modulations is different. We obtain as Hurst parameter H of the annealed sample, H_{AN} = 0.56 >> H_{AP} (= 0.11). Considering that $H_{substrate}$ = 0.13, stronger correlated roughness and surface serration is expected for the as-prepared sample. Finally, for the lateral correlation lengths Λ_c, we identify $\Lambda_{c,ANN} \sim 3\Lambda_{c,AP}$. Hence, solvent annealing decreases the lateral distance at the air-polymer interface over which substrate lateral correlation is transferred to the annealed polymer layer.

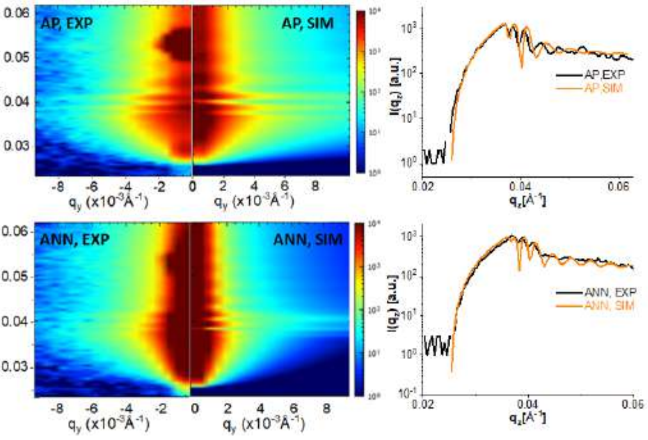

Figure 3.4:
Experimental (EXP) and simulated (SIM) 2D GISAXS patterns for as-prepared (top row) and annealed (lower row) samples showing the scattered intensity distribution along (q_y) and across (q_z) the sample's plane. Intensity scale: 1 to 10^4. Right panel: 1D intensity cuts along the detector plane, I(q_z), from the EXP (black) and SIM (orange) GISAXS patterns.

[1] M. Alvarez-Paino, A. Munoz-Bonilla, M. Fernandez-Garcia, *Nanomaterials* **7**, 48-92 (2017)

[2] E. Koufakis, T. Manouras, S. H. Ãnastasiadis, M. Vamvakaki, *Langmuir* **36**, 3482-3493 (2020)

[3] A. Nika, *PhD thesis, University of Athens* , 47625 (2020)

[4] G. Pospelov, W. Van Herck, J. Burle, J. M. Carmona Loaiza, C. Durniak, J. M. Fisher, M. Ganeva, D. Yurov, J. Wuttke, *J. Appl. Cryst.* **53**, 262-276 (2020)

[5] G. Coulon, J. Daillant, B. Collin, J. J. Benattar, Y. Gallot, *Macromolecules* **26**, 1582-1591 (1993)

[6] J. Zhang, D. Posselt, D. M. Smilgies, J. Perlich, K. Kyriakos, S. Jacksch, C. M. Papadakis, *Macromolecules* **47**, 5711-5718 (2014)

3.3 Positive influence of ionic liquid post-treatment of PEDOT:PSS thin films on the domain morphology and doping level

A. L. Oechsle, S. Bernstorff[1], P. Müller-Buschbaum

[1] Elettra, Trieste, Italy

The usage of thermoelectric (TE) materials to directly convert heat waste into electrical power is a very attractive technique to combat energy dissipation and save valuable resources. Especially polymer-based organic TE materials are advantageous candidates, providing a large-scale, low-cost solution-based processability of low or non-toxic, lightweight, and flexible TE devices. In recent years, the blend poly(3,4-ethylene dioxythiophene):poly(styrene sulfonate) (PEDOT:PSS) has gained a lot of attention for the use in TE devices and much effort has been done to optimize the TE performance by various treatment approaches [1-4]. A very auspicious way to improve the TE properties of PEDOT:PSS thin films, is the post-treatment with ionic liquids (ILs) [5]. It turned out this IL post-treatment increases the Seebeck coefficient (S) and the electrical conductivity (σ), two main TE parameters, simultaneously.

In order to reveal the respective underlying effects, we prepared PEDOT:PSS thin films and post-treated them with three different ILs, ethyl-3-methylimidazolium dicyanamide (EMIM DCA), allyl-3-methylimidazolium dicyanamide (AMIM DCA), and 1-ethyl-3-methylimidazolium tetracyanoborate (EMIM TCB), in varying concentrations. With these post-treated films we performed S measurements, applying a temperature gradient of 75 °C.

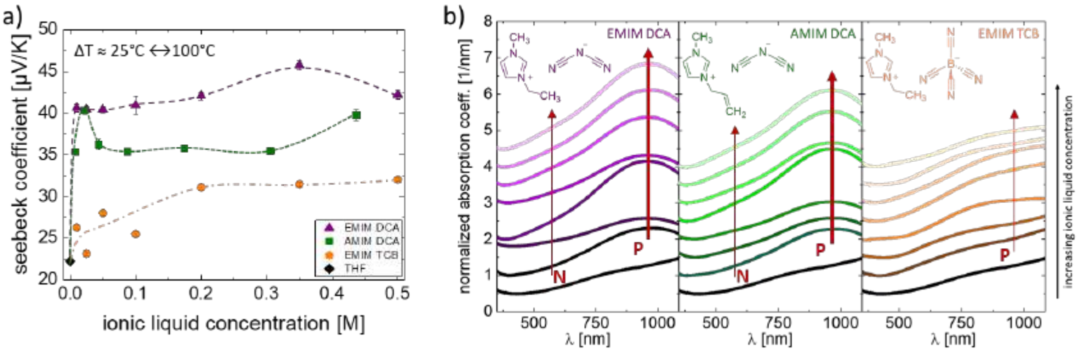

Figure 3.5:
a) Seebeck coefficient and b) UV-vis spectra of PEDOT:PSS thin films post-treated with the ILs EMIM DCA (purple), AMIM DCA (green), and EMIM TCB (orange) in increasing concentrations. Graphics were adapted with permission from [6].

From Fig. 3.5a, it is clear to see that S is improving with increasing concentration of the respective IL, strongest for the post-treatment with EMIM DCA. Comparing with UV-vis spectra taken for the same samples, Fig. 3.5b, we can observe that also the absorption changes with increasing IL concentration, strongest for EMIM DCA. Specifically in the wavelength area between 900 nm and 600 nm, absorption peaks arise, indicating the formation of polaronic (**P**) and neutral (**N**) states, respectively, and therefore an S favorable reduction of the PEDOT doping level.

Fig. 3.6a shows the results of conductivity measurements of the IL post-treated PEDOT:PSS thin film. Similar to the S trend, we also observe an increase of σ with increasing IL concentration, strongest again for EMIM DCA. As we expect that the σ increase is due to a rearrangement of PEDOT rich domains within the thin films, we performed GISAXS experiments at the SAXS beamline at Elettra synchrotron. From modeling of the obtained GISAXS data, we were able to calculate the PEDOT domain distribution, shown in Fig. 3.6b. This domain size distribution indicates that, compared to the pristine PEDOT:PSS film, upon IL post-treatment the lager

PEDOT rich domains shrink in size and amount, leading to smaller and more densely packed domains. This finer distributed domain morphology improves the inter-domain conductivity and consequently improves the overall film conductivity.

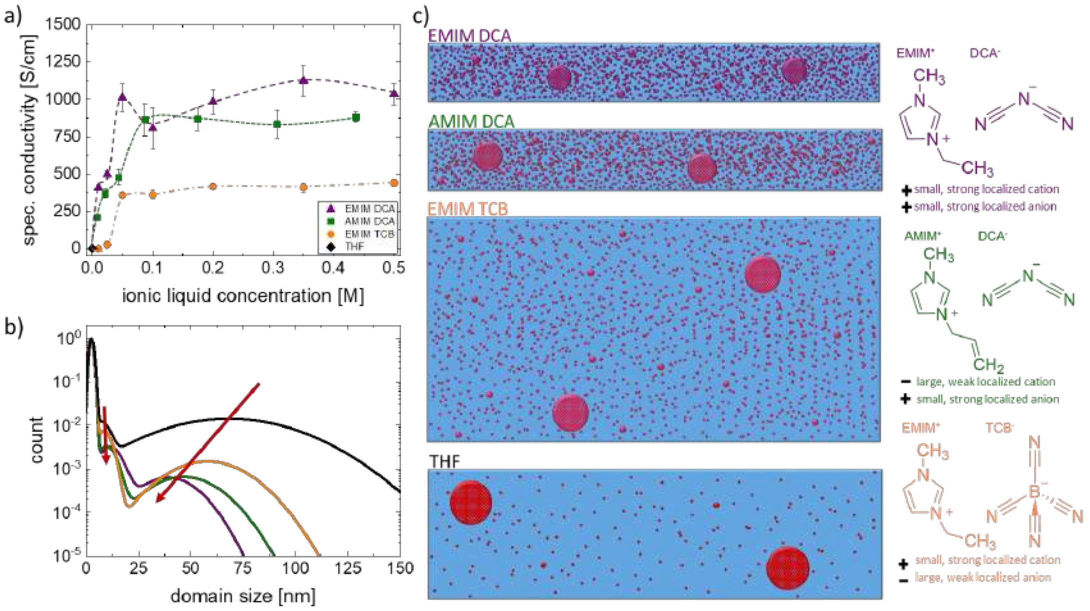

Figure 3.6:
a) Conductivity of PEDOT:PSS thin films post-treated with the ILs EMIM DCA, AMIM DCA, and EMIM TCB in varying concentrations. b) Comparison of domain size distributions of the PEDOT:PSS films post-treated with the highest concentrations of the respective IL, obtained from GISAXS data. c) Schematic sketch of the occurring changes in the morphology and doping level of the PEDOT:PSS thin films caused by the IL post-treatment, including the chemical structure and properties of the used ILs. Graphics were partly adapted permission from [6].

The illustration in Fig. 3.6c schematically summarizes the simultaneously occurring decrease in the charge carrier concentration (increase of S) and the rearrangement of the PEDOT:PSS film morphology (increase of σ). Greatest improvements were achieved by using EMIM DCA, which is, compared to AMIM DCA and EMIM TCB, the IL with the smallest and strongest localized cation and anion. This study gives an important insight into how and which IL characteristics are beneficial to boost the TE performance of PEDOT:PSS thin films.

[1] L. Bießmann, N. Saxena, N. Hohn, M. A. Hossain, J. G. C. Veinot, P. Müller-Buschbaum, *Adv. Electron. Mater.* **5**, 1800654 (2019)

[2] C. M. Palumbiny, J. Schlipf, A. Hexemer, C. Wang, P. Müller-Buschbaum, *Adv. Electron. Mater.* **2**, 1500377 (2016)

[3] C. M. Palumbiny, C. Heller, C. J. Schaffer, V. Körstgens, G. Santoro, S. V. Roth, P. Müller-Buschbaum, *J. Phys. Chem. C* **118**, 13598 (2014)

[4] N. Saxena, J. Keilhofer, A. K. Maurya, G. Fortunato, J. Overbeck, P. Müller-Buschbaum, *ACS Appl. Energy Mater.* **1**, 336 (2018)

[5] N. Saxena, B. Pretzl, X. Lamprecht, L. Bießmann, D. Yang, N. Li, C. Bilko, S. Bernstorff, P. Müller-Buschbaum, *ACS Appl. Mater. Interfaces* **11**, 8060 (2019)

[6] A. L. Oechsle, J. E. Heger, N. Li, S. Yin, S. Bernstorff, P. Müller-Buschbaum, *Macromol. Rapid Commun.* **42**, 2100397 (2021)

3.4 Optoelectronic, spectroscopic and morphological properties of zwitterionic polymers as interlayers in organic solar cells and the impact of oxygen plasma on solar cell performance

S. Coen, A. Vagias[1], J. Eichhorn[2], A. Laschewsky[3,4], P. Müller-Buschbaum

[1] MLZ, Garching, Germany
[2] WSI, Garching, Germany
[3] Universität Potsdam, Potsdam-Golm, Germany
[4] Fraunhofer IAP, Potsdam-Golm, Germany

Organic solar cells have recently reached peak power conversion efficiencies (PCE) of PCE$\sim$18% by engineering novel active layer materials [1]. The device performance depends on the efficiency by which electrons are collected by the electrode. The output efficiency depends strongly on the optimization of all underlying structural layers of an organic solar cell module. Apart from the well-explored active layers, the interlayers between the electrode and the active layer have also a crucial role in the organic solar cell performance. In addition, the organic solar cell performance can be affected by weathering effects, such as prolonged exposure to sunlight and varying atmospheric conditions [2]. The focus of this work lies on the optoelectronic and morphological characteristics of polysulfobetaines as interlayers in organic solar cells. In particular, polysulfobetaines belong to polyzwitterions [3]. They carry both positive and negative charges in their structure which leads to a certain non-zero dipole moment while they simultaneously fulfill the condition of electroneutrality [3]. This pronounced dipole moment has a two-fold benefit: First, it can enhance the amount of surface dipoles that this macromolecule can carry. It has also been shown that thin sulfobetaine-based interlayers could efficiently decrease the work function of overlaying electrodes [4]. Hence, we anticipate that the electron transport between active layer and the electrodes can be optimized by the presence of polyzwitterionic interlayers. Second, from a manufacturing aspect, this polarity in polysulfobetaines is a strong advantage as it allows polar solvents to be used for the interlayer processing. Therefore, the integrity of the active layer during interlayer deposition can be preserved. Hence, orthogonal solvency between active layer and interlayer can be ensured. This provides the advantage that solution-processing can be utilized also for the interlayer deposition which allows much easier upscaling to industrially-relevant solar cell manufacturing processes such as spraying, roll-to-roll fabrication [5].

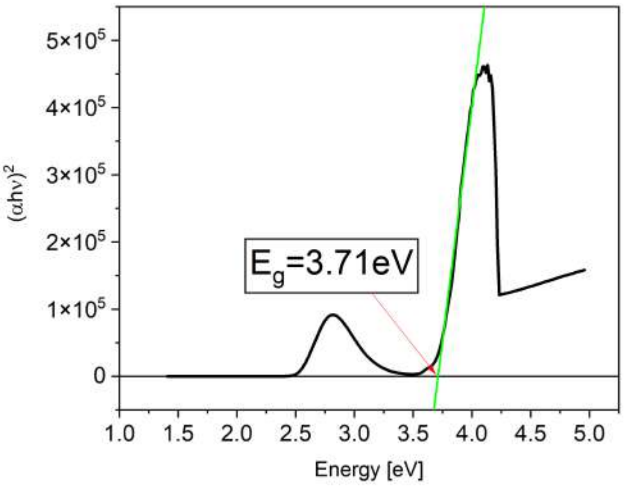

Figure 3.7:
Tauc plot representation obtained from UV-vis spectra of dilute (c_{pol} = 2mg/ml) PSPE$_{272}$ solutions in trifluoroethanol (TFE). Green line denotes the fit and the red arrow denotes the obtained energy bandgap E_g at E_g = 3.71 eV.

The use of a solution-processed interlayer allows to bypass challenges from inorganic interlayers such as MoOx. With inorganic interlayers, vapor deposition has to be used and this limits compatibility to upscale processing methods such as roll-to-roll deposition. In particular, trifluoroethanol (TFE) solutions of poly-(3-((2-(methacryloyloxy)ethyl)dimethylammonio)propane-1-sulfonate) polysulfobetaine polymers, abbreviated as $PSPE_{272}$, were prepared at c_{pol} = 2 mg/ml, c_{pol} = 5 mg/ml and c_{pol} = 10 mg/ml. Thin films of $PSPE_{272}$ were obtained by spin-coating at 1500 rpm for 900 s followed by 900 s in solvent vapor annealing. We acquired UV-VIS spectroscopy data on dilute (c_{pol} = 2 mg/ml) solutions of $PSPE_{272}$ in TFE at ambient temperature. The Tauc plot representation (Fig. 3.7) allows to calculate an energy bandgap (E_g) of E_g = 3.71 eV.

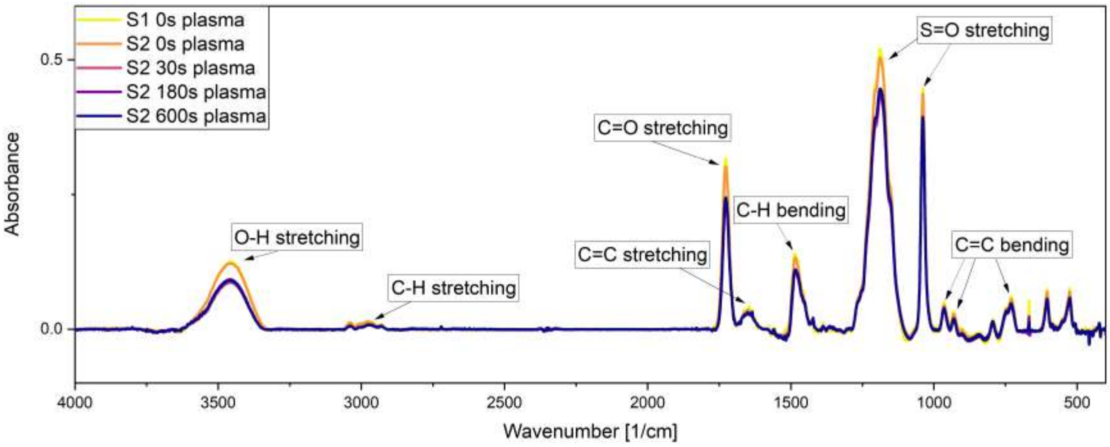

Figure 3.8:
FTIR spectra of $PSPE_{272}$ as pristine film and after 30, 180 and 600 s of oxygen plasma treatment.

In addition, morphological characteristics of the spin-coated films have been collected for samples pre-exposed to oxygen plasma (S2) (P = 83% at 250W) and for non-plasma treated samples (S1). Variable oxygen plasma exposure times (30, 180, 600 s) have been utilized. Optical microscopy images (not shown) suggest a distorted surface morphology after oxygen plasma treatment with some crevasse-like cracks between polymer regions at microscopic length scale. The impact of oxygen plasma treatment at the molecular level (Fig. 3.8) was also assessed using FTIR spectroscopy. We note as primary effect a decrease in peak intensities at different wavenumbers including the S=O vibration at ν=1190 cm^{-1}. Further UPS experiments at Walter Schottky Institute (WSI) are ongoing to determine the HOMO and LUMO levels for $PSPE_{272}$. GISAXS and XRR measurements are also in progress and will allow to probe the surface uniformity and roughness features of the spin-coated PSPE layers. The next step involves realizing a solar cell architecture with $PSPE_{272}$ as interlayer and PBDBTCl-DTBT:BTP-4F as active layer. The performance characteristics of the organic solar cells will be assessed in presence and absence of oxygen plasma.

[1] Q. Liu, Y. Jiang, K. Jin, J. Xu, W. Li, J. Xiong, J. Liu, Z. Xiao, K. Sun, S. Yang, X. Zhang, L. Ding, *Science Bulletin* **925**, (2020)

[2] W. Xu, R. Xia, T. Ye, L. Zhao, Z. Kan, Y. Mei, C. Yan, X. W. Zhang, W. Y. Lai, P. E. Keivanidis, W. Huang, *Adv. Sci.* **3**, 1500245, (2016)

[3] A. Laschewsky, A. Rosenhahn, *Langmuir* **35**, 1056-1071 (2019)

[4] Z. A. Page, Y. Liu, V. V. Duzhko, P. Thomas, T. Emrick, T. P. Russell, T. Emrick, *Science* **346**, 441-444, (2014)

[5] C. Duan, L. Wang, K. Zhang, X. Guan, F. Huang, *Adv. Mat.* **23**, 1665-1669, (2011)

3.5 Comparison of optical and structural properties of different perovskite compositions derived with slot-die coating

C. G. Lindenmeir, A. Vitaloni, L. K. Reb, M. A. Reus, P. Müller-Buschbaum

In the last couple of years, the awareness of perovskite solar cells (PSCs) has grown a lot, due to their high power conversion efficiencies (PCE) of up to 25 %, [1] their low manufacturing costs and easy upscaling with low waste solution based deposition techniques like slot-die coating. [2] To further improve the PCE and the long-term stability, perovskite-based materials offer a variety of tunable chemical constituents that allow to create different perovskite compositions to find the best one for solar cells. Therefore, the aim of this work is to develop a better understanding of crystallization and drying of different perovskite films by using optical and structure characterization methods based on X-ray scattering.

We print perovskite films at room temperature with a slot-die printer on blank glass slides and glass slides with a pre-deposited indium tin oxide (ITO) layer, which serves as the bottom electrode. The two different perovskite solutions compared in this work both consist of lead iodide (PbI_2) and methylammonium iodide (MAI) with the additive formamidinium iodide (FAI) dissolved in a mixture of 2-methoxyethanol (2-ME) and dimethyl sulfoxide (DMSO). To compare the two compositions with and without FAI, two different measurement techniques are used. To gain optical properties like the band gap of the films, UV-vis is used. to determine the structure, we use X-ray diffraction (XRD).

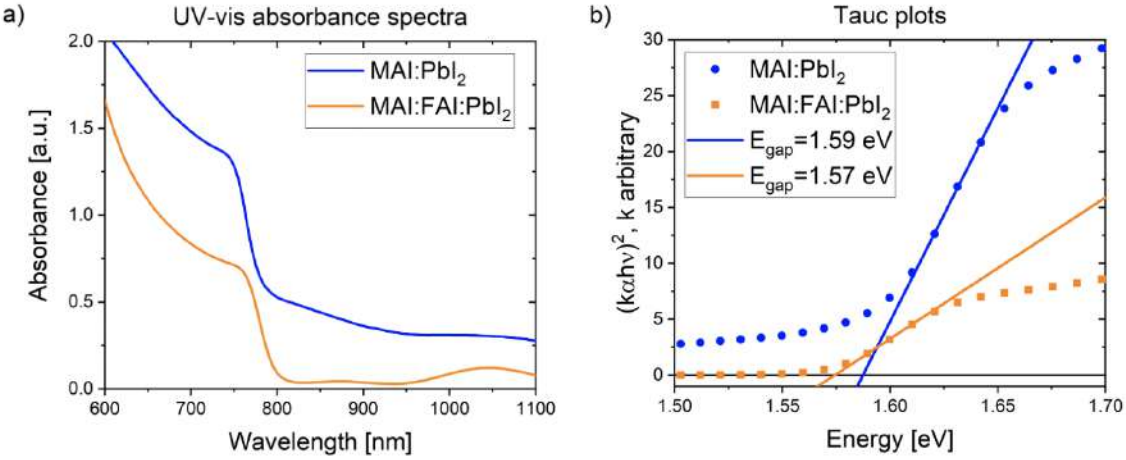

Figure 3.9:
a) UV-vis absorbance spectra and b) Tauc plot of two different slot-die coated perovskite films.

In Fig. 3.9a we present the UV-vis absorbance spectra of the two different perovskite compositions. When comparing these two measurements, both films show strong absorption below 750 nm. Between 750 and 800 nm there is a visible sharp edge in both curves. Below this edge, both films do not absorb light any more. Using the absorbance data one can create the so-called Tauc plot that allows to estimate the band gap energies, seen in Fig. 3.9b. By comparing the calculated band gap energies, it can be observed that the band gap energy of the film with FAI additive is slightly smaller than for the film without FAI. It is possible to see that the influence of additive components that tune the cation of pure MAPI does not strongly affect the band gap energies.
In the second part, the crystalline structure of the two different compositions is compared via XRD. As seen in Fig. 3.10 we observe strong differences in the XRD data. In the upper data,

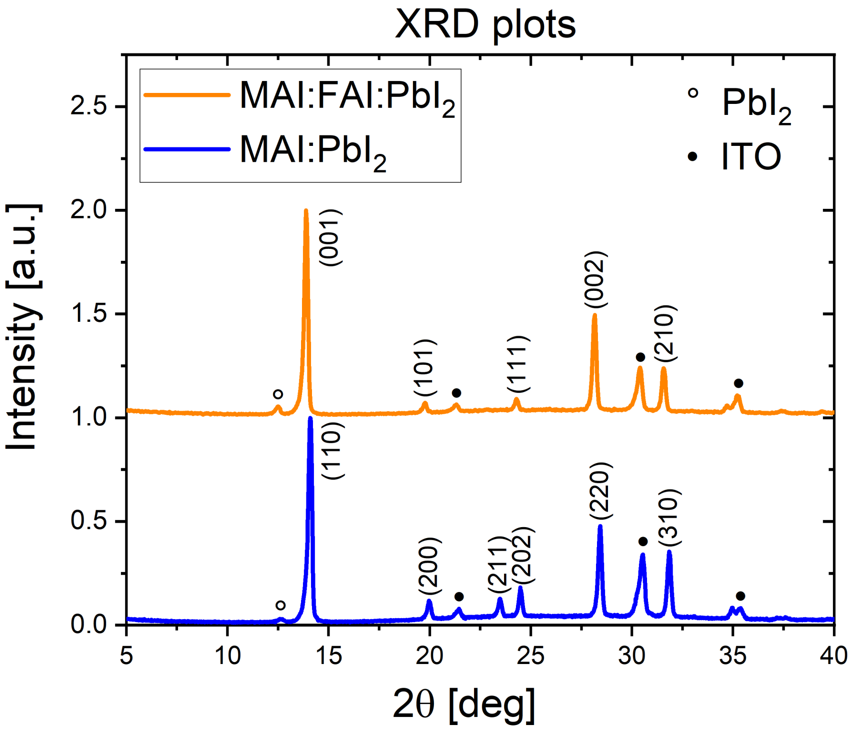

Figure 3.10:
XRD data of two different perovskite compositions. The peaks of tetragonal (bottom) and cubic (top) perovskite are labeled via (hkl) Miller indices. Solid and empty circles denote ITO and PbI_2 peak contributions respectively in the XRD plot.

only one peak at around $2\theta \approx 24$ degrees is present, whereas there are two peaks at the same 2θ value in the lower data panel. Thus, the perovskite film with FAI additive crystallizes in cubic structure and the film with pure MAPI in tetragonal structure. In addition to that, one can see that in both films a small PbI_2 excess remains.

Interestingly, small additives that modify the organic cation (20% FA) are enough to stabilize the cubic alpha-phase of perovskite that usually is only observed at elevated temperatures above 60 °C. This additive does not affect the band gap energy and therefore the absorption behavior remains unchanged. However, we expect the cubic phase to show different crystallization during printing and phonon-lattice interaction upon solar cell operation that will be analyzed in the future to extend our basic knowledge of printed perovskite films on the way to high efficiency and stable printed perovskite solar cells.

[1] J. Jeong, M. Kim, J. Seo, H. Lu, P. Ahlawat, A. Mishra, Y. Yang, M. A. Hope, F. T. Eickemeyer, M. Kim, Y. J. Yoon, I. W. Choi, B. P. Darwich, S. J. Choi, Y. Jo, J. H. Lee, B. Walker, S. M. Zakeeruddi, L. Emsley, U. Rothlisberger, A. Hagfeldt, D. S. Kim, M. Grätzel, J. Y. Kim, *Nature* **592**, 381–385 (2021)

[2] M. A. Reus, L. K. Reb, A. F. Weinzierl, C. L. Weindl, R. Guo, T. Xiao, M. Schwartzkopf, A. Chumakov, S. V. Roth, P. Müller-Buschbaum, *Adv. Optical Mater.*, accepted (2022)

3.6 Fabrication of plasmonic nanostructures in optoelectronic devices

T. Guan, P. Müller-Buschbaum

Incident-radiation-induced surface plasmon polaritons (SPPs) and localized surface plasmon resonance (LSPR) are the main aspects of plasmonic applications. Recently, various plasmonic metal-dielectric composites have been introduced in different optoelectronic devices such as photovoltaics (PVs), photodetectors (PDs), and light-emitting diode (LEDs) [1]. For optoelectronic devices, light and electric management are key issues for the performance enhancement. The so-called near field which is defined as electromagnetic fields near metal nanoparticles under light illumination, has facilitated as promising technology for light harvest and energy transfer. Plasmonics in optoelectronic devices could give rise to optical and electronic effects as well as contribute to enhancing performance. The plasmonic effect can suppress electron-hole recombination and increase the number of charge carriers in the devices. Various metal and semiconductor nanocrystals have intriguing plasmonic properties for optoelectronic devices [2]. Among them, gold nanoparticles (Au NPs) were one of the most attractive materials due to facilte tunability in synthesis and in optical properties. Many types of AuNPs, including the precise shapes, sizes, and spacings of nanospheres (NSs), nanorods (NRs), nanostars, nanocubes, etc., have been incorporated into the devices [3]. However, to pave the way for large-scale applications, a systematic fundamental study of plasmonic enhanced optoelectronics still needs to be further explored. Therefore, it is crucially important to optimize Au NPs based plasmonic nanostructures for achieving highly-efficient optoelectronic devices.

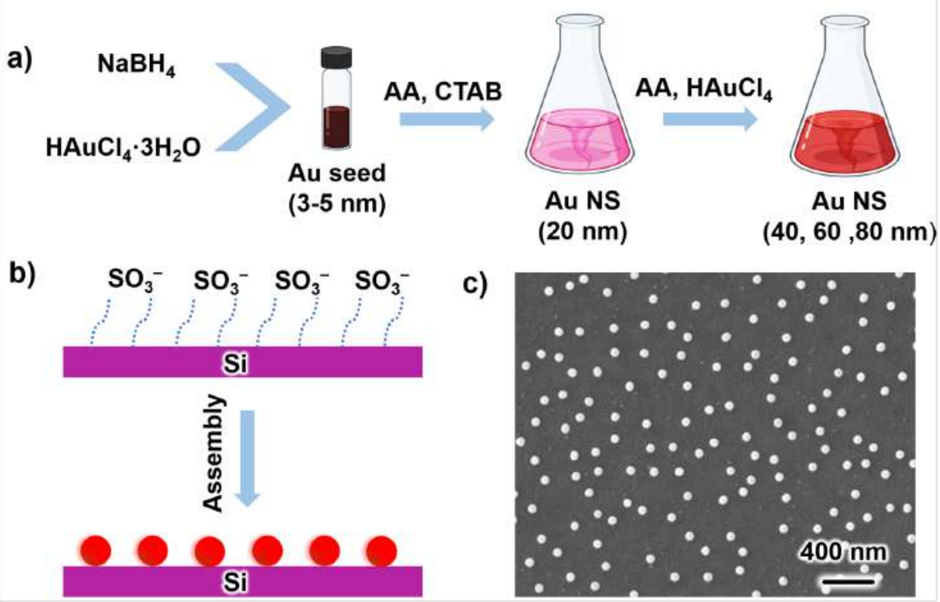

Figure 3.11:
Schematic diagram of Au NPs a) synthesis and b) assembly process and corresponding SEM images of Au NPs array on the Si substrate.

To achieve overall practical advantages in Au NP-based optoelectronic devices, we find a new strategy to fabricate large scale Au NPs arrays by a self-assembly method. Before the Au NPs array fabrication, we synthesize different sizes of Au NPs through seed growth methods as is shown in Fig. 3.11a. We obtain Au seeds with $\sim$ 3-5 nm size and with the reaction of gold chloride trihydrate ($HAuCl_4$) and sodium borohydride ($NaBH_4$). We then add ascorbic acid

(AA) as a reducing agent, cetrimonium bromide (CTAB) as a surfactant to grow the Au NPs to ∼20 nm. Finally, we can grow the sizes of Au NPs to 40 nm, 60 nm, and 80 nm by addition of different concentrations of $HAuCl_4$ and AA. After self-assembled Au NPs with chemical bond adsorption as is shown in Fig. 3.11b, we can gain a large scale Au NPs array on solid substrates such as Si, TiO_2, ZnO, etc. We note that the Au NPs are well-dispersed on a Si substrate and could effectively avoid the common aggregation problem of Au NPs for their practical application in light-harvesting systems. Fig. 3.12 shows that the Au NPs arrays are successfully introduced in optoelectronic layers of the devices. The top and bottom images of Fig. 3.12 show 20 nm and 80 nm Au hybrid NPs with PbS quantum dot (QDs) film respectively.

The perovskite layers are well crystalline with the insertion of Au NPs, as shown in the top image of Fig. 3.12b. From the cross-section SEM image, we can find that the Au NPs are positioned at the interface of the device. We proved that the large scale Au NPs arrays are successfully applied in both, PbS and perovskite based optoelectronic devices, which means that we achieve a universal relevance. Besides, grazing-incidence small/wide-angle X-ray scattering (GIS/WAXS), which has been proven successful in probing inner film morphology, will be used to further study the optoelectronic active layers of the device [4]. We expect that this hybrid plasmonic nanostructure could contribute to the performance enhancement in optoelectronic devices.

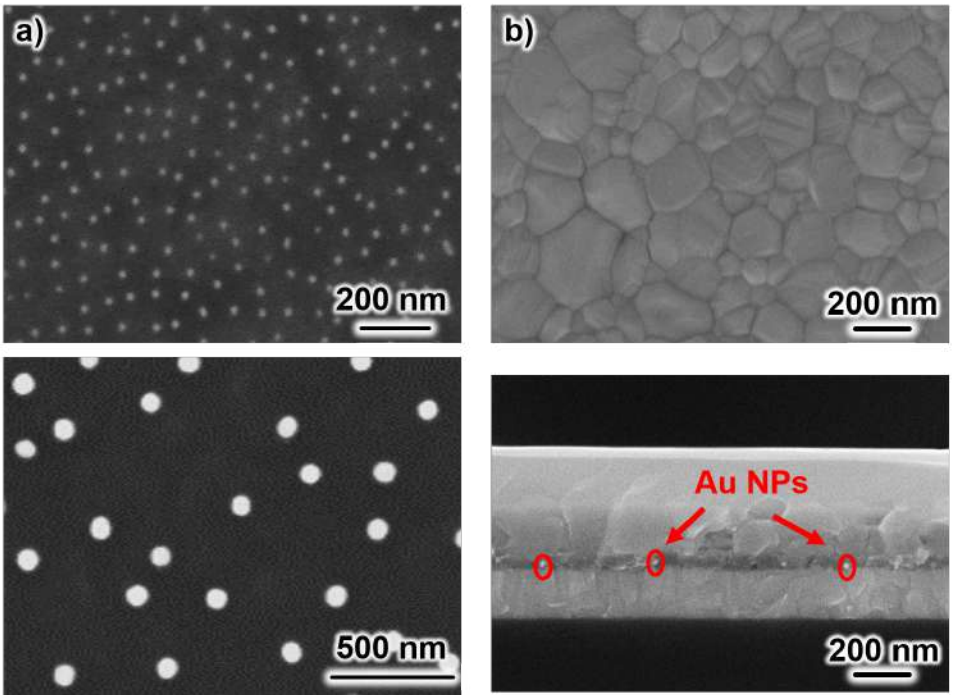

Figure 3.12: SEM images of Au NPs hybrid with a) PbS and b) perovskite film respectively.

[1] Z. Liang, J. Sun, Y. Jiang, L. Jiang, X. Chen, *Plasmonics* **9**, 859–866 (2014)

[2] S. Liu, R. Jiang, P. You, X. Zhu, Ji.Wang, F. Yan, *Energy Environ. Sci.*, **9**, 898-905 (2016)

[3] A. Zada, P. Muhammad, W. Ahmad, Z. Hussain, S. Ali, M. Khan, Q. Khan, M. Maqbool, *Adv. Funct. Mater.* **30**, 1906744 (2020)

[4] J. Schlipf, P. Müller-Buschbaum, *Adv. Energy Mater.* **7**, 1700131 (2017)

3.7 Investigation of the charge transport in ionic liquid post-treated PEDOT:PSS thin films with *in situ* impedance spectroscopy

T. Schöner, A. L. Oechsle, P. Müller-Buschbaum

Thermoelectric generators offer the potential to generate electric energy from a temperature gradient. Starting from the past when these devices were developed and used for space applications, at present a big application potential lies in waste-heat harvesting from e.g. combustion engines. The internet-of-things paves the way to the future use of thermoelectric devices in our daily life [1]. Previous thermoelectric generators were mainly based on inorganic compounds like bismuth, tellurium, silver or lead, which are difficult to process, often toxic and expensive. Our research focuses on thermoelectric materials based on polymers as they enable large-scale and low cost processability and possess advantageous properties as lightness, water-solubility and low thermal conductivity. For the purpose of enhancing the thermoelectric properties of poly(3,4-ethylene dioxythiophene):poly(styrene sulfonate) (PEDOT:PSS), thin PEDOT:PSS films are post-treated with ionic liquids (ILs). This procedure enables the IL anions to react with the positively charged PEDOT chains, which is basically a reduction process, that diminishes the charge carrier concentration. Moreover, excess PSS gets washed out of the films leading to an improved inter-domain conductivity. This IL treatment increases the thermoelectric power-factor as simultaneously both the Seebeck-coefficient and electrical conductivity are tuned. Recent studies showed an increase of the power factor up to 236 μWm^{-1}K^{-2} for PEDOT:PSS films post-treated with the IL ethyl-3-methylimidazolium dicyanamide (EMIM DCA) [2].

In electrochemical systems, charge transport is due to both, electronic and ionic charge contributions. The ionic contribution to the Seebeck coefficient in our IL treated PEDOT:PSS thin films is still not quantified. Therefore, we aim for *in situ* impedance spectroscopy that allows to investigate the electronic and ionic charge carrier contribution due to their different transport kinetics and polarization phenomena. The enhancement of thermopower due to thermodiffusion of ionic charge carriers refers to the Soret effect, that can be used to investigate the influence of the ionic Seebeck voltage in the samples of interest [1].

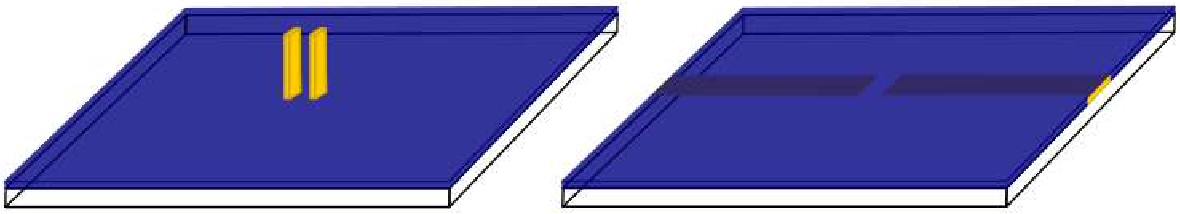

Figure 3.13:
Two different approaches in order to contact IL doped PEDOT:PSS thin films. The left side shows a film contacted with two gold pins on top. On the right side the pins were evaporated on the glass substrate and the film was later-on spin coated. The measured area is defined as the area enclosed between the pins.

For quantitative impedance spectroscopy measurements, it is important to have a defined geometry of the setup to enable the reasonable comparison of the results to other measurements. Fig. 3.13 demonstrates different approaches to contact the sample and execute measurements. In order to characterize electrochemical systems with impedance spectroscopy it is crucial to have a sufficient understanding about the investigated system [3]. The data can be interpreted by either the Voigt's model or the Maxwell's model, whereby the first represents an approach to connect the sub circuits in series. Maxwell's model is used to describe parallel processes with components connected in parallel and more appropriate to figure out distinctive electronic and ionic processes [1]. The results are analyzed by fitting their data into a Nyquist-plot using an equivalent circuit model. Fig. 3.14 shows exemplary equivalent circuit models and a Nyquist-plot, that can be used to describe solid electrochemical systems.

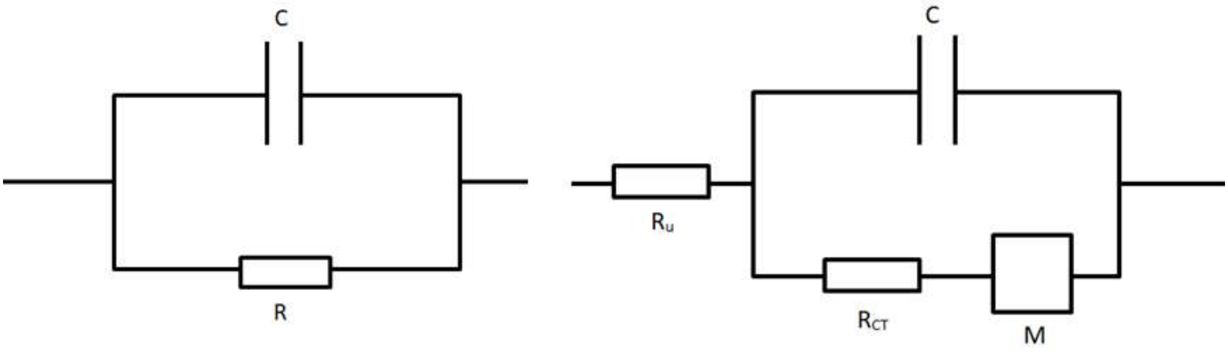

Figure 3.14:
Electrical circuit models and a Nyquist-plot. The left side shows a simple RC-junction. On the right side an equivalent circuit model can be seen, that potentially describes PEDOT electrodes with an electrolyte resistance R$_u$ followed by a capacitance C in parallel with a charge transfer resistance R$_{CT}$. M represents a linear diffusion element. Different circuit components represent different intrinsic processes.

Recently we worked on optimizing the electrical contacts of the samples in order to provide stable measurements and a more well-defined geometry. The measurements showed that the choice of contacts has an influence on the measurements and thus it is essential to complete this first step in order to continue with further measurements. Possible problems are film penetration due to pressing the pins on the film surface, which can be solved by providing stable contact areas on the surface, that can be either painted or evaporated on the film using a template. Also the measurement setup itself may give rise to residual impedances, so that external inductances and capacitances (impedance of the Device Under Test "DUT") have to be eliminated using impedance compensation (open & short circuit compensation, load compensation).

Next steps include finding the equivalent circuit model that describes best the intrinsic charge transport processes in the films and to investigate the influence of environmental influences such as humidity and temperature on the electric and ionic charge transport in PEDOT:PSS thin films post-treated with ionic liquids. For all these steps, the task is to build an impedance spectroscopy setup that can be placed in e.g. a humidity chamber or be combined with a heater heating the sample homogeneously. This research aims to provide a better understanding of the thermoelectric properties under different environmental influences in order to define the operation range and parameters of thermoelectric films based on polymers in different applications.

[1] H. Wang, U. Ail, R. Gabrielson, M. Berggren, X. Crispin, *Adv. Energy Mater.* **5**, 1500044 (2015)

[2] A. L. Oechsle, J. E. Heger, N. Li, S. Yin, S. Bernstorff, P. Müller-Buschbaum, *Macromol. Rapid Commun.* **42**, 2100397 (2021)

[3] T. Stöcker, A. Köhler, R. Moos,*J. Polym. Sci. B Polym. Phys.* **50**, 976-983 (2012)

3.8 Influence of solvent additives on molecular dynamics in polymer-fullerene blends

D. M. Schwaiger, W. Lohstroh[1], P. Müller-Buschbaum

[1] MLZ, Garching, Germany

In the development of a new generation of organic solar cells, which provide potentially lower fabrication costs, shorter energy payback times as well as reduced environmental toxicity, compared to conventional silicon technology, and the possibility to produce semitransparent devices on flexible substrates, still several challenges have to be overcome. One of them is their stability against ambient conditions as oxygen in the atmosphere and light irradiation itself cause chemical and physical degradation of the used materials. In the present work, we study a PTB7:PCBM film under operating conditions with focus on molecular dynamics. This polymer:fullerene blend is one of the well-studied model systems for active layer materials in organic photovoltaics. Numerous studies, mainly focused on their photovoltaic performance and structural aspects, have been published. Several performance enhancing methods were reported to be successful in order to increase the power conversion efficiency up to almost 10 %. Among them, two of the most promising are an alcohol post-treatment of the film to remove residual solvent [1] and the addition of solvent additives to the solution, which can lead to a more favorable microstructure of the polymer-fullerene blend [2]. In this study we investigate the effect of both, a methanol post-treatment and of the addition of 3 % 1,8-diiodooctane (DIO) to the casting solution on PTB7 side chain dynamics. For the investigation of the polymer side chain dynamics, quasi-elastic neutron scattering experiments were performed at the cold neutron Time-of -Flight spectrometer TOFTOF at MLZ (Garching). This instrument measures the energy transfer between neutrons and the sample by a comparison of the neutrons´ Time-of-Flight before and after the interaction with the sample material. This energy transfer is a measure for motions inside the sample. The extremely large incoherent scattering cross-section of hydrogen atoms and the fact, that they are highly abundant in the PTB7 side chains, makes this method very well suited for the investigation of dynamics in this system. Whereas we have shown before, that a methanol treatment of the film has no significant influence on polymer dynamics, the introduction of DIO into the casting solution seems to impact internal dynamics tremendously [3].

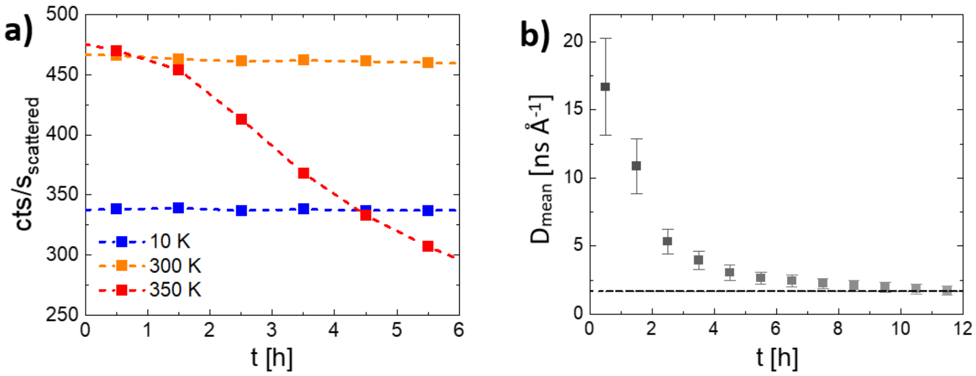

Figure 3.15:
a) scattering count rates of a 1:1.5 PTB7:PCBM blend film, produced with 3% DIO added to the casting solution; b) evolution of the calculated mean diffusion coefficient ⟨D⟩ at 400 K over the course of the experiment; Each value represents an average over 1 h.

Fig. 3.15b shows the development of the calculated mean diffusion coefficient for a PTB7:PCBM film, casted from chlorobenzene solution with 3% DIO as solvent additive over the course of a

12 h measurement at a temperature of 400 K. Since the diffusion coefficient was expected to be rather constant at stable temperature conditions, a look into the scattering statistics (Fig. 3.15a) gives the hint, that the sample might have changed during the experiment. While the rate of scattered neutrons is constant at 10 K and at 300 K, it decreases dramatically at 350 K. This feature is unique to the sample produced with DIO and does not appear in any other measurement, which implies that the DIO itself might be responsible for the unusual behavior and the calculated mean diffusion coefficient is a hybrid, composed out of PTB7 side chain dynamics and DIO molecular diffusion. As the temperature increases over 300 K, DIO gets more volatile and leaves the PTB7:PCBM film, which leads to the observed reduction of both, the scattering rate as well as the mean diffusion coefficient.

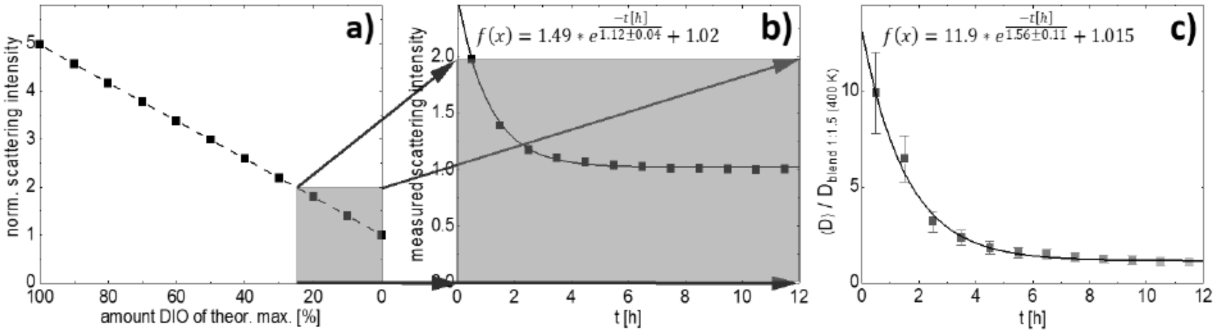

Figure 3.16:
a) Calculated scattering intensity, dependent on theoretical DIO content b) measured scattering intensity c) relative mean diffusion coefficient; all normalized to a pure PTB7:PCBM sample.

Fig. 3.16 visualizes the effects explained above. Fig. 3.16a relates the DIO content to the scattering intensity of the film, normalized to the scattering of a film, produced without DIO. 100% represents the entire amount of DIO used in the solution. The shaded area marks the actually measured range, according to scattering intensities. Thus, 25% of the DIO was not removed by the regular drying procedure. This 25% residual DIO accounts for approximately the same scattering rate as the PTB7:PCBM film itself, which is confirmed by Fig. 3.16b, showing the actually measured scattering intensity over 12 h. The decay of this curve can be seen as direct measure for DIO loss of the film. In parallel, Fig. 3.16c shows the decay of the mean diffusion coefficient, normalized to D of the pure film. A comparison of the two decay constants yields interesting insights about the film formation process. While the DIO content in the film decays at a rate of -0.89, the calculated mean diffusion coefficient decays at a rate of -0.64, which is significantly slower. This observation shows that DIO introduces mobility into the film, which also remains after evaporation of the solvent additive. The dried film is still undergoing reorientations, represented by a higher diffusion coefficient and remains more mobile on molecular level, compared to the film that was produced without any solvent additive. Thus, the desired structure, which should be realized with the help of DIO is not stable if the solvent additive is not removed properly in a controlled process. This incomplete removal of DIO has also been reported before and a rapid change of the photovoltaic parameters could be attributed to this effect.

[1] S. Guo, B. Cao, W. Wang, J.-F. Moulin, P. Müller-Buschbaum, *ACS Appl. Mater. Interfaces*, **7**, 4641 - 4649 (2015)

[2] S. Guo, E. Herzig, A. Naumann, G. Tainter, J. Perlich, P. Müller-Buschbaum, *J. Phys. Chem. B*, **118**, 344 - 350 (2014)

[3] D. M. Schwaiger, W. Lohstroh, P. Müller-Buschbaum, *Macromolecules*, **51**, 6534 - 6542 (2021)

3.9 Structure of molybdenum nitride films as hole-selective contacts of crystalline silicon solar cells determined with X-ray scattering

Y. Li, C. Jiang[1], B. Sun[2], P. Müller-Buschbaum

[1] SINANO, Suzhou, China

[2] Soochow University, Suzhou, China

Molybdenum nitride (MoN_x) films prepared by magnetron sputtering method has been investigated as hole-selective layer for crystalline silicon(c-Si) solar cells due to its proper work function and high conductivity [1]. However, its hole-selectivity is worse than MoO_x, which is mainly correlated to the poor interface passivation between Si and MoN_x. Thicker MoN_x films (~200 nm) had a better open circuit voltage and fill factor in devices than thinner MoN_x films (~20 nm), showing that thicker films induce a better surface passivation and charge carrier transport. In this work, the interface between MoN_x and Si is compared to the one between MoO_x and Si through X-ray reflectivity (XRR). The phase structure and domain size of MoN_x films with different thicknesses are determined with grazing-incidence wide-angle (and small-angle) X-ray scattering (GIWAXS and GISAXS) to figure out efficient methods for improving the hole-selectivity of MoN_x films.

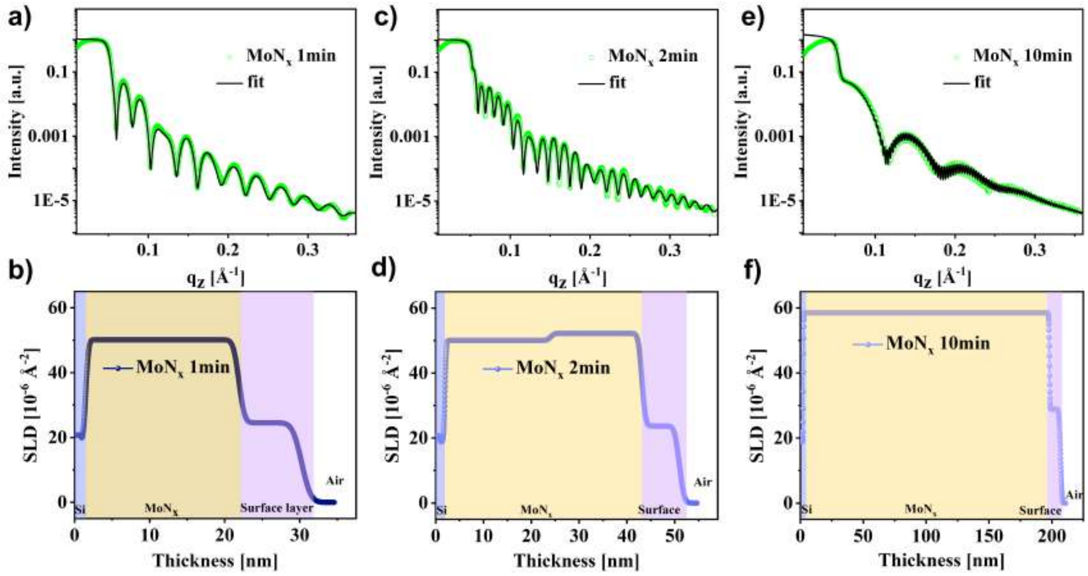

Figure 3.17:
XRR data (symbols) and fits (lines) with corresponding SLD profiles of MoN_x films deposited for 1 min (a, b), 2 min (c, d), and 10 min (e,f). The surface layer region is highlighted with purple color.

Through fitting the XRR curves of the MoN_x films (Fig. 3.17), the scattering length density (SLD) is found to increase from 50.1 to 58.5*10^{-6}Å^{-2} with the thickness changing from 28 to 200 nm. This development demonstrates that the stoichiometric fraction of MoN_x films changes during the deposition process. Moreover, a surface layer with a thickness of 8 nm and an SLD ranging from 23.7 to 28.9*10^{-6}Å^{-2} exists for all three MoN_x films (stored in air for 8 months), which should be related to surface oxidation induced by water and oxygen in the air [2]. The surface SLD value is close to the one of thermally evaporated MoO_x films. For fresh MoO_x films, the SLD decrease from 32.2 to 30.1 *10^{-6}Å^{-2} with thickness changing from 22 to 58 nm and remains at 30.1*10^{-6}Å^{-2} with a thickness of 130 nm. An extra surface layer is not seen in fresh MoO_x films. The interfacial layer between MoN_x and Si ranges from 0.6 nm to 1.5 nm with increasing film thickness, demonstrating that a little interface reaction occurred for long time storage. It is surprising that the thickness of the MoO_x/Si interface layer is also between 0.7 and 1.0 nm from XRR fits, which was reported to be 2-3 nm with high resolution transmission electron microgram (HRTEM) [3]. We suppose that the MoO_x/Si interface thickness may increase further with storage time, which will be confirmed by future XRR experiments.

MoN_x films investigated in this work are amorphous and only a broad intensity bump is seen in the 2D GIWAXS data, which is similar with the XRD of amorphous MoO_x film prepared by vacuum thermal evaporation [4]. 2D GISAXS data in Fig. 3.18 provide more structural information for different thickness values. In the vertical line cuts, fringes similar to XRR occur. The Yoneda peak position increases with film thickness, which is in line with the increasing trend of the SLD parameters with thickness. Film of 50 nm shows two Yoneda peaks corresponding to its SLD and confirm that this film consists of different components. Horizontal line cuts and their fits at the Yoneda peak position show that the smallest domain size increases from 4 to 13 nm when the film thickness increases from 28 to 200 nm and the proportions of the smallest domains in all films are above 97%.

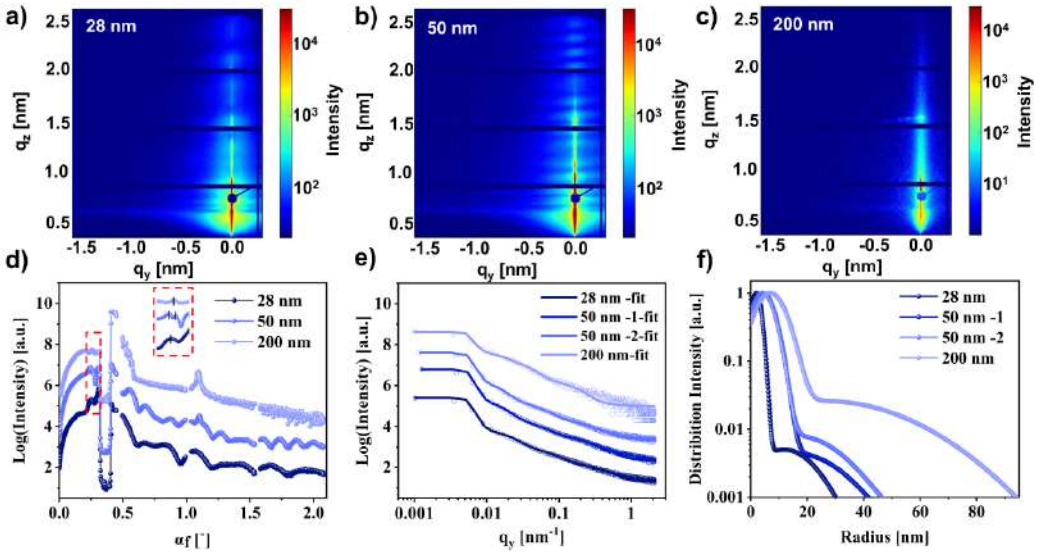

Figure 3.18:
2D GISAXS data of MoN_x films with thickness of a) 28 nm, b) 50 nm and c) 200 nm. d) Vertical line cuts with inset of the Yoneda peak region, e) horizontal line cuts at each Yoneda peak, and f) distribution intensity of different domain sizes in the three MoN_x samples.

This work demonstrates the advantages of XRR and GISAXS in analyzing the structure of amorphous carrier-selective passivating layers for c-Si solar cells. Thicker MoN_x films show larger SLD, thicker interface and larger domain size, which correlates to a better surface passivation and hole transport properties. The detailed structure analysis gives reasonable explanation for device performance. This clear structure-function relationship provides guidance for designing excellent carrier-selective passivation contacts for c-Si solar cells in the future.

[1] Y. Li, Y. Li, G. Zhang, J. Li, D. Liang, Y. Wu, T. Song, X. Yang, D. Li, C. Jiang, B. Sun, *Phys. Status Solidi RRL* **15**, 2100159 (2021)

[2] Z. B. Wei, P. Grange, B. Delmon, *Appl. Surf. Sci.* **135**, 107-114 (1998)

[3] S. Cao, J. Li, Y. Lin, T. Pan, G. Du, J. Zhang, L. Yang, X. Chen, L. Lu, N. Min, M. Yin, D. Li, *Sol. RRL* 1900274 (2019)

[4] N. Oka, H. Watanabe, Y. Sato, H. Yamaguchi, N. Ito, H. Tsuji, Y. Shigesato, *J. Vac. Sci. Technol. A* **28**, 886-889 (2010)

3.10 Quantum dot based next generation optoelectronic devices

H. Zhong, W. Chen, M. Schwartzkopf[1], S. V. Roth[1,2], P. Müller-Buschbaum

Colloidal quantum dots (CQDs) have generated great interest in various optoelectronic devices because of their size-tunable bandgap and, low-temperature solution processability. Lead sulfide (PbS) CQDs, with a strong absorption coefficient and large Bohr radius, are capable of harvesting infrared photons of the solar spectrum beyond the absorption edge of crystalline silicon and perovskites, enabling PbS CQDs to receive significant attention in optoelectronic applications. Nevertheless, several issues are impeding the further improvement of performance in optoelectronic devices: (1) The surface trap states of CQDs. QDs' incomplete surface passivation on the one hand causes the oxidization in the ambient atmosphere, leading to a poor stability. On the other hand, QDs' surface ligands dictate the stacking behavior in QDs solids, directly affecting the electronic coupling between adjacent QDs. (2) The interfacial defects between different functional layers. The numerous interfacial defect states act as recombination centers, easily capturing charge carriers during the device operation.

The basic principle of QDs' ligand exchange for device application is to increase the electronic coupling between the QDs and reduce QDs' surface defects. There are a wide variety of strategies for QDs' surface engineering, which basically can be classified as solution-phase ligand exchange and solid-state ligand exchange. In solid-state ligand exchange, the film deposition and ligand exchange are conducted simultaneously, where the deposited CQD film treated by the short-chain ligand solvent and subsequently multiple rinse-step with the protic solvent may suffer from ligand loss and the introduction of additional charge traps [1]. While in the solution-phase ligand exchange, the ligand exchange completed in the solution can replace the long ligands with short ones more thoroughly [2] and the desired film thickness can be obtained by one-step deposition using the QD ink with high concentration. QD ink shows great promises for the commercialization of PbS QDs based optoelectronic devices. The PbS QDs films on the glass substrate by slot-die coating are prepared. As is shown in Fig. 3.19, after the treatment of ligand exchange, the statistical inter-dot distance for PbS QDs solid decreases from 4.8 nm to 3.9 nm. Moreover, the as-synthesized PbS QDs with oleic acid (OA) ligand shows prominent Bragg peaks from the body-centered cubic (BCC) superlattice [3], while the QDs solid treated with short PbX (X=I, Br) ligands appears much more disordered and larger distribution of inter-dot distance, which may come from the aggregation of QDs due to the instability of QDs ink. Thus, the improvement of QD ink stability is necessary and the operational conditions for slot-die printing need to be further investigated.

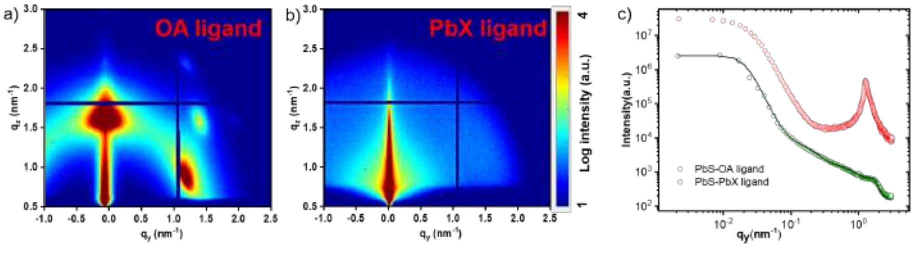

Figure 3.19:
2D GISAXS data of PbS QDs solids with a) OA ligands and with b) PbX ligands, and c) their respective horizontal line cuts from the 2D GISAXS data.

In terms of the interfacial engineering between the electron transport layer (ETL) and active layer, the depletion region plays an important role in the charge carrier's collection. The material engineering of QDs active layer including the surface ligands exchange initiates the focus of the depletion region. Given CTL, there are mainly three requirements, which are proper energy alignment between CTL and active layer, balanced free carriers density, and good physical stability [4]. Meanwhile, the doping of existing CTL and the incorporation of an interlayer between major CTL and the active layer are generally used methods. As the most widely used ETL materials in the QDs based optoelectronic devices, the modifications of ZnO nanoparticles (NPs) have been investigated for the development of devices. Among the doping of ZnO, indium-doped ZnO (IZO) has drawn attention. IZO layer is not only commonly used as a transparent electrode but also the electron transport layer due to its high transmission in the solar spectrum and high electron carrier mobility. The sputtered IZO films on the two different templates ITO glass and ITO glass with ZnO nanoparticle film are prepared. As is shown in Fig. 3.20, the spin-coated ZnO NPs film with 150 nm completely covers the sputtered ITO film on glass, presenting smaller and more densely packed grains. After the sputtered IZO with 12 nm on these two templates, the agglomeration occurs in the glass/ITO/IZO sample and many cracks and voids are observed, while the polydisperse clusters in the glass/ITO/IZO sample are packed adjacently with visible borders. Based on scanning electron microscope (SEM) images, the quantitive analysis of film morphology and the dynamic growth process of sputtered IZO on these two different templates are necessary for a detailed understanding.

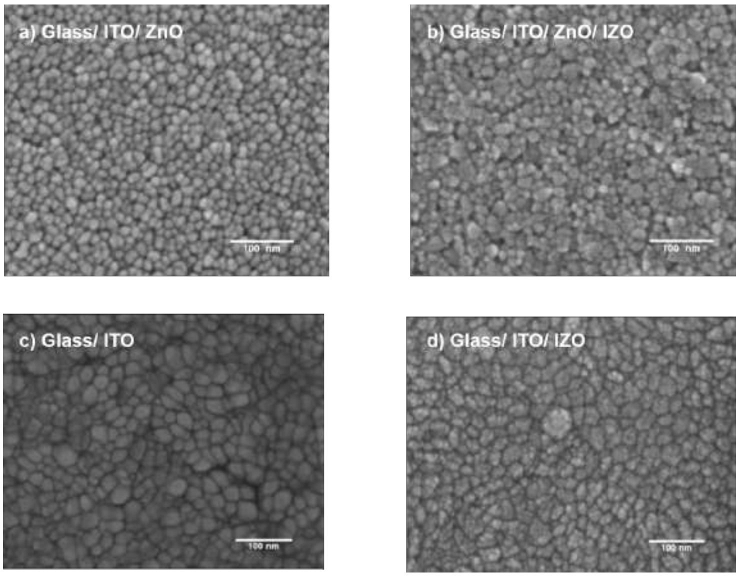

Figure 3.20:
The SEM images of a) Glass/ITO/ZnO, B) Glass/ITO/ZnO/IZO, c) Glass/ITO and d) Glass/ITO/IZO films.

[1] W. Gong, P. Wang, D. Dai, Z. Liu, L. Zheng, Y. Zhang, *J. Mater. Chem. C.* **9**, 2994–3025 (2021)

[2] S. Zheng, J. Chen, E. M. J. Johansson, X. Zhang, *iScience.* **23**, 101753 (2020)

[3] W. Chen, H. Tang, N. Li, M. A. Scheel, Y. Xie, D. Li, V. Körstgens, M. Schwartzkopf, S. V. Roth, K. Wang, X. W. Sun, P. Müller-Buschbaum, *Nanoscale Horiz.* **5**, 880–885 (2020)

[4] H. Lee, H. J. Song, M. Shim, C. Lee, *Energy Environ. Sci.* **13**, 404–431 (2020)

3.11 Mapping inhomogeneities and structure properties of perovskite films with nano-focus WAXS

N. Li, S. Pratap, A. Davydok[1], C. Krywka[1], P. Müller-Buschbaum

[1] DESY, Hamburg, Germany

Hybrid perovskite materials are one of the most promising candidates for next-generation photovoltaic and optoelectronic applications. Until now, the fabrication of hybrid perovskite films is mainly achieved through spin-coating of complex solution-based precursors. Although spin-coating, a pioneering technique that is still being studied, is capable of producing high-performance perovskite solar cells (PSCs) on a lab scale, it is extremely challenging to execute in high-through and scalable coating processes to yield a perovskite films on a large area. Therefore, spray-coating technology has been used to deposit perovskite films, attracting extensive attention. As a common industrial coating technique, spray-coating method is simple, low-cost and compatible with flexible substrates, which expand their practical development as flexible and wearable devices. These intriguing advantages has recently led to the demonstration of fully spray-cast PSCs with a power conversion efficiency of 19.4% [1].

As reported in the literature, the internal atomic scale structure of hybrid perovskite films, such as crystal orientation, lattice constant and crystal size, play a significant role on the device performance. To date, the most widely employed techniques to investigate such information are grazing-incidence wide-angle X-ray scattering (GIWAXS) and X-ray diffraction (XRD). In most cases, these conventional techniques determine an ensemble average of structural features probed over a macroscopic area. However, the local inhomogeneity of perovskites cannot be revealed.

Moreover, as it is well-known, hybrid perovskite films are sensitive to moisture, resulting in irreversible degradation, and thus limitation of the perovskite device performance [2]. Therefore, the issue about how the degradation products such as PbI_2, hydrates, and delta phases, are distributed within the perovskite films when processing under normal atmosphere needs to be explored. Therefore, we made use of nano-focused WAXS for mapping of a perovskite film over larger scales. In the present work, spatially resolved WAXS scans in a transmission mode were performed on a spray-cast hybrid perovskite film namely $(CH_3NH_3PbBr_3)_{0.50}(CH(NH_2)_2PbI_3)_{0.50}$, abbreviated as $(MAPbBr_3)_{0.50}(FAPbI_3)_{0.50}$, in a grid of about 80 μm × 20 μm using a step-size of 500 nm (Fig. 3.21). The step-size was chosen according to the nanobeam dimensions of 250 nm × 250 nm (FWHM).

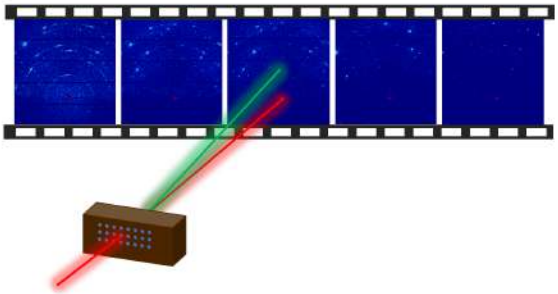

Figure 3.21: Schematic illustration of the nano-focus WAXS measurements.

This method provides a way to determine local structural information that could not be accessed using conventional grazing-incidence small-angle scattering (GISAXS), GIWAXS, or XRD. Even though nano-XRD has been used to investigate the perovskite films [3], it is the first time that the structure dependence over the depth (normal to the plane of the film) is reported.

The X-ray beam energy was adjusted to 12.75 keV to minimize beam damage to the perovskite films, since the Pb L-III edge is located at 13.04 keV. Moreover, lower beam energies are favorable for achieving better transmission signals, as beyond the Pb L-III edge, around 13.47 keV, the Br K-edge is located. The chosen X-ray beam energy turned out to be well-suited for high-transmission signals and minimized beam damage for the investigated sample. Data acquisition time was set well below the exposure limit for radiation damage. Typical signals in the 2D WAXS data correspond to well-defined Bragg transmission peaks from the polycrystalline perovskite film. After radial integration, the Bragg peaks are indexed according to the expected perovskite crystalline structure. The investigated sample provides strong Bragg reflexes indicative of high crystallinity (see Fig. 3.22). The pure phases are present in deeper layers, while the degradation impurities are located close to the surface.

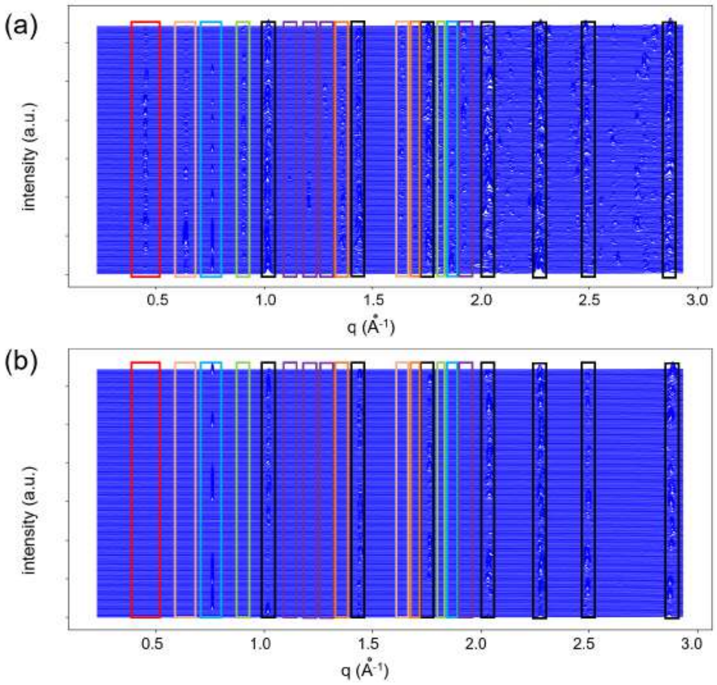

Figure 3.22:
Exemplary radial integration of 2D WAXS data of the $(MAPbBr_3)_{0.50}(FAPbI_3)_{0.50}$ film taken at different depths: (a) 5 μm and (b) 20 μm. Characteristic peaks are highlighted with colored boxes.

[1] J. E. Bishop, J. A. Smith, D. G. Lidzey, *ACS Appl. Mater. Interfaces* **12**, 48237-48245 (2020)

[2] T. A. Berhe, W. N. Su, C. H. Chen, C. J. Pan, J. H. Cheng, H. M. Chen, M. C. Tsai, L. Y. Chen, A. A. Dubale, *Energy Environ. Sci.* **9**, 323–356 (2016)

[3] S. Lilliu, T. G. Dane, M. lsari, J. Griffin, A. T. Barrows, M. S. Dahlem, R. H. Friend, D. G. Lidzey, J. E. Macdonald, *Adv. Funct. Mater.* **26**, 8221-8230 (2016)

3.12 Slot-die coating PbI_2 layers towards a 2-step perovskite solar cell printing

T. Baier, M. A. Reus, P. Müller-Buschbaum

To increase the amount of energy that is captured by solar cells, perovskites might be used in so-called perovskite solar cells (PSCs) in the future. Their advantages are that they have high power conversion efficiencies and low-cost materials are applied. There are several different technologies for thin film deposition, as for example spin-coating and printing. To make this technology ready for the large-scale production, slot-die coating is one of the most promising thin-film deposition techniques for organic-inorganic hybrid perovskite materials. The used slot-die coater is shown in Fig. 3.23a.

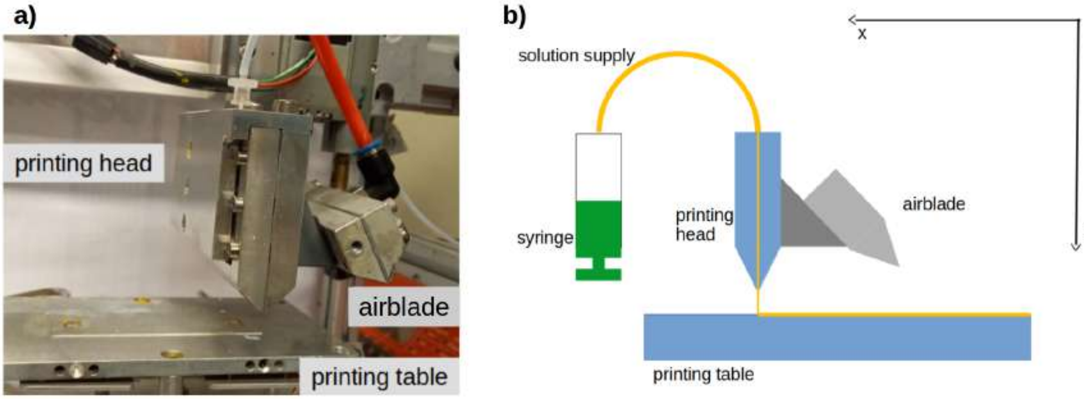

Figure 3.23: a) Picture of the printer setup and b) sketched working principle of a slot-die coater.

Figure 3.23b shows the way a slot-die coater works. There is a heatable printing table to place the sample onto and also an in x- and z-direction movable printing head through which the printable solution forms a meniscus in contact with the substrate. The solution is pushed into the printing head by a syringe. Furthermore, an airblade is used to improve the drying process by applying a constant airflow onto or above the printed sample [1].

There are two different methods to create a perovskite layer via slot-die coating: One-step and two-step deposition methods. Using the one-step deposition method, the solution containing all precursor materials to create the perovskite is deposited at once contrary to the two-step slot-die coating. Within the two-step slot die coating method, the PbI_2 precursor solution is printed firstly and in a second printing step the mixed solution is deposited to convert the initial PbI_2 layer into the final perovskite layer. Interdiffusion and conversion to perovskite are commonly triggered by an external heat supply (annealing).

Even though one-step slot-die coating seems to be more favorable concerning the production procedure because the final solar cell is prepared with one printing step less, the 2-step slot-die coating has the advantage of not handling the same solvents for all precursors, more chemical flexibility and most important more control during the film deposition process. Therefore, orientation tuning of the final perovskite crystals is simpler as well [1,2].

Towards a 2-step slot-die coated solar cell, each layer has to be optimized separately. In this work, we focus on the PbI_2layer optimization. The solution was created by dissolving PbI_2 in DMF and DMSO overnight.

The print process depends on several parameters, such as printing temperature, printing speed, annealing temperature, airflow of the airblade, annealing time and height between substrate and print head. Therefore, to get an optimal film deposition, each parameter needs to be varied while all other parameters remain constant.

Therefore, the printing temperature was changed between room temperature (≈ 25 °C) and 100 °C. At each temperature, two samples were printed and annealed afterwards. To check the dependencies between layer thickness and temperature, the thickness of each printed layer was measured via DektakXT profilometer. The Fig. 3.24a shows the dependencies between printing temperature and film thickness.

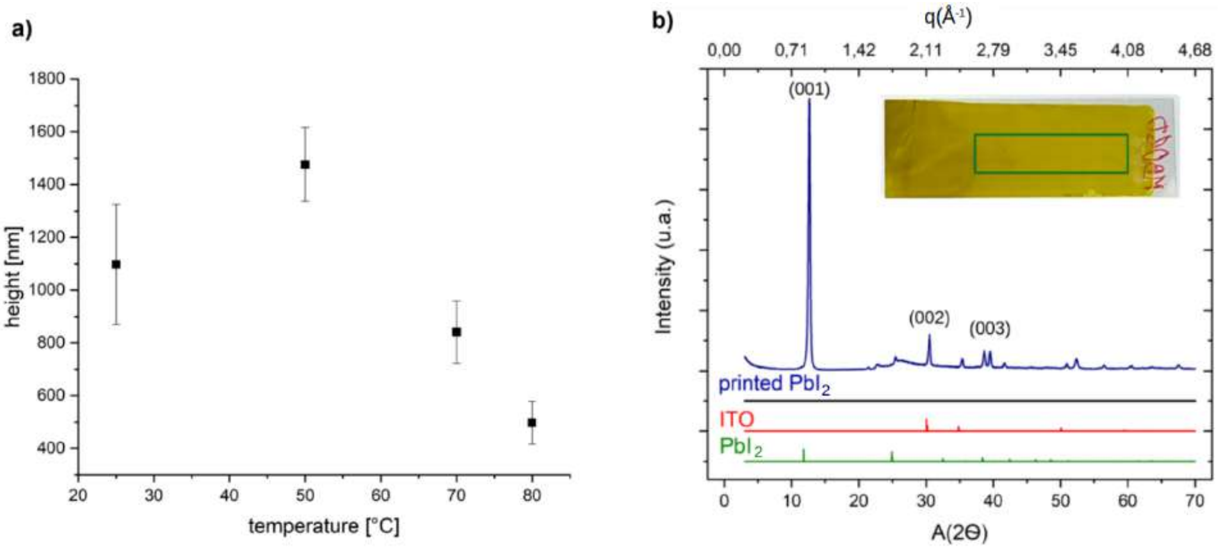

Figure 3.24:
a) Dependencies between printing temperature and layer thickness of a PbI_2 layer b) XRD data of a printed PbI_2 layer out of DMF/DMSO and simulated spectra of PbI_2 and ITO.

As can be seen in Figure 3.24a the thickness of the PbI_2 layer depends on the printing temperature. Even though the sample at 80 °C seems more favorable than at a temperature of 70 °C due to smaller error bars and a thinner printed layer, a temperature of 70°C can be chosen as the optimal one after taking the results of Fig. 3.24a) and the homogeneity of the sample into account.

Finally, a set of parameters was identified to create a PbI_2 layer that can be seen in the top right of Fig. 3.24b. The sample was printed from right to left and a homogeneous part is surrounded by a green rectangle. An excess solution from printing creates the non-homogeneous artefact of the left part of the sample. Furthermore, an XRD spectrum of the fabricated PbI_2 layer is also shown in Fig. 3.24b. There are three PbI_2 peaks visible which are the (001)-peak at $2\Theta \approx 10$ °, the (002)-peak at $2\Theta \approx 30$ ° and the(003)-peaks at $2\Theta \approx 40°$.

The next steps will be to compare the current solvent system for a PbI_2 layer with one including γ-butyrolacton (GBL) and also add different additives. Furthermore, the second printing step will be part of the future research.

[1] J. B. Whitaker, D. H. Kim, B. W. Larson, F. Zhang, J. J. Berry, M. F. A. M. van Hest, K. Zhu, *Sustain. Energy Fuels* **2**, 2442-2440 (2018)

[2] L. Oesinghaus, J. Schlipf, N. Giesbrecht, L. Song, Y. Hu, T. Bein, K. Zhu, P. Docampo, P. Müller-Buschbaum, *Adv. Energy Mater.* **3**, 1600403 (2016)

[3] M. L. Petrus, J. Schlipf, C. Li, T. P. Hujar, N. Giesbrecht, P. Müller-Buschbaum, M. Thelakkat, T. Bein, S. Hüttner, P. Docampo, *Adv. Energy Mater.* **7**, 1700264 (2017)

4 Photovoltaics

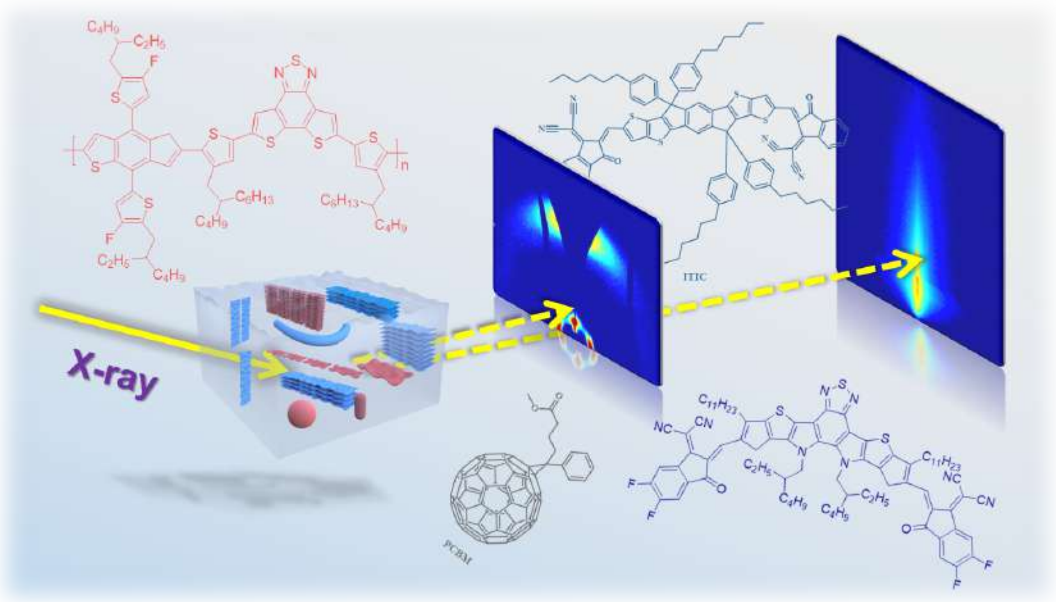

4.1 The role of ionic liquid additives in crystal orientation and photovoltaic properties of perovskite solar cells

Y. Zou, S. Yin, L. V. Spanier, J. E. Heger, P. Müller-Buschbaum

Halide perovskite solar cells (PSCs), one of the most promising photovoltaic technologies, have developed very rapidly in recent years. The certified power conversion efficiency (PCE) values have arrived at 29 % for perovskite-silicon tandem cells [1]. However, commercial application of PSCs will still need time, because the long-term operation stability and longevity are among the key limiting criteria that lead to the bottleneck of perovskite usage. Ionic liquids with superior electrical conductivity and thermal stability are used as effective and practical dopants to improve the long-term operation stability and the photovoltaic performance of PSCs [2]. Herein, we selected three types of ionic liquids based on structural analysis to examine the influence of ionic liquids on film morphology through component doping and interface modification. In more detail, we used $Pyr_{13}BF_4$, $BMIMBF_4$ and EMIMOTF. We discovered that the incorporation of ionic liquids into the perovskite precursor solution is beneficial for obtaining homogeneous films from spherical nanoparticles, as well as improves the roughness of the perovskite films.
We performed scanning electron microscopy (SEM) measurements to investigate the influence of the ionic liquids on the film morphology, as shown in Fig. 4.1 a-d. The SEM images revealed that the ionic liquids-containing perovskite films show a better coverage and higher uniformity compared to the perovskite films without any ionic liquid treatment. We further performed a statistical analysis on the grain size distribution of these films, and the results are shown in Fig. 4.2a-d. The results of the grain size distribution revealed that the ionic liquids-containing perovskite films exhibit a rather narrow particle size distribution and a larger average grain size as compared to the ones without ionic liquids. The formation of perovskite thin-film is influenced by nucleation and crystal growth. A fast nucleation and a slow crystal growth rate favor

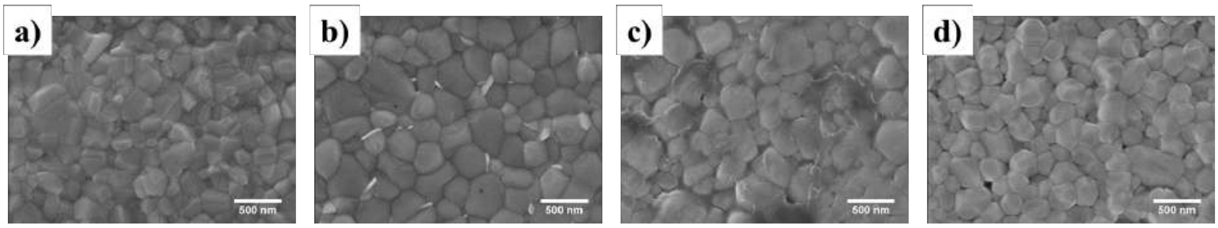

Figure 4.1:
Top-view SEM images of perovskite films treated with various ionic liquids a) control; b) Pyr13BF4; c) BMIMBF4; d) EMIMOTF.

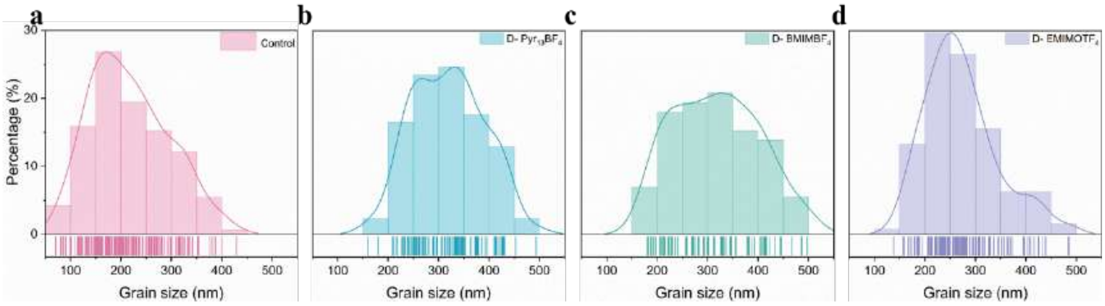

Figure 4.2:
The statistical grain size distribution of the perovskite film treated with various ionic liquids a) control; b) Pyr13BF4; c) BMIMBF4; d) EMIMOTF.

the formation of high-quality perovskite films with more surface coverage and fewer defects [3]. The imbalance between nucleation and growth rates accelerates the growth of dendritic perovskite structure, which is detrimental to the device performance. According to the SEM images, the crystal size of the ionic liquid-containing films is similar as well as uniformly distributed, and the overall grain size is increased. This could be because the incorporation of ionic liquid induces the formation of a large number of crystal nuclei that distribute uniformly on the substrate and delays the solvent volatilization due to intermolecular hydrogen bonding with DMF.[3] Under the synergistic effects of nucleation and crystallization, the crystal grains grow slowly and synchronously. When the crystal grains collide, then the crystal growth stagnates, forming uniformity and full coverage perovskite films.

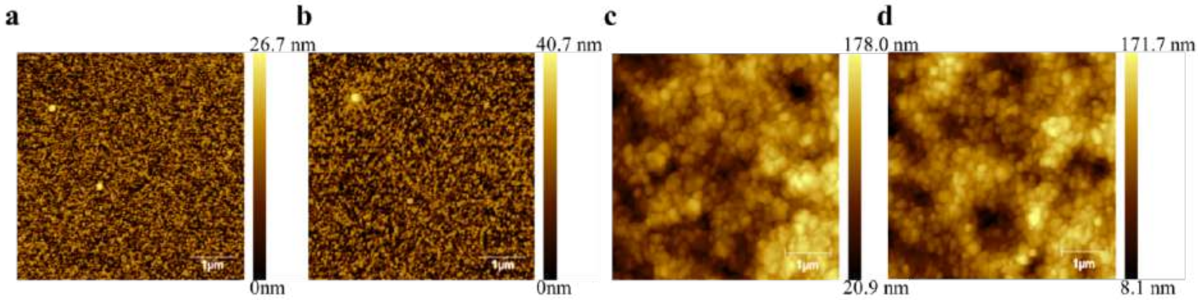

Figure 4.3:
AFM topography images of a) SnO_2. b) SnO_2-$Pyr_{13}BF_4$. c) Control. d) D-$Pyr_{13}BF_4$. The scan size is 5×5 μm.

Furthermore, we also performed atomic force microscopy (AFM) to evaluate the roughness of the film surface. Fig. 4.3 shown the AFM images of these films. We found that the roughness of the SnO_2 surface would be greatly influenced by the post-treatment of ionic liquids solution (dissolved in methanol), the roughness increased from 0.9 nm to 1.2 nm after ionic liquids treatment. This roughness change is consistent with the poor wettability without plasma treatment observed during the spin-coating of the perovskite precursor. Whereas for the perovskite films with the introduction of ionic liquids, the roughness decreased from 29.4 nm to 28.6 nm. The reduced roughness indicated that ionic liquid introduction could optimizes the smoothness of the films. This also facilitates the deposition of the hole transport layer and contributes to a better contact between the perovskite layer and the hole transport layer. As a result, we found that the incorporation of ionic liquids can improve the film quality, obtaining uniform and large-grain films. On the other hand, it could also increase the smoothness of the film and facilitate HTL deposition on the perovskite surface.

[1] A. Al-Ashouri, E. Köhnen, B. Li, A. Magomedov, H. Hempel, P. Caprioglio, J. A. Márquez, A. B. M. Vilches, E. Kasparavicius, J. A. Smith, N. Phung, D. Menzel, M. Grischek, L. Kegelmann, D. Skroblin, C. Gollwitzer, T. Malinauskas, M. Jošt, G. Matič, B. Rech, R. Schlatmann, M. Topič, L. Korte, A. Abate, B. Stannowski, D. Neher, M. Stolterfoht, T. Unold, V. Getautis, S. Albrecht, *Science* **370**, 1300–1309 (2020)

[2] C. Liu, Y. B. Cheng, Z. Ge, *Chem. Soc. Rev.*, **49**, 1653-1687 (2020)

[3] Z. Huang, X. Hu, C. Liu, L. Tan, Y. Chen, *Adv. Funct. Mater.* **27**, 1703061 (2017)

4.2 Perovskite quantum dots for photovoltaic applications

A. Krifa, M. A. Reus, L. K. Reb and P. Müller-Buschbaum

Lead halide perovskite quantum dots (PQDs) or nanocrystals (NCs) are a class of semiconductor nanocrystals with chemical formula ABX_3, where A represents an organic (formamidinium cation (FA^+), or, methylammonium cation (MA^+)) or inorganic (Cs^+) cation, B is a cation (Pb^{2+}), and X is a halide anion (Br^- and I^-) (see Fig. 4.4a) [1]. In recent years, they have attracted tremendous attention in photovoltaic devices, light emitting diodes (LEDs) and photodetectors due to their outstanding optoelectronic properties.

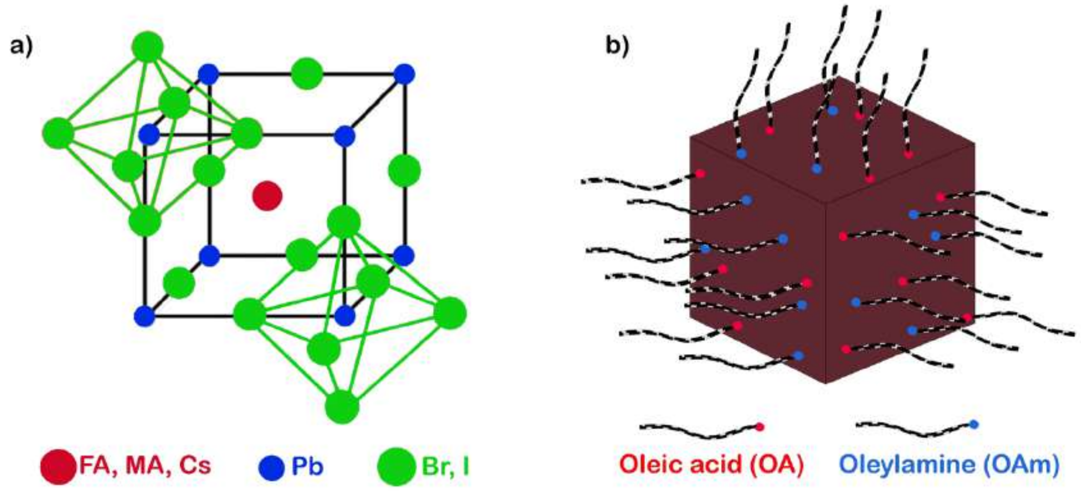

Figure 4.4:
Schematic representations a) of a perovskite quantum dot (PQD) crystal structure (ABX_3) and b) of a PQD surrounded by OAm and OA ligands.

In the last few years, one of the greatest achievements of researchers is the development of fairly easy methods to synthesize PQDs, such as hot-injection (HI) and room temperature (RT) methods like supersaturated recrystallization (SR) and ligand-assisted precipitation (LARP) [2]. Nowadays, the most developed method is the HI method, which is based on two reaction steps. First, the synthesis of Cs-oleate by the reaction of caesium carbonate (Cs_2CO_3), oleic acid (OA) and octadecene (ODE) under nitrogen environment. Once Cs-oleate is synthesized, it is added as a precursor in a second reaction in a 3-neck flask containing PbX_2 (X=Br or I), ODE, oleylamine (OAm) and OA under specific temperature. The 3-neck flask is then immediately immersed in an ice bath [3]. Through these steps, the PQDs surrounded with ligands could be synthesized as shown in Fig. 4.4b. One of the most interesting properties of PQDs is the tunability of their bandgap over the entire visible spectrum. This is not only achieved by changing their composition but also by varying the heating temperature during the synthesis: Increasing the reaction temperature leads to an increase in the size of the PQDs, which results in a red shift of the PL peak [2].
The crude solution obtained by the HI method contains not only the as-prepared quantum dots but also additional ligands, unreacted precursors, aggregates of PQDs, etc. [4] To purify the solution and redisperse the PQDs in a suitable non-polar solvent such as toluene, hexane, or octane, a centrifuge is used. In a first purification process, we try to collect all synthesized QDs and redisperse them in a non-polar solvent. For this purpose, the crude solution is centrifuged at high rpm (revolutions per minute) for a few minutes. This causes the PQDs, which have a higher density than other unreacted species or by-products, to precipitate at the bottom of

the tube, while the supernatant, which contains most of the ligands and unreacted precursors, is discarded. The precipitated PQDs, which are currently in powder form, are mixed with a non-polar solvent and shaken to redisperse them again (see Fig. 4.5a). In a second purification process, we aim to eliminate the large aggregation of the PQDs. To do this, the solution obtained is centrifuged again, but at a lower rpm and for shorter time. As a result, the large aggregates are deposited at the bottom of the tube. In this case, the supernatant is removed and stored, but the precipitate is discarded (see Fig. 4.5b). For the fabrication of PQD solar cells, not only a purified PQD solution is needed, but also a PQD solution of higher (>50mg/ml) concentration. To calculate the concentration of a solution, the supernatant from the second purification process is re-centrifuged to precipitate all PQDs. Once the new supernatant is discarded, the precipitate can be weighed and then redispersed in a certain amount of solvent for a specific required concentration.

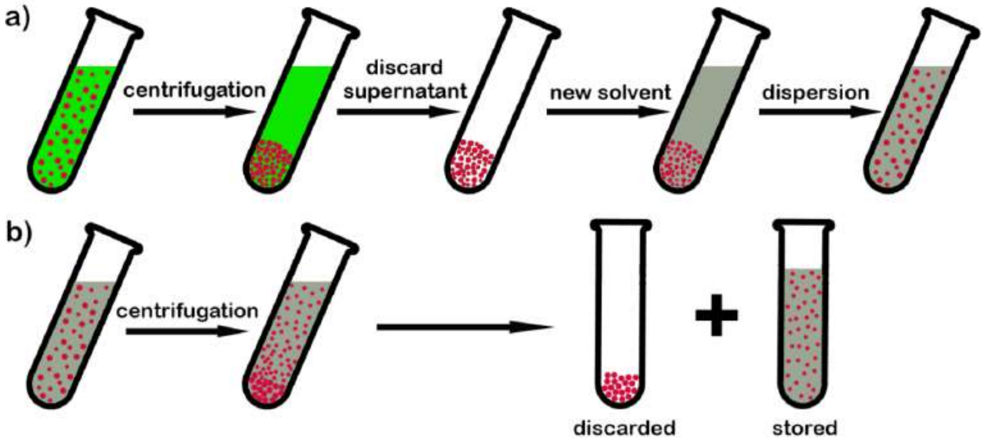

Figure 4.5:
Scheme of purification processes for perovskite quantum dot (PQD) solution: a) Removal of additional ligands and unreacted precursors, then addition of a new solvent. b) Removal of large aggregates for a highly purified solution.

PQD solar cells have shown great potential to overcome many drawbacks of bulk perovskite solar cells, such as stability and tolerance to defects, due to the ability to control the surface properties of PQDs, mainly by modifying ligands like oleic acid (OA) and oleylamine (OAm). These ligands, located on the surface of the quantum dots, play a crucial role in the stability of the solution containing the PQDs by preventing the PQDs from aggregating together and losing their quantum properties. [5] Thus, OA and OAm are well-known long-chain ligands for the synthesis of PQDs. However, in the fabrication of PQD solar cells, the long-chain ligands affect interdot coupling and decrease carrier transport between QDs, which leads to a decrease in the PCE value of the solar cell. Therefore, in PQD solar cells, the long-chain ligands should be replaced by shorter ligands that could prevent aggregation of the PQDs but to allow easy charge carrier transport.

[1] Y. Zhou, Y. Wang, *Perovskite Quantum Dots: Synthesis, Properties and Applications*, eBook ISBN: 978-981-15-6637-0

[2] Y. Zhao, J. Li,Y. Dong, J. Song, *view Isr. J. Chem.* **59**, 649-660 (2019)

[3] A. Dey, J. Ye, A. De, E. Debroye, S. K. Ha, E. Bladt, A. S. Kshirsagar, M. A. Scheel, P. Müller-Buschbaum *et al.*, *ACS Nano* **15**, 10775-10981 (2021)

[4] D. Chen, X. Chen, *J. Mater. Chem. C* **7**, 1413-1446 (2019)

[5] J. Chen, D. Jia, E. M. J. Johansson, A. Hagfeldt, X. Zhang, *Energy Environ. Sci.* **1**, 224-261 (2021)

4.3 Tuning perovskite crystal size with chloride additive for slot-die coated perovskite solar cells

A. Vitaloni, L. K. Reb, M. A. Reus, P. Müller-Buschbaum

Among emerging PV technologies, perovskite solar cells (PSCs) are considered to be one of the most promising ones, with record-breaking power conversion efficiencies (PCE) exceeding 25 % in 2021 [1]. Due to appealing characteristics such as low weight and flexibility of the devices, significantly lower energy payback times, low-cost solution-based manufacturing processes, and possible integration with existing technologies in the form of tandem solar cells, PSCs have created significant attraction over the last ten years. Efforts to improve the efficiency are mostly focused on spin-coated devices, however this fabrication process is not industrially scalable and lately many efforts have been devoted to enlarging the device area and fabricating commercial-size PSC modules to enable real-world usage [2].

Figure 4.6:
Part of the most important elements of a slot-die coater, such as die head (left), stage (bottom) and air knife (center), are visible in this picture. The solution flows in the die head and exit from its bottom, where a meniscus is formed between the die head and the substrate. Gas quenching is used to evaporate the solvent and trigger crystallization.

To overcome this limitation, we use slot-die coating to deposit the perovskite active layer. By optimizing this method, we were able to obtain a uniform and homogeneous film of approximately 15 cm^2 that can be easily scaled up to larger sizes. The optimal thickness for manufacturing high-efficiency solar cells depends on the material.The flexibility of the slot-die coating technique allows us to obtain the ideal thickness by adapting the concentration of the solution to the experimental parameters of the printing process. In Fig. 4.6 we show the printing setup, the printing process and the transition from liquid solution (yellow area) to crystalline film (black) triggered by the use of an air flow to quickly evaporate the solvent from the used ink.

In this work, we explored the effect of chloride (Cl^-) anions by tuning the standard perovskite $CH_3NH_3PbI_3$ formulation (MAPI) to $CH_3NH_3PbI_{3-x}Cl_x$ (MAPI+MACL). Cl^- is a smaller anion compared to iodide (I^-) and thus has a higher chemical reactivity that can impact chemical reaction kinetics. The effect on the crystallization kinetics is studied by systematically investigating different formulations containing Cl^- as additive in various amounts. In order to do so, perovskite thin films of 14 different formulations were prepared on glass substrates. The notation is the following: methylammonium iodide (MAI): lead iodide (PbI_2) : methylammonium chloride (MACL). The formulations are obtained by keeping MAI constant at 1, and by varying lead iodide and MACL, between 1-1.2 and 0-0.35 respectively. X-ray diffraction (XRD) data are collected on the 14 obtained spin-coated samples. In the XRD data, the perovskite peak full width half maximum (FWHM) has been determined/extracted for each formulation to calculate the crystal size based on Scherrer equation. The result of the analysis is shown in Fig. 4.7.

We observe that the crystal size is significantly increased by the addition of Cl^- as also reported in literature [3]. The result is confirmed by scanning electron microscopy (SEM) images of the film surface (see Fig. 4.8).

In contrast to literature, however, we find that if excess MACL balances the extra PbI_2, the crystal size is not increasing as much. This shows that it is important to vary not only the

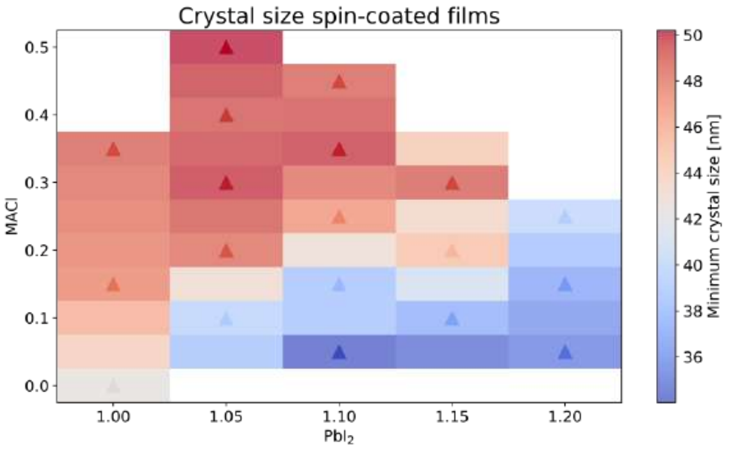

Figure 4.7:
Crystal size obtained from XRD data analysis for the formulations investigated (triangles) and interpolated for the missing data. The crystal size rises significantly for increased methylammonium chloride (MACL) concentration.

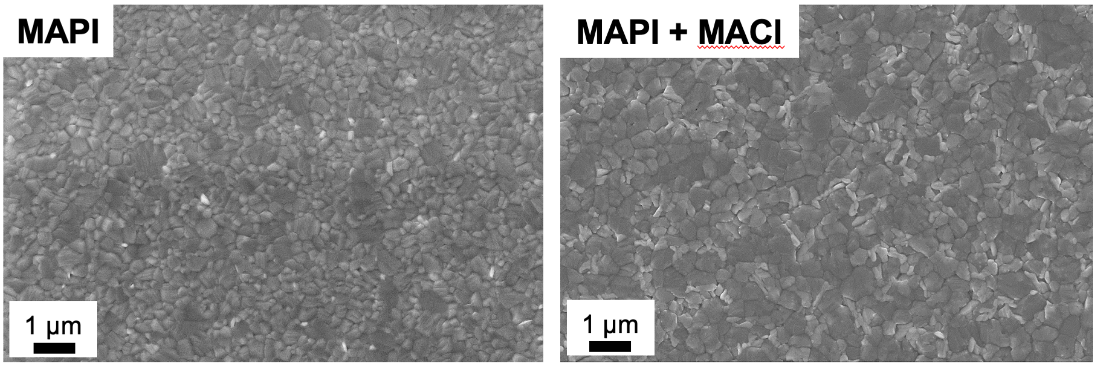

Figure 4.8:
SEM surface micrographs of slot-die coated MAPI (left) and MAPI+MACL (right) thin-films. The images confirm the effect of MACL on the crystal size observed from the XRD analysis.

MACL additive but to exclude effects that might be present due to pure MA excess.
An optimized stoichiometry of the precursor solution allows to tune crystal size and in turn will help to increase the performance of derived solar cells. With increasing grain size the performances of the PSCs increases and grain boundaries are reported to lower the efficiency due to higher chance of charge carrier recombination. With our study, we add on understanding to the optimization of the crystallization kinetics in printed PSCs – a key challenge on the way to upscaling PSC modules with high efficiency.

[1] H. Min, D. Y. Lee, J. Kim, G. Kim, K. S. Lee, J. Kim, M. J. Paik, Y. K. Kim, K. S. Kim, M. G. Kim, T. J. Shin, S. I. Seok, *Nature* **598**, 444-450 (2021)

[2] Y. Rong, Y. Ming, W. Ji, D. Li, A. Mei, Y. Hu, H. Han, *J. Phys. Chem. Lett.* **10**, 2707-2713 (2018)

[3] K. O. Kosmatos, L. Theofylaktos, E. Giannakaki, D. Deligiannis, M. Konstantakou, T. Stergiopoulos, *Energy Environ. Mater.* **2**, 79-92 (2019)

4.4 Degradation mechanism of perovskite solar cells under 1-sun illumination and humidity

K. Sun, S. Bernstorff[1], P. Müller-Buschbaum

[1] Elettra, Trieste, Italy

Organic-inorganic hybrid perovskites (OIHPS), with long carrier diffusion length, large absorption coefficient and low trap density, are regarded as one of the most promising materials for next generation solar cells [1]. The power conversion efficiency (PCE) of perovskite solar cells (PSCs) has meanwhile reached PCE$\sim$25.5% [2]. Nevertheless, the operation stability of PSCs in humid environments, under light soaking and impacted with other environmental factors, remains a hurdle towards their commercial use. In this regard, it is crucial to understand the degradation mechanism under different stresses and therefore give the hints for enhancing the longevity of PSCs. Some earlier work has shown that with a consecutive exposure to 1-sun illumination, phase segregation can easily take place especially in mixed halide perovskites, which causes the reduction of open circuit voltage (V_{OC}) and solar cell performance [3]. Also, perovskite can decompose to hydrate products and finally lead iodide (PbI_2) in high humidity environment. Despite that some pioneering work has been conducted with the aim to understand the degradation mechanisms under both light and humidity exposure conditions, the full picture is yet still to be fully understood.

A key factor to a higher PCE is the morphology of the perovskite active layer. It is well-known that pinholes and voids can provide a direct contact between the hole transport layer (HTL)/Au and the electron transport layer (ETL)/ITO in a typical n-i-p device, acting as a shunting path, which leads to a decrease of the solar cell performance [4]. Additionally, pinholes and voids can serve as non-radiative centers to reduce the charge carrier lifetime of the perovskite. Thus, it is of particular interest to investigate the structural changes during the device operation. Herein, we use grazing-incidence small-angle X-ray scattering (GISAXS) to probe the structural changes and simultaneously monitor the evolution of solar cell performance during the device operation with I-V tracking.

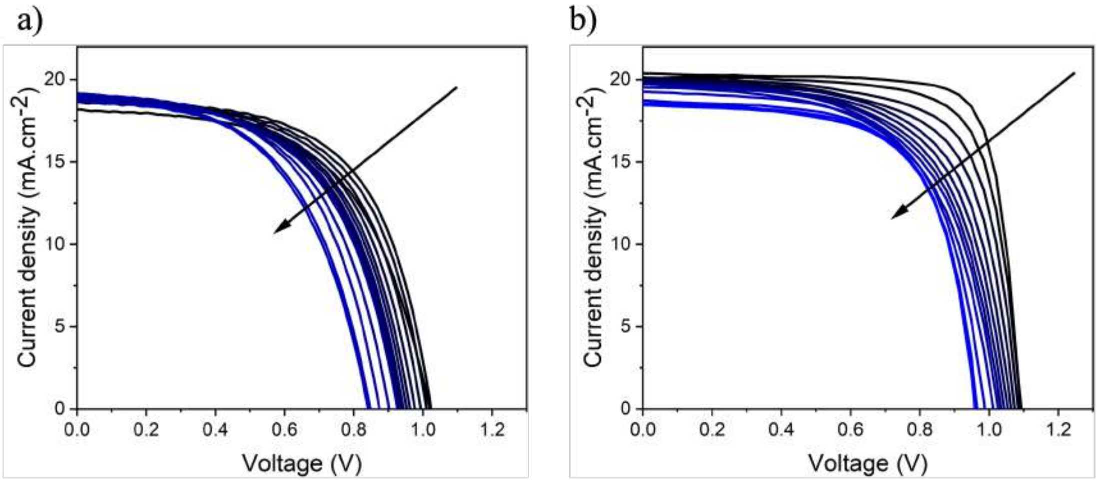

Figure 4.9:
Device performance as a function of time for the a) reference (*ref*) sample and the b) CsFAMA sample.

In this work, we use $(MAPbBr_3)_{0.08}(FAPbI_3)_{0.92}$ and $(MAPbBr_3)_{0.08}(FAPbI_3)_{0.92}$ with 5% cesium iodide (CsI) as our samples, denoted as reference (*ref*) and CsFAMA, respectively. Fig. 4.9 depicts the evolution of solar cell performance of the (*ref*) and the CsFAMA devices, respectively. For the (*ref*) cell, the main loss of solar cell performance can be attributed to losses in the open circuit voltage V_{OC} and in the fill factor (FF), as shown in Fig. 4.9a. However, in contrast to the (*ref*) sample, after adding CsI, the device showed a slower decay of the solar cell performance including the short current density (J_{SC}) and V_{OC}. Thus, CsFAMA devices are more stable as compared to (*ref*) devices.

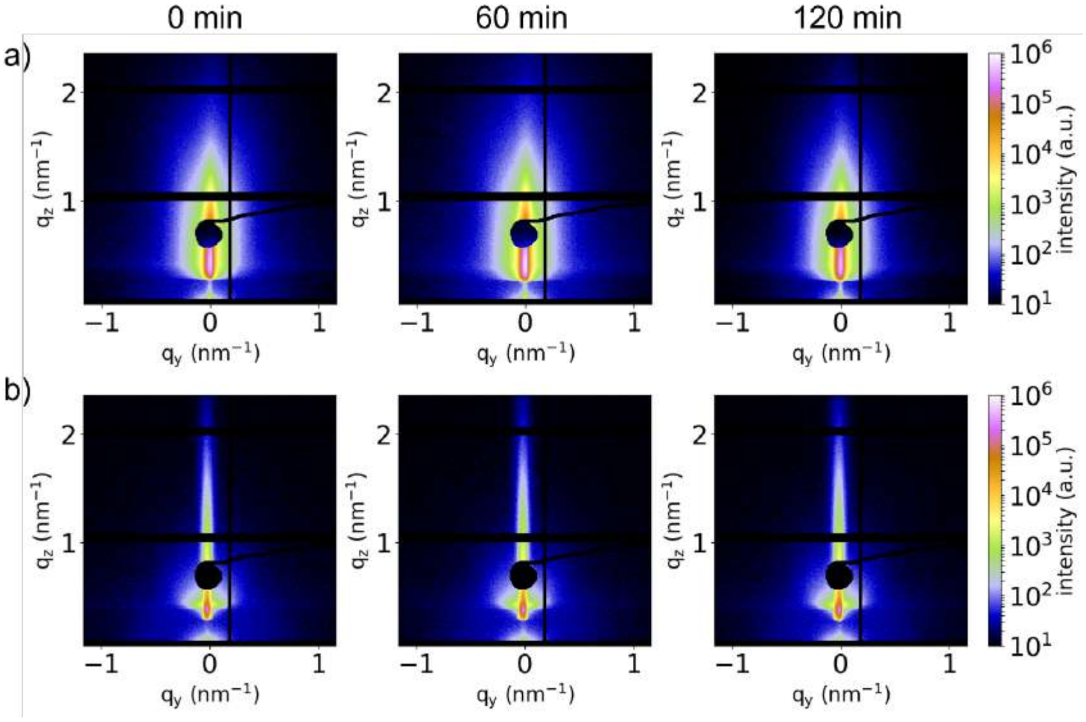

Figure 4.10:
2D GISAXS data measured during the operation at 0, 60 and 120 min for the a) reference sample and the b) CsFAMA sample.

GISAXS measurements (Fig. 4.10) were conducted at the Austrian SAXS beamline of the Elettra synchrotron source to reveal the morphology evolution of perovskite film during its operation. These 2D GISAXS data show the structural stability of both, (*ref*) and CsFAMA devices against light and humidity. Very obviously, the 2D GISAXS patterns of the (*ref*) and CsFAMA samples are distinctly different. During the device operation, the changes per sample type are rather small. To further quantify the results from the 2D GISAXS data, we will perform the horizontal line cut at the Yoneda region of the material of interest and model them in the framework of local disperse approximation (LMA) and distorted wave Born approximation (DWBA).

[1] Y. Lin, Y. Fang, Y. Shao, S. J. Stuard, M. M. Nahid, H. Ade, Q. Wang, J. E. Shield, N. Zhou, *Nat. Commun.* **10**, 1-11 (2019)

[2] H. Ruderer, D. Y. Lee, J. Kim, M. J. Paik, Y. K. Kim, K. S. Kim, M. G. Kim, *Nature* **598**, 444-450 (2021)

[3] N. Lin, Y. Luo, Z. Chen, X. Niu, X. Zhang, J. Lu, R. Kumar, J. Jiang, H. Liu, X. Guo, *Joule* **4**, 1743-1758 (2020)

[4] P. Kaienburg, P. Hartnagel, B. E. Pieters, J. Yu, D. Grabowski, Z. Liu, J. Haddad, U. Rau, T. Kirchartz, *J. Phys. Chem. C* **122**, 27263-27272 (2018)

4.5 Improving the performance of perovskite quantum dot solar cells

H. T. Myint, A. Krifa, L. K. Reb, M. A. Reus, P. Müller-Buschbaum

The role of metal halide-based perovskite quantum dots is increasingly important in the field of optoelectronic applications in light emitting diodes (LEDs), lasers and especially solar cells (SCs). Its potential as a next-generation photovoltaic devices is due to its excellent properties like band gap energy tunability, high photoluminescence quantum yields, and ease of chemical stabilization. The quantum confinement effect of these quantum dots leads to these unique photoelectric and luminescent properties.
Perovskite quantum dots have the chemical composition ABX_3 (Fig. 4.11), where A stands for organic or inorganic cations (formamidinium, methylammonium, cesium), B for lead or tin cations, and X is a halide (Cl, Br, I) anion [1]. The performance of the solar cells is improved by different engineering techniques of surface, composition and device architecture, as well as by enhancing their operational stability. Compositional design by the substitutions or mixtures of different cations or anions benefits from the adjustable band gap energy to advance optoelectronic properties [1].

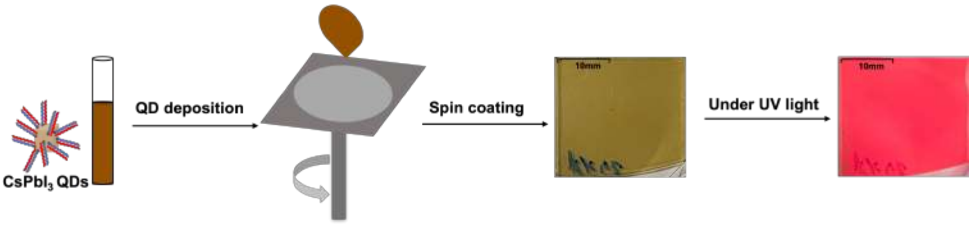

Figure 4.11:
Schematic diagram of thin film deposition by solution-based spin-coating of the perovskite quantum dots.

The influence of the surface chemistry on the stability and photovoltaic performance is also controlled by the surface ligands [2,3]. During the synthesis of perovskite quantum dots, long-chain organic ligands such as oleic acid (OA), oleylamine (OLA) are commonly used as capping ligands so that the quantum dots do not aggregate. The counteraction of the long-chain ligands to the Van der Waals attraction between perovskite quantum dots suppresses the growth of the nucleation sites of the crystal. However, as a drawback, ligands could under conditions hinder charge transport and limit the performance of the solar cells. Therefore, ligand surface engineering has been one of the most important steps to improve the stability by removing or exchanging long-chain ligands with short-ligand ones [3].

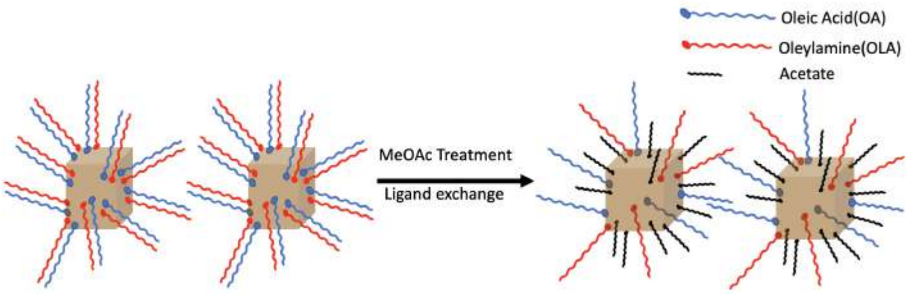

Figure 4.12:
Schematic diagram of ligand exchange process. A washing step with MeOAc removes the long OA and OLA ligands and replaces with shorter acetate ligands to improve the electronic properties of the perovskite quantum dot film.

The fundamental and effective surface modification is to use methyl acetate (MeOAc) as a ligand-exchange solvent in the post-synthetic process (see Fig. 4.12). This enhances the electronic coupling of the perovskite quantum dots, which leads to better charge carrier mobility, and then consequently increases the conductivity of the films. Moreover, the defect passivation of the perovskite quantum dots surface is also improved from this process [4].

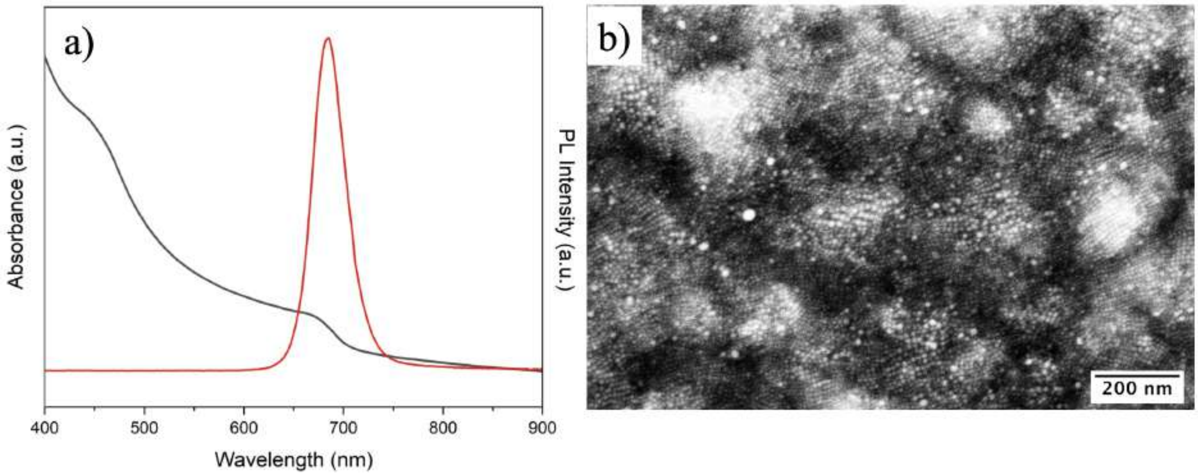

Figure 4.13:
Optical and morphological properties of $CsPbI_3$ perovskite quantum dots. a) The UV-vis absorption and PL spectra demonstrate its characteristic absorption/emission wavelength around 690nm. b) Scanning electron microscopy (SEM) measurement shows an average particle size of these perovskite quantum dots of around 8-10 nm.

Fabricating high-quality perovskite thin films is also crucial in the solar cell industries. The techniques for solution-based thin-film deposition are optimized to to yield high-quality layers that are uniform, compact, and pinhole- free [4].

The pioneering research for lab-scale studies is done with spin-coating techniques that focus to optimize the morphology of the films, as well as to link morphological features to functional properties in the thin film. In this project, we investigate the optical and morphological properties of $CsPbI_3$ perovskite quantum dots. First results of opto-electronical measurements and morphology characterization can be seen in Fig. 4.13.

Our next steps are to optimize and upscale the production of perovskite quantum dots thin films for the application of solar cells with high power conversion efficiency. The printing of the perovskite quantum dots using the blade-assisted slot-die printing technique will be used to achieve high power conversion efficiencies together with scalable low-cost solar cells.

[1] J. Chen, D. Jia, E. M. J. Johansson, A. Hagfeldt, X. Zhang, *Energy Environ. Sci.* **1**, 224-261 (2020)

[2] R. Han, Q. Zhao, J. Su, X. Zhou, X. Ye, X. Liang, J. Li, H. Cai, J. Ni, J. Zhang, *J. Phys. Chem.C* **125**, 8469-8478 (2021)

[3] K. Chen, Q. Zhong, W. Chen, B. Sang, Y. Wang, T. Yang, Y. Liu, Y. Zhang, H. Zhang, *Adv. Funct. Mater.* **29**, 24, 1900991 (2019)

[4] Z. Saki, M. M. Byranvand, N. Taghavinia, M. Kedia, M. Saliba, *Energy. Environ. Sci.* **14**, 5690 (2021)

4.6 Halogen-free solvents in fullerene-free organic solar cell fabrication and their impact on performance stability

L. V. Spanier, M. Schwartzkopf[1], S. V. Roth[1], P. Müller-Buschbaum

[1] DESY, Hamburg, Germany

In recent years, organic solar cells (OSCs) attracted increasing attention due to their relatively easy scalability in their fabrication and extraordinarily high gravimetric power densities. Especially the advent of new small-molecule acceptor (SMA) materials as replacement for difficult-to-synthesize fullerenes sparked a wide variety of OSC systems with highly tunable properties. In order to make the manufacturing process of the bulk-heterojunction (BHJ), i.e. the active layer, more environmentally friendly, increased efforts have recently been made in order to overcome the necessity for harmful and toxic solvents such as chloroform (CF).
In this work, we examine the impact of using different solvents on the performance and *operando* morphology of the OSCs, utilizing a PTQ-2F:BTP-4F thin-film BHJ. In order to achieve good solubility of the non-fullerene BTP-4F acceptor material, solutions from chlorobenzene (CB), ortho-xylene (oXY), and 1,2,4-trimethylbenzene (TMB) were heated to elevated temperatures respectively, while solutions from CF remained at room temperature.

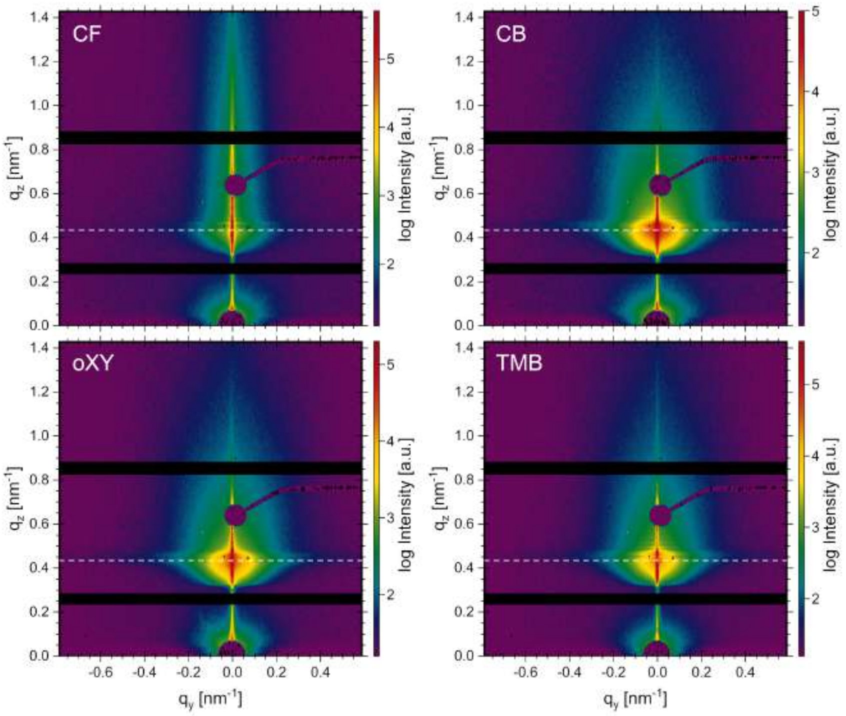

Figure 4.14:
2D GISAXS data of PTQ-2F:BTP-4F BHJs processed from the different solvents CF, CB, oXY, and TMB. The position of the Yoneda-peak of PTQ-2F is indicated by a white horizontal dashed line.

Investigations of the internal morphology of PTQ-2F:BTP-4F BHJs from the different solvents were conducted by means of grazing-incidence small-angle X-ray scattering (GISAXS) measurements at the P03 beamline at DESY, as shown in Fig. 4.14. The CF-processed films thereby not only showed a narrowed 2D intensity distribution along the q_y-direction, but also increased scattering intensity along the q_z-axis, indicating a lower uncorrelated roughness of internal interfaces. The strong variation in the scattering profile in q_y showcases also, that the solvent composition strongly influences the size distribution of the PTQ-2F polymer domains contained within the BHJ. Overall, the BHJ thin-films processed from CB, oXY and TMB share similar mesoscopic morphologies, which has been attributed to their similar drying kinetics in previous studies [1].

We furthermore investigated the *operando* performance stability of thus produced organic solar cells, featuring PTQ-2F:BTP-4F BHJs from the respective solvents, under illumination with a simulated AM1.5 spectrum, while probing the internal morphology using 2D GISAXS (see Fig. 4.15).

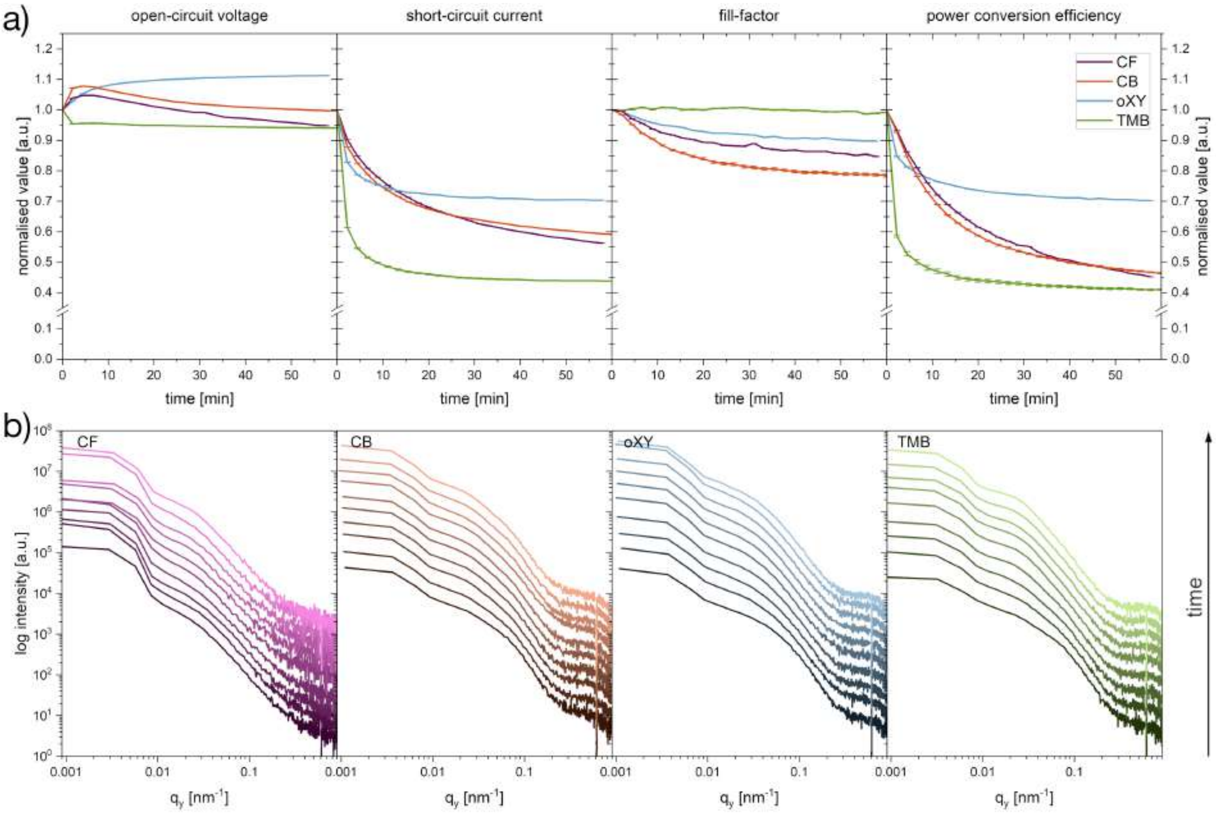

Figure 4.15:
a) Degradation under illumination of normalized device parameters including: open-circuit voltage (V_{OC}), short-circuit current density (J_{SC}), fill factor (FF), and power conversion efficiency (PCE) of PTQ-2F:BTP-4F OSCs based on different solvents. b) Time-evolution of selected horizontal 2D GISAXS line-cuts centered around the PTQ-2F Yoneda peak.

We found the reduction in short-circuit current density (J_{SC}) being the driving factor for the degradation of power conversion efficiency (PCE), whilst the fill-factor (FF) exhibits relatively high stability and the open-circuit voltage (V_{OC}) does even increase in some cases. This behavior of the photo-current has previously been correlated with the growth in polymer domain sizes, leading to a reduced interface-to-volume ratio between the polymer and SMA within the BHJ, thus reducing the probability for excitons to dissociate [2]. This mechanism is also indicated by *operando* GISAXS measurements, showing a narrowing scattering intensity along the q_y-direction from a growing fraction of larger diameter polymer domains. It is interesting to highlight the close similarity between the degradation behavior of OSCs from CF and CB, while oXY-processed OSCs show the highest temporal stability. This work is an important step towards further understanding and optimizing the influence of solvent composition on the morphology and thus stability of organic solar cells.

[1] H. Zhao, H. B. Naveed, B. Lin, X. Zhou, J. Yuan, K. Zhou, H. Wu, R. Guo, M.A. Scheel, A. Chumakov, S. V. Roth, Z. Tang, P. Müller-Buschbaum, and W. Ma, *Advanced Materials* **32**, 2002302 (2020)

[2] K. S. Wienhold, W. Chen, S. Yin, R. Guo, M. Schwartzkopf, S. V. Roth, and P. Müller-Buschbaum, *Solar RRL* **4**, 2000251 (2020)

4.7 Slot-die coating of PBDB-T-2F:BTP-4F films for use in organic solar cells

C. Gutiérrez-Bolaños, L. A. Kohlmaier, L. V. Spanier, P. Müller-Buschbaum

Organic solar cells (OSCs) are among the most promising candidates for next-generation photovoltaics as they have shown an increasing improvement in power conversion efficiencies (PCEs) while maintaining low fabrications costs, and beneficial properties such as high flexibility, low weight and transparency. In OSCs based on blends of a polymer electron-donor and non-fullerene small molecule acceptor, considerable increase in the device performance was gained, reaching PCE values of more than 18% already [1]. The polymer:small molecule blend forms an interpenetrating network with homogeneous regions of each material, which is typically called bulk heterojunction (BHJ). The BHJ layer is the photoactive layer where sunlight is harvested [2].

In contrast to the classical rigid silicon solar cells, the solution-based manufacturing processes of OSCs such as spray-coating and printing allow more viable means of production. These techniques, at the same time, enable OSCs to be used in new and more versatile applications, where different architectural objects and devices need to be covered with thin, light, flexible solar cells, for instance, smart windows, foldable smart roofs and future aerospace technologies [3]. In recent years, the use of printing methods, such as slot-die coating, is increasing popularity as fabrication method as it entails great potential for large scale fabrication of devices. As printing techniques involve complex evolution of the organic thin film structure and morphology, the nanostructure of the films needs to be studies. For this purpose, grazing-incidence small-angle X-ray scattering (GISAXS) can be used for the analysis of the inner crystal structure and the corresponding domains of the printed polymer films [4].

In the present study, the polymer PBDB-T-2F was used as donor and BTP-4F as non-fullerene acceptor with chloroform (CF) as solvent to form the BHJ active layer of the OSCs. Slot-die coating was used as fabrication method for the thin film active layer. The objective was to prepare BHJ active layers with thickness of 150 ± 20 nm, which as reported in literature is a good thickness range for OSCs to optimize light harvesting [5]. Multiple substrates were coated with different coating parameters in order to get a better insight into the reproducibility of the slot-die coating process and to investigate their impact on the properties of the so-formed thin films.The desired thickness was achieved. Optical microscopy showed a first insight on the general film homogeneity of the coated thin films on the large scale. A broad spectral range of absorbance for the polymer system was confirmed with UV-vis spectroscopy. A good film homogeneity was achieved after exploring the boundaries of the so-called printing window. The structure of the active layer was also studied by performing static GISAXS measurements at the beamline P03 at the Deutsches Elektronen-Synchrotron (DESY). The blend

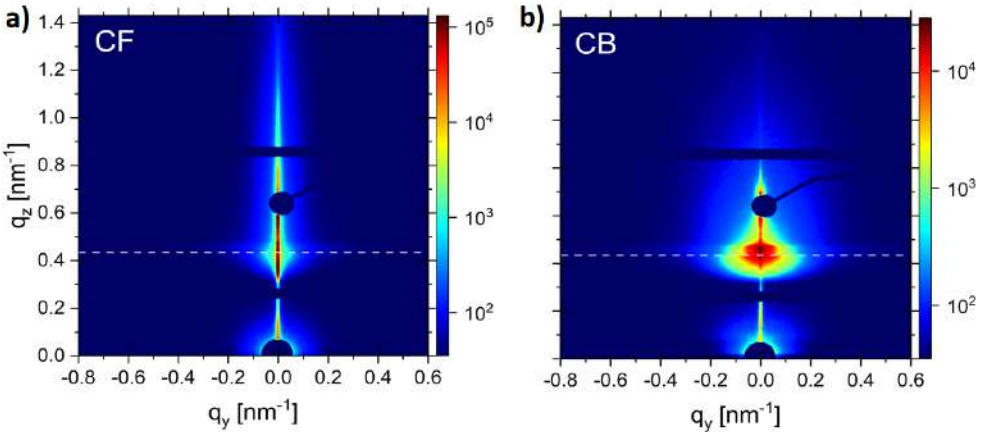

Figure 4.16: GISAXS static measurements for (a) PBDB-T-2F:BTP-4F in CF and (b) PBDB-T-2F:BTP-4F in CB. The dotted white line indicates the Yoneda peak position of PBDB-T-2F.

PBDB-T-2F:BTP-4F was slot-die coated on silicon substrates from a solution with two different solvents, CF and chlorobenzene (CB) and was analyzed. In Fig. 4.16 the corresponding 2D GISAXS data are shown. The scattering of the film printed out of CF indicates a smoother film morphology. In contrast, an increased diffuse scattering is observed in the case of the CB-processed thin film. It could indicate higher uncorrelated roughness of internal interfaces and smaller structural sizes.As a next step, the optimized slot-die coating parameters were selected to build the active layer of various OSCs. The device efficiency of the printed OSCs was measured with a solar simulator. The highest measured PCE was 6.85 %. To gain a better understanding about the morphological changes of the printed OSCs during device operation, operando GISAXS measurements were performed at the synchrotron radiation facility Elettra.
In addition, the degradation experiment was repeated with an identical solar cell in the Munich laboratories without the presence of the intense X-ray beam. The device data were recorded for the initial 25 min of operation (see Fig. 4.17). In addition, after 140 min device performance data were obtained again. An interpolation allowed to combine both initial and final data. As seen from the normalized representation, the decrease in the short circuit current is the leading degradation mechanism as it was reported before also for other OSC systems.

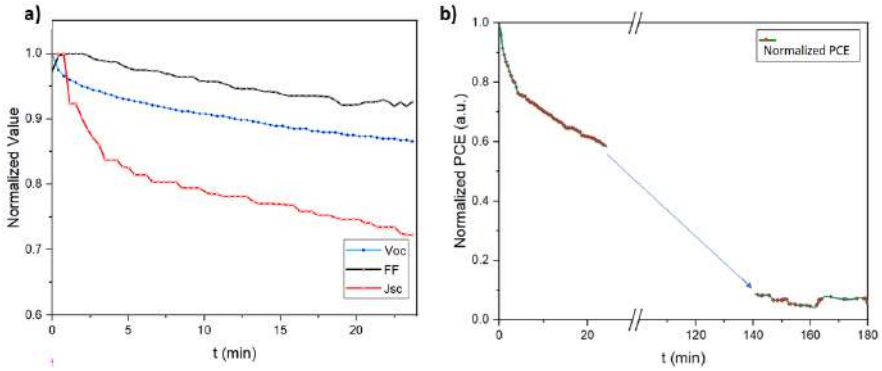

Figure 4.17:
Organic Solar Cell parameters. a) Fill factor (FF), short circuit current density (Jsc), and open circuit voltage (Voc) measured under illumination. b) OSC PCE evolution during 3 h illumination.

The system PBDB-T-2F:BTP-4F in CF can present several technical challenges during the slot-die coating process due to the fast drying of the solution, and thus clogging of the slot-die coating head during the print process. However, this problem could be controlled by cleaning thoroughly the slot-die head inlet and cleaning the slot-die head after every coating attempt. Sometimes, *infusion* of chloroform in the slot-die head meniscus mask is needed to promote the flow of the solution. However, functional solar cells were fabricated and a PCE of 6.85 % was reached. The system's microscopic morphology was analyzed as well as its degradation behaviour. Further analysis on the morphology of the thin films needs to be explored in order to move into next steps for optimization of the polymer and solvent systems used. As well as in the organic photovoltaic power efficiencies.

[1] Q. Liu, Y. Jiang, K. Jin, J. Qin, J. Xu, W. Li, J. Xiong, J. Liu, Z. Xiao, K. Sun, S. Yang, X. Zhang, L. Ding, *Science Bulletin* **65**, 272-275 (2020)

[2] C. Yan, S. Barlow, Z. Wang, H. Yan, A. K. Jen, S. R. Marder, X. Zhan, *Nat. Rev. Mat.* **3** (2018)

[3] L. K. Reb, M. Bohmer, B. Predeschly, S. Grott, C. L. Weindl, G. I. Ivandekic, R. Guo, C. Dreißigacker, R. Gernhauser, A. Meyer, P. Müller-Buschbaum, *Joule* **4**, 1880–1892 (2020)

[4] P. Müller-Buschbaum, *Synchrotron Radiation in Materials Science* **1**, 191–238 (2018)

[5] J. Yuan, Y. Zhang, Li. Zhou, G. Zhang, H. Yip, T. Lau, X. Lu, C. Zhu, H. Peng, P. A. Johnson, M. Leclerc, Y. Cao, J. Ulanski, Y. Li, Y. Zou, *Joule* **3**, 1140-1151 (2019)

4.8 Dynamic and static spin-coating of organic solar cells

M. Di Girolamo, X. Jiang, P. Müller-Buschbaum

Organic solar cells (OSCs) represent a promising green solar energy technology. State-of-the art devices present excellent power conversion efficiencies (PCEs), with champion devices exceeding 18%. These results were achieved mostly thanks to the synthesis of new active layer materials, especially non-fullerene acceptors (NFAs), and device engineering [1]. Most of the champion organic solar cells reported in the literature rely on spin-coating, while printed devices still present lower efficiencies today. The performance gap occurs because of significant differences in the drying kinetics and morphology of spin-coated and printed active layers [2]. Therefore, fabrication methods remarkably influence the efficiency of a device. OSCs with the active layer realized through static or dynamic spin-coating show considerable divergence in their characteristics. The distinction between the two techniques is drawn by the way, in which the precursor solution is spread onto the substrate. The two spin-coating methods are shown in Fig. 4.18.

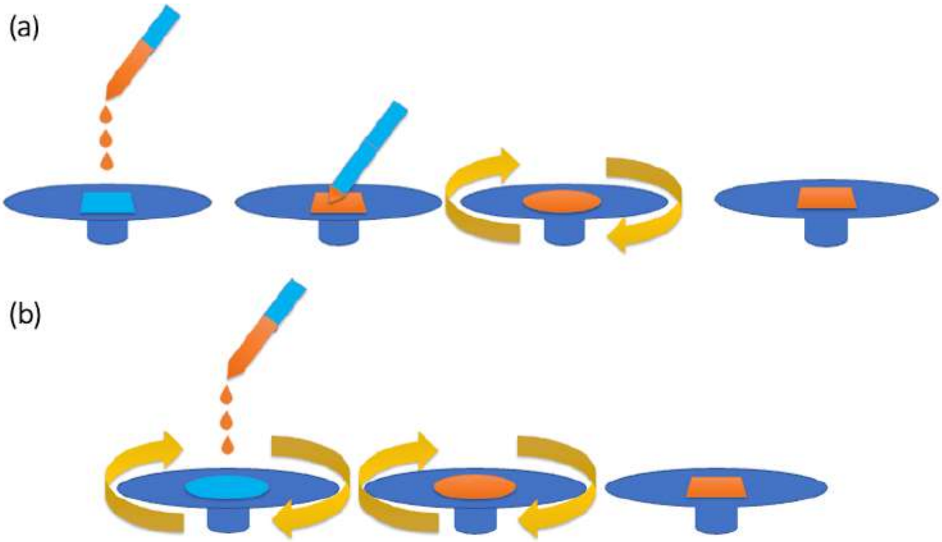

Figure 4.18:
A schematic representation of (a) static and (b) dynamic spin-coating. In static spin-coating, the solution is dropped onto the substrate and spreaded out with the pipette, then rotation starts. In dynamic spin-coating, the solution is dropped on the substrate during rotation.

Static spin-coating consists of placing the precursor solution on the substrate with the help of a volumetric pipette. The spin-coater at this point is not rotating, and the solution is quickly spreaded out onto the entire surface with the pipette tip. Immediately afterwards, rotation starts. During this procedure, the operator has to be fast and precise, making sure that the substrate is fully and thoroughly coated, while avoiding solvent evaporation or air bubble formation before the rotation starts. Moreover, while the pipette touches the substrate damage needs to be avoided, therefore extreme dexterity and carefulness is required. On the other hand, in dynamic spin-coating, the substrate is already rotating on the spin-coater, while the solution is dropped onto it. Experimental errors are definitely reduced in comparison to the static procedure, as the substrate is not touched by the pipette and the drying process is entirely regulated by the centrifugal force. Therefore, the method yields more reproducible results. Evidence of this can be seen in Fig. 4.18, as during static spin-coating it can easily occur that the whole substrate gets not fully coated, or the evaporation process starts before rotation, leaving visible traces on the film. As it can be seen in Fig. 4.19, the dynamic spin-coated device seems to be thinner. As the rotation speed and time used for fabrication was the same throughout the two methods, this represents a considerable difference. Thickness enormously influences performance: If a layer is thick, the number of charge carriers might be improved because of more absorption. In very thick films, the charges need to travel a long distance before being collected by the electrodes, which can have a negative impact. When the transit time is longer, the risk of recombination increases. These phenomena directly influence the PCE [3]. Thickness measurement results for different active layer systems presented in Fig. 4.20 show a pattern where static spin-coating yields thicker devices.

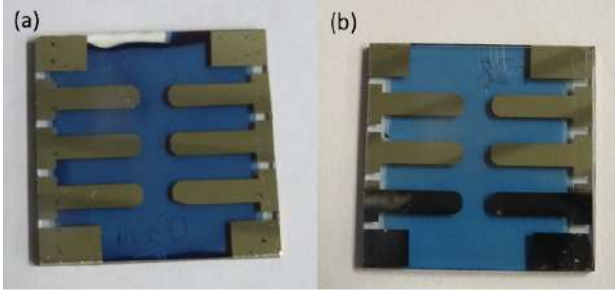

Figure 4.19:
Comparison of samples realized through (a) static and (b) dynamic spin-coating. On the edges of the static spin-coated sample, it is possible to see an uncoated spot and some darker areas, where the solvent had evaporated before rotation started. The dynamic sample presents a defect-free surface.

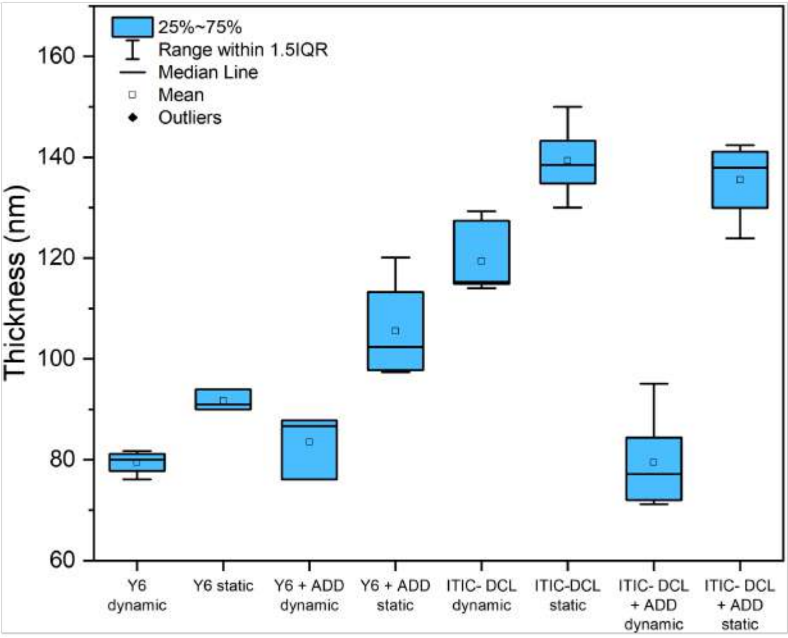

Figure 4.20:
Thickness measurements obtained by the profilometer for different devices realized both with static and dynamic spin-coating. The systems used all combine PM6 as a donor material with the different non-fullerene acceptors (NFAs) Y6 and ITIC-DCL. Systems with a functional additive (+ADD) are also shown. The used additive was 1-chloronaphthalene.

To summarize, the fabrication method used in the realization of an organic solar cell, especially during active layer deposition, is directly linked to the device performances. Different approaches during spin-coating, from static to dynamic, influence directly the thickness and therefore the performance parameters. Moreover, dynamic spin-coating yields more reproducible devices with fewer defects and more homogeneous evaporation.

[1] H. Gao, X. Wan, Z. Xuan, W. Ma, J. Xin, C. Li, Y. Chen, *J. Mater. Chem. C* **10**, 2742-2748 (2022)

[2] K. Zhao, H. Hu, E. Spada, L. K. Jagadamma, B. Yan, M. Abdelsamie, Y. Yang, L. Yu, R. Munir, R. Li, G.N. Ndjawa, *J. Mater. Chem. A* **4**, 16036-16046 (2016)

[3] M. S. Kim, B.G. Kim, J. Kim, *ACS Appl. Mater. Interfaces* **1**, 1264-12691 (2009)

4.9 Solvent effects on the printed active layer for high performance non-fullerene organic solar cells

X. Jiang, P. Chotard, S. V. Roth [1], P. Müller-Buschbaum

[1] DESY, Hamburg, Germany

Slot-die coating has been regarded as a powerful method due to the upscaling manufacturing possibilities for organic solar cells (OSCs). Thus, developing a straightforward and low energy consumption printing process is crucial for further commercialization, such as low-temperature conditions. In addition, the active layer morphology is crucial for achieving high efficiency in OSCs, which demonstrates the strong relevance of the donor-acceptor formation in different conditions (e.g. temperature assistance, host solvent, atmosphere) during film drying. Therefore, deeper insights into the influence of the host solvent on the active layer morphology are very important for the low-temperature fabrication method [1]. In this work, we fabricate slot-die coated organic solar cells with a wide bandgap donor polymer (PDTBT2T-FTBDT) and a non-fullerene acceptor (BTP-4F). Their chemical structures are shown in Fig. 4.21a. The host solvents chloroform (CF) and chlorobenzene CB) are selected to tune the morphology of the PDTBT2T-FTBDT and BTP-4F as well as their blends. To further understand the influence of the solvent, we also studied the effect on the respective donor and acceptor.

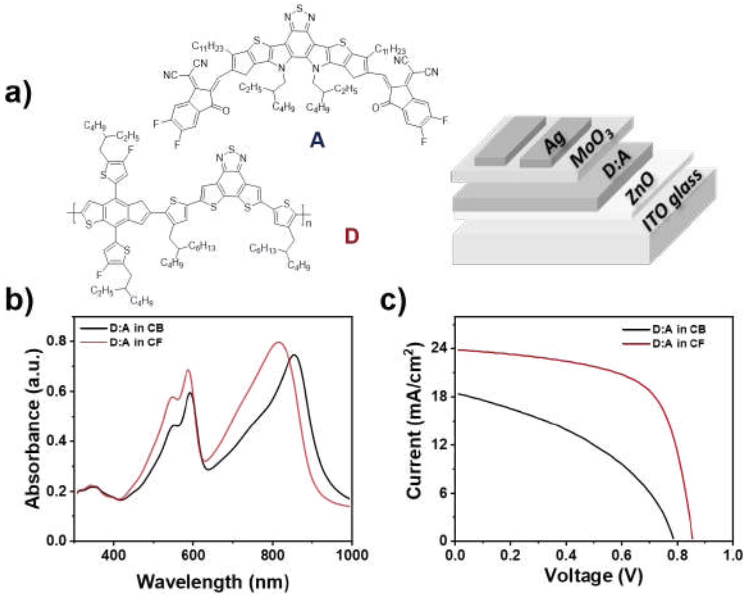

Figure 4.21:
a) Chemical structure of the donor PDTBT2T-FTBDT (D) and acceptor BTP-4F (A) and the inverted device geometry of the printed OSC device in this work. b) UV-vis absorption spectrum of printed active layer processed with CB and CF, respectively. c) J-V curves of the best-performing inverted devices based on the printed PDTBT2T-FTBDT:BTP-4F active layers.

The effect of different host solvents on the optical properties is investigated by UV-vis spectroscopy. As shown in Fig. 4.21b, the CF-processed PDTBT2T-FTBDT:BTP-4F blend film exhibits a higher absorption in the whole spectral range, where the PDTBT2T-FTBDT shows a λ_{0-0} peak at 587 nm, a λ_{0-1} peak at 546 nm and BTP-4F at 809 nm. In contrast, CB-processed PDTBT2T-FTBDT:BTP-4F blend films show a lower absorption. The PDTBT2T-FTBDT λ_{0-0} peak redshifts to 591 nm with a shoulder at 549 nm and the BTP-4F peak redshifts to 858 nm, suggesting preferable J aggregates in mixtures processed with CB. The solvent effect on the photovoltaic performance was systematically studied from the organic solar cells with an inverted structure. As seen in Fig. 4.21c, the printed active layer processed with CB solvent, shows a performance of 6.02% ,with a V_{oc} of 0.79 V, a J_{sc} of 18.49 mA/cm^2, and a FF of 41.39%. Notably, the active layer printed with CF solvent exhibited a promising PCE of 13.16% with a J_{sc} of 23.84 mA/cm^2, a FF of 64.49%, and a V_{oc} of 0.86 V, respectively.

The inner structure of the printed donor, acceptor and blend thin-films processed with different solvents is investigated with GISAXS measurements (see Fig. 4.22a-d). Horizontal line cuts of

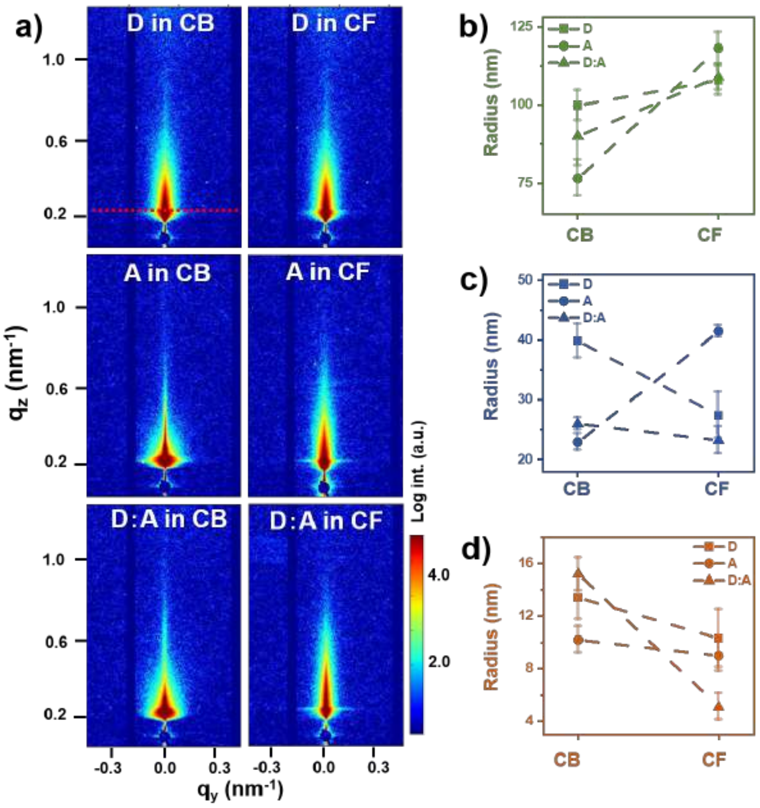

Figure 4.22:
a)2D GISAXS image of the donor, acceptor and blend thin films processed from CB and CF solvent, respectively (The red horizontal dashed line represents the Yoneda peak position of the material). Comparison of the average domain radii for the b) large, c) medium, d) small structure PDTBT2T-FTBDT, BTP-4F is abbreviated in D, A respectively.

the 2D GISAXS data are performed at the Yoneda peak position of the material, in order to investigate the characteristic structures [2]. The average large-radii domains of donor, acceptor and the blend are (107 ± 10) nm, (77 ± 7) nm and (50 ± 5) nm in CB, while they change to (81 ± 7) nm, (113 ± 10) nm and (93 ± 8) nm in CF solvent. The middle-radii domain of donor, acceptor and the blend are (33 ± 5) nm, (21 ± 4) nm and (28 ± 4) nm, and they turn into (27 ± 4) nm, (41 ± 4) nm and (22 ± 3) nm in CB solvent. The average small-radii domain of donor, acceptor and blend are (12.8 ± 3.5) nm, (9.5 ± 2.3) nm and (20.3 ± 1.5) nm processed with CB solvent, and decreased to (6.6 ± 2.2) nm, (8.6 ± 2.1) nm and (5.1 ± 1.5) nm processed with CF solvent. As shown in Fig. 4.22b, the average large radii of the blend film processed with CB is the smallest among the PDTBT2T-FTBDT, BTP-4F and blend thin films, which suggests that the blend structure is influenced by both, the donor and the acceptor. However, compared with CB-solvent-processed samples, the large-radii of the blend thin film processed with CF solvent increases. This is the same trend as for BTP-4F, but opposite to the behavior of PDTBT2T-FTBDT. It signifies that the large-radii of the blend film are more dependent on BTP-4F rather than on PDTBT2T-FTBDT if processed with CF. However, the change in the middle-radii of the blend film is more in line with the PDTBT2T-FTBDT behavior in CF solvent. Since the BTP-4F size does not change much in both solvents, the decrease in the small-radii processed with CF solvent of the blend thin film is mainly due to the decrease in the structure of PDTBT2T-FTBDT. It should be noted that the small-radii of the blend thin film are pronouncedly decreased in the CF solvent. According to previous studies, the small-radii domains on the order of tens of nanometers demonstrate a suitable structure size for the extraction of charge carriers [1]. Therefore, the blend thin films processed with CF solvent are expected to provide better performing OSCs compared to CB solvent.

[1] X. Jiang, P Chotard, K. Luo, F. Eckmann, S. Tu, M. S. Reus, S. Yin, J. Reitenbach, C. L. Weindl, M. Schwartzkopf, S. V. Roth, P. Müller-Buschbaum, *Adv. Energy Mater.* **10**, 2103977 (2022)

[2] P. Müller-Buschbaum, M. Stamm, *Macromolecules* **31**, 3686–3692 (1998)

4.10 Simultaneously enhanced performance and stability of NFA solar cells with PETMP interfacial process

Z. Li, C. Ma[1], P. Müller-Buschbaum

[1] SINANO, CAS, Suzhou, China

Organic solar cells have called great research interest due to their various advantages such as their light weight, flexibility and the possibility to use designable materials. With the rapid development of novel non-fullerene acceptors (NFA), the power conversion efficiency (PCE) of NFA solar cells has reached over 19% [1], while the limited illumination stability is still a big issue before real application [2]. For NFA solar cells, the degradation at the ZnO/BHJ interface under illumination proved to be one of the key sources for performance decrease. It was reported that the hydroxyl radicals of ZnO forming under illumination would cause the degradation of the acceptor materials. They could be effectively suppressed by modifying ZnO with a radical trapping agent, of which 2-phenylethyl mercaptan (PET) showed the best effect [3]. Unfortunately, PET is highly toxic with a bad smell, which is not acceptable for industrial use. Here, a molecule with similar end group as PET, namely PETMP, is used as alternative since it has four sulfhydryl groups in one molecule. Interestingly, PETMP is able to suppress the formation of hydroxyl radicals as well as to improve the device stability, just like PET does. Moreover, PETMP can improve the J_{sc} of devices and simultaneously enhance the device performance and stability.

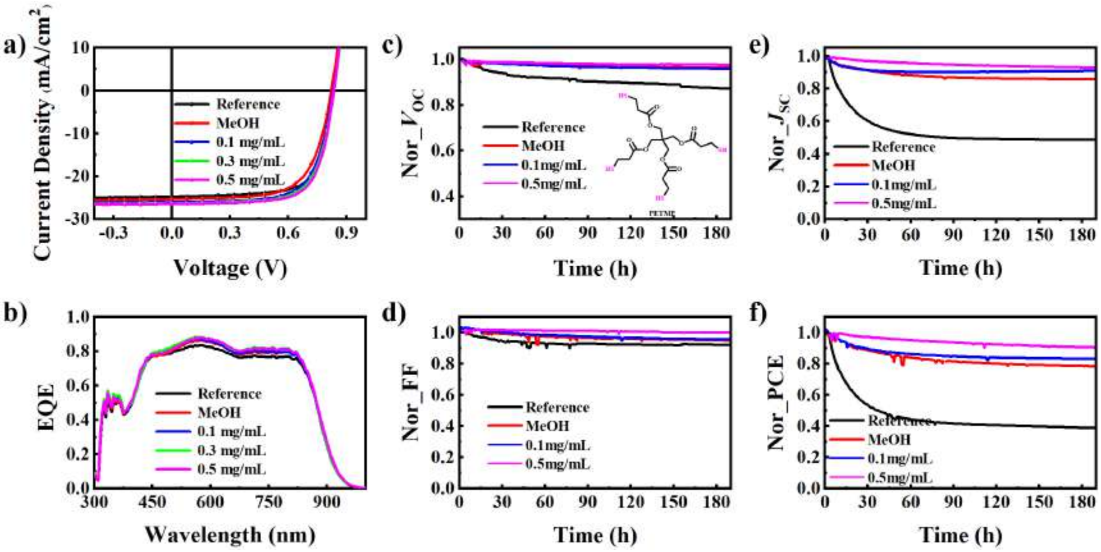

Figure 4.23:
a) J-V curves and b) EQE curves of PM6:Y6 devices modified with different concentration of PETMP, c) Normalized V_{oc}, d) Normalized FF, e) Normalized J_{sc}, f) Normalized PCE degradation curves of PM6:Y6 devices modified with different concentration of PETMP under illumination.

Fig. 4.23a and b show the J-V curves and EQE curves of PM6:Y6 devices modified with different concentration of PETMP, from which we can see that the J_{sc} of the devices increased gradually with higher concentration, while too much PETMP would cause a poor FF due to the interfacial barrier. Furthermore the devices were put under LED illumination. Fig. 4.23c to f demonstrate the V_{oc}, FF, J_{sc} and PCE changes with time. It can be seen that MeOH could improve the device stability greatly since it's a hydroxyl radiation trapper agent as well. Interesting, PETMP could further suppress the interfacial degradation and slow down the performance decay, especially on J_{sc} and FF. Such a modification effect is quite similar with that of PET as reported before, suggesting the same function of PETMP here.

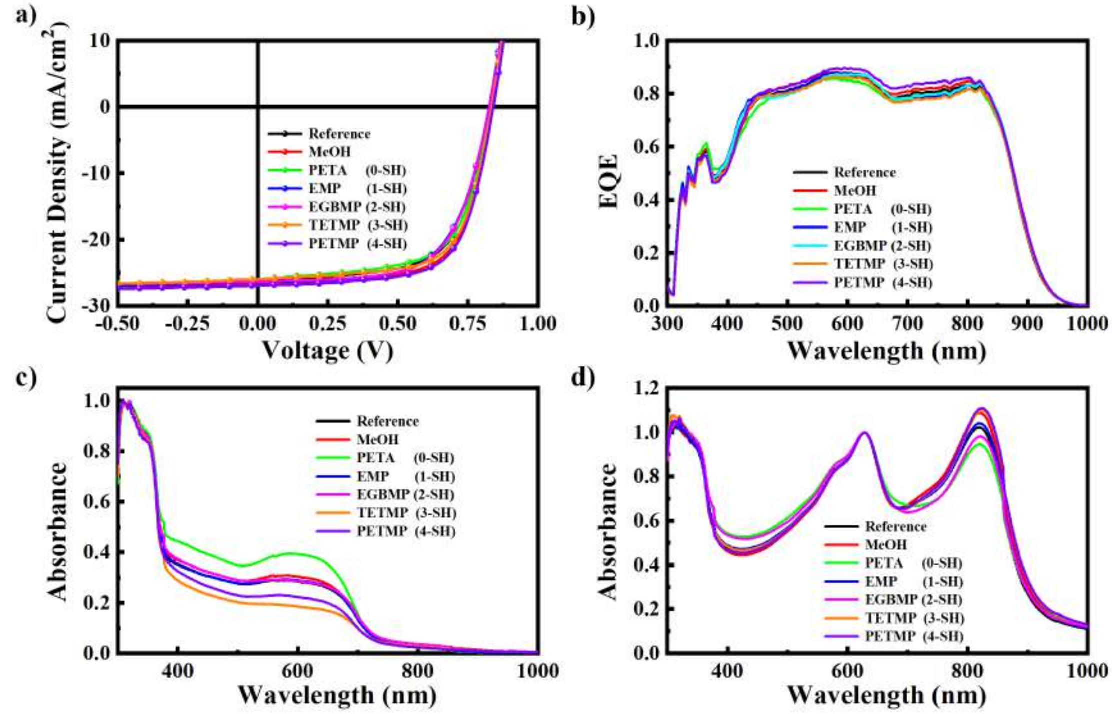

Figure 4.24:
a) J-V curves and b) EQE curves of PM6:Y6 devices modified with different sulfhydryl derivatives, UV-vis absorption spectra of c) ZnO modified with different sulfhydryl derivatives and d) PM6:Y6 films on ZnO modified with different sulfhydryl derivatives.

Fig. 4.24a and b show the J-V curves and EQE curves of PM6:Y6 devices modified with different sulfhydryl derivatives, where only modification with more sulfydryls could improve the JSC as well as PCE. Fig. 4.24c and d demonstrate the UV-vis absorption spectra of ZnO films and PM6:Y6 films on ZnO. The improved absorption of ZnO films after interfacial modification may cause the difference in device performance (especially FF). The relatively enhanced signal of Y6 in blend films may be related to the improvement of Jsc.

In summary, PETMP could suppress the formation of hydroxyl radicals on the ZnO surface and improve the stability of inverted polymer solar cells. For the suspected mechanism of improved performance, PETMP may also affect the vertical phase separation through the interaction between sulfydryl and active layer. More characterizations are to be carried out to find the detailed mechanisms. This work provides a perfect interfacial modification agent replacing PET that suppresses the formation of hydroxyl and improves the stability of NFA solar cells, which could promote the development of their further application.

[1] Y. Cui, Y. Xu, H. Yao, P. Bi, L. Hong, J. Zhang, Y. Zu, T. Zhang, J. Qin, J. Ren, Z. Chen, C. He, X. Hao, Z. Wei, J. Hou, *Adv. Mater.* **33**, 2102420 (2021)

[2] C. Liao, Y. Hsiao, K. Tsai, N. Teng, W. Li, J. Wu, J. Kao, C. Lee, C. Yang, H. Tan, K. Chung, Y. Chang, *Sol. RRL* **5**, 2000749 (2021)

[3] B. Liu, Y. Han, Z. Li, H. Gu, L. Yan, Y. Lin, Q. Luo, S. Yang, C. Ma, *Sol. RRL* **5**, 2000638 (2020)

5 Polymer-hybrid systems

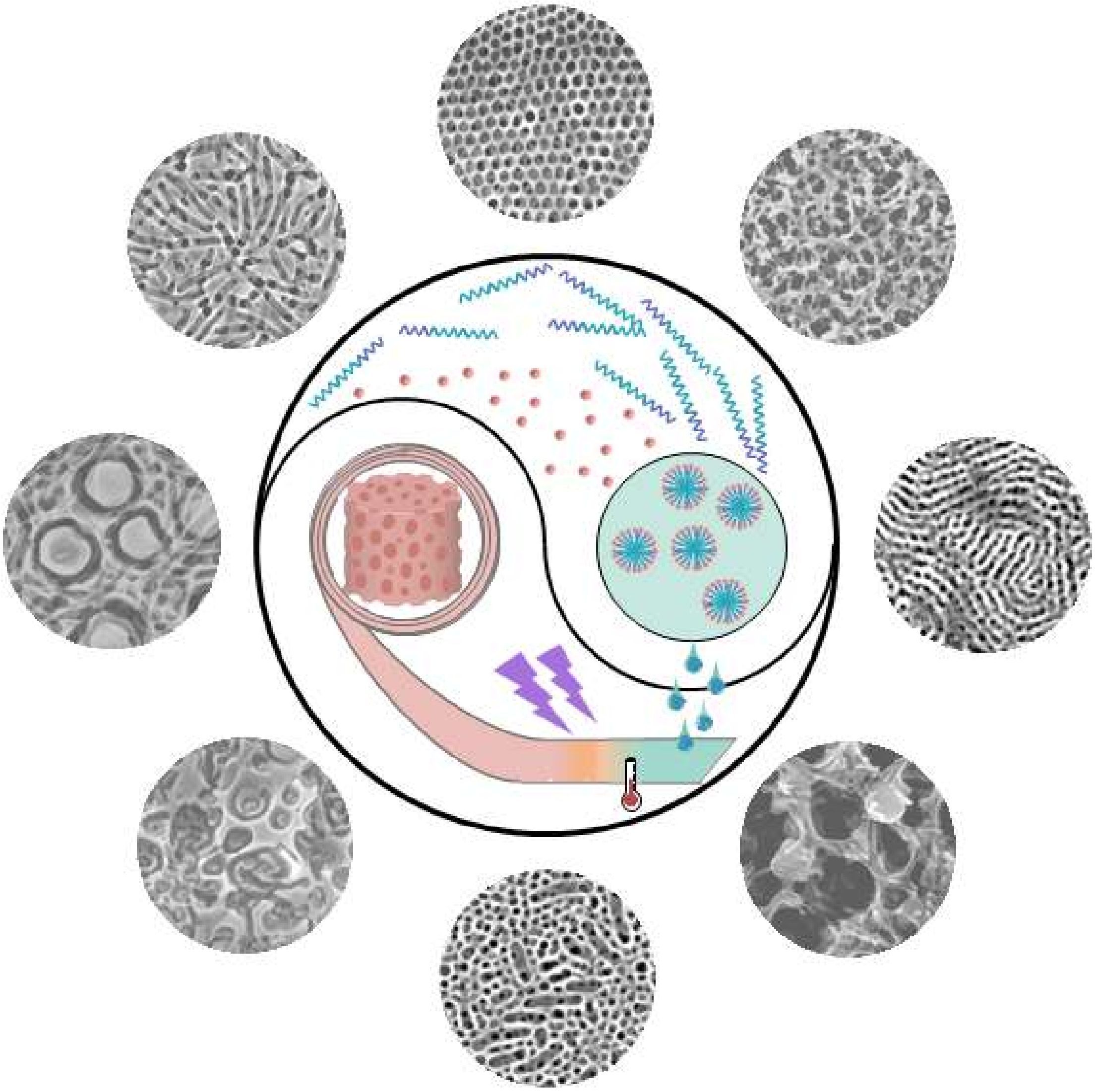

5.1 Utilitzing *in situ* GISAXS to monitor the self-assembly of slot-die printed hybrid diblock copolymer thin films containing mixed magnetic nanoparticles

C. R. Everett, M. Bitsch[1], M. Plank[2], M. Gallei[1], M. Schwartzkopf[3], S. V. Roth[3,4],
P. Müller-Buschbaum

[1] Saarland University, Saarbrücken, Germany
[2] TU Darmstadt, Darmstadt, Germany
[3] DESY, Hamburg, Germany
[4] KTH, Stockholm, Sweden

Thin films composed of diblock copolymers (DBCs) and embedded magnetic nanoparticles (MNPs) are unique hybrid materials that gained attention for applications such as magnetic sensing and magnetic data storage [1]. Such films advantageously combine the properties of both the organic and inorganic components. DBCs are comprised of two different polymers covalently bonded to each other. When the two blocks are immiscible, microphase separation occurs, which leads to the formation of periodic nanostructures. By tuning the volume fraction of the two blocks in relation to one-another, DBCs can form spherical, cylindrical, gyroid, or lamellar structures inside thin films [2]. This makes DBC films interesting as scaffolds for inorganic particles [3]. MNPs have attracted interest in many fields and demonstrate unique size-dependent properties.

For ferromagnetic MNPs, where the magnetic domains align parallel to one another, decreasing particle diameter leads to an increase in coercivity, the ability of the particle to resist demagnetization. This is important in magnetic data storage devices as a high coercivity equates to better data stability. However, with decreasing particle size, some critical diameter exists below which the MNPs lose their ferromagnetic behavior and become superparamagnetic, making them no longer appropriate for data storage applications [1].

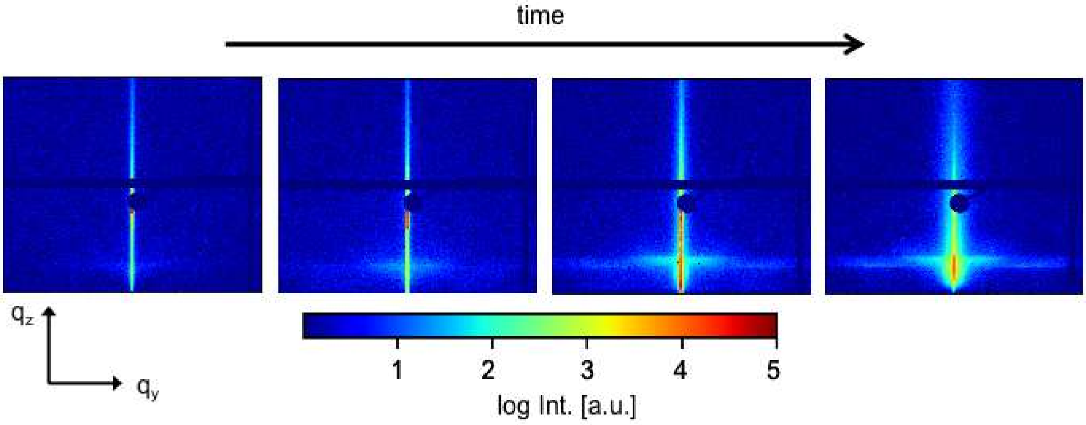

Figure 5.1:
GISAXS data measured during the self-assembly process of a slot-die printed PS-*b*-PMMA film containing both Ni and Fe_3O_4 nanoparticles.

In the present work, the self-assembly of a magnetic hybrid DBC thin film containing two types of MNPs fabricated in a slot-die printing process was investigated using grazing-incidence small-angle X-ray scattering (GISAXS). Slot-die printing was chosen as the film deposition technique as it is fast, gives uniform thickness control, and scales up for large, industrially-relevant fabrication processes [4]. Ultra high molecular weight (UHMW) polystyrene-*block*-poly(methyl methacrylate) (PS-*b*-PMMA), nickel nanoparticles (Ni, 1 wt%), and magnetite nanoparticles

(Fe_3O_4, 1 wt%) were chosen as the solution precursors. The Ni nanoparticles were coated with PMMA ligands while the Fe_3O_4 nanoparticles were coated with oleic acid ligands. GISAXS data of the self-assembly process can be seen in Fig. 5.1. Immediately after deposition, scattering from the wet solution dominates the scattering pattern. As the film begins to dry, the formation of in-plane structures within the film can be observed.

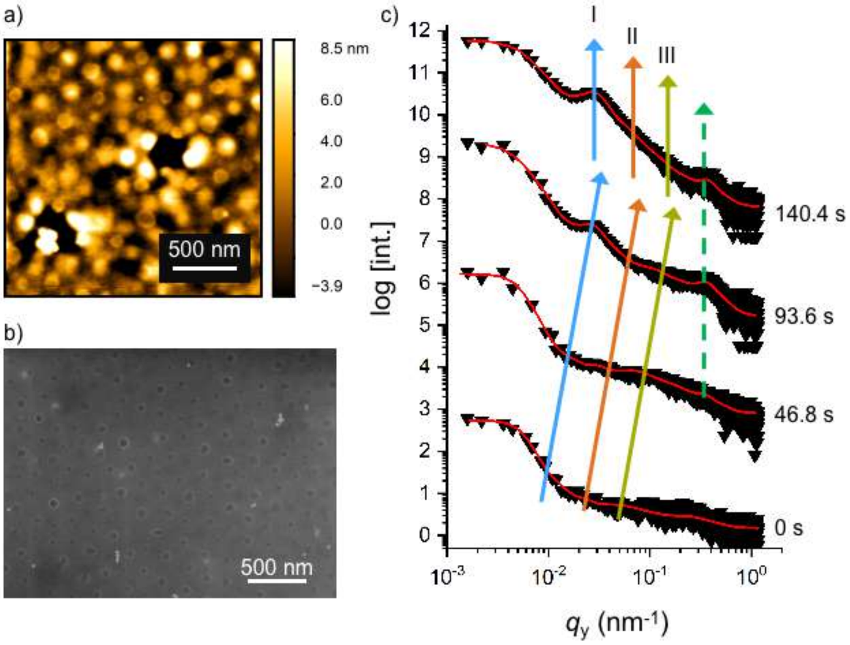

Figure 5.2:
(a) AFM and (b) SEM images of the final dry film. (c) Selected 1D horizontal cuts and their respective fits (red lines) from the self-assembly of a PS-*b*-PMMA film containing both 1 wt% Ni and 1 wt% Fe_3O_4 nanoparticles. The blue, orange and yellow arrows represent the structure factors of the PMMA cylinders, Ni nanoparticles, and Fe_3O_4 nanoparticles, respectively.

Fig. 5.2a and Fig. 5.2b show the atomic force microscopy (AFM) and scanning electron microscopy (SEM) micrographs of the final dry film. The microphase separation of the DBC film is clearly seen in both images, with the PMMA domains forming ordered cylindrical domains inside a PS matrix. Nanoparticles also appear on the surface of the film. To understand how the inner film structure evolves, horizontal line cuts at the material characteristic Yoneda region are performed on the 2D GISAXS data. Fig. 5.2c shows selected line cuts and their respective fits that are marked with the features I (blue arrow), II (orange arrow), and III (yellow arrow). These important features are the structure factors of the upright PMMA cylinders, of the Ni nanoparticles, and of the Fe_3O_4 nanoparticles, respectively. Up until 103 s, at which point the stable dry film is reached, structure I shifts from smaller q_y values to larger q_y values. This is due to the evaporation of the solvent, which leads to a decrease in the average center-to-center distance and radius of the PMMA cylinders from 415 nm to 176 nm and from 107 nm to 49 nm, respectively. After the dry film state is reached, further structural evolution does not occur as the polymer chains are no longer mobile. Similarly, a shift in q_y values for structures II and III is also observed and the center-to-center distance of the nanoparticles decreases from 230 nm to 95 nm and from 82 nm to 38 nm for the Ni and Fe_3O_4 nanoparticles, respectively. The radii of the nanoparticles remains unchanged.

[1] W. Cao, S. Xia, X. Jiang, M. Appold, M. Opel, M. Plank, R. Schaffrinna, L. P. Kreuzer, S. Yin, M. Gallei, M. Schwartzkopf, S. V. Roth, P. Müller-Buschbaum, *ACS Appl. Mater. Interfaces* **12**, 7557-7564 (2020)

[2] H. Hu, M. Gopinadhan, C. O. Osuji, *Soft Matter* **10**, 3867-3889 (2014)

[3] S. Xia, L. Song, W. Chen, V. Körstgens, M. Opel, M. Schwartzkopf, S. V. Roth, P. Müller-Buschbaum, *ACS Appl. Mater. Interfaces* **11**, 21935-21945 (2019)

[4] R. Patidar, D. Burkitt, K. Hooper, D. Richards, T. Watson, *Mater. Today Commun.* **22**, 100808 (2020)

5.2 Interaction of colloidal inks with nanoporous cellulose

C. Harder[1], A. E. Alexakis[2], B. Sochor[1], A. Vagias[3], L. Porcar[4], E. Malmström[2], P. Müller-Buschbaum, S. V. Roth[1,2]

[1] DESY, Hamburg, Germany
[2] KTH, Stockholm, Sweden
[3] MLZ, Garching, Germany
[4] ILL, Grenoble, France

Our goal is to fabricate colloidal photonic layers exploiting structural colors in cellulosic materials. One prominent example from nature is the color blue, which stems from reflection and interference effects and is not induced by pigments [1]. The optical properties of the colloidal photonic layer depend on the distribution of the colloids on the substrate material [2]. This distribution is a result of the self-assembly of colloidal particles during the drying process after spraying deposition [3]. Therefore, the aim of our experiments is to follow the colloidal layer development during the spray-coating of colloidal inks used for layer formation on nanoporous templates. As a porous material, we use layers of cellulose nanofibrils (CNF) – so-called nanopaper. CNFs are a wood-based material with a high aspect ratio (length ~500 nm and small diameter ~5 nm) and with a tunable negative surface charge [4]. The aqueous colloidal ink is based on polymer colloids with a hydrophobic core and a cationic hydrophilic shell. This shell hydrophilicity makes it possible to disperse these colloids to a 0.1 wt% concentration in water [5]. The concentration of 0.1 wt% is particularly suitable for spray-coating, this being the main deposition technique of this project. Hence, it is crucial to understand the colloid-CNF-water interactions, as they govern the self-assembly in the wet layer after spray deposition.

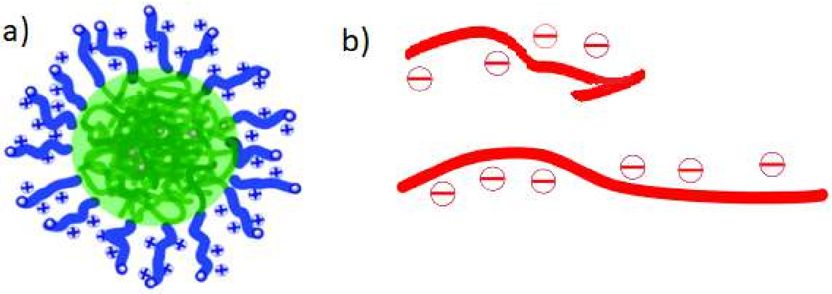

Figure 5.3:
Sketches of a) PDMAEMA-*b*-PMMA polymer colloids and of (b) CNF (not to scale). The colloids consist of a hydrophobic core (green) and cationic hydrophilic shell (blue). The CNF have a surface charge of about 1000 $\frac{\mu\text{mol}}{\text{g}}$.

To explore the interaction of the colloids with CNF in the dispersion state typically used for spray-coating conditions, we performed small-angle neutron scattering (SANS) experiments at D22 of the Institute Laue Langevin (ILL) in Grenoble. We measured in D_2O pure PDMAEMA-*b*-PMMA latex colloids (Fig. 5.3a), pure CNF (Fig. 5.3b) and a 1:1 vol:vol dispersion of a CNF with colloids. Colloids with both completely deuterated and completely protonated PMMA core were synthesized. Fully protonated PDMAEMA was the shell polymer and the CNF $[C_6H_{10}O_5]n$ was also fully protonated. The calculated neutron scattering length densities (SLD) are shown in Table 1. The SANS data (Fig. 5.4) were analyzed by the SasView software [6]. In the fully protonated colloidal suspension, the polymer colloid structure can be modeled by a polydisperse core-shell sphere. SANS modeling allowed us to extract the size of both core and shell.

The core radius of 34.2 ± 0.3 nm and a shell size of 3.3 ± 0.3 nm were obtained together with a size polydispersity of 25% for the core and 22% for the shell with the polydispersities described

Table 1: Calculated neutron SLDs for the various components of the measured particle dispersions.

Material	PDMAEMA	D8-PMMA	PMMA	CNF	H_2O	D_2O
SLD [10^{-6} Å^{-2}]	0.8228	7	1.059	1.76	-0.559	6.35

by a log-normal distribution. The hydrodynamic radius of the full colloids was determined to be 90.9 ± 4.2 nm by dynamic light scattering. This size difference with the overall particle size by SANS (75 ± 1nm) is anticipated, as in SANS the absolute size is obtained without the hydration layer as calculated by dynamic light scattering.

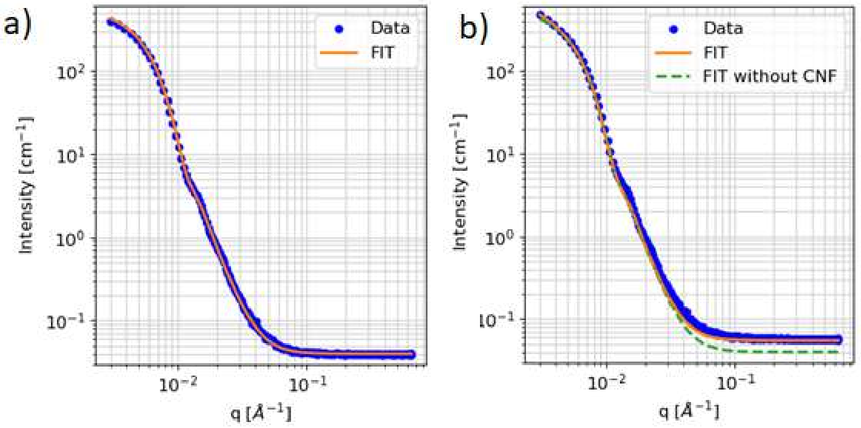

Figure 5.4:
One-dimensional SANS curves in absolute intensity scale of the protonated colloidal dispersions at c_{pol} = 0.1wt% for 1410 repeat units of MMA and 25 repeat units of DMAEMA. Panel (a) denotes single component colloidal dispersions and (b) hybrid dispersions of colloids with CNF. The solid line represents a fit with a polydisperse core-shell spherical form factor without (green) and with (orange) CNF contribution.

The SLD of $1 \cdot 10^{-6}$ Å^{-2} of the core provides an indication of relatively hydrophobic micellar core interior. The PDMAEMA shell is fully hydrated to almost 98% D_2O by volume. The SANS modeling does not need the use of a structure factor, which implies that the colloids do not interact with each other in that low concentration (c_{pol} = 0.1wt%). In the hybrid solutions, the CNF increases the background and influences the shape of the SANS curve between 1.5 $\cdot 10^{-2}$ Å^{-1}. and 4 $\cdot 10^{-2}$ Å^{-1}. The completion of SANS modeling in all single component and hybrid suspensions is the next step in the analysis.

[1] K. Li, C. Li, H. Li, M. Li, Y. Song, *iScience* **24**, 2,102121, (2021)

[2] G. Herzog, K. Abul, M. Mottakin, G. Benecke, A. Buffet, R. Gehrke, J. Perlich, M. Schwartzkopf, V. Körstgens, R. Meier, M. A. Niedermeier, M. Rawolle, M. A. Ruderer, P. Müller-Buschbaum, W. Wurth, S. V. Roth, *Langmuir* **28**, 21, 8230–8237 (2012)

[3] G. Herzog, G. Benecke, A. Buffet, B. Heidmann, J. Perlich, J. F. H. Risch, G. Santoro, M. Schwartzkopf, S. Yu, W. Wurth, S. V. Roth, *Langmuir* **29**, 36, 11260-11266 (2013)

[4] C. J. Brett, N. Mittal, W. Ohm, M. Gensch, L. P. Kreuzer, V. Körstgens, M. Månsson, H. Frielinghaus, P. Müller-Buschbaum, L. D. Söderberg, S. V. Roth, *Macromolecules* **52**, 12, 4721–4728 (2019)

[5] A. E. Alexakis, J. Engström, A. Stamm, A. V. Riazanova, C. J. Brett, S. V. Roth, P. O. Syrén, L. Fogelström, M. S. Reid, E. Malmström, *Green Chem.* **23**, 5, 2113-2122, (2021)

[6] http://www.sasview.org/

5.3 Morphology control of titania thin films in a low temperature process

G. Pan, C. Ehgartner[1], N. Hüsing[1], P. Müller-Buschbaum

[1] Universität Salzburg, Salzburg, Austria

Flexible photovoltaic devices have attracted increasing interest for their potential usage in wearable electronics, remote power, and automobiles [1]. Transparent plastic substrates, such as polyethylene terephthalate (PET) or polyethylene naphthalate (PEN), have been employed in various flexible solar cells. The usage of plastic substrates requires a fabrication process at low temperatures (<150 °C) to avoid the deformation of the substrates [2]. Moreover, a low-temperature processing route achieves the demand for devices to have a reduction of energy consumption and pay-back times. However, in a conventional fabrication process, the mesoporous titania (TiO_2) films used as electron transport layers (ETLs), are fabricated with solution-processed precursors, generally followed by a high-temperature calcination process (400-500 °C), which crystallizes TiO_2 [3]. To address this challenge, a low-temperature route towards mesoporous films is needed, which holds promise for simple fabrication of solar cells, such as the high-efficiency perovskite solar cells based on mesoporous TiO_2 films. Thus, a special titanium precursor ethylene glycol-modified titanate (EGMT) is introduced for fabrication of ordered mesoporous TiO_2 films in a low-temperature process.
In the present work, TiO_2 thin films are fabricated at low temperature (<100°C) with a sol-gel method assisted with a structure-directing polymer template. We use the amphiphilic diblock copolymer polystyrene-*b*-polyethylene oxide (PS-*b*-PEO) as a structure-directing template, which selectively incorporates EGMT. Ultraviolet (UV) irradiation is selected as a low-temperature route for diblock copolymer removal since the high energy of the UV light could break the polymer bonds [4].

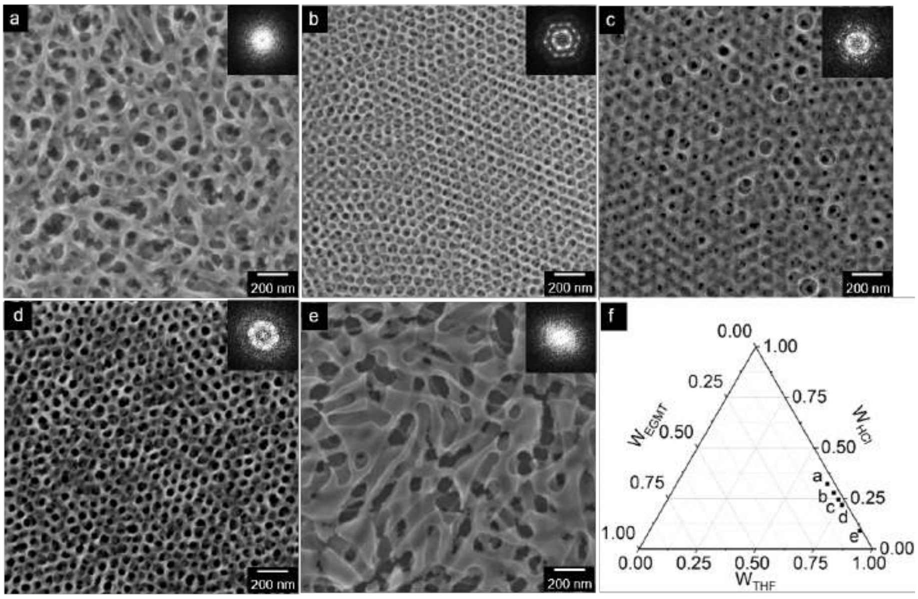

Figure 5.5:
SEM images of the titania films prepared with different ratios of precursor, solvent, and catalyst. The upper right insets refer to the corresponding 2D-FFT patterns. The weight ratios of EGMT:HCl:THF for (a) to (e) are shown in (f) in the components' phase diagram.

Fig. 5.5 shows SEM topography images of the TiO_2 films prepared with different ratios of precursor, solvent, and catalyst. Two-dimensional fast Fourier transformation (2D-FFT) patterns extracted from the SEM images are shown as inset on the top right corners of the respective image. By changing the ratio of sol-gel solution components, various nanostructures can be achieved. At a low ratio of tetrahydrofuran (THF), a foam-like morphology is obtained. With increasing the content of THF, the foam-like structure transforms to highly ordered mesoporous arrays with a hexagonal distribution. By increasing the ratio of THF further, the titania film obtains a worm-like nanostructure.

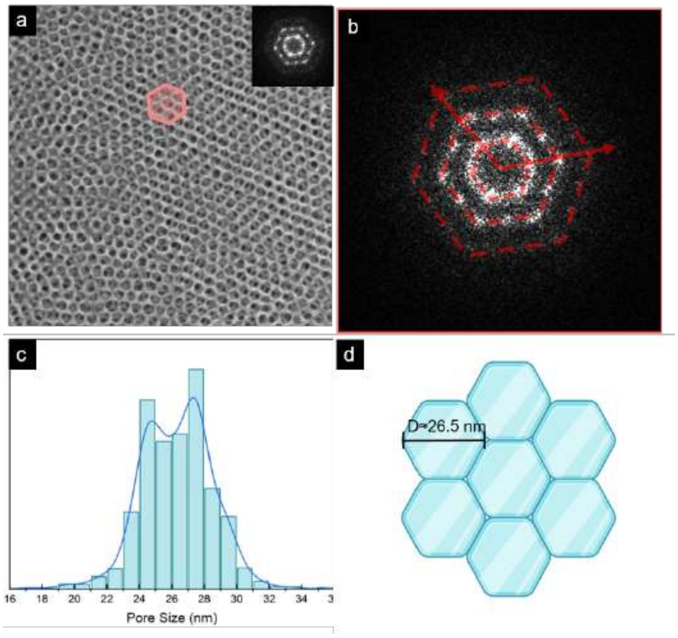

Figure 5.6:
(a) Surface SEM image of titania (TiO_2) film. The corresponding 2D-FFT pattern is displayed in the inset on the top right corner. (b) A magnified 2D-FFT pattern of the titania film with red dotted line to stress the pattern. (c) The pore size distribution extracted from the SEM image by ImageJ software. (d) Schematic of the titania nanoparticles forming a honeycomb-like structure.

A detailed analysis of ordered morphology is shown in Fig. 5.6. Three sets of hexagonal dots are shown on the 2D-FFT pattern of the TiO_2 film (a magnification image shown in Fig. 5.6b), indicating a highly ordered honeycomb-like arrangement of the titania nanostructure. Moreover, a pore size of $\sim$ 26 nm for the titania mesoporous nanostructure is calculated from the pore size analysis in Fig. 5.6c.

[1] X. Fu, L. Xu, J. Li, X. Sun, H. Peng, *Carbon* **139**, 1063-1073 (2018)

[2] A. Kogo, Y. Sanehira, Y. Numata, M. Ikegami, T. Miyasaka, *ACS Appl. Mater. Interfaces* **10**, 2224-2229 (2018)

[3] I. M. Hossain, D. Hudry, F. Mathies, T. Abzieher, S. Moghadamzadeh, D. Rueda-Delgado, F. Schackmar, M. Bruns, R. Andriessen, T. Aernouts, F. Di Giacomo, *ACS Appl. Energy Mater.* **2**, 47–58 (2018)

[4] L. Song, A. Abdelsamie, C .J. Schaffer, V. Körstgens, W. Wang, T. Wang, E. D. Indari, T. Fröschl, N. Hüsing, T. Haeberle, P. Lugli, S. Bernstorff, P. Müller-Buschbaum, *Adv. Funct. Mater.* **26**, 7084–7093 (2016)

5.4 Inorganic-organic hybrid nanostructures based on protein templating

L. F. Huber, M. Schwartzkopf[1], S. V. Roth[1,2], P. Müller-Buschbaum

[1] DESY, Hamburg, Germany
[2] KTH, Stockholm, Sweden

Globally most electricity is still produced by burning fossil fuels like gas, coal or oil [1]. Typical efficiencies for state-of-the-art fossil fuel heat engines in power generation are between 30 % and 50 %. Therefore, more than 60 % of the global energy for electricity generation is lost to waste heat [2]. Additionally, almost all areas of industrial production suffer from large energetic losses as well. Thus, there is a tremendous potential for energy recovery in almost all production areas. The Seebeck effect enables the conversion of low-grade waste heat into electrical power.

Our research work is focused on substituting the commonly used, rare and toxic thermoelectric materials like lead and tellurium with abundant and environmentally friendly alternatives. Changes in the nanostructure of thermoelectric materials can drastically improve the thermoelectric figure of merit (ZT) [3,4]. To achieve this, a protein is used to template titania. We print the organic-inorganic layer using a meniscus guided slot-die coater. This approach enables low-cost and large-scale solution-based production. Titania is used as the thermoelectric material. As the inorganic precursor for titania, TIBALD (titan(IV)-bis-(ammoniumlactato)-dihydroxid) is used, since it is water soluble and therefore enables the use of deionized (DI) water as the solvent. A calcination temperature of 500 °C for 3 hours enhances crystallinity and leads to anatase crystal structure [5]. The protein β-lactoglobulin is chosen as the template, as it is structurally responsive to the pH value and enables different device morphologies. It is also a well-understood foaming agent in the food industry, enabling a porous structure. The morphological impact of different pH values and polymer concentrations during solution processing on the titania thin-films was investigated using SEM, GISAXS and GIWAXS measurements. Also electrical conductivity and the Seebeck coefficient were measured for differently templated devices.

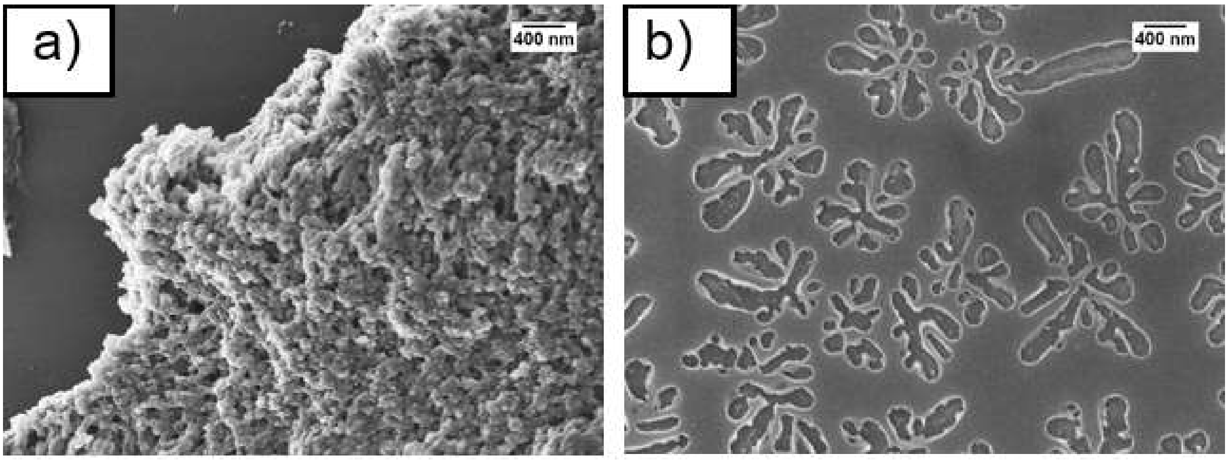

Figure 5.7: SEM images of slot-die coated titania samples after calcination at a) pH 7 and b) pH 2.

As can be seen in Fig. 5.7 the shape, size and amount of titania aggregates changes strongly for different pH values. For neutral pH, less in number and more rectangular aggregates were found with sizes between 5 to 15 μm. For the acidic template, many smaller structures were found with sizes between 0.4 and 1.5 μm with elongated flower-like shapes.

To understand the structure formation during printing, the time evolution of the average domain sizes and the average domain distances can be analyzed. This can be done with high statistical relevance by performing *in situ* GISAXS and *in situ* GIWAXS measurements.[6]

Grazing-incidence X-ray scattering is a powerful non-destructive technique that enables morphological investigation at the nanoscale. These experiments were performed at the P03 beamline at the DESY synchrotron in Hamburg. By using a high brilliance synchrotron, the structure formation process can be successfully temporally resolved.

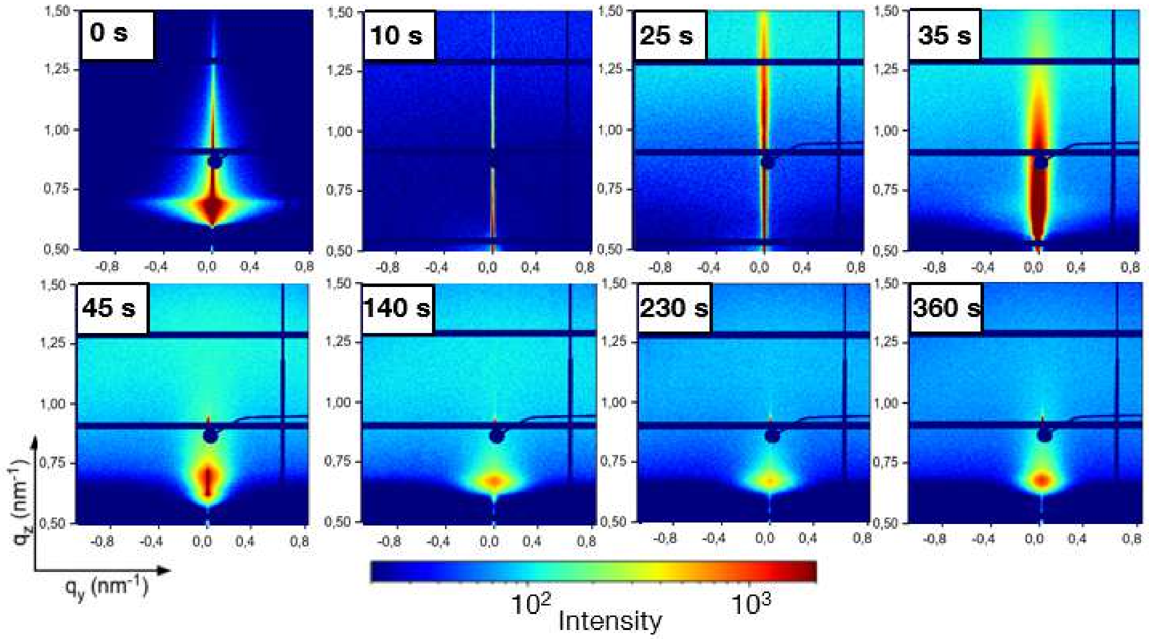

Figure 5.8:
In situ 2D GISAXS data of the structure formation of printed β-lactoglobulin titania thin films (pH 2) on glass substrates. A time of 0 s represents pure glass before printing.

From the 2D detector images (Fig. 5.8), horizontal line cuts near the Yoneda region are performed and then fitted in GISAXSfit software. The samples are printed at 100 °C and become dry after 40 to 45 s. In conclusion, a templating effect of the β-lactoglobulin protein for titania thin films can be observed for different pH values.

[1] BP, Statistical Review of World Energy 69th edition, 1-68 (2020)

[2] C. Forman, et al. *Renew. Sust. Energ. Rev.* **57**, 1568-1579 (2016)

[3] F. U. Parás-Hernández, et al. *Nano Energy* **74**, 104854 (2020)

[4] K. B. Masood, et al. *Thermoelectricity and Advanced Thermoelectric Materials*. Woodhead Publishing, 261-311 (2021)

[5] D. J. Kim, et al. *Mater. Lett.* **57**, 355-360 (2002)

[6] L. Oesinghaus, J. Schlipf, N. Giesbrecht, L. Song, Y. Hu, T. Bein, P. Docampo, P. Müller-Buschbaum, *Adv. Mater. Interfaces* **3**, 1600403 (2016)

5.5 Morphological study on the slot-die printed PS-*b*-P4VP and PS-*b*-P4VP/FeCl$_3$ thin films

S. Yin, T. Tian, Y. Li, C. M. Papadakis, P. Müller-Buschbaum

Block copolymer (BCP)-assisted self-assembly shows great potential in multiple applications. In the present work, with the assistance of an upscalable slot-die coating technique, PS-*b*-P4VP (poly(styrene-*block*-4-vinylpyridine)) and PS-*b*-P4VP/FeCl$_3$ films are printed for investigating the self-assembly behavior of the block copolymers. The micellization of the diblock copolymer in solution, as well as the morphological information about deposited thin-films are investigated with DLS and SEM measurements. Fig. 5.9a shows the normalized autocorrelation curves acquired at a scattering angle of 90 °, in which two and three decays are detected for PS-*b*-P4VP and PS-*b*-P4VP/FeCl$_3$ solutions in dimethylformamide (DMF), respectively. The first decay is ascribed to the diffusion of individual polymer chains, and the slow second and third decay are rather weak and presumably result from the diffusion of larger objects. The corresponding hydrodynamic radii R_h are shown in Fig. 5.9b. The R_h values corresponding to the single PS-*b*-P4VP and the Fe^{3+}-complexed PS-*b*-P4VP polymer chains are determined to be (4.1 ± 0.2) nm and (4.0 ± 0.2) nm, respectively. In addition, peaks located at (166 ± 6) nm and (72 ± 3) nm are detected for the PS-*b*-P4VP and the PS-*b*-P4VP/FeCl$_3$ solutions, respectively. Since the PS-*b*-P4VP concentration studied in the present work is well above of reported CMC of the block copolymer, micelles as well as their corresponding assemblies can be expected in the solution [1]. By calculation, the contour length of the PS-*b*-P4VP used in the present work is at $\sim$ 29 nm, which is smaller than the values detected with DLS. Thus, the formed structures are more complex including a complexation structure between Fe $^{3+}$ and PS-*b*-P4VP. Possibly, pre-assemblies of the polymer chains form 1D cylindrical micelles in the solution, which are larger than spherical micelles. Such individual micelles can further fuse into larger objects as depicted in Fig. 5.9c. In another aspect, the coordination effect between Fe^{3+} and the vinyl pyridine groups might

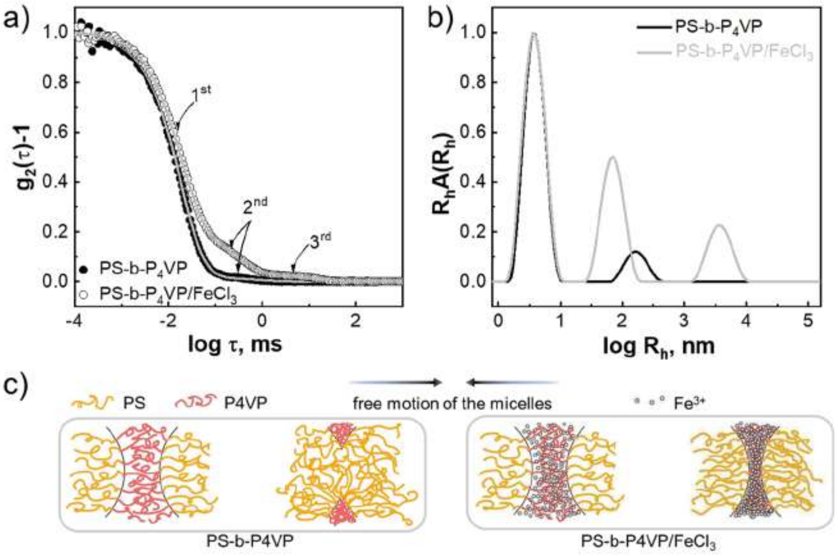

Figure 5.9:
(a) Normalized autocorrelation functions at 2θ = 90 ° and (b) the corresponding distribution functions of hydrodynamic radii R_h of the PS-*b*-P4VP (green) and PS-*b*-P4VP/FeCl$_3$ (orange) DMF solutions. The decay positions of the autocorrelation functions are marked with arrows. The inset shows the complexation between the PS-*b*-P4VP chains and Fe^{3+}. (c) Possible fusion model of the PS-*b*-P4VP and PS-*b*-P4VP/FeCl$_3$ micelles in the solution.

lead to entanglements of the P4VP chains within micellar shells and eventually to intermicellar agglomeration between P4VP shells. Thus, the detected peak positions at (72±3) nm and (166±6) nm in Fig. 5.9b can be ascribed to the scattering of non-spherical micelles. The additional weak scattering detected in the micrometer range for the PS-*b*-P4VP/$FeCl_3$ solution is likely due to the formation of the micellar assemblies in the solution.
The microstructure of the final dry PS-*b*-P4VP and PS-*b*-P4VP/$FeCl_3$ films is detected with SEM measurements. Three distinct positions are selected for imaging, as shown in Fig. 5.10. Dimple-type structures are found to consist of PS cores and a P4VP matrix for both thin films due to the poor solubility of the PS blocks in DMF [2]. Compared to the hybrid PS-*b*-P4VP/$FeCl_3$ film, the pure PS-*b*-P4VP thin film exhibits significantly enlarged domain sizes and conspicuous structural inhomogeneity along the printing direction.

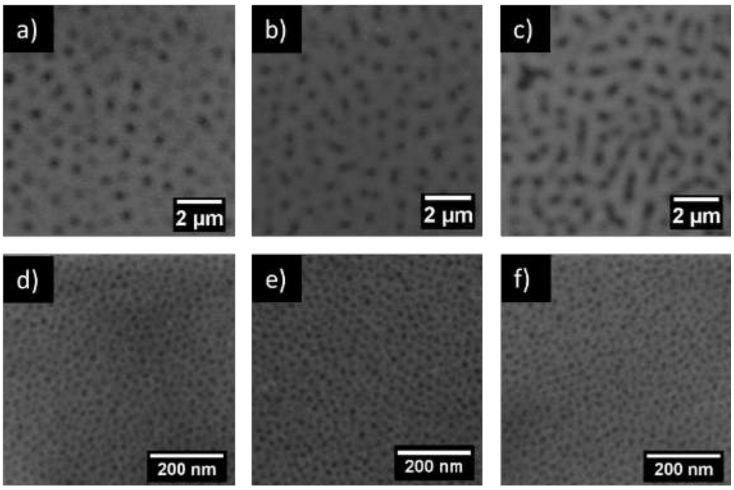

Figure 5.10:
SEM images showing surface morphologies at three different positions of (a-c) pure PS-*b*-P4VP and (d-f) hybrid PS-*b*-P4VP/$FeCl_3$ films. The images are shown sequentially in the printing direction. Corresponding distances between two adjacent SEM images are $\sim$ 1 cm.

The structural differences in terms of domain sizes, homogeneity, and regularity of the two films can be related to the aggregates in the solution and the interaction between the polymer chains and the polar silicon substrate. The DLS characterization demonstrates that the P4VP chains are more stretched in the PS-*b*-P4VP chain in the DMF solution, and in the thin-film geometry the P4VP block has a preferential interaction with the polar silicon substrate due to its (P4VP) larger surface energy than that of the PS block. The high mobility of the P4VP polymer chains in the DMF solution might induce the fusion of the PS-*b*-P4VP micelles during the thin-film deposition process, which is assumed to provoke the structural inhomogeneity shown in Fig. 5.10a to c. Compared to the PS-*b*-P4VP film, the decreased domain sizes, enhanced homogeneity and structural order of the PS-b-P4VP/$FeCl_3$ counterpart can be primarily attributed to decreased micellar sizes caused by the complexation of the Fe^{3+} and the P4VP chains. The complexation of the Fe^{3+} significantly restricts the stretching of the P4VP chains, which therefore inhibits their preferential interaction with the silicon substrate. Consequently, smaller domain sizes are observed in SEM images (Fig. 5.10 d to f) [3].

[1] Z. Wu, M. Cai, J. Cao, J. Zhang, X. Luo, *Int. J. Nanomed* **12**, 487 (2017)

[2] Y. Chen, W. Zhao, J. Zhang, *RSC Adv.* **7**, 4226-4236 (2017)

[3] S. Yin, T. Tian, C. L. Weindl, K. S. Wienhold, Q. Ji, Y. Cheng, P. Müller-Buschbaum, *ACS Appl. Mater. Interfaces* **14**, 3143-3155 (2022)

5.6 Diblock copolymer directed co-assembly of ZnO hybrids using slot-die coating technique

T. Tian, S. Yin, S. Tu, K. S. Weinhold, C. L. Weindl, S. Liang, M. Schwartzkopf[1], S. V. Roth[1,2], P. Müller-Buschbaum

[1] DESY, Hamburg, Germany

[2] KTH, Stockholm, Sweden

Inspired by the rich phase separation behavior as well as the well-established theoretical phase diagrams of diblock copolymers, they can serve as soft-templates and have been extensively documented to access a multitude of functionalized ZnO materials with varied morphologies [1]. Therefore, a comprehensive apprehension of the structure-directing effect from the polymer template is important for the reliable and controllable construction of co-assembled ZnO materials. In this work [2], slot-die printing technique is introduced for the thin film deposition and the template effect from the amphiphilic polystyrene-*block*-poly(ethylene oxide) (PS-*b*-PEO) on both the surface and inner morphologies of ZnO hybrids is investigated in detail.

As displayed in Fig. 5.11a, a typical fingerprint-like morphology for the slot-die coated PS-*b*-PEO film surface can be observed, in which darker PEO microdomains alternate to brighter PS matrix, approaching the structural assignment of PEO cylinders and PS host. Highlighted by the red circle and blue rectangle in Fig. 5.11a, the round and elongated dark PEO domains coexist. After the incorporation of the ZnO components, the SEM image shows significantly enhanced contrast owing to the highly conductive nature of ZnO (Fig. 5.11b). The preferential segregation of brighter ZnO objects inside both worm-like and spherical PEO regions is visible, separating the composite film into ZnO-incorporated PEO domains (denoted as PEO/ZnO) and PS domains. Unfortunately, the structural order of PS-*b*-PEO film is destroyed by the selective localization of ZnO in PEO domains as confirmed from the absence of the FFT ring.

As seen in the GISAXS pattern of PS-*b*-PEO film (Fig. 5.11c), the presence of prominent rod-like Bragg reflection clearly hints the ordered nanostructures. Interestingly, the introduction of high-electron-density ZnO phase not only causes much stronger lateral scattering observed in PS-*b*-PEO/ZnO hybrid film (Fig. 5.11d) but also alters the propagation of the scattering signal along the q_z direction, leading to so-called dynamic intensity modulation and distinguishable splitting of the Yoneda region. To track the structural changes by ZnO embedment, the intensity cuts along the in-plane direction (q_y) are integrated at the q_z positions equivalent to the critical angles of selected domains. As plotted in Fig. 5.11f, the two interdomain distances increase from 50 ± 4 nm and 23 ± 1 nm for PEO in polymer film to 60 ± 6 nm and 27 ± 4 nm for PEO/ZnO in the composite film. Following a consistent tendency, the domain radius grows from 14.5 ± 1.1 nm and 7.7 ± 0.5 nm for PEO in polymer film to 26.6 ± 2.4 nm and 10.1 ± 0.8 nm for PEO/ZnO in the composite film. Such an expansion of the interdomain spacing is a direct outcome of the swelling of PEO domains upon the preferential localization of ZnO. Besides, in the hybrid film a third structure appears with an interdomain distance of 11.5 ±0.4 nm and domain size of 4.2 ± 0.3 nm.

As shown in the 2D GIWAXS data presented in Fig. 5.11g, the characteristic crystallinity peaks of the PEO domain can be observed in the PS-*b*-PEO film, while the tethering of the ZnO phase to the PEO blocks appear to frustrate the crystallization, as the crystallinity features diminish. The corresponding azimuthal integration of the 2D GIWAXS data also corroborates the crystallinity loss of the PEO domains after the ZnO has been embedded (see Fig. 5.11i) Therefore, the distribution of phase-selective ZnO yields the crystalline-to-amorphous transition for PEO domains, which suggest that the spatial distribution of PEO-selective components would reduce the chain length of crystallizable PEO and then inhibits the PEO crystallization.

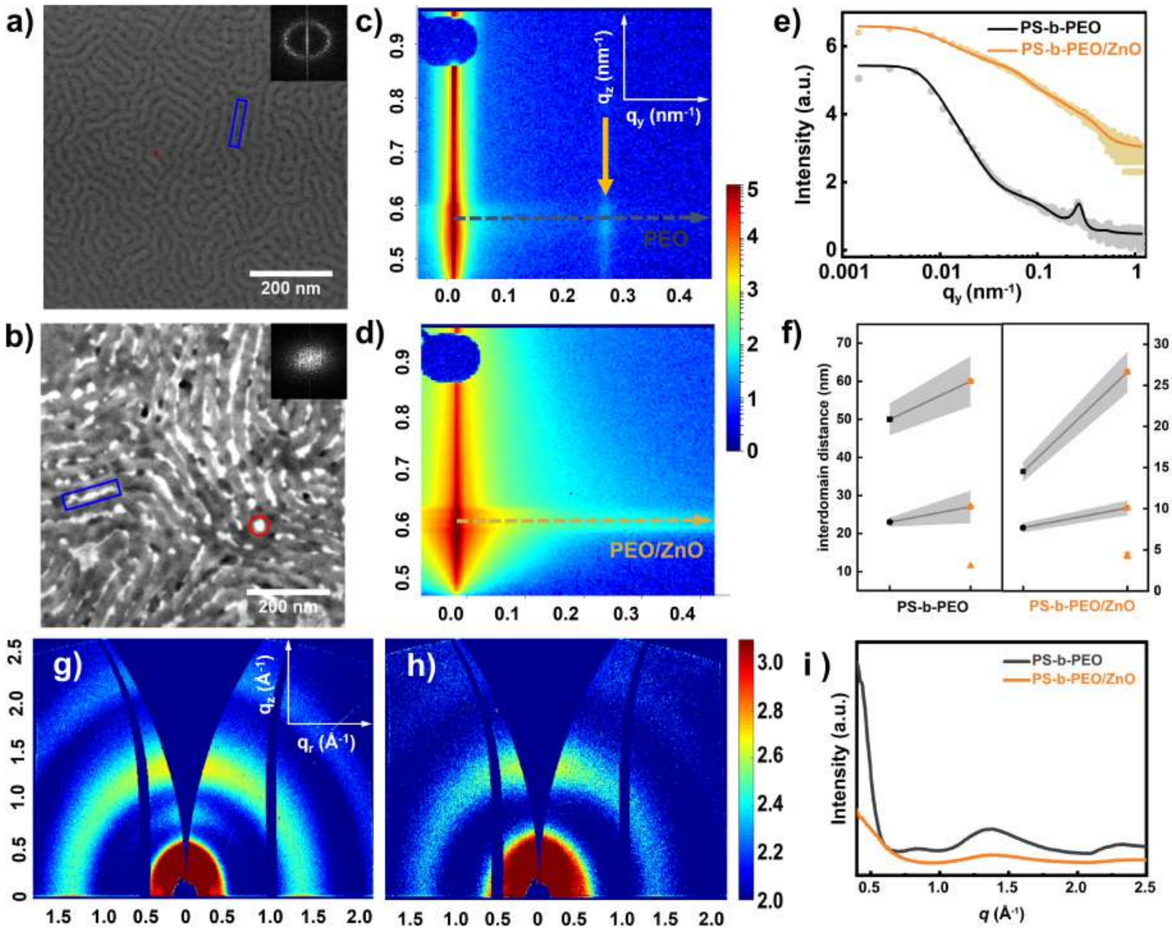

Figure 5.11:
High-magnification (80 k) SEM top-view images of a) pure PS-*b*-PEO film and b) PS-*b*-PEO/ZnO composite film. The upper-right insets are the corresponding 2D FFT patterns. 2D GISAXS data for c) pure PS-*b*-PEO film and d) PS-*b*-PEO/ZnO composite film. The dashed green arrow in (c) and the dashed red arrow in (d) along q_y direction schematically display the Yoneda peak positions of PEO domains and PEO/ZnO domains for performing horizontal cuts, respectively. The yellow arrow in (c) indicates the appearance of the characteristic peak related to the domain spacing. e) Horizontal line cuts from the 2D GISAXS data (solid dots) together with the fit curves. f) Characteristic interdomain distance and domain size obtained from the respective fits. 2D GIWAXS data of g) pure PS-*b*-PEO film and h) PS-*b*-PEO/ZnO composite film. i) Azimuthal integrals from the corresponding 2D GIWAXS data.

[1] K. Sarkar, M. Rawolle, E. M. Herzig, W. Wang, A. Buffet, S. V. Roth, P. Müller-Buschbaum, *ChemSusChem* **6**, 1414-1424 (2013)

[2] T. Tian, S. Yin, S. Tu, C. L. Weindl, K. S. Weinhold, S. Liang, M. Schwartzkopf, S. V. Roth, P. Müller-Buschbaum, *Adv. Funct. Mater.* **31**, 2105644 (2021)

5.7 *In situ* GISAXS investigation of high power impulse magnetron sputtering (HiPIMS) of silver on PS and P4VP

Y. Bulut[1], K. Reck[2], M. Schwartzkopf[1], J. Drewes[2], T. Guan, S. Liang, T. Strunskus[2], F. Fraupel[2], P. Müler-Buschbaum, S. V. Roth[1,3]

[1] DESY, Hamburg, Germany
[2] CAU, Kiel, Germany
[3] KTH, Stockholm, Sweden

Nanostructuring of polymer-metal interfaces demonstrates great potential for the improvement of organic electronics e.g. for organic photovoltaics or flexible sensors [1]. Especially using high power impulse magnetron sputtering (HiPIMS) as deposition technique offers an improvement of the adhesion and crystallinity of the as deposited metal film on sensitive polymer substrates compared to conventionally evaporated metal and oxide layers. Yet, the origin of this improved materials properties remain speculative. One route to overcome the knowledge gap are *in situ* investigation of HiPIMS deposition using combined grazing-incidence small- and wide-angle X-ray scattering (GISAXS/GIWAXS). Hence, we investigate the layer growth of Ag on polystyrene (PS) and poly-4-vinylpyridin (P4VP) thin films during HiPIMS. PS is selected as a well-known model system acting as reference to earlier work on magnetron sputter deposition. P4VP is used to investigate the influence between charged metal ions and the lone pair of P4VP as shown in Fig. 5.12. As metal we use silver (Ag), which is frequently used for optoelectronic applications.

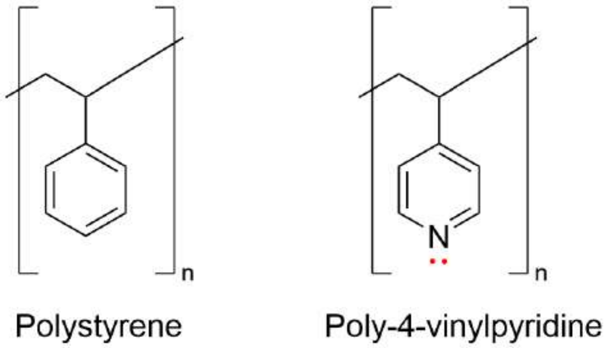

Figure 5.12:
Polystyrene (PS) and poly-4-vinylpyridin (P4VP). The lone pair of P4VP is marked red for an improved visualization.

A frequently used technique to obtain polymer thin films in the nanometer thickness regime is spin-coating. The polymer thin films of PS and P4VP (Fig. 5.12) were prepared by spin-casting (3600 rpm for 30 s) on pre-cleaned Si substrates. The *in situ* GISAXS/GIWAXS investigations were performed with a custom-made mobile deposition chamber developed by the group from CAU Kiel [1] and upgraded with a unidirectional HiPIMS source. This deposition chamber was mounted at the beamline P03, PETRA III, DESY, Hamburg. For the *in situ* experiments, a PILATUS 2M detector (Dectris, Switzerland) with a pixel size of 172x172 μm^2 was used as GISAXS detector and a custom-shaped LAMBDA 9M detector (Xspectrum, Germany) with a pixel size of 55 μm in simultaneous GIWAXS geometry. The experiments were performed using an incident angle of α_i =0.4° and an X-ray wavelength of 1.05 Å. The sample-to-detector distance (SDD) was set to SDD = 3230 mm. For quantitative analysis, horizontal line cuts were done at the Yoneda peak of PS and P4VP to obtain the average lateral size and morphology of the clusters on the polymer surface.

Fig. 5.13 shows the corresponding horizontal line cuts of the 2D GISAXS data, which were measured *in situ* during the HiPIMS deposition of Ag on PS and P4VP. The data are shown at selected thicknesses of deposited Ag, namely for δ_{Ag} = 1.7, 2.7, 3.7 and 4.7 nm, extracted from the *in situ* GISAXS data.

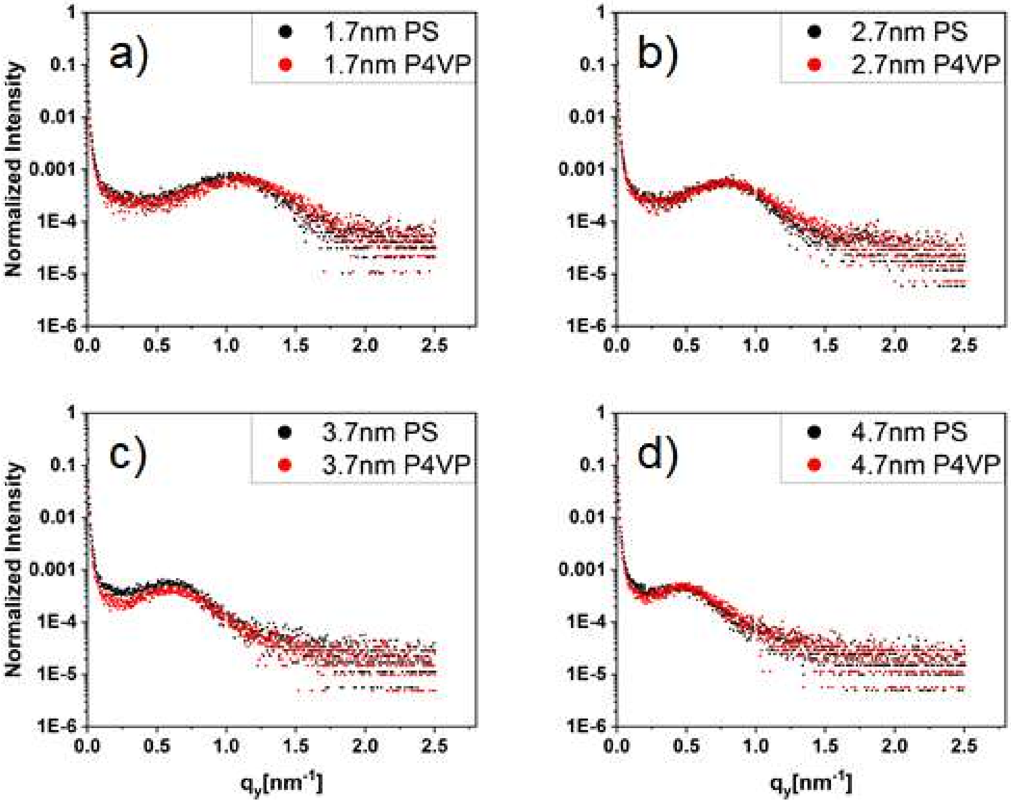

Figure 5.13:
GISAXS Yoneda cuts of the *in situ* HiPIMS deposition of Ag on PS and P4VP for deposited Ag thicknesses of δ_{Ag} = 1.7 nm (a), 2.7 nm (b), 3.7 nm (c) and 4.7 nm (d).

In Fig. 5.13a there is a small variation of the Ag structure deposited on PS and P4VP visible with the maxima positions being slightly different: $q_{y,P4VP}$ = 1.11 nm^{-1} and $q_{y,PS}$ = 1.06 nm^{-1}. The distance between clusters on P4VP seems to be smaller than on PS, which can be attributed to the lone pair of the P4VP in Fig. 5.12b. The lone pair of the P4VP might behave as an anchor point for the first impinging Ag^+ ions and might stabilize the positive charge through coordination. This leads to an increased cluster density with smaller clusters for P4VP. In addition, a tail of the intensity is visible for P4VP around q_y = 1.5 nm^{-1}. This implies a different shape, distribution in radii or shape. For $\delta_{Ag} \geq$ 2.7 nm (Fig. 5.13b) the side peak position overlap. At δ_{Ag} = 3.7 nm and 4.7 nm, a slight difference in peak intensity is observed, but no difference in tails around 1.0 nm^{-1} anymore. Thus, the distance of the clusters seems to be identical, yet some slight difference in shape or radii occur, as found in Fig. 5.13c and Fig. 5.13d. For $\delta_{Ag} \geq$ 4.7 nm it seems that the cluster formation behaves similar in both structure and morphology for PS and P4VP. Complementary investigations using IR spectroscopy are planned to investigate the effect of the pyridinium ring on stabilization of the deposited clusters.

[1] M. Gensch, M. Schwartzkopf, W. Ohm, C. J. Brett, P. Pandit, S. Koyiloth Vayalil, L. Bießmann, L. P. Kreuzer, J. Drewes, O. Polonskyi, T. Strunskus, F. Faupel, A. Stierle, P. Müller-Buschbaum, S. V. Roth, *ACS Appl. Mater. Interfaces* **11**, 29419 (2019)

6 Materials for energy storage

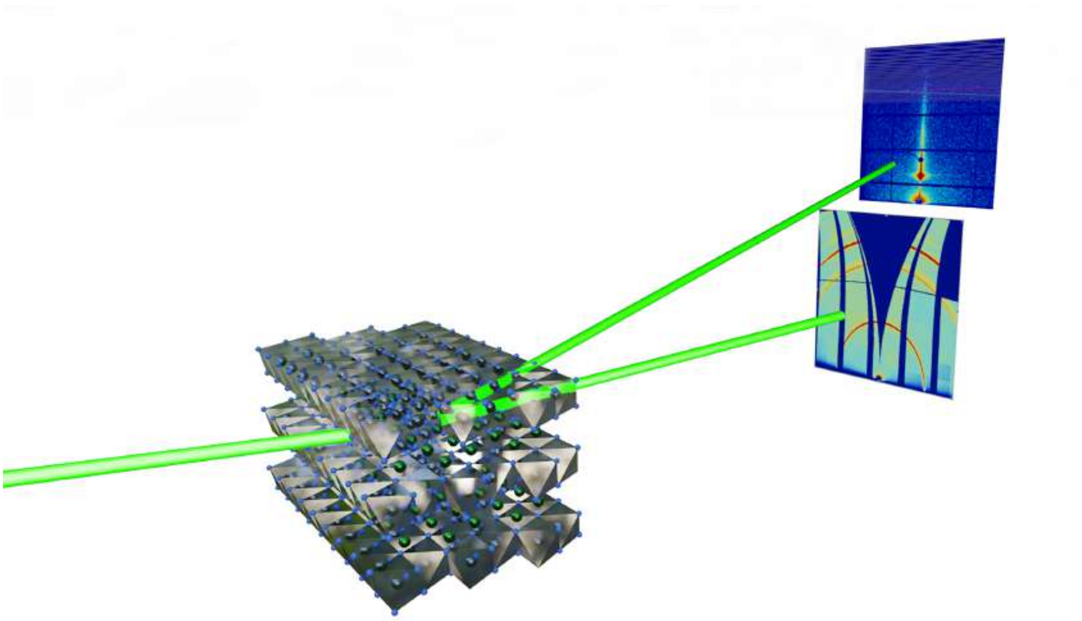

6.1 Diblock-copolymer templated Si/Ge/C thin films for Li-ion batteries

C. L. Weindl, C. E. Fajman[1], T. F. Fässler[1], P. Müller-Buschbaum

[1] Chemie Department,Technische Universitat München, Garching, Germany

With high energy density, long lifespan, and environmental friendliness, lithium-ion batteries (LIBs) represent one of the most attractive energy storage devices and play more and more important role in modern society. In the markets of portable electronics, electric vehicles and small-scale energy storage systems this technology is already present. For higher performances, changing the anode material from graphite to silicon (Si) or germanium (Ge) could enhance the capacity multiple times. Si in particular is a potential anode material due to environmentally friendly production, resource abundance, low cost and its outstanding high theoretical capacity 4200 mAh/g (roughly ten times larger than state-of-the-art graphite) [1]. Although Ge has meaningful drawbacks as commodity price and abundancy, it benchmarks Si and graphite in conductivity and Li^+ diffusivity [2].

There are several different approaches to template inorganic semiconductor thin films such as lithography, molecular beam epitaxy or chemical vapor deposition. However, these technologies have the significant disadvantages that the processes are comparatively expensive and time-consuming. Our concept is to synthesize porous SiGe thin films in a sol-gel process via an amphiphilic diblock copolymer template as already well investigated with TiO_2 [3]. Contrary to former projects, where only Ge was templated with diblock copolymers, in the present work also Si is present in the Zintl-phase [4]. These clusters are polyanionic cages formed in intermetallic compounds between alkali or alkaline earth metals and p-block semimetals [5]. In this study the non-oxide source of the two semiconductors is the precursor $K_{12}Si_{17-x}Ge_x$. With this concept, different SiGe ratios can be achieved by varying the content of Si in the synthesized precursor itself. For the sol-gel approach, polystyrene-*b*-polyethylene oxide (PS-*b*-PEO) is used as the structure agent. The polymer solution is blended with a Si/Ge Zintl-phase dissolved in ethylenediamine (*en*). The solution is then spin-cast on pre-cleaned silicon substrates. As *en* is not a perfect solvent for the polymer, microphase separation of the polymer in the thin film can be enhanced by using dichloromethane as a highly selective solvent for the PEO block. An additional solvent vapor annealing (SVA) increases the PEO mobility again and leads to a film rearrangement. After the removal of the template with a temperature of 600 °C in vacuum (see Fig. 6.1), the final porous structure can be observed.

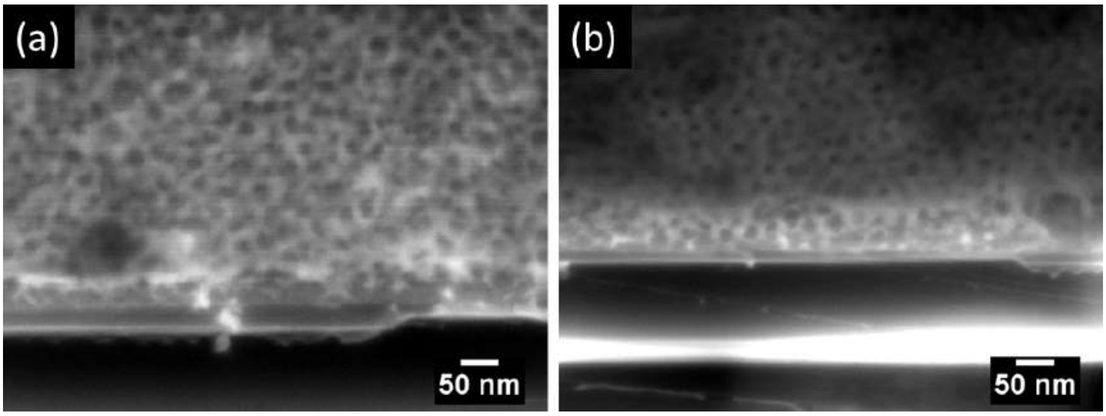

Figure 6.1: Scanning electron microscopy (SEM) cross-section images of pyrolized Si/Ge thin films without (a) and with solvent vapor annealing (b).

The SEM images reveal porous structures for the reference (Fig. 6.1a) and the SVA sample (Fig. 6.1b). Due to a high degree of order especially in the SVA thin film (Fig. 6.1b), the structural rearrangement could be proven. In the cross-section array of the films, also a vertical alignment of the PS spheres can be observed. The SVA thin film shows a spherical packing, whereas the formation in the reference follows no ordered structure. Additionally, the size of the voids for the reference sample shows larger deviations than for the SVA thin film. Elemental investigations reveal oxygen residues in the thin film, which will have a huge impact on the optoelectronic properties. Nevertheless, crystalline Ge could be observed in both films, which is vital for a high conductivity in the thin film.

Although the structures could be rearranged homogeneously with the SVA treatment, backfilling with a liquid electrolyte would still be challenging due to these small voids. Therefore, we are currently working on PS nanobead templates (see Fig. 6.2) in the micrometer regime, which are printed on copper anodes to gain a hierarchical structure by backfilling this with the polymer/precursor solution.

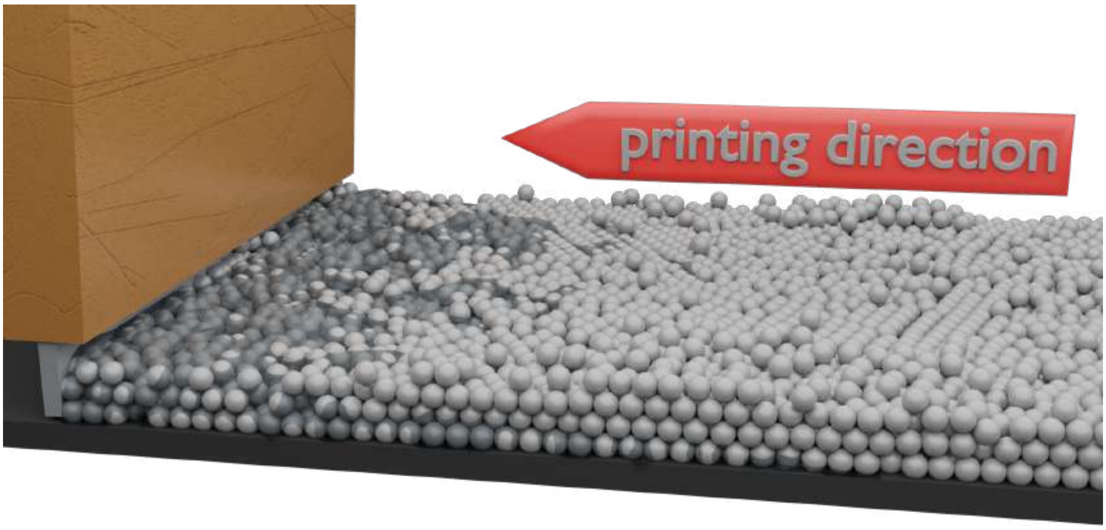

Figure 6.2: PS template printing with a slot-die printer and water as solvent.

[1] X. Zuo, Y. Wen, Y. Qiu, Y. Cheng, S. Yin, Q. Ji, Z. You, J. Zhu, P. Müller-Buschbaum, L. Ma, P. G. Bruce, Y. Xia, *ACS Appl. Mater. Interfaces* **39**, 43785–43797 (2020)

[2] Y. Yang, S. Liu, X. Bian, J. Feng, Y. An, C. Yuan, *ACS Nano* **3**, 2900–2908 (2018)

[3] N. Hohn, S. J. Schlosser, L. Bießmann, S. Grott, S. Xia, K. Wang, M. Schwartzkopf, S. V. Roth, P. Müller-Buschbaum, *Nanoscale* **11**, 5325-5334 (2018)

[4] N. Hohn, A. E. Hetzenecker, M. A. Giebel, S. Geier, L. Bießmann, V. Körstgens, N. Saxena, J. Schlipf, W. Ohm, P. S. Deimel, F. Allegretti, J. V. Barth, S. V. Roth, T. F. Fässler, P. Müller-Buschbaum, *Macromolecules* **4**, 2048–2055 (2019)

[5] M. M. Bentlohner, M. Waibel, P. Zeller, K. Sarkar, P. Müller-Buschbaum, D. Fattakhova-Rohlfing, T. F. Fässler, *Angew. Chem.* **7**, 2487–2491 (2016)

6.2 Dynamics of the lithium distribution in the graphite anode of an 18650-type lithium-ion battery during electrochemical charging

D. Petz, P. Müller-Buschbaum, A. Senyshyn[1]

[1] MLZ, Garching, Germany

The present study deals with the structure characterization of cylindrical 18650-type lithium-ion batteries. Such batteries consist of two porous electrodes, which are physically isolated by a porous separator. A more detailed scheme for the specific cell used in this work is shown in Fig. 6.3a, which has been obtained using µm-sized X-ray computed tomography. Pores in electrodes are filled with a liquid electrolyte, which enables diffusion of Li^+-ions between the electrodes, where they can be de-/intercalated into the host-framework. This rocking-chair behavior leads to a dynamical distribution of the Li^+-ions throughout the cell. As de-/intercalation of lithium from/to the electrode materials leads to changes in the lattice parameters, these processes are also connected to stress of the material. These changes in the lattice parameter can be quantified by diffraction measurements and correspondingly enable the determination of the amount of lithium intercalated into the electrode materials. Since neutrons interact with the nucleus, neutron diffraction is more sensitive to the light lithium in comparison to the synchrotron-based X-ray diffraction. The influence of the cell geometry to the lithium distribution *in situ* has been reported before [1], but *operando* investigations were not applied before.

Spatially-resolved neutron powder diffraction was performed at STRESS-SPEC (FRM II, Garching, Germany) on a 18650-type lithium-ion battery based on LFP|C chemistry. A small rhomb-like gauge volume with a height of 20 mm in central plane was formed with a 2 mm sample slit and the radial collimator in front of the 2D detector (central angle: 26° in 2Θ; acceptance width: 2mm). The overall volume, which has been investigated, is sketched in Fig. 6.3b. During a measurement the cell was dis-/charged with a CCCV-protocol using 2 A ($\approx$ 2 C-Rate) and a cut-off of 55 mA ($\approx$ 1/20 C-Rate) between 2.0-3.6 V, before the cell was moved to another gauge volume. The obtained diffraction pattern enabled investigations of the dis-/charging process of the graphite anode.

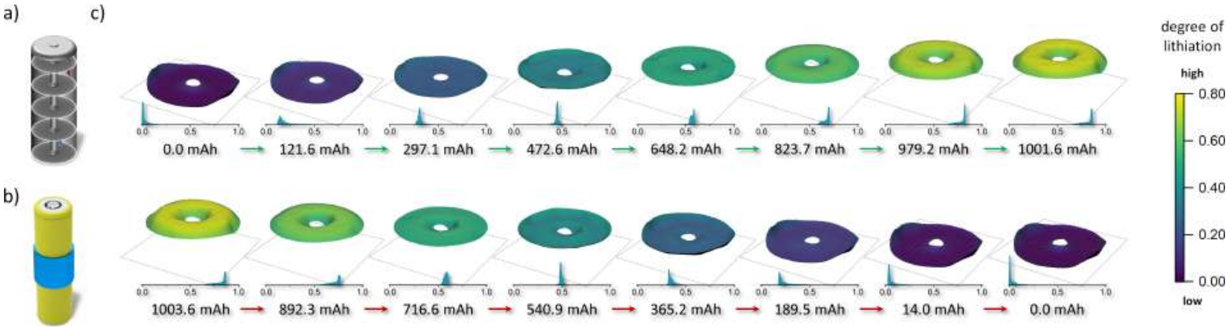

Figure 6.3:
a) Reconstruction of the cell components of the investigated LFP|C cylindrical 18650-type cell investigated with µm-sized X-ray CT; b) Investigated volume during the neutron diffraction experiment; c) False color representation of the Degree of Lithiation (DoL) of the graphite anode during charging (upper row) and discharging (lower row) supplemented by the corresponding histograms below

The lithium distribution during charging (upper row) and discharging (lower row) is displayed for selected states in Fig. 6.3c. In the discharged state, the anode exhibits a lower lithiation in the middle of the electrode stripe and slightly higher lithium content towards the center of the cell

and the cell housing. During charging, this distribution inverts, where in the fully charged state a higher lithiation is observed in the middle of the electrode stripe compared to the inner part of the cell and the cell housing. This behavior can be seen best in the histograms (displayed below the distributions in Fig. 6.3c), where at overall low lithiation states a small tail occurs towards higher values and a tail towards lower lithiation values in the charged state.
The inhomogeneous lithium distribution over the electrochemical charging cycle can be seen from the 2D histogram in Fig. 6.4a, where the x-axis represents the number of the diffraction pattern (and therefore time), the y-axis represents the Degree of Lithiation (DoL) of the graphite anode and the color code represents the counts of the corresponding DoL in a specific state. The lithiation follows the electrochemical capacity (on top) as one would expect.

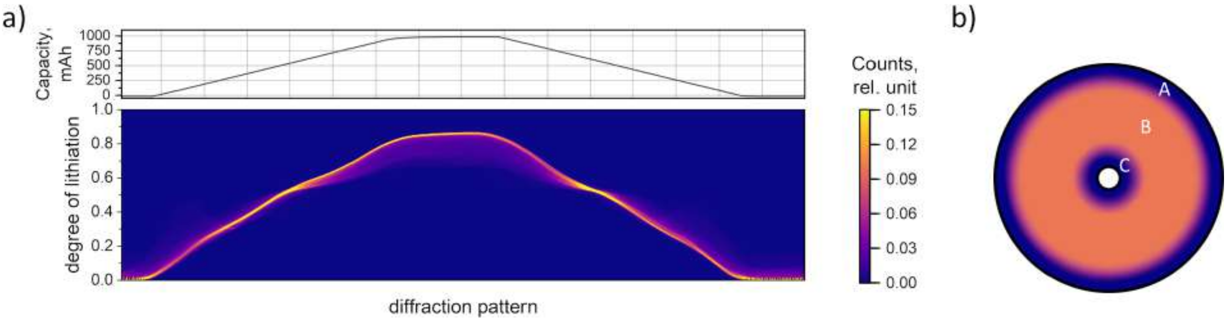

Figure 6.4:
a) False color representation of the histograms of the Degree of Lithiation (DoL) during charging and discharging along with the cell capacity (on top); b) Sketch of differently stressed areas in the cell

At a DoL of slightly above 0.5, the entire graphite anode is quite homogeneous lithiated, which corresponds to the stage II (LiC_{12}) phase throughout nearly the entire cell. Due to a potential drop between stage II and stage I (LiC_6), the formation of stage I is restricted until all lower lithiated graphites reach stage II. Further lithiation then leads to the formation of LiC_6, which occurs preferrably at the middle of the electrode stripe as seen in Fig. 6.3c.
From the lithiation dynamics presented in Fig. 6.3c, different areas of cell stress can be identified. As mentioned in the beginning, de-/intercalation of the electrode material comes along with stress of the material. Therefore, areas with a wider lithiation window during electrochemical cycling undergo a higher stress and have therefore a higher potential for local failures, which prohibit the operation of the whole cell. Three areas of material stress have been identified and are sketched as A)-C) in Fig. 6.4 b). Region near the cell housing (A) and region in the very inner of the cell (C) operate in a narrower lithiation window compared to the middle of the electrode stripe (B). Therefore, cell failure is more likely in area (B). On the other hand, the lower lithiation window of area (A) and (C) are responsible for a reduction of the general cell capacity as the full lithiation potential of the electrode material is not fully used.
The knowledge about the dynamics of the lithium distribution in lithium-ion batteries pave the way for new cell designs with a more homogeneous usage of the battery materials. In turn, more uniform usage of the cell materials leads to both higher energy/power densities and longer lifetimes minimizing changes in the materials of the batteries, which is potentially a cheap way for improving lithium-ion battery performance and lifetime.

[1] D. Petz, M. J. Mühlbauer, A. Schökel, K. Achterhold, F. Pfeiffer, T. Pirling, M. Hofmann, A. Senyshyn, *Batter. Supercaps.*, **4**, 327-335 (2021)

6.3 Single-ion conducting polymers for application in lithium-ion batteries

F. A. C. Apfelbeck , P. Müller-Buschbaum

Lithium-ion batteries are a key element in today's energy supply and enable a comfortable and connected world. However, in most of the lithium-ion batteries flammable ionic liquids are utilized as electrolyte, which can threaten the safety of the end user. In addition to that, the use of lithium metal as anode, which has a ten times higher specific capacity compared to graphite, in combination with liquid electrolytes is not feasible due to the formation of dendrites which can lead to short circuits. For this reason, polymer electrolytes are an interesting candidate for next generation lithium-ion batteries. One of the most prominent representative of polymer electrolytes is the lithium ion conducting polyethylene oxide (PEO) mixed with a corresponding salt e.g. lithium bis(trifluormethylsulfonyl)amid (LiTFSI), which is a dual-ion conducting system. In contrast to that, single-ion conducting polymers, in which the anions are attached to the backbone of the polymer and only the lithium cations are mobile, are a promising group of polymers since they exhibit sufficient high ionic conductivities and, more important, a theoretical transference number of one, which is accompanied with the suppression of dendritic growth in lithium metal batteries [1].

The single-ion conducting polymer used in this work is poly((trifluoromethane)sulfonimide lithium styrene) (PSTFSILi) which has a polystyrene backbone and LiTFSI attached to it. In order to investigate the structural evolution of solid polymer electrolytes during battery operation with transmission X-ray scattering techniques a special capillary cell setup has been developed by Möhl et al. [2] Here, two stainless steel wires are coated with the cathode (lithium iron phosphate, LFP) and anode material (graphite), respectively. Then the wires are brought in close vicinity and the polymer solution is drop-casted between them. After the solvent is evaporated, a polymer film has been formed and connects the two electrodes. In Fig. 6.5a the photograph of a capillary cell is shown and Fig. 6.5b represents first charging and discharging characteristics.

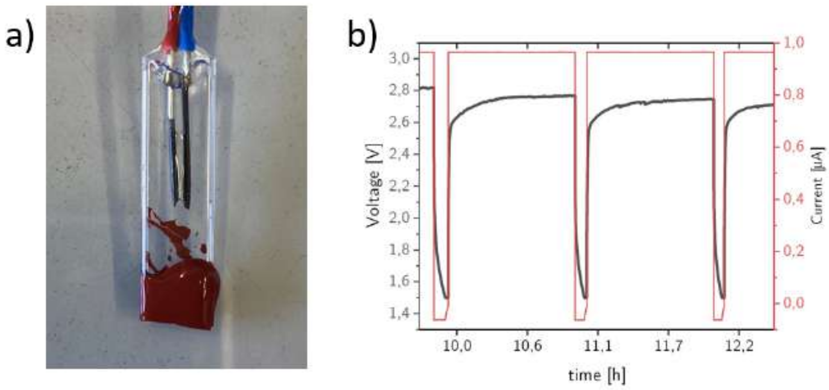

Figure 6.5:
(a) Photograph of a capillary cell. The two stainless steel wires are coated with the electrode material and connected by a free-standing polymer film. (b) First charge and discharge curves at room temperature emphasize battery characteristics.

A major drawback of using polymer electrolytes is the inferior contact between the electrodes due to the bad wettability, which leads to high contact resistances. Therefore, a common way to circumvent this problem is to use the polymer not only as electrolyte but also as binder for the electrode slurry preparation instead of a conventional and insulating polymer like polyvinylidenfluoride (PVDF) in order to enhance ion conduction in the electrode. It has already been shown that a composition of PVDF and a single-ion conducting polymer (1:1 wt%) as binder results in superior battery performance with a liquid electrolyte [3]. In this work, a systematic approach is chosen in order to reveal the optimum polymer composition. Thus, a series of six LFP cathodes (LFP : carbon black : polymer = 80:10:10) with various weight ratios of PVDF and PSTFSILi and hence different lithium contents is prepared. First, its surface morphology is investigated by scanning electron microscopy (SEM). Fig. 6.6a shows a 0:100 sample. The large domains represent the LFP particles, whereas the smaller ones are the carbon black additive.

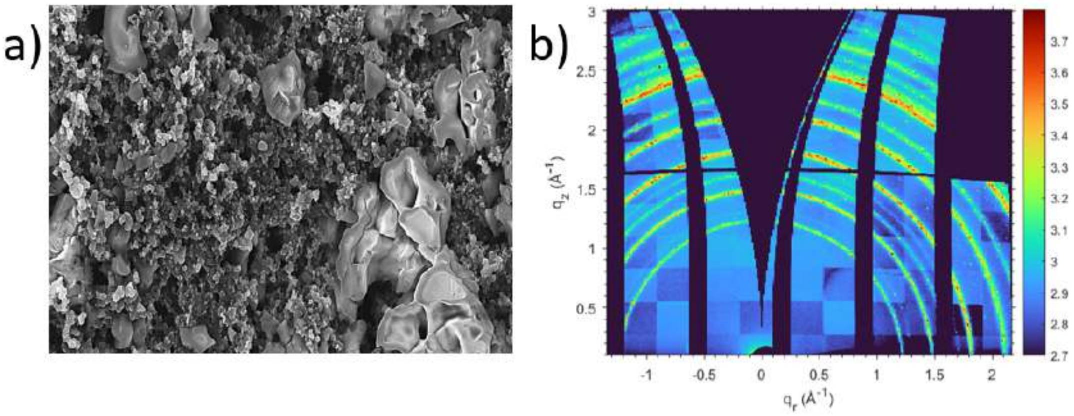

Figure 6.6:
(a) Representative top-view SEM image and (b) GIWAXS detector image of an LFP electrode with PVDF:PSTFSILi = 0:100.

Since the polymer binder has an encasing property, it can be recognized as a white paste, which gives the particles a smooth appearance. In addition to that, to our best knowledge grazing-incidence small-angle X-ray scattering (GISAXS) experiments have not been performed yet on such electrodes. GISAXS experiments were here performed for the first time. This method has the potential to become a standard complementary technique for battery electrodes investigation and to provide information for a better understanding of electrochemical impedance spectroscopy (EIS) data [4]. In the GISAXS measurement, the alignment of the rough samples is done by means of the horizon instead of the specular peak. In Fig. 6.6b the GIWAXS detector image of the associated sample is shown. Here, the rings indicate the presence of small crystallites, which have a high disorder in the electrode with respect to the substrate [5].
In future work, the series of LFP electrodes will be further analyzed. Especially, the relation between EIS, battery performance and GISAS data is of great interest and can help to better understand the behavior of batteries. Additionally, the capillary cell will be optimized regarding battery cycling and *in operando* experiments will be executed.

[1] J. Zhu, Z. Zhang, S. Zhao, A. S. Westover, I. Belharouak, P. F. Cao, *Adv. Energy Mat.* **11**, 2003836 (2021)

[2] G. E. Möhl, E. Metwalli, P. Müller-Buschbaum, *ACS Energy Lett.* **3**, 1525–1530 (2018)

[3] Q. Shi, L. Xue, Z. Wei, F. Liu, X. Du, D. D. Des Marteau, *J. Mater. Chem. A.* **1**, 15016 (2013)

[4] M. Gaberšček , *Nat. Comm.* **12**, 6513 (2021)

[5] P. Müller-Buschbaum, *Adv. Mat.* **26**, 7692–7709 (2014)

6.4 Sol-gel based mesoporous silica thin films for lithium-ion battery anodes

I. Pivarníková, P. Müller-Buschbaum

Both, silicon (Si) and silicon oxide (SiO_x)-based materials have been considered as some of the most promising candidates for lithium-ion battery anodes, due to their environmental friendliness, low cost, large abundance and most interestingly – their high theoretical gravimetric capacity (Si: 4200 mAh/g, SiO_2: 1965 mAh/g) [1]. On the other hand, Si and SiO_x can suffer from low intristic electrical conductivity and large volume expansion during the lithiation and delithiation process. Therefore, upon cycling within the battery these materials suffer from low mechanical stability, quicker degradation, poor cyclic stability and capacity loss and can cause serious safety issues.

In order to solve the above mentioned problems, there has been an increased demand for designing mechanically stable, yet flexible structures that can accommodate the volume changes and buffer the developing mechanical stress. In this work, we focus on the synthesis of a special system - nanostructured porous Si and SiO_x thin films via wet chemical methods. The functional nanostructured thin films can be used for several applications, such as photovoltaic cells, gas sensors, membranes, optical devices and lithium-ion battery anodes. The sol-gel synthesis of certain other mesoporous inorganic films (TiO_2, SnO_2) has been previously reported [2,3].

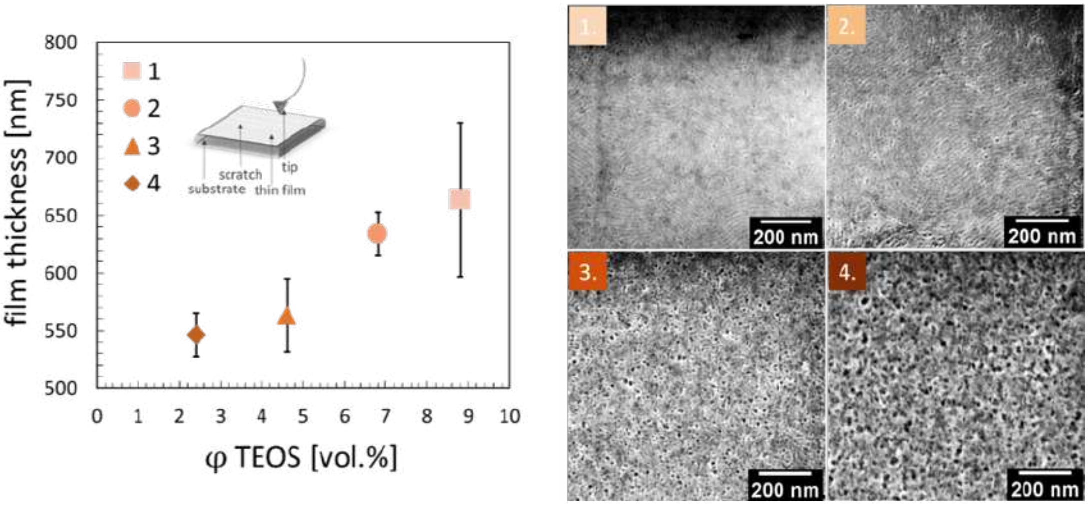

Figure 6.7:
(a) Profilometry measurements of synthesized thin films: four samples with different tetraethoxysilane (TEOS) composition; inset shows the principle of a profilometry measurement on a thin film; (b) SEM images of the four examined samples with varied precursor to polymer ratios.

The highly ordered porous thin films were prepared via cooperative sol-gel process, which belongs to the group of the wet chemical synthesis methods [4]. The prepared solution consists of tetraethoxysilane (TEOS), which serves as an inorganic silica precursor and the poly(ethylene oxide)-block-poly(propylene oxide)-block-poly(ethylene oxide) (PEO-*b*-PPO-*b*-PEO) non-ionic triblock copolymer (Pluronic F108), which serves as an organic template. As a solvent, the mixture of ethanol, deionized H_2O and aditionally HCl is used to provide acidic conditions. The resulting solution was coated onto cleaned silicon substrates via spin-coating. The solvent evaporation via spin-coating induces the polymer micelle formation, assembly with inorganic precursor and polycondensation of the silica network. Optimization of the spin-coating conditions (e.g. choice of a spin-coating speed, acceleration speed, time etc.) has been performed in order to reach a successful preparation protocol of the desired films. The template removal was done by a thermal treatment (calcination) at 400 °C for 4 hours with the heating rate 1 °C/min. Afterwards, the porous structured transparent Si thin films are obtained. The synthesized porous thin films were characterized using several different techniques, such as profilometry, ellipsometry, scanning electron microscopy (SEM) and grazing-incidence small-angle X-ray scattering (GISAXS).

In Fig. 6.7a, we can observe that the thickness of the thin films can be tuned by adjusting the synthesis conditions, in this case, by adjusting the amount of the used TEOS precursor. The thickness of non-calcined thin films (freshly spin-coated) can range between 500-750 nm.The tunability of porosity and/or pore size can be also performed by adjustment of the precursor to polymer ratio, which we can observe on the SEM images in Fig. 6.7b.

Thin films with thickness in the nanometer range are perfect candidates for usage of the non-destructive GISAXS technique, which allows us to investigate the inner morphology of the thin film. In Fig. 6.8a, we can observe an example of two dimensional (2D) GISAXS data of our thin film hybrid system. The one dimensional (1D) line cuts were performed at the material-specific Yoneda peak position with maximum scattering intensity. The horizontal line cut is schematically indicated as a red rectangular zone and the cuts for samples with different composition are plotted in Fig. 6.8b. With more suitable modelling of these line cuts in the future, several pore parameters including radii and center-to-center distances will be extracted.

In the future, the work will also focus on the optimization of the thin film preparation process in order to reach properties suitable for Li-ion battery anode application, such as suitable thickness, conductivity, porosity or microstructure.

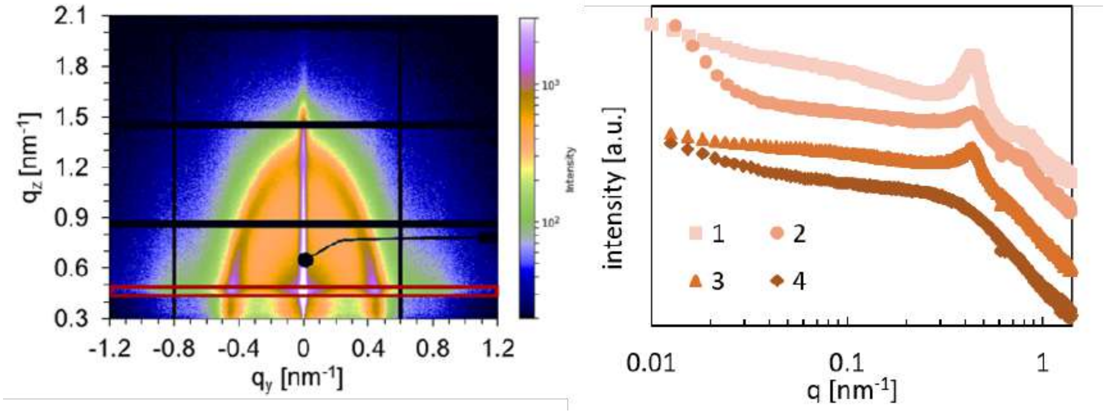

Figure 6.8:
(a) Example of 2D GISAXS data showing the position of the horizontal line cut (red box);
(b) Horizontal line cuts of the 2D GISAXS data from all four samples with 2 distinct peaks suggesting an ordered microstructure.

[1] X. X. Zuo, J. Zhu, P. Müller-Buschbaum, Y. J. Cheng, *Nano Energy* **31**, 113-143 (2017)

[2] N. Li, L. Song, L. Bießmann, S. Xia, W. Ohm, C. J. Brett, E. Hadjixenophontos, G. Schmitz, S. V. Roth, P. Müller-Buschbaum, *Adv. Mater. Interfaces* **6**, 1900558 (2019)

[3] S. Yin, T. Tian, K. S. Wienhold, C. L. Weindl, R. Guo, M. Schwartzkopf, S. V. Roth, P. Müller-Buschbaum, *Adv. Mater. Interfaces* **7**, 2001002 (2020)

[4] H. Zou, S. Wu, J. Shen, *Chem. Rev.* **108**, 3893-3957 (2008)

6.5 Solid polymer electrolytes for high-energy cathode materials

T. A. Pham, R. Gilles[1], P. Müller-Buschbaum

[1] MLZ, Garching, Germany

Nowadays, lithium ion batteries (LIB) have established themselves as the major energy storage system and are an essential part of our daily lives. One aim in research is the improvement of the LIB in order to increase their performance. Whereas commercial LIB are commonly operated with graphite as anode material, the usage of Li metal can improve the capacity and energy. The major advantages of Li metal are its high theoretical capacity and low electrochemical potential making it the optimal anode material. However, there are still obstacles such as Li dendrite growth that inhibit the use of Li metal in commercial cell batteries that operate with liquid electrolytes.

In order to increase the safety, solid polymer electrolytes (SPE) can be used since they are mechanically more stable and thus, prevent the growth of Li dendrites towards the cathode. Poly(propylene carbonate) (PPC) is one of many SPE. It is an amorphous, biodegradable polymer with low cost. The main advantage of PPC as SPE is its high intrinsic electrochemical stability of $\sim$ 4.6 V [1]. Hence, PPC can be combined with state-of-the-art cathode materials such as $\mathrm{LiNi}_{1-x-y}\mathrm{Mn}_x\mathrm{Co}_y\mathrm{O}_2$ that operate at a voltage above 4.3 V without oxidizing. Additional to the polymer host, Li salt is required in order to fabricate a functional SPE. Here, lithium bis(trifluoromethanesulfonyl)imide (LiTFSI) and PPC were dissolved in acetontrile and mixed in different Li to propylene carbonate ratios ([Li:PC] ratio) (see Fig. 6.9a and b). Capillary cells that are shown in Fig. 6.9c were prepared by drop-casting the polymer-salt solution onto two stainless steel current collectors and then sealed subsequently. Additionally, free-standing films were fabricated (see Fig. 6.9d).

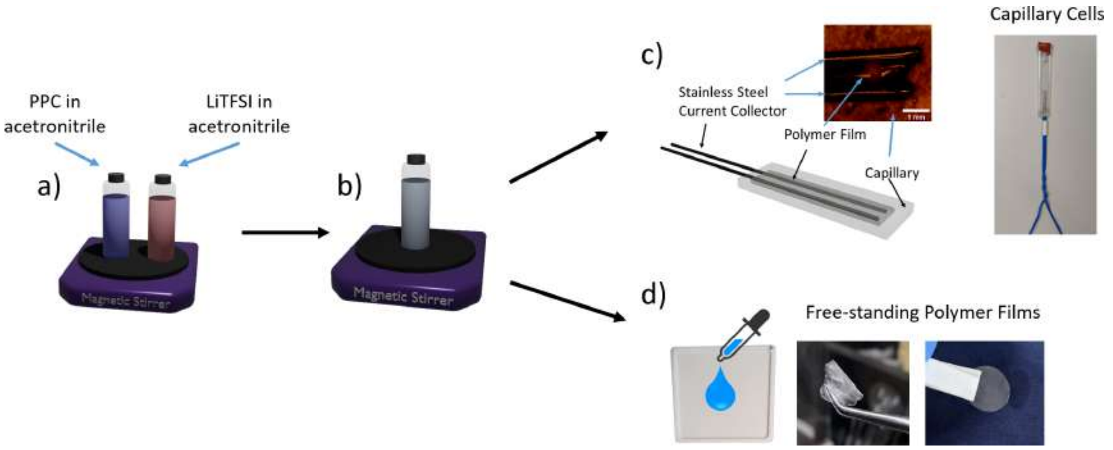

Figure 6.9:
Preparation of solid polymer electrolyte. PPC and LiTFSI are (a) dissolved in acetonitrile and (b) mixed with different [Li:PC] ratios. Drop-casting of the polymer salt solution is used in order to prepare capillary cells (c) while free-standing polymer films are fabricated by (d) casting the solution onto a teflon dish and subsequently peeling off the dried film.

With differential scanning calorimetry, the glass transition temperature T_G was determined on films with different [Li:PC] ratios. With increasing Li salt concentration, the glass temperature decreases (see Fig. 6.10a), which corresponds to the behavior of other aliphatic polycarbonates [2]. Electrochemical impedance spectroscopy was used in order to investigate the ionic conductivity of the capillary cells. In Fig. 6.10b the impedance data was fitted for samples with a [Li:PC] ratio of 0.1 and 0.15 using an equivalent circuit model. From the internal resistance R_i and the geometry of the capillary cell, the ionic conductivity σ was determined. The ionic conductivity increases with higher Li salt concentrations that is in accordance with the dependence of the T_G trend on the [Li:PC] ratio. By lowering the T_G, the polymer segmental motion is further promoted resulting in a higher conductivity [3].

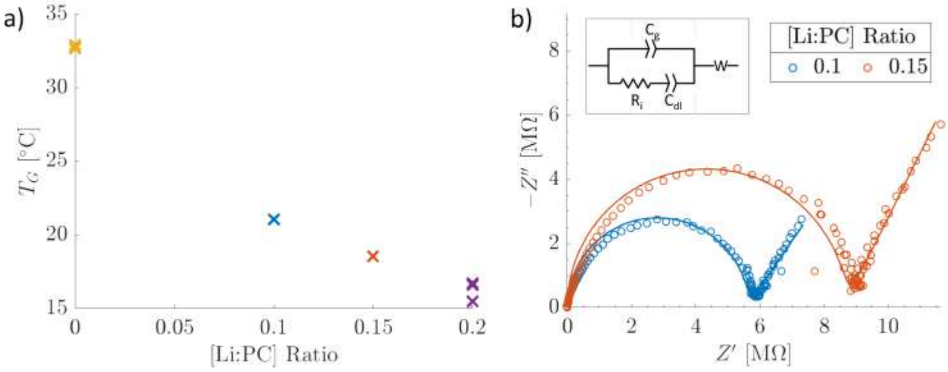

Figure 6.10:
Panel (a): Glass transition temperature T_G, for different [Li:PC] ratios, determined by differential scanning calorimetry; panel (b): Nyquist plots with ionic conductivity σ for different [Li:PC] ratios.

Furthermore, cathodes were fabricated by coating $LiNi_{0.80}Co_{0.05}Al_{0.15}O_2$ with binder and conductive carbon onto Al current collector sheets. The porosity of the cathodes was determined before and after calendering (see Fig. 6.11). During this step, the void in between the particles of the electrode is decreased which is important in order to decrease contact resistances. In further experiments, the SPE will be tested with the cathode material in order to gain more insight in the compatibility of those materials from performance point-of-view and scattering experiments will be conducted to study the structure of both cathode and SPE more thoroughly.

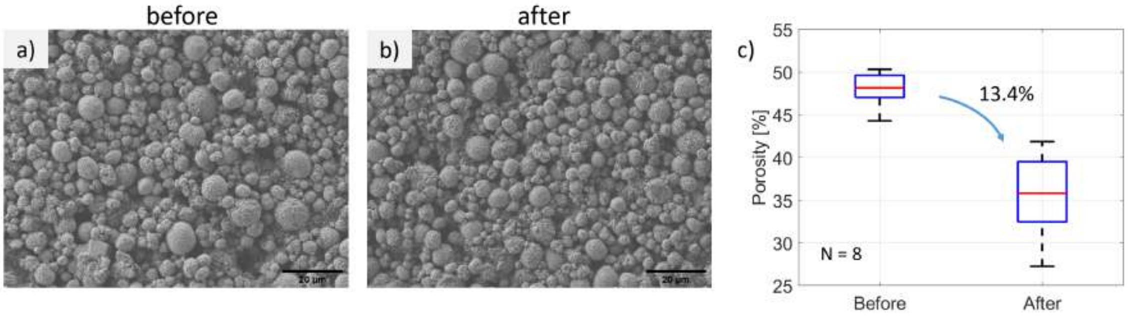

Figure 6.11:
SEM image of cathode surface (a) before and (b) after calendering. The porosity, shown as boxplot in (c), was calculated using the geometric dimensions and the weight of the cathodes.

[1] J. Zhang, X. Zang, H. Wen, T. Dong, J. Chai, Y. Li, B. Chen, J. Zhao, S. Dong, J. Ma, L. Yue, Z. Liu, X. Guo, G. Cui, L. Chen, *J. Mater. Chem.* **5**, 4940-4948 (2017)

[2] Y. Tominaga, K. Yamazaki, *Chem. Commun.* **50**, 4448-4450 (2014)

[3] A. Kisliuk, V. Bocharova, I. Popov, C. Gainaru, A. P. Skolov, *Electrochim. Acta* **299**, 191-196 (2019)

6.6 High-concentration lithium-ion electrolyte overcomes the challenges of high-temperature lithium batteries

T. Zheng, Y. Cheng[1], P. Müller-Buschbaum

[1] NIMTE, Ningbo, China

Lithium metal battery has been regarded as the "holy grail" for next generation energy storage systems because of its high theoretical specific capacity (3860 mAh/g) and low electrode potential (-3.04 V vs. standard hydrogen electrode) [1]. Traditional Li-ion batteries, on the other hand, are severely constrained in high-temperature applications due to the low thermal stability of the electrolyte/electrode interface and electrolyte decompositions in the cell [2].

Herein, we have demonstrated a new electrolyte that achieved an excellent stable long-term cycling at 100 °C, well beyond the typical 60 °C limits of normal conventional Li-ion batteries. The highly-concentrated lithium oxalyldifluoroborate (LiODFB) was selected as the only lithium salt with a carefully designed high thermal stability solvent group. As a result, this unique high-concentration electrolyte can promote to form a stable and inorganic solid electrolyte interface (SEI) layer on the electrode at elevated temperatures, leading to improved performance in MCMB/Li and lithium iron phosphate (LFP)/Li half-cells, and achieved reversible capacities of 160 and 350 mAh/g, respectively, with Coulombic efficiencies (CEs) $>$99.3 % .

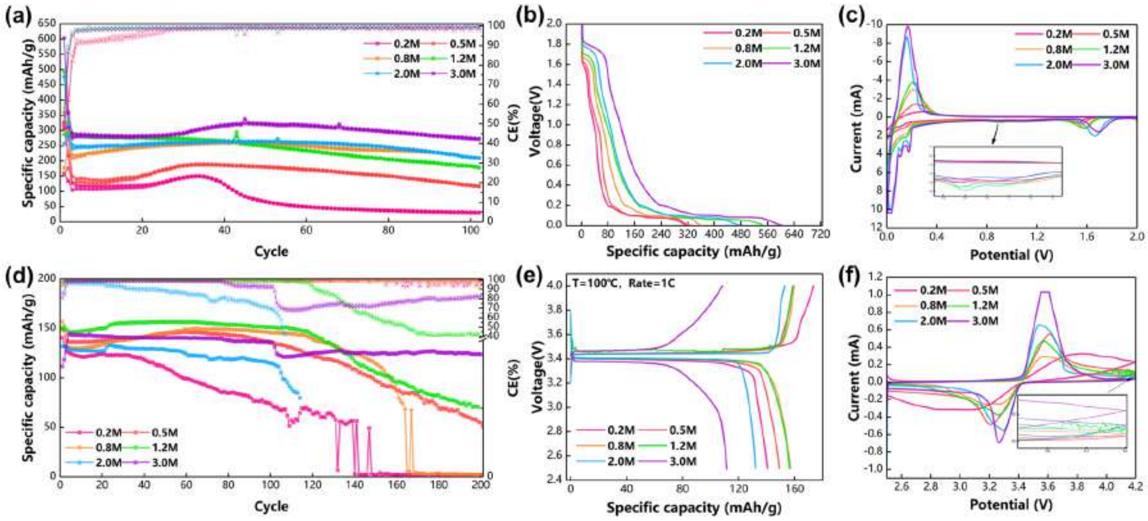

Figure 6.12:
Performance of Li/MCMB half cells at 100 °C: a) Long cycling test, b) first discharging curves, c) CV from 0 to 2 V and the performance of Li/LFP half cells at 100 °C: d) Long cycling test, e) first charge/discharge curves, f) CV from 2.5 to 4.2 V

As shown in Fig. 6.12a, b and c, the Li/MCMB half cells were all tested in the high-temperature environment at 100 °C at the rate of 1.0 °C/min. With increasing concentration of LiODFB in carbonate electrolytes, the stability of the Li/MCMB half-cell at high temperatures has improved considerably. The half-cell with 0.2 M concentration electrolyte had the lowest starting capacity at approximately 180 mAh/g, and the cell's specific capacity dropped obviously after 37 cycles, which was ascribed to the poor conductivity of the low concentration electrolyte and the electrolyte's consumption. Furthermore, Li/MCMB cells using electrolytes, whose concentration is higher than 0.5 M, all follow a similar pattern: with increasing concentration, the cell's initial capacity increases as well as its capacity retention improves. In addition, a small plateau around 1.6 V in the first discharge curves of different concentration electrolytes becomes more obvious as the concentration increases, which means the LiODFB decompose to form a more stable SEI film on the surface of MCMB. Fig. 6.12c shows the CV of half-cells in different electrolytes ranging from 0 - 2.0 V, which also illustrates the previous phenomenon: when the concentration of LiODFB rises, the electrolyte's overall conductivity rises, and the intensity of the MCMB reaction peak goes up. Moreover, Fig. 6.12d, e, and f illustrate the electrochemical performance of the Li/LFP half-cells at 100 °C at a rate of 1.0 °C/min. The phenomenon is similar to that of Li/MCMB, in that the cell's capacity retention improves significantly with increasing concentration, and the first cycle's capacity improves as well. The Li/LFP cell with the highest concentration of LiODFB electrolyte has the least polarization, as shown by the first-cycle charge/discharge curves. Additionally, the CV curves for the voltage range 2.5-4.2V demonstrate that the high concentration electrolyte has a stronger response intensity than the low concentration electrolyte, which is due to the high concentration electrolyte's excellent electrical conductivity. Because the decomposition of lithium salt at high concentration can produce a denser and more inorganic CEI film to inhibit the corrosion of Al, the corrosion peak at 4.2V attributed to the Al collector at high temperature is much less intense than that of the low concentration, suggesting that the high concentration electrolyte can inhibit the corrosion of Al collector.

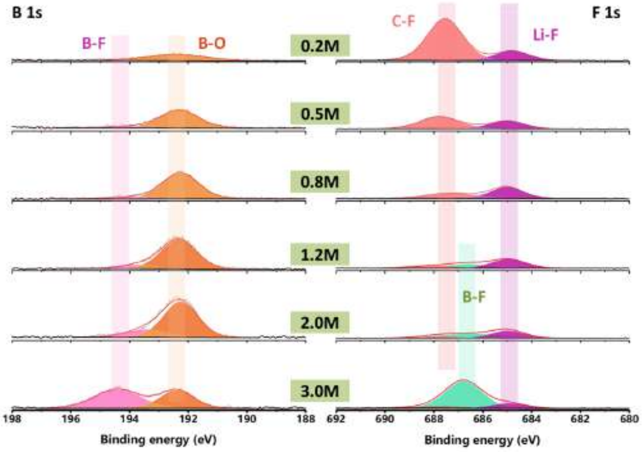

Figure 6.13: The XPS data of B 1s and F 1s after 100 cycles in different electrolytes.

Fig. 6.13 illustrates the B 1s and F 1s peaks of the SEI film on the surface of Li/MCMB half-cells in different electrolytes after 100 cycles as seen with XPS. Obviously, the peak intensity corresponding to 195 eV (attributed to B-F peak) appears to rise with increasing LiODFB concentration, which might be partly due to LiODFB not being entirely decomposed. The XPS data of F 1s also show that the peak intensity of C-F gradually decreased while the peak intensity of B-F grew, suggesting that the SEI layer consisted of more inorganic compounds.

In summary, the high-concentrated LiODFB electrolyte may significantly increase the stability of lithium metal batteries at high temperatures, which is due to the huge amount of LiODFB dissolved in the solvent, which prevents solvent molecule disintegration and promotes the formation of a denser, more inorganic SEI film.

[1] C. Yan, X. B. Cheng, Y. Tian, X. Chen, X.-Q. Zhang, W.-J. Li, J.-Q. Huang, Q. Zhang, *Adv. Mater.* **30**, 1707629 (2018)

[2] T. Zheng, J. Xiong, B. Zhu. X. Shi, Y.-J. Cheng, H. Zhao, Y. Xia, *J. Mater. Chem. A* **9**, 9307–9318 (2021)

6.7 Hybrid energy harvester based on the combination of triboelectric nanogenerator and solar cell

T. Xiao, P. Müller-Buschbaum

Developing clean energy lies in the heart of a sustainable development of human society [1]. Triboelectric nanogenerators (TENGs) originating from Maxwell's displacement current represent a new type of energy harvester for harnessing ambient mechanical energy based on the coupling of triboelectrification and electrostatic induction effect [2]. Compared with other counterparts, such as electromagnetic generators, owing to the light-weight, low-cost, and easy fabrication, TENGs become one of the most promising candidates in the replacement of conventional fossil fuels and attract worldwide attention in the past years. Since TENGs have been first proposed in 2012, many kinds of TENGs have been fabricated for converting various energies into electricity [3]. However, to further increase the energy harvesting efficiency and broaden application fields, integrating TENGs with other kinds of energy harvesters in one device is a possible way to meet these needs.

In the present work, in order to suit for potential applications in soft robotics and smart home systems, a TENG-based hybrid energy harvester is designed and fabricated on the flexible polyethylene terephthalate (PET) substrate. This hybrid device consists of a single-electrode mode TENG component and a PbS quantum dots (QDs) based solar cell component, which can harness both mechanical and solar energy from ambient environment to directly generate electricity through two different working mechanisms. The structure of as-fabricated hybrid energy harvester is schematically shown in Fig. 6.14a, which is with the common configuration of ITO-PET/ZnO/PbS QDs/Au as the solar cell under the bottom and covered by the fluorinated ethylene propylene (FEP) film on the top as the dielectric material for TENG. Here, gold serves as both the bottom electrode for TENG and the anode for solar cell. Fig. 6.14b presents a photograph of the hybrid device at bending state, showing its good flexibility.

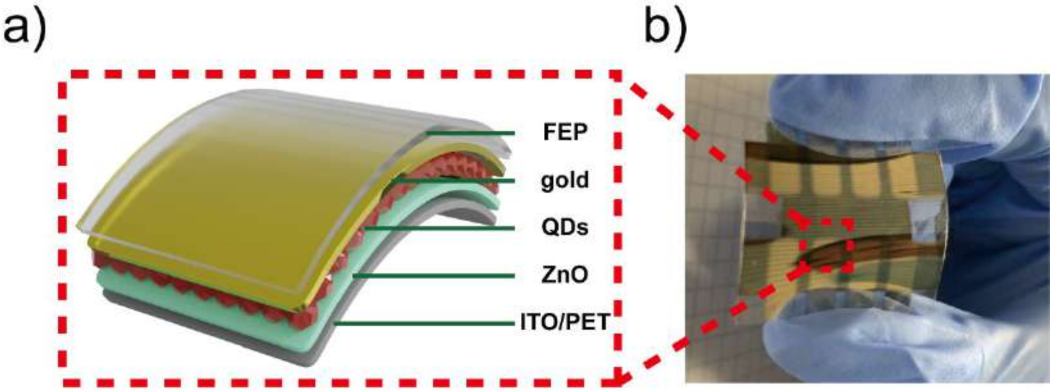

Figure 6.14:
a) Schematic illustration of as-fabricated hybrid energy harvester. b) Photograph of the realized hybrid device at bending state.

For the output performance of the hybrid device, we begin with the solar cell component. It can be observed from Fig. 6.15a that the power conversion efficiency (PCE) of the solar cell component from the champion sample achieves PCE = 4.9% with a short-circuit current (J_{sc}) of J_{sc} = 22.8 mA/cm^2, an open-circuit voltage (V_{oc}) of V_{oc} = 0.54 V and a fill factor (FF) of FF = 40%. Fig. 6.15b shows that simultaneously 41.0 V of average output voltage is obtained by the TENG component under pressing. Moreover, in order to investigate the bending stability of the hybrid device, grazing-incidence small-angle X-ray scattering (GISAXS) is used to characterize the morphology changes of the mesoscale structure [4]. Fig. 6.15c shows the horizontal line cuts from the 2D GISAXS data together with the respective best fits of the solar cell component at different states. Here, because of the similar critical angle of ZnO and PbS, the peak I originates from the inter-dot distance between neighboring ZnO nanoparticles (NPs) in the function layer. Besides, the peak II originates from the inter-dot distance between neighboring PbS QDs in the film. According to the modelling results, the inter-dot distances of ZnO NPs and QDs remain nearly stable at 3.8 ± 0.6 nm and 1.5 ± 0.3 nm, respectively, after bending. Thus, the fabricated device has a high stability on the structure level against bending. From Fig. 6.15d, we can also see that there is only a 2.2% decrease (from 41.0 V to 40.1 V) on average output voltages of the TENG component after 1000 times bending, demonstrating the high bending stability of the whole hybrid device.

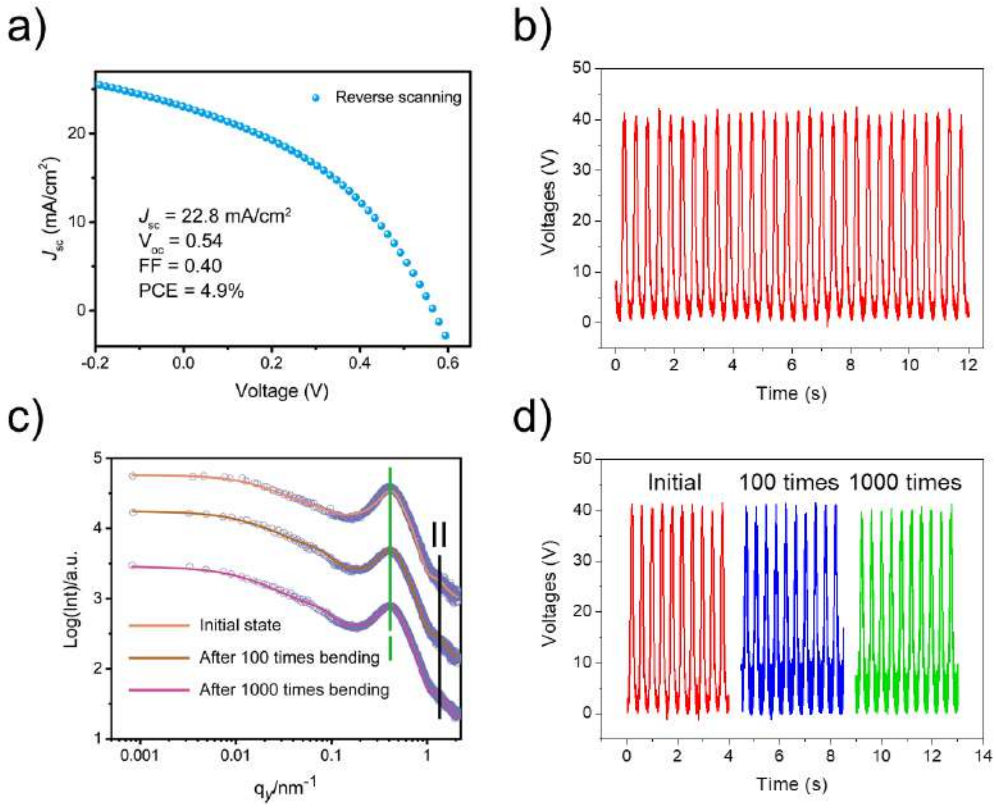

Figure 6.15:
a) Output performance of solar cell component. b) Average output voltages of TENG component. c) Horizontal line cuts with fits at different states. d) Average output voltages of TENG component at different states.

[1] B. O'regan, M. Grätzel, *Nature* **353**, 737 (1991)

[2] Z. L. Wang, *Mater. Today* **20**, 74 (2017)

[3] L. Zheng, Z. Lin, G. Cheng, W. Wu, X. Wen, S. Lee, Z. L. Wang, *Nano Energy* **9**, 291-300 (2014)

[4] P. Müller-Buschbaum, *Adv. Mater.* **46**, 7692-7709 (2014)

6.8 Structural behavior of delithiathed $Li_xNi_{0.8}Co_{0.15}Al_{0.05}O_2$ ($x < 1$) battery cathodes by *ex situ* neutron powder diffraction

T. Hölderle, P. Müller-Buschbaum, A. Senyshyn[1]

[1] MLZ, Garching, Germany

Among the rich choice of commercial cathode materials in lithium-ion batteries ($LiCoO_2$, $LiFePO_4$, $LiNiO_2$, etc.), one of the most encouraging and state-of-the-art positive electrode is the high nickel content transition metal oxide $Li_xNi_{0.8}Al_{0.15}Co_{0.05}O_2$ (NCA). Since its structure experiences increasing distortion along the *c*-axis, while lithium ions are extracted from the material during deintercalation process, the limitations of the overall electrochemical cell performance are nowadays often associated with the cathode materials in lithium-ion batteries [1]. For instance, there is an ongoing debate about the battery performance due to the presence of anti-site defects (cation mixing) in the structure of high nickel content cathodes in lithium-ion batteries, where the partial occupation of the octahedral lithium sites by nickel may result in the blocking of the lithium diffusion pathways and consequently in the performance fading of the cell [2]. Therefore, an *ex situ* neutron powder diffraction study on differently lithiated NCA cathode materials harvested from "fresh" commercial 18650-type battery cells was investigated with the focus on the structural parameters of the frozen-in state of charges. In total, 26 cells were opened and prepared for measurements under argon atmosphere. Data acquisition was performed with a wavelength of λ = 1.5482 Å at the instrument SPODI at FRM II. The obtained neutron data was further fitted with quantitative full-profile Rietveld refinement, using the FullProf program package. The calculated diffraction patterns contained the signal from the NCA phase and an additional aluminum phase, originating from the positive current collector of the battery cell attached to the NCA material. Structural parameters of the unit cell dimension *c* show a complex behavior as seen in Fig. 6.16. Therefore, lattice parameter *c* increases with increasing state-of-charge until a critical deintercalation point of Li_x = 0.25 is reached. Upon further delithiation, the length of lattice parameter *c* decreases rapidly. This finding is in good agreement with the interatomic distances between lithium and oxygen (3a-6c) that show a similar behavior in their bond lengths. Besides that, structural parameters of the unit cell dimensions along *a* have been found to decrease linearly with an ongoing extraction of lithium ions out of the NCA structure. This behavior is further confirmed by the analysis of the distances between transition metals and oxygen positions (3b-6c) that show a linear decrease in their bond length with a higher state-of-charge.

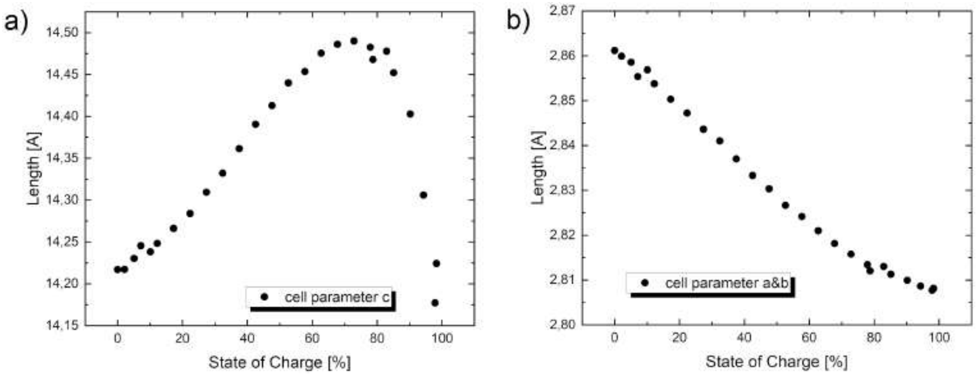

Figure 6.16:
Lattice dimensions of NCA lattice parameters in a) *c*-direction and b) *a*-direction plotted as function of the "frozen-in" state-of-charge.

On basis of these evolutions, the built-up unit cell volume displays a decreasing behavior towards a higher state-of-charge. The specific structural evolution of the lattice parameters results as well in a further change of the unit cell volume, where the same critical deintercalation point Li_x of the lattice parameter in c direction marks a sudden and increasing shrinkage of the unit cell volume. A further delithiation of the NCA structure increases the possibility of the previously described problem of cation mixing appearing due to lower amounts of lithium ions on the octahedral lithium site (3a-site). Thus, the content of lithium ions on the 3a-site exhibits a linear decrease facing a higher state-of-charge as seen in Fig. 6.17. Further chemical reference analysis conducted by an ICP-OES method fit well with the Rietveld-refined lithium content.Simultaneously, the remaining transition metals are potentially able to occupy both octahedral positions (3a, 3b) of the structure. Thus, it is hard to distinguish between the distribution over the octahedral positions and to detect cation mixing in the structure. Consequently, modelling was used to describe antisite defects in high nickel content lithium batteries [2,3]. Occupation factors of the transition metals cobalt and aluminum were fixed to initial values on the 3b-site leaving only nickel and lithium free to distribute between both octahedral positions. The dispersion of 3a, as well as 3b-site, was further separated into a lithium and nickel proportion for each octahedral site, where 3a (Li1/Ni1) and 3b (Li2/Ni2) were further refined by supposing that g(Li2)= g(Ni1) and g(Ni1) + g(Ni2) = g_{total}(Ni). Thus, the occupation of transition metals (Li2, Ni2, Co, Al) located on the 3b-site of the structure show a constant behavior and do not change at a fully occupied state. The refined nickel occupation (green) on the 3a-site is found almost at zero, fitting well to the results at the 3b-site. Since the occupations of transition metals (3b-site) and nickel (3a-site) do not change during the electrochemical performance, the appearance of anti-site defects in the NCA structure is rather unprovable. Consequently, by using neutron diffraction an essential message to the discussion on the appearance of anti-site defects in high nickel content transition metal oxide electrodes can be made, which is in line with the superior performance of NCA cathodes.

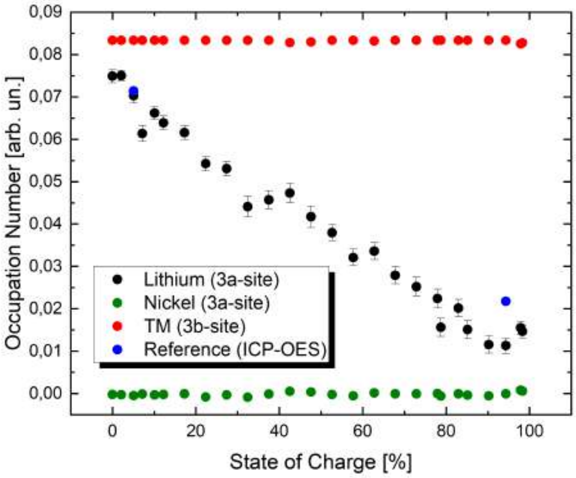

Figure 6.17:
Site occupations as a function of state-of-charge for lithium (black) and nickel (green) on the octahedral 3a-site as well as for transition metals (red) on the 3b-site. In blue two ICP-OES chemical analysis are given as a reference.

[1] O. Dolotko, A. Senyshyn, M. J. Mühlbauer, K. Nikolowski, S. Ehrenberg, *J. Power Sources* **255**, 197-203 (2014)

[2] J. Zheng, Y. Ye, T. Liu, Y. Xiao, C. Wang, F. Wang, F. Pan, *Acc. Chem. Res.* **52**, 2201-2209 (2019)

[3] M. Ma, N. A. Chernova, B. H. Toby, P. Y. Zavalij, M. S. Whittingham, *J. Power Sources* **165**, 517-534 (2007)

6.9 Influence of lithium additive and solvent on NMC111 cathode for lithium ion batteries

Y. Liang, P. Müller-Buschbaum

Lithium ion batteries (LIBs) with a wide range of applications have emerged as the most promising candidate for electrochemical energy storage due to its higher specific energies, volumetric energy densities and power densities. A typical LIB consists of three components, cathode, electrolyte and anode. During charge and discharge process, Li^+ shuttles between two electrodes, meanwhile, lithium dendrite will growth and the Coulombic efficiency (CE) will decrease with Li plating and stripping [1]. Notably, to alleviate the abovementioned hindrances and fulfill the high demands on high capacity and stable LIBs, more and more state-of-art materials have been explored such as $LiNi_{0.9}Mn_{0.05}Co_{0.05}O_2$ for cathode materials and fluorinated $Li_3YBr_{5.7}F_{0.3}$ for electrolyte materials [2-3]. Nevertheless, fundamental research on the component composition and the effect of additive and solvent on LIBs is still lacking. It is of great value to get a deep understanding and therefore optimize the fabrication process for future studies on the electrode/electrolyte interface of LIBs.

Herein, we select the cathode side as the research object to find out the effect of different solvent and extra lithium additive on the performance of LIBs. $LiNi_{0.33}Mn_{0.33}Co_{0.33}O_2$ is the active material in the cathode composition, LiTFSI is the extra lithium additive, 1-methyl-2-pyrrolidone (NMP) and dimethylformamide (DMF) are used as solvents. The respective samples were named as Ref/NMP, Ref with LiTFSI/NMP and Ref with LiTFSI/DMF. The Li/cathode cells were assembled to observe the battery performance.

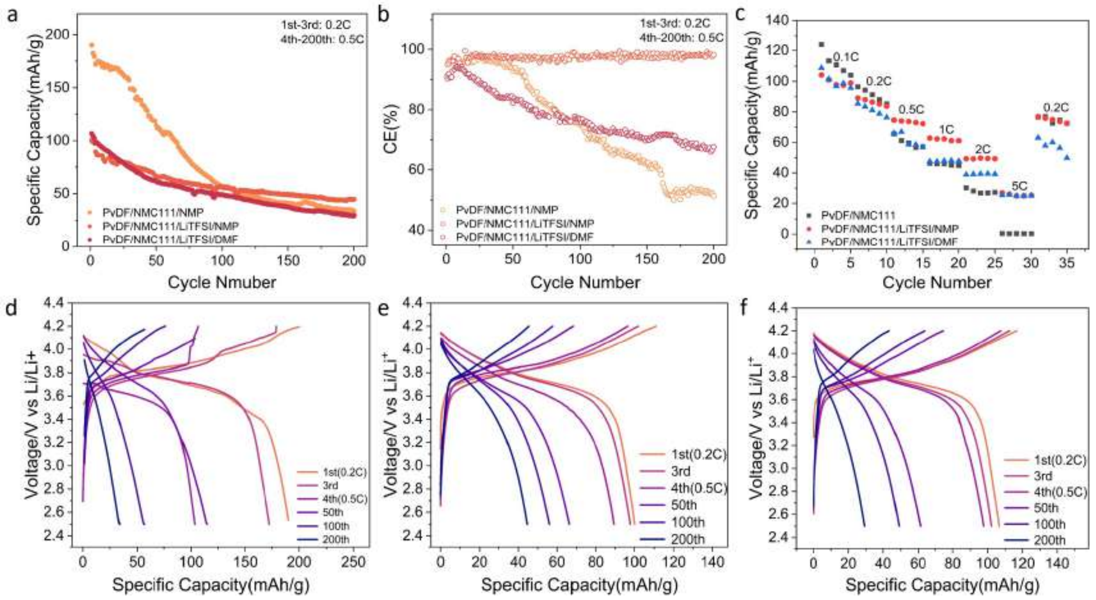

Figure 6.18:
Li/cathode cell performance of a) Specific capacity, b) Coulomb efficiency, c) rate test and Voltage profiles of d) Ref/NMP, e) Ref with LiTFSI/NMP and f) Ref with LiTFSI/DMF.

As shown in Fig. 6.18a and b, with the cut off voltage of 4.2 V at C/5 and C/2 charge/discharge rate, Ref/NMP has the highest specific capacity at the beginning (189 mAh/g), while it drops dramatically within 100 cycles and the CE shows the same tendency. This behavior is consistent with the results of the voltage profiles (Fig. 6.18d). This decrease is a typical phenomenon, since the Li metal anode is thermodynamically unstable in the organic electrolyte, causing the depletion of the electrolyte with the consumption of Li metal and the rapid shrinkage of the capacity and efficiency. After adding extra LiTFSI to the reference sample, despite the decrease of the initial capacity, the sample displayed an excellent cycle stability with a Coulombic efficiency above 96% until 200 cycles and the capacity dropped slightly. Comparing the sample with DMF as solvent, even though it shows a smaller polarization than the other samples, a continuous capacity fading is observed (Fig. 6.18f) and the capacity decreases to over 35% in 200 cycles. In addition, the electrochemical performance at increasing charge/discharge rate is evaluated (Fig. 6.18c). The cell with LiTFSI/NMP shows a better capacity at high rate (>1C) and a better capacity retention when the rate is back to C/5.

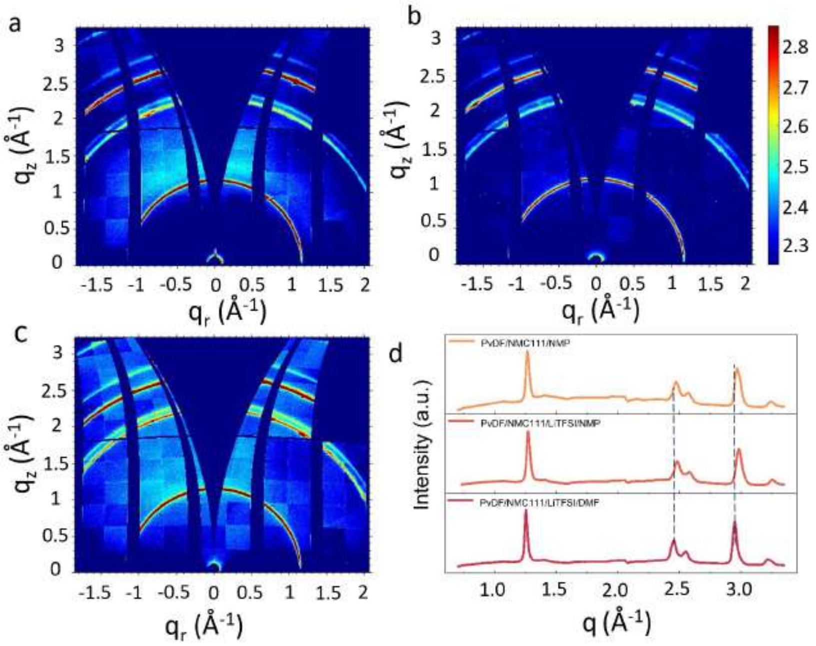

Figure 6.19:
2D GIWAXS image of a) Ref/NMP, b) Ref with LiTFSI/NMP, c) Ref with LiTFSI/DMF and d) cake cut of three samples.

The information about the crystal structure of the cathodes is determined with GIWAXS measurements (Fig. 6.19). The 2D data show a clear NMC111 crystalline phase in all three samples. There is no clear orientation seen in the 2D data, while the high intensity at some specific spots indicates the presence of small highly ordered regions. The cake cuts of 2D GIWAXS data are shown in Fig. 6.19d. The Bragg peaks show a clear shift towards smaller q values, indicating a larger lattice constant and a wider interplanar distance in the crystals.

In summary, for NMC cathode materials, adding extra lithium can increase the cycling stability and Coulombic efficiency. For the solvent, DMF could cause an adverse effect in the battery performance along with a change in the lattice structure.

[1] F. Duffner, N. Kronemeyer, J. Tübke, J. Leker, M. Winter, R. Schmuch, *Nature Energy* **6**, 123-134 (2021)

[2] C. Wang, J. Liang, Y. Zhao, M. Zheng, X. Li, X. Sun, *Energy Environ.Sci.* **14**, 2577-2619 (2021)

[3] T. Yu, J. Liang, L. Luo, L. Wang, F. Zhao, G. Xu, X. Bai, R. Yang, S. Zhao, J. Wang, J. Yu, X. Sun, *Adv. Energy Mater.* **11**, 2101915 (2021)

6.10 Design, fabrication and nano-scale characterization of novel SEI layers

Z. Xu, Y. Xia[1], Y. Cheng[1], P. Müller-Buschbaum

[1] NIMTE, Ningbo, China

Lithium (Li) has a high specific capacity of 3860 mAh g^{-1} and a low electrochemical potential (-3.04 V), promising to be a high energy density lithium metal battery (LMB). However, the growth of lithium dendrites during charging and discharging would penetrate the separators in LMBs, which leads to short circuit or even fire, thus causing serious safety problems of LMBs [1]. To inhibit the growth of lithium dendrites and significantly improve the safety of LMBs, the solid electrolyte interphase (SEI) layer is of growing interest. Different methods for the optimization of adjusting mechanical and electrical properties of the SEI layer, including regulating the composition of the electrolyte, the composition of the interface and the morphology, were reported.

In the present work, we focus on optimizing the SEI layer for high specific energy LMBs through localized iodination for an interface and ion modulation.In the standard electrolyte (PC (Propylene Carbonate)/FEC (Fluoroethylene carbonate)/DMC (Dimethyl carbonate)=7.5/2/0.5 v/v/v, 1 M $LiPF_6$ (Lithium hexafluorophosphate), 5 wt% LiTFSI (Lithium bis(trifluoromethanesulfonyl)imide)), a small amount of additive (poly (N-vinylimidazole) quaternized with iodide, molecular weight 16.5 g/mol, 21% quaternization, abbreviated as PVIM) was added.

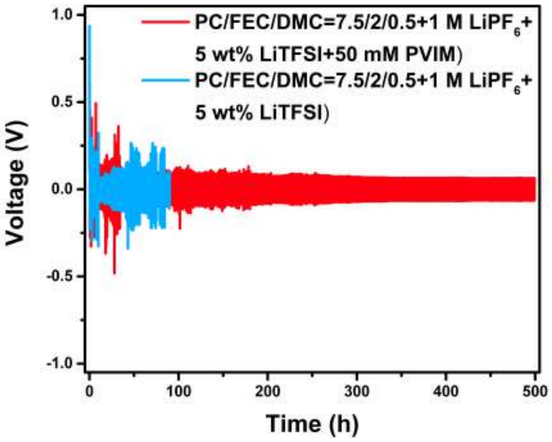

Figure 6.20:
Plating/exfoliation process of lithium/lithium symmetrical cells in two electrolytes: with PVIM electrolyte additive (red) and without electrolyte additive (blue).

As shown in Fig. 6.20, the Li-Li symmetrical cells with the PVIM additive electrolyte can cycle for 500 cycles under the charge/discharge conditions with a capacity setting of 1 mAh cm^{-2} (red curve) and a current density of 2 mA cm^{-2}, while the control sample can only cycle for nearly 100 cycles (blue curve). On the one hand, PVIM releases iodine ions during the dissolution process, which can effectively improve the ionic conductivity of the electrolyte. In addition, iodine ions can spontaneously form I^{3-}, which can react with dead lithium, inhibit the formation of lithium dendrites and increase the efficiency of lithium utilization. On the other hand, the nitrogen-containing functional group in the imidazole group can form a solid electrolyte layer with high ionic conductivity, which inhibits the formation of lithium dendrites.

As an alternative approach, the enhancement of the SEI layer structural stability can be tailored with a modification of the lithium metal surfaces using an amphiphilic diblock copolymer.

Different amphiphilic diblock copolymers, such as PS-*b*-PEO, PS-*b*-P4VP, and lithium salts were used to modify the surface of lithium metal anodes. For example, 40 mg of PS-*b*-P4VP and 40 mg of LiTFSI were dissolved in N,N-dimethylformamide (DMF) and subsequently transferred to the lithium metal surface by spin-coating to form a polymer/lithium salt composite layer on the lithium metal surface. As can be seen in Fig. 6.21, the amphiphilic block copolymer forms an island-matrix-type two-phase morphology due to the difference in hydrophilicity/oleophilicity of the amphiphilic block copolymer in combination with microphase separation. P4VP/LiTFSI forms a brighter and more homogeneous island structure with 20 nm-diameter, while PS forms a darker matrix structure. In the subsequent electrochemical testing of the Li-Li symmetrical cells (Fig. 6.22), the electrolyte used was EC (Ethylene carbonate)/DEC (diethyl carbonate)/DMC=1/1/1 v/v/v, 1 M $LiPF_6$.

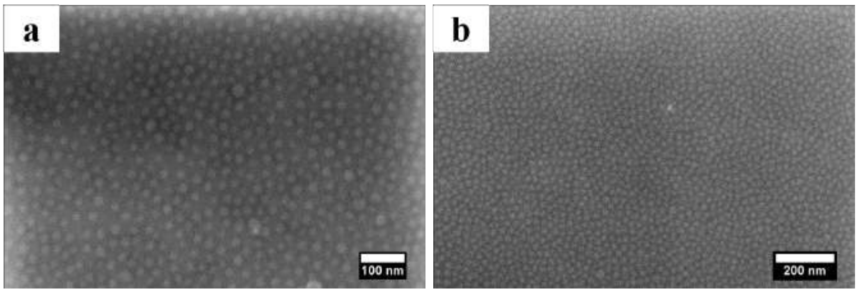

Figure 6.21:
SEM surface morphology images of PS-*b*-P4VP/LiTFSI@Li at (a) higher and (b) lower magnification.

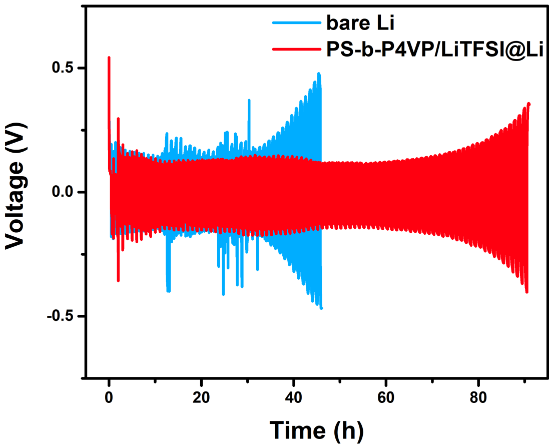

Figure 6.22:
Plating/exfoliation process of lithium/lithium symmetrical cells with bare Li (blue), PS-*b*-P4VP/LiTFSI@Li (red).

The surface modification of the lithium metal effectively improves the stability of the cells with cycling for 80 cycles, compared to only 35 cycles for the control sample. The PS part provides a good mechanical support, while P4VP/LiTFSI provides a good ionic conductivity. In addition, the regular surface structure effectively inhibits the growth of irregular lithium dendrites by suppressing the inhomogeneous current density caused by local ion aggregation.

[1] J. Bae, Y. Qian, Y. Li, X. Zhou, J. Goodenough, G. Yu, *Energy Environ. Sci.* **12**, 3319–3327 (2019)

6.11 Revealing the morphology-ionic conductivity relationship in polymer-titania hybrid electrolytes for lithium-ion batteries

S. J. Schaper, E. Metwalli, M. V. Kaeppel, A. Kriele[1], R. Gilles[2], K. N. Raftopoulos[3],
P. Müller-Buschbaum

[1] GEMS, Geesthacht, Germany
[2] MLZ, Garching, Germany
[3] Department of Chemistry and Technology of Polymers, Cracow University of Technology, Poland

Building better batteries became a complex task due to the multitude of materials interacting within the electrochemical cell. By tuning the electrode materials, the established electrolytes need to be refined. Hybrid polymer electrolytes comprised of a conducting polymer and an (inorganic) additive for stability and/or ionic conductivity enhancement are promising candidates for the next-generation, safe, and high performing lithium-ion-batteries [1]. Revealing the relationship between morphology and ionic conductivity of the PS-*b*-PEO:LiTFSI:TiO_2-NP hybrid polymer electrolyte enables a more focused electrolyte optimization [2].

Using a high molecular weight $PS_{16.4}$-*b*-PEO_{110} diblock copolymer with a PEO fraction of 87 wt%, the lithium bis(trifluoromethanesulfonyl)imide (LiTFSI) salt, and titania (TiO_2) nanoparticles (NPs) (functionalized with dodecylphosphonic acid and hexylamine) dissolved in trichloromethane, samples were prepared via drop-casting. The molar ratio between EO monomers and Li^+-ions was kept constant ($[Li^+]/[EO] = 0.1$), while the TiO_2-NP content was varied from 0.5 wt% to 43 wt%, compared to the total sample weight. Potentiostatic electrochemical impedance spectroscopy (PEIS) (Fig. 6.23) was used to measure the ionic conductivity σ of the PS-*b*-PEO:LiTFSI:TiO_2-NP hybrid polymer electrolytes. Even a very small difference in TiO_2-NP content (2.5 wt% or 3.9 wt%) has a huge impact on the ionic conductivity σ (Fig. 6.23a). The temperature T dependence of the ionic conductivity σ in the measured range (25 °C $< T <$ 155 °C) is described with the Vogel-Fulcher-Tammann (VFT) equation [3]:

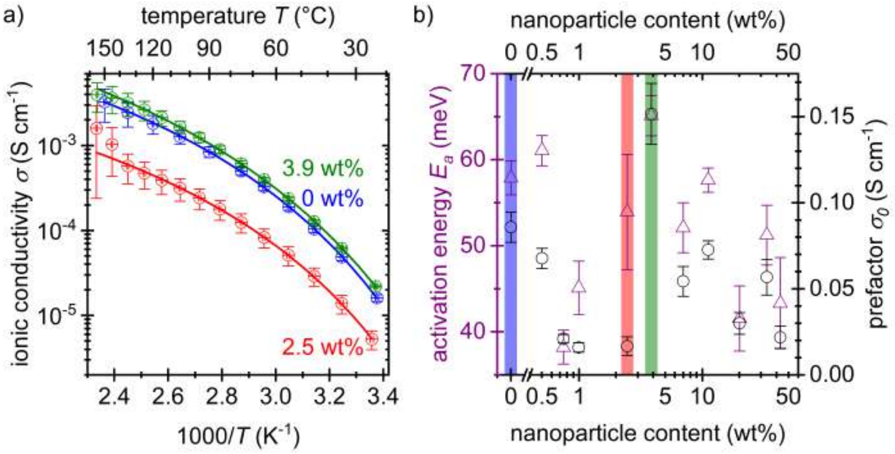

Figure 6.23:
a) Arrhenius plot of the PS-*b*-PEO:LiTFSI:TiO_2-NP hybrid polymer electrolytes with TiO_2-NP contents of 0 (blue), 2.5 wt% (red), and 3.9 wt% (green). Lines represent fits with the Vogel-Fulcher-Tammann (VFT) equation. b) *Pseudo*-activation energy E_a (violet triangles) and prefactor σ_0 (black circles) versus the TiO_2-NP content. Colored boxes mark the TiO_2-NP contents presented in a).

$$\sigma = \sigma_0 \cdot exp\left(\frac{-E_a}{k_B(T - T_0)}\right)$$

The prefactor σ_0 is correlated to the amount of free charge carriers in the electrolyte, here Li^+-ions. These Li^+-ions have to overcome an energy barrier to travel in the electrolyte; this barrier is the pseudo activation energy E_a. Below a certain temperature T_0, which is usually about 50 °C below the glass transition temperature, σ becomes zero; k_B is the Boltzmann-constant. E_a and σ_0 are shown in Fig. 6.23b versus the TiO_2-NP content. At 2.5 wt% TiO_2-NP content, the E_a value is similar to that of the electrolyte without TiO_2-NPs. However, σ_0 is far lower at 2.5 wt% TiO_2-NP content, explaining the worse ionic conductivity, in comparison to the electrolyte without TiO_2-NPs. The highest σ_0 at 3.9 wt% TiO_2-NP content overcompensates the only slightly higher E_a. A further increase of the TiO_2-NP content up to 43 wt% only leads to a very slight decrease in σ as σ_0 and E_a balance each other out. Small-angle X-ray scattering (SAXS) (Fig. 6.24) provides insights into the nanoscale morphology of the PS-*b*-PEO:LiTFSI:TiO_2-NP hybrid polymer electrolytes. Fig. 6.24 reveals the origin of the high amount of free Li^+-ions at a TiO_2-NP content of 3.9 wt%. Dense TiO_2-NP aggregates (accompanied by slightly decreasing TiO_2-NP distance D_s) gradually destroy the self-assembled nano-morphology of the PS-*b*-PEO for TiO_2-NP contents $\geq$ 3.9 wt%. For smaller TiO_2-NP contents, the PS-*b*-PEO morphology remains intact but the distance of of the PS cylinders, D_c, shrinks compared to the bare PS-*b*-PEO:LiTFSI electrolyte. However, the radius of these PS cylinders, R_c, as well as the radius of the TiO_2-NPs, R_s, both remain constant. Hence, the TiO_2-NPs only incorporate into the PEO and block the pathways for Li^+-ions in the persisting PS-*b*-PEO morphology, where the conducting channels become even narrower due to the decreasing D_c. Once the confining PS-*b*-PEO morphology ruptures upon increase of TiO_2-NP content, a high amount of free Li^+-ions increase the ionic conductivity σ, compared to the PS-*b*-PEO:LiTFSI electrolyte.

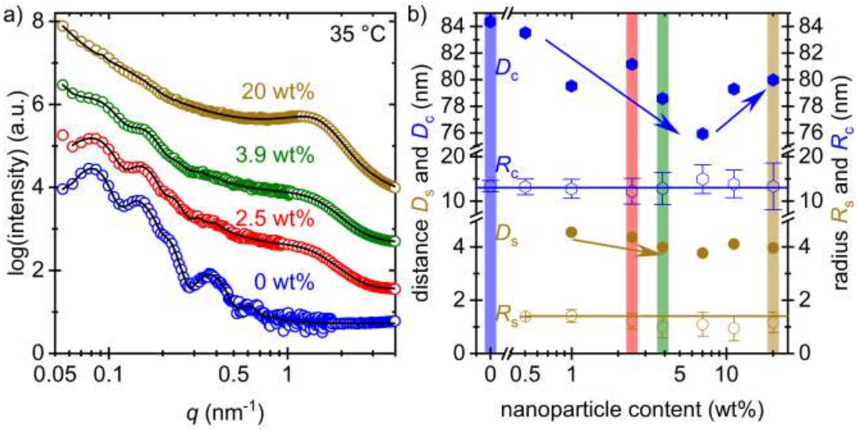

Figure 6.24:
a) 1D SAXS profiles of the PS-*b*-PEO:LiTFSI:TiO_2-NP hybrid polymer electrolytes with TiO_2-NP contents of 0 (blue), 2.5 wt% (red), 3.9 wt% (green), and 20 wt% (brown). Black lines show the fits with hexagonally ordered PS cylinders (radius R_c) with distance D_c in a PEO matrix and TiO_2-NP spheres (radius R_s) with distance D_s. b) Distance D_s and D_c (closed symbols) and radius R_s and R_c (open symbols) versus the TiO_2-NP content. Arrows guide the eye and colored boxes mark the TiO_2-NP contents presented in a).

Concluding, only a small TiO_2-NP content (3.9 wt%) results in the best performing PS-*b*-PEO:LiTFSI:TiO_2-NP hybrid polymer electrolyte due to the large amount of unconfined Li^+-ions in a disrupted polymer nanoscale morphology. Being an entirely solution-based process, the sample preparation can be easily transferred to large-scale productions like printing and spraying.

[1] J. Wang, S. Li, Q. Zhao, C. Song, Z. Xue, *Adv. Funct. Mater.* **31**, 2008208 (2021)

[2] S. J. Schaper, E. Metwalli, M. V. Kaeppel, A. Kriele, R. Gilles, K. N. Raftopoulos, P. Müller-Buschbaum, *ACS Appl. Energy Mater.* **4**, 13438-13443 (2021)

[3] K. M. Diederichsen, H. G. Buss, B. D. McCloskey, *Macromolecules* **50**, 3831-3840 (2017)

7 Real-time characterizations

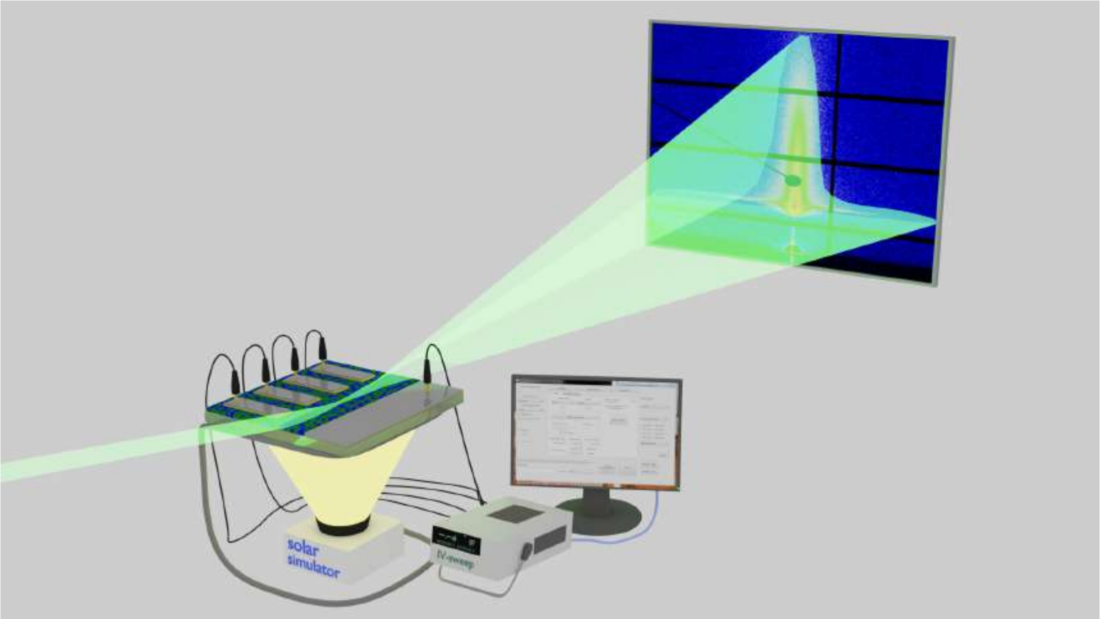

7.1 Small details make the difference: effects of atmospheres on solar cells during degradation process

R. Guo, P. Müller-Buschbaum

Over the past ten years, constant research efforts have intensely increased the solar to device power conversion efficiencies (PCE) of perovskite solar cells from PCE $\sim$ 3.8 % to PCE $\sim$ 25.5 %. The stability issue is the main barrier from taking steps to industrialization. Although a consensus statement stability assessment and reporting for perovskite photovoltaics had been established, a small detail may lead to a large discrepancy. For example, most scientists in the lab could equate a nitrogen and a vacuum atmosphere in the experimental protocol, because we mainly use both of them to avoid the effects of water or oxygen in the air. However, our recent results confirm that this approach is wrong when this simplification is applied to our experiments. The effects of atmospheres should not be overlooked even if they are inert.
We use synchrotron radiation-based *operando* grazing-incidence X-ray scattering methods on perovskite solar cells via the standard protocol to study the degradation mechanism of perovskite solar cells (Fig. 7.1).

Figure 7.1: Architecture of peroskite solar cells.

We find [1] that perovskite solar cells experience a significant lattice shrinkage, a phase segregation into a $FAPbI_3$ phase as the minority phase, and a large amount of $(MAPbBr_3)_{0.17+x}(FAPbI_3)_{0.83-x}$ as the majority phase for the perovskite layer under standard one-sun illumination (AM1.5 G) in vacuum. In contrast, continuous operation in nitrogen under the same illumination intensity has only induced a slight lattice shrinkage of the perovskite materials (Fig. 7.2).

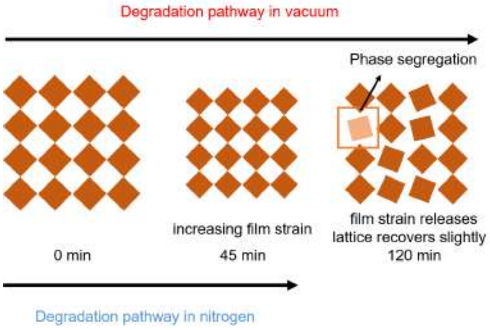

Figure 7.2:
Schematic diagram projecting different lattice dynamics and phase stability when perovskite solar cells are operated under vacuum and nitrogen.

Moreover, grazing incidence small-angle X-ray scattering helps us discover that crystals inside the perovskite film with diameters lower than 40 nm break into smaller crystals during the operation under vacuum (Fig. 7.3a). These small crystals act as pinholes in the PSCs, which harm the performance of the devices. However, in nitrogen, the morphology of the perovskite layer remains stable. The loose space structure of spiro-OMeTAD offers physical pathways for such results. In vacuum, an outgassing process of MA molecules from the perovskite layer cause crystal breakage during solar cell operation. In nitrogen, such a loose space structure allows for the diffusion of nitrogen molecules into the active layer underneath (Fig. 7.3b). This process can decrease the free energy via an exothermic process. Thus, we speculate that the physical adsorption of nitrogen could play an important role in reducing the film strain and maintaining the lattice and phase stability, which is also related to a larger activation energy barrier for phase segregation.

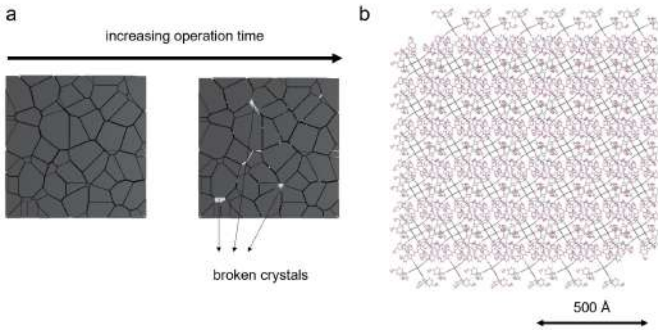

Figure 7.3:
a) Scheme that illustrates the improved strength of the perovskite film to suppress further deformation through the increase of grain boundaries due to broken crystals. b) Schematic diagram of nitrogen molecules (yellow symbols) diffusing through the spiro-OMeTAD layer expressed by a blue (side chains) and grey (intermolecular π-π stackings) mixed space frame during the operation of solar cells under nitrogen. The zoomed inset indicates the loose structures of spiro-OMeTAD allowing the diffusion of nitrogen molecules.

The aforementioned different behaviors under vacuum and nitrogen cause in turn a different degree of device performance loss. Given the more stable lattice, structure, and morphology behavior when the perovskite solar cells are operated under nitrogen, the perovskite solar cells show a better stability compared with those solar cells operated under vacuum (Fig. 7.4).

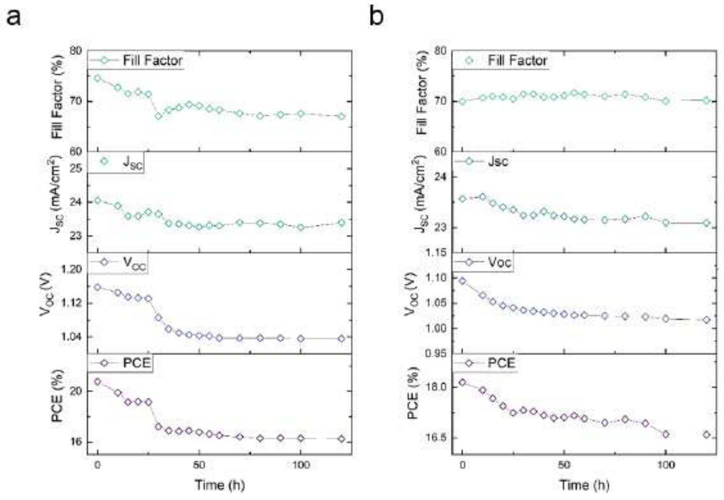

Figure 7.4:
Evolution of Fill Factor, shprt-circuit current density (J_{SC}), open-circuit voltage (V_{OC}) and PCE for perovskite solar cells operated under (a) vacuum and (b) nitrogen.

We hope that the researchers who use vacuum or nitrogen as a solution to avoid the effects of water and oxygen in the air should take an eye on how a vacuum or nitrogen condition would affect their experimental results obtained from different characterization methods like scattering, spectroscopy, and microscopy. There could be a surprising avenue for new knowledge.

[1] R. Guo, D. Han, W. Chen, L. Dai, K. Ji, Q. Xiong, S. Li, L. K. Reb, M. A. Scheel, S. Pratap, N. Li, S. Yin, T. Xiao, S. Liang, A. L. Oechsle, C. L. Weindl, M. Schwartzkopf, H. Ebert, P. Gao, K. Wang, M. Yuan, N. C. Greenham, S. D. Stranks, S. V. Roth, R. H. Friend, P. Müller-Buschbaum, *Nat. Energy* **6**, 977-986 (2021)

7.2 In situ GIWAXS perovskite interdiffusion-reaction analyzed with the python package INSIGHT

M. A. Reus, L. K. Reb, C. Rosemann[1], M. Schwartzkopf[1], S. V. Roth[1], P. Müller-Buschbaum

[1] DESY, Hamburg, Germany

Capturing kinetic processes in thin films is of great interest in the fields of, e.g., organic and hybrid photovoltaics, as well as responsive polymers. Kinetic processes inside the thin film can only be adequately investigated by transient methods that are fast enough for the respective kinetics. X-ray scattering experiments with high brilliance synchrotron radiation allow for high count rates even when integration time is short. Together with improved detector systems that become increasingly more sophisticated in data capturing rate, noise reduction and pixel size, high time-resolved X-ray scattering experiments can be achieved. For thin films, especially grazing-incidence wide- and small-angle X-ray scattering (GISAXS and GIWAXS) are powerful investigation methods for thin-film morphology analysis including crystal structure information. However, with increased frame rates a strongly increasing image number is generated. This development creates challenges in data visualization, analysis, and reduction for the scientists, who want to extract the maximum of information from a large number of transient images.

Here, we introduce the Python software package INSIGHT (In SItu Grazing-incidence Heuristic Tool) for efficient and flexible data handling of 2D GIXS images [1]. The features implemented in INSIGHT aim at a complete coverage of scientific needs from the experiment to publication-ready plotting of extracted data. A common workflow involves visualization of raw data and transformation to q-space (reshaping) for the extraction of crystallographic-relevant information. This is usually followed by focusing on regions of interest, e.g., azimuthal tube cuts and radial cake cuts for orientation and phase information, respectively. The general workflow used by INSIGHT is shown in Fig. 7.5.

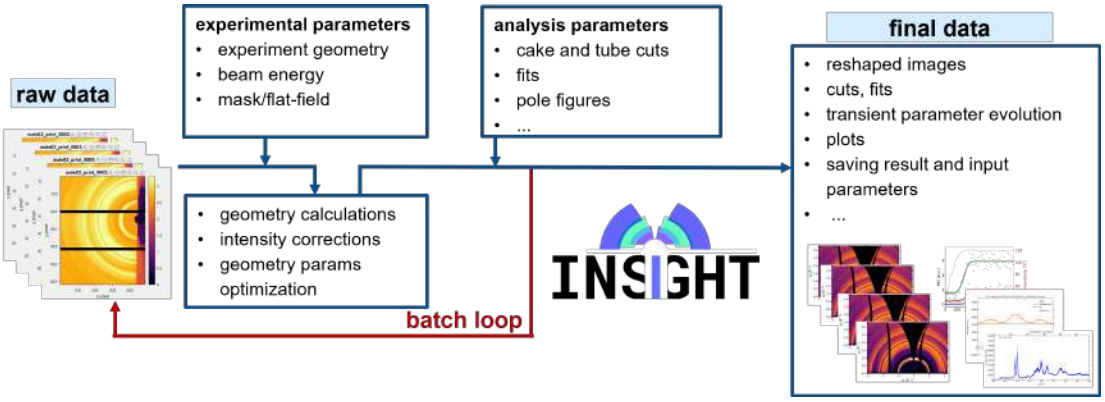

Figure 7.5:
Workflow of the Python package INSIGHT for efficient data reduction of 2D grazing-incidence scattering data.

However, it is of key interest in analyzing kinetic processes that all software features mentioned above can be consecutively applied to a complete image sequence (batch processing). Flexibility is of great importance to providing software for a wide range of scientific experiments.
To demonstrate the capabilities of INSIGHT, the analysis of *in situ* GIWAXS data from thermally triggered interdiffusion reaction of methylammonium iodide and lead iodide to methylammonium lead iodide (MAPI) is exemplarily shown. A raw and reshaped image is shown in

Fig. 7.5a. The total calculation time including reshaping and intensity corrections for a Pilatus 300k detector image takes 150 ms on an average office computer. Pseudo-XRD patterns from radial cake cuts of the 2D GIWAXS images are shown in Fig. 7.6b including Gaussian fits for each Bragg reflex. INSIGHT can apply the specified reshaping, cut, and fit parameters to each individual frame. Cuts and fit parameters are accessible to the user at any step of the process. In this case, the Bragg peak amplitude is of interest to track the phase formation of MAPI over the annealing process (Fig. 7.6c). A clear rise in MAPI amplitude is seen (green) and a simultaneous drop in amplitudes corresponding to the precursor-solvent-adduct (red colors).

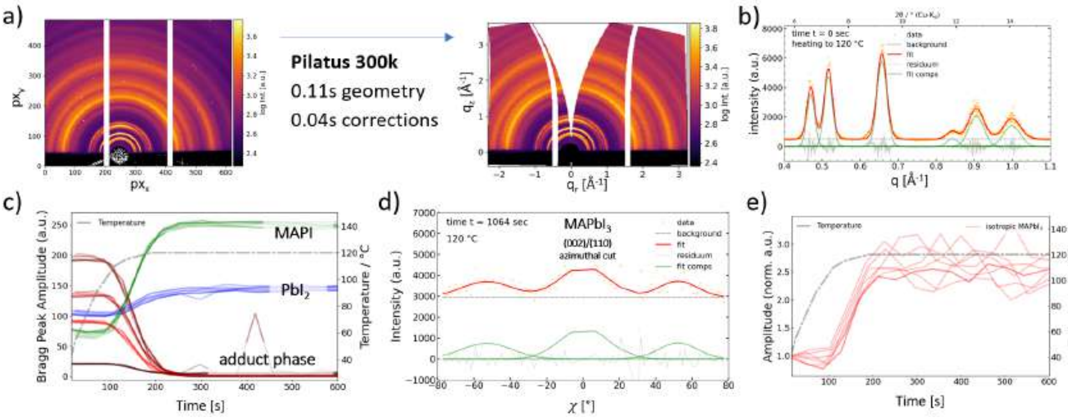

Figure 7.6:
a) Raw and reshaped 2D GIWAXS detector image before the annealing process. b) Full radial cake cut of 2D GIWAXS image (pseudo-XRD) before the annealing process. c) Phase evolution (Bragg peak amplitude) extracted from 2D GIWAXS images using INSIGHT. d) Tube cut of the MAPI (110)/(002) Bragg reflex, showing 3 distinct orientations and a large fraction of isotropically oriented crystallites. e) Normalized Bragg peak amplitude evolution for isotropic MAPI crystallites during the annealing process.

INSIGHT is also capable of in-depth orientation (texture) analysis as shown in Fig. 7.6c and 7.6d. First, tube cut limits must be carefully defined for the Bragg ring of interest. INSIGHT collects all pixels that fall into the defined q-range and sorts them to their respective azimuthal angle χ. Then, a fit is defined: For MAPI this includes three Gaussian functions and constant background. The cuts and fits are executed for every single image and the resulting parameters are then available for further analysis or plotting. The relative orientation evolution of isotropically oriented MAPI is shown in Fig. 7.6c. A steep rise in isotropically oriented MAPI crystallites of around 250 % is visible.

In conclusion, we introduce the Python software package INSIGHT for 2D GIXS image treatment from visualization of raw data up to publication-ready plotting of multi-step analysis results. Thus, this tool offers great possibilities for the scientists who work with large amounts of, e.g., *in situ* or *in operando* GIXS data to capture kinetic processes. In the future, the software will become available.

[1] M.A. Reus, L.K. Reb, C. Rosemann, M. Schwartzkopf, S.V. Roth, P. Müller- Buschbaum, INSIGHT, https://www.groups.ph.tum.de/functmat/forschung/insight/

7.3 *In situ* photoluminescence characterization of slot-die coated perovskite layers for photovoltaics

A. F. Weinzierl, M. A. Reus, P. Müller-Buschbaum

Perovskite solar cells (PSC) are a promising candidate to evolve the solar energy market due to high-energy conversion efficiencies and low-cost material usage. However, many perovskite configurations suffer from long-term stability problems. Formamidinium/cesium lead iodide/bromide (FACs) are promising to overcome this issue as active layer of such solar cells, since they do not undergo disadvantageous phase transitions at temperatures where solar cells are typically operated. At room temperature, the standard formamidinium lead iodide composition undergoes a phase transition to a photoinactive orthorhombic crystal structure [1]. Inhibiting cesium lowers the Goldschmidt tolerance factor to an ideal range between 0.8-1.0, thus resulting in a stabilization of a photoactive cubic structure [2].

Crucial for FACs is the development of a suitable solvent system together with an optimized printing process enabling to produce homogeneous layers and, as a result, PSCs with high performance and high stability. With this understanding, obtaining an understanding of the morphology of such layers is beneficial. One method to look into the formation and the ongoing processes during and after printing is photoluminescence (PL). Since the slot-die coating technique is used in this work, a PL setup for this printer device is designed and constructed.

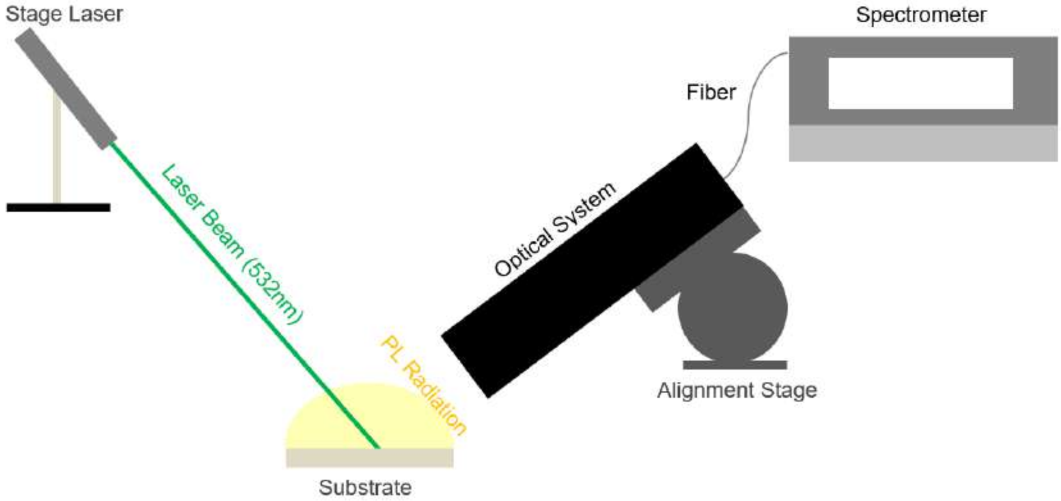

Figure 7.7:
Schematic of the *in situ* photoluminescence setup, which will be combined with the printer to enable multimodal measurements.

One focus of this work is the optimization of the slot-die coating process for the fabrication of FAC based PSCs. In general, to achieve high efficiency, it is favourable to print homogeneous layers with low surface roughness. This means to control and optimize a variety of slot-die coating parameters, such as gap height, pump rate and velocity. Moreover, the chemical characteristics of the precursor and solution have to be taken into account. Since formamidinium is very prone to moisture, a nitrogen flow for the drying is set to be decisive for the quality of these films. Furthermore, the printing temperature is dependent on the properties of the solvents used. Conceptual orientation is to use solvents with comparatively high vapor pressure and low boiling point, promising fast drying at low temperatures as a consequence [3].

During slot-die coating, but especially during drying, the layer undergoes morphological changes due to nucleation, crystallization and rearrangement effects which are worth to be determined in detail. Since perovskites are active for photoluminescent processes, measuring the photoluminescence spectrum of a film with a specific composition can give insight into these distinct formation processes. For implementing such a system, it is necessary to have an excitation source with specific photon energy higher than the band gap to generate excitons. Therefore, a green laser with output wavelength of 532 nm is used (Fig. 7.7). These excitons undergo different recombination processes leading to emission of photons. To collect this radiation, a specific optical system is needed. An aspherical lens collects and distributes the signal to a collimator after filtering the signal by cutting off the unwanted laser radiation. Afterwards, the collimated signal is fed via an optical fiber into the spectrometer where the signal is processed.

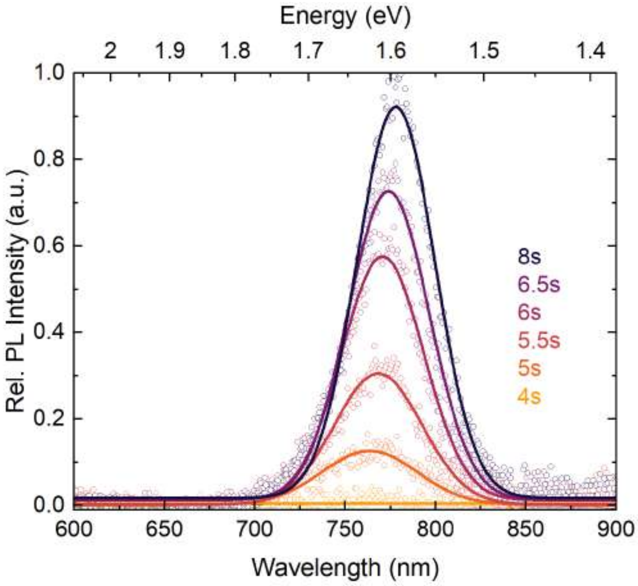

Figure 7.8:
Photoluminescence (PL) intensity evolution for various times after starting the printing process at the wavelength range of 600 nm to 900 nm. Here, the FAC layer was printed at 55 °C. Dotted points are the measured values to which a Gaussian fit is applied (continuous lines).

For an FAC film printed on a heated substrate at a temperature of 55 °C, the PL signal development during the beginning of the drying process can be seen in Fig. 7.8. As long as the film is wet, no PL signal can be observed. With the start of nucleation, small perovskite crystals are steadily formed [4], giving a continuously rising intensity red shifted over time that can be fitted by a Gaussian distribution centered at ∼775 nm. Summing up, *in situ* PL opens the possibilities to obtain insight into the morphology of the perovskite film formation, e.g. of FAC, during printing with high time resolution. The PL results can be furthermore combined in parallel with other investigation methods, such as *in situ* grazing-incidence wide-angle X-ray scattering (GIWAXS) to enable truly multimodal measurements [5].

[1] C. Yi, J. Luo, S. Meloni, A. Boziki, N. Ashari-Astani, C. Grätzel, S. M. Zakeeruddin, U. Röthlisberger, M. Grätzel, *Energy Environ. Sci.* **9**, 656-662 (2016)

[2] Z. Li, M. Yang, and J. Park, S. Wei, J. Berry, K. Zhu, *Chem. Mater.* **28**, 284-292 (2016)

[3] Y. Deng, C. H. Van Brackle, X. Dai, J. Zhao, B. Chen, J. Huang, *Sci. Adv.* **5**, (2019)

[4] S. Pratap, F. Babbe, N. S. Barchi, Z. Yuan, T. Luong, Z. Haber, T. -B. Song, J. L. Slack, C. V. Stan, N. Tamura, C. M. Sutter-Fella, P. Müller-Buschbaum, *Nat. Commun.* **12**, (2021)

[5] O. Filonik, M.E. Thordardottir, J. Lebert, S. Pröller, S. Weiß, L. J. Haur, A. Priyadarshi, P. Fontaine, P. Müller-Buschbaum, N. Mathews, E. M. Herzig, *Energy Technol.* **7**, (2019)

7.4 Analysis of quasi-2D perovskite crystallization induced by small molecules

J. Zhou, X. Dong[1], L. Cai[1], M. Fung[1], P. Müller-Buschbaum

[1] FUNSOM, Suzhou, China

Metal halide perovskite light-emitting diodes (PeLEDs) are regarded as alternative candidates for next-generation display technologies due to their high efficiency, superior color purity and tunable bandgap [1]. However, various defects are easily formed in perovskite films prepared by spin-coating method, due to the ionic properties of perovskite materials and rapid crystallization [2]. These defects can significantly reduce the performance of PeLEDs [3].

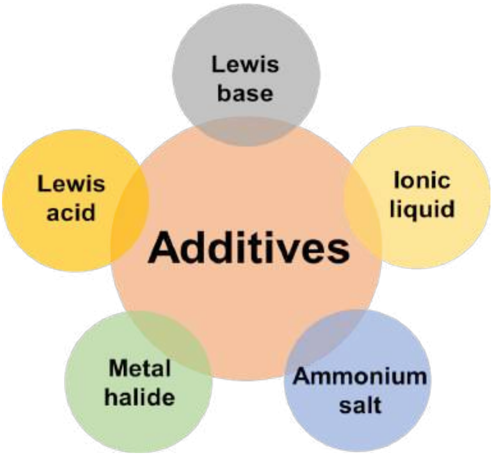

Figure 7.9: Various additives to reduce the defects in perovskites.

To reduce the non-radiative recombination loss, the introduction of additives into the perovskite precursor solution for defect passivation is an effective method. Fig. 7.9 shows the types of commonly used additives, which can be mainly divided into Lewis acids and bases, ionic liquids, metal halides and organic amine salts. The passivation mechanism of various materials is also different. For instance, in Lewis base or acid, the atoms containing oxygen, sulfur and nitrogen have unbound electrons, which can coordinate with lead ions in halogen vacancies, thereby reducing the defects in perovskite films [4]. In addition, the molecular structure of the additive also has an important influence on the quality of the perovskite films. Therefore, understanding the mechanism of the additive to reduce the defects and affect the quality of the perovskite film is of great significance for further improving the performance of PeLEDs. Here, from the perspective of molecular structure, we select additives with different functional groups to reveal the influence of additives on the formation of high-quality perovskite films and high-efficiency PeLEDs.

From Fig. 7.10, the taurine additive can obviously affect the crystalline characteristics of the (100) and (110) plane of the perovskite films without changing the crystal structure. Especially with the increase of the additive concentration, it can be seen from the (110) plane that the crystal size of the perovskite within 30-53 degree is obviously enhanced. In addition, the size of the perovskite grains gradually decreases with the increase of taurine additive concentration (see Fig. 7.10f), which will enhance the confinement effect and improve the exciton recombination efficiency to a certain extent.

Moreover, the effect of taurine on the crystallization rate of the perovskite is also investigated. The perovskite solution is excited by ultraviolet light in the process of spin-coating, so the

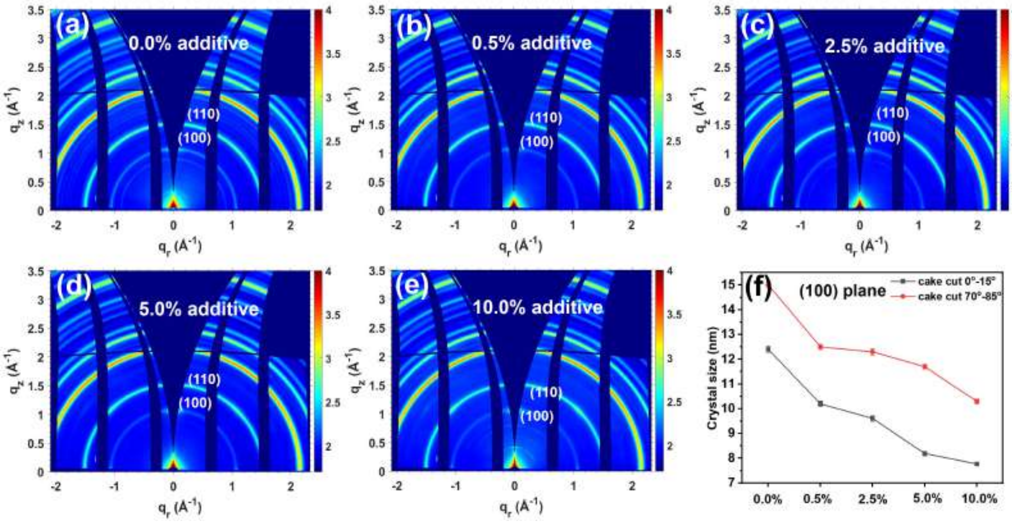

Figure 7.10:
GIWAXS images of perovskite films with different taurine ratios: a) 0.0, b) 0.5, c) 2.5, d) 5.0, e) 10. f) Grain size of perovskite films with various additive concentrations as determined from different cake cuts.

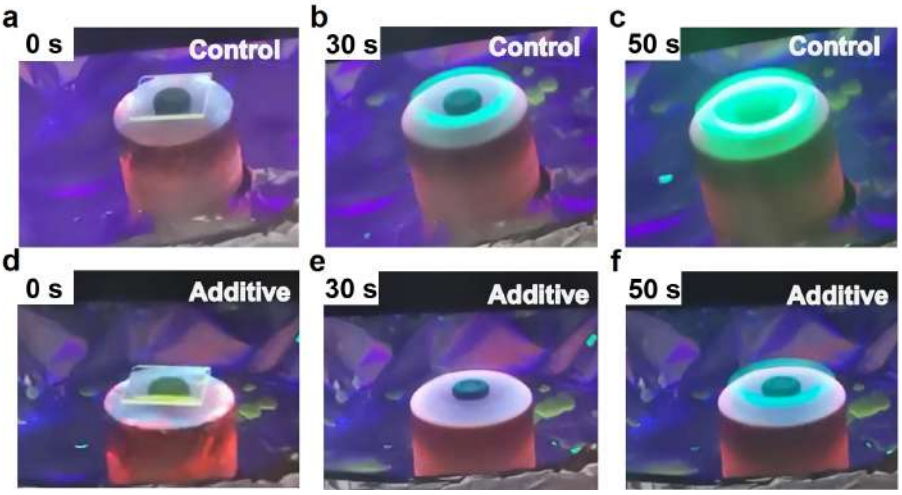

Figure 7.11: Film formation of the perovskite solution w/wo taurine during spin-coating process.

film-forming process can be directly observed in real time. As can be seen from Fig. 7.11, when the spin-coating time is 30 s, the sample with taurine does not show obvious photoluminescence compared with the reference sample, which indicates that the additive can effectively slow down the crystallization rate and essentially reduce the defects center of the perovskite film. This is important for the improvement of the efficiency of PeLEDs.

[1] Y. H. Kim, H. Cho, J. H. Heo, T. S. Kim, N. Myoung, C. L. Lee, S. H. Im, T. W. Lee, *Adv. Mater.* **27**, 1248-1254 (2015)

[2] J. M. Ball, A. Petrozza, *Nat. Energy* **1**, 1-13 (2016)

[3] H. Oga, A. Saeki, Y. Ogomi, S. Hayase, S. Seki, *J. Am. Chem. Soc* **136**, 13818-13825 (2014)

[4] Q. Jiang, Y. Zhao, X. Zhang, X. Yang, Y. Chen, Z. Chu, Q. Ye, X. Li, Z. Yin, J. You, *Nat. Photon.* **13**, 460-466 (2019)

7.5 Slot-die printing of the active layer of water-based hybrid solar cell followed with *in situ* GIWAXS

V. Körstgens, L. Diaz Piola, K. Stallhofer[1], M. Nuber[1], M. Schwartzkopf[2], H. Iglev[1],
R. Kienberger[1], S. V. Roth[2], P. Müller-Buschbaum

[1] LS Laser- und Röntgenphysik, TUM, Garching, Germany
[2] DESY, Hamburg, Germany

In new generation photovoltaics, not only high efficiencies and long-term stability are relevant, but also the sustainability of the overall production process. For an ultimately environmentally friendly pathway, water would be the processing solvent of choice. We produce the active layers for hybrid solar cells containing titanium dioxide (TiO_2) nanoparticles treated by laser ablation, mixed with the water-soluble donor polymer poly[3-(potassium-6-hexanoate)thiophene-2,5-diyl (P3P6T) [1, 2]. We investigate the *in situ* drying kinetics in a slot-die printing process with a home-built printer suitable for X-ray scattering experiments at large scale facilities [3]. Conjugated semiconducting polymers such as P3P6T are semicrystalline in nature, showing crystalline and amorphous domains. The conductivity in crystalline phases is much higher compared to that of amorphous phases, and therefore the study of the degree of crystallinity, the size of crystal areas and the orientation of the crystallites is of fundamental importance. Grazing-incidence wide-angle X-ray scattering (GIWAXS) serves as a powerful tool to extract information about the crystalline regions of the probed thin film and it is especially suited for kinetic investigations.

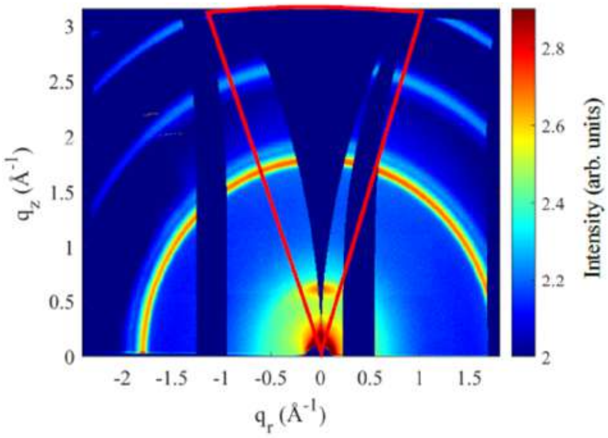

Figure 7.12:
Exemplary vertical azimuthal sector integral for GIWAXS measurements on the active layer TiO_2:P3P6T (1:1) on a glass substrate. Debye-Scherrer-like rings correspond to the TiO_2 reflections, while the intensity spot around $(q_r,q_z) = (0, 0.6)\ ^{-1}$ originates from P3P6T.

In Fig. 7.12 an exemplary *ex situ* GIWAXS measurement of a printed hybrid film is shown after complete drying. The time evolution covering the *in situ* process is illustrated in Fig. 7.13, and it summarizes the most important features of the experiment. The region around $q = 0.5 - 0.7^{-1}$ corresponds to the polymer crystalline (100) planes and the growth of the peak is observed as time evolves. This value emerges from the structure factor of water, which quantifies of the average separation distance of water molecules.

The solid lines indicate the literature values of anatase and rutile titania reflections. The most interesting feature in Fig. 7.13 is the dynamics of the polymer crystallinity. The crystallite sizes obtained through the Scherrer equation together with the lattice constant evolution for P3P6T is shown in Fig. 7.13. For stage I, since the polymer is completely dissolved, these values are not defined. For the crystallite size D, a rapid growth from $D \approx 2$ nm to $D \approx 5$ nm is observed in stage II, which slowly plateaus thereafter during stage III. At stage IV, a steady growth is seen during the dry state.

To ensure that no significant evolution in the film takes place after the end of the *in situ* measurement, the sample is measured *ex situ* a few minutes after deposition, and it is indeed observed that the final crystalline state of the polymer is reached. The final obtained crystallite size is $D = 5.83 \pm 0.07$ nm, which is in good agreement with previous experiments for systems using TiO_2:P3P6T [2].

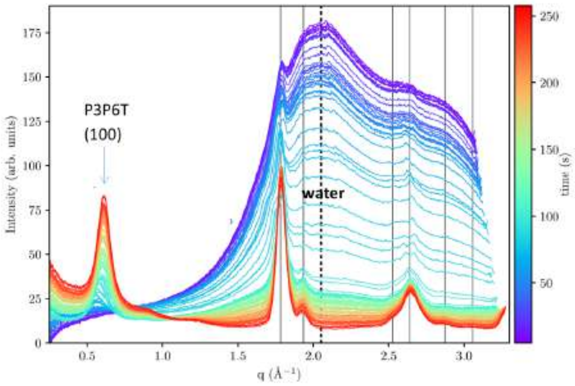

Figure 7.13:
GIWAXS vertical sector plot intensity as a function of the total scattering vector q for the time sequence during the drying process. The dashed line indicates the intensity peak of water and the solid lines the anatase and rutile phases of titania nanoparticles. The Bragg peak for the P3P6T polymer is marked with an arrow.

With respect to the lattice constant parameter, a rapid decrease is observed in stages II and III, which is slowed down in stage IV and plateaus to its final value. Again, no significant differences are observed in the *ex situ* measurement. The overall change in lattice constant goes from $k \approx 11.7$ to $k \approx 10.3$. Remarkably, this difference is in good agreement with the length scales of water molecule sizes.

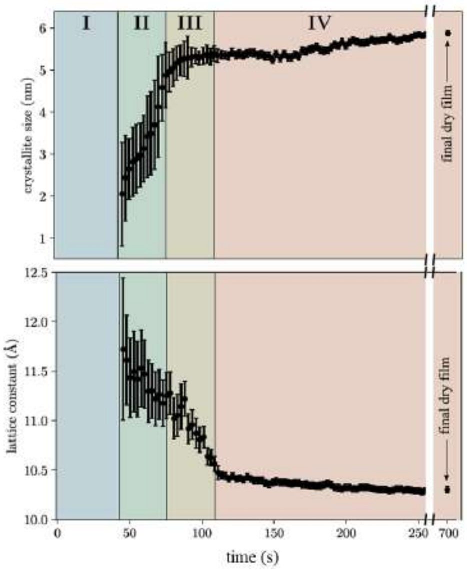

Figure 7.14:
a) Crystallite size and b) lattice constant of P3P6T during the drying of the active layer obtained by Scherrer analysis. The colored regions represent the different drying stages. In stage I no polymers crystals are formed and crystal-related values are not defined. Starting at stage II, polymer crystals start to form and grow rapidly, while their lattice constant k decreases. Thereafter, a moderate growth is seen in stage III, where the lattice constant decreases at the same rate. At stage IV, both values plateau towards the final state.

In summary, the *in situ* GIWAXS experiment sets up a consistent basis to clearly identify stages during the drying process within the compared parameters, namely the intensity of the (100) peak of P3P6T and water, the average crystallite size and the lattice constant of the polymer. A full picture of the drying process is obtained when the results of the corresponding *in situ* GISAXS experiment is taken into account.

[1] V. Körstgens, S. Pröller, T. Buchmann, D. Mosegui Gonzalez, L. Song, Y. Yao, W. Wang, J. Werhahn, G. Santoro, S. V. Roth, H. Iglev, R. Kienberger, P. Müller-Buschbaum, *Nanoscale* **7**, 2900 (2015)

[2] K. Stallhofer, M. Nuber, R. Kienberger, V. Körstgens, P. Müller-Buschbaum, H. Iglev*J. Phys. Chem. C* **123**, 28100 (2019)

[3] K. S. Wienhold, V. Körstgens, S. Grott, X. Jiang, M. Schwartzkopf, S. V. Roth, P. Müller-Buschbaum, *ACS Appl. Mater. Interfaces* **11**, 42313 (2019)

7.6 Superlattice deformation in PbS quantum dot films: *In situ* GISAXS study on the unit cell phase transition by uniaxial strain

J. E. Heger, K. Schneider[1], M. Schwartzkopf[2], S. V. Roth[2], P. Müller-Buschbaum

[1] IPF, Dresden, Germany
[2] DESY, Hamburg, Germany

Colloidal quantum dots (CQD) are crystals in the range of several nanometers that can be considered as artificial atoms, since they feature strong quantum confinement in all three dimensions. Different CQD sizes result in varying confinement strengths and hence modified energy states. This reflects in tunable optoelectronic properties, such as a controlled absorbance spectrum, that make CQDs promising candidates for next-generation solar cells. Surface attached ligands make the crystals soluble in a large numbers of solvents and hence solution-processible with industrially-relevant techniques, such as spray-coating and printing. When deposited to a thin film, CQDs are known to form highly ordered arrangements within superlattices. With an increasing inter-dot distance of neighboring CQDs, the coupling becomes stronger and electronic states start to form band structures [1]. Moreover, CQDs on flexible substrates change their optoelectronic properties upon applying strain [2]. Especially when it comes to real-world applications such as solar cells on flexible substrates, changes in the inter-dot distance by strain must be further understood and correlated to the performance. In this work, we investigate the superlattice deformation by uniaxial strain in lead sulfide (PbS) CQD films with *in situ* grazing-incidence small-angle X-ray scattering (GISAXS). For studying the morphology of thin films, GISAXS is a powerful tool that allows probing a high sample volume despite the thin film thickness, which is typically in the range of tens to hundreds of nanometers. However, GISAXS requires a precise sample alignment with respect to the X-ray beam, which is challenging to control on flexible substrates exposed to uniaxial strain. For this reason, we used a custom-built sample holder based on four cylinders. The cylinders guide the sample during stretching and provide a stable sample alignment during the experiment. The PbS film is deposited on a flexible substrate and clamped into the sample holder. Stepping motors stretch the PbS film perpendicular to the X-ray beam. With this set-up, a deformation up to 30% of the initial sample length in 5% steps is achieved.

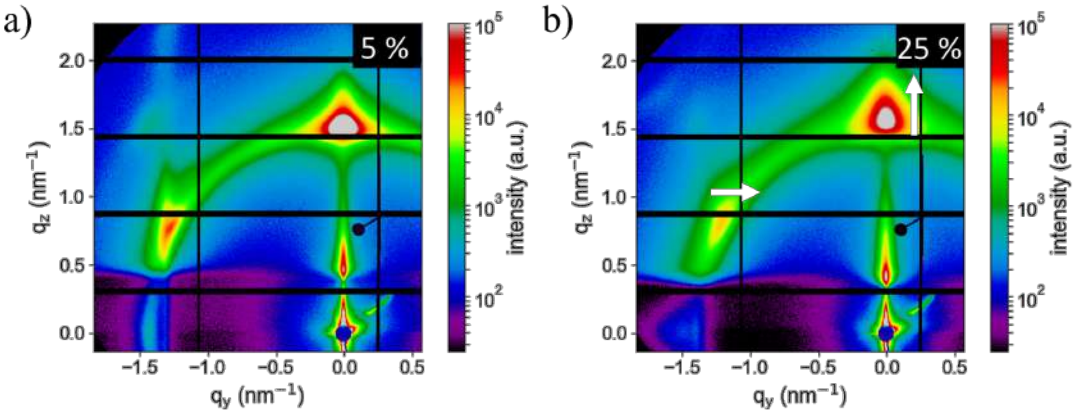

Figure 7.15:
2D GISAXS detector images taken at a uniaxial strain of a) 5% and b) 25%. As uniaxial strain increases, the superlatice reflexes shift towards lower q_y and higher q_z, respectively, as indicated with white arrows.

The 2D GISAXS data for 5% strain and 25% is shown in Fig. 7.15. The ring-shaped intensity distribution with two prominent reflexes results from the PbS superlattice. For the applied strain of 5% in Fig. 7.15a, the reflexes result from face- and body-centered cubic (FCC-BCC) unit cells. This nested FCC-BCC structure is known from our earlier work on PbS QD films [3]. In Fig. 7.15b, the reflexes of the sample stretched to 25% are shifted towards lower q_y and higher q_z values, respectively, as compared to the state at 5% strain in Fig. 7.15a. These shifts indicate expansion and contraction along different unit cell axes, respectively, and hence a transition in unit cell symmetry from cubic to tetragonal (BCT). We calculate the unit cell lattice constants a, b, and c from the q-positions of the two prominent reflexes. The condition a = b = c holds for the cubic phase, whereas a = b $\neq$ c holds for the tetragonal phase. The aspect ratio $\frac{a}{c}$ is shown in Fig. 7.16.

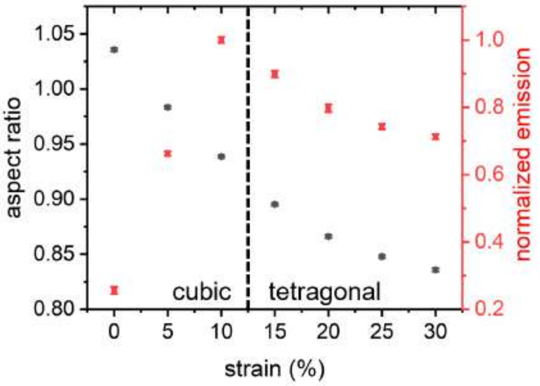

Figure 7.16:
Aspect ratio $\frac{a}{c}$ of lattice constants a and c decreases with applied strain. Normalized photoluminescence emission features a strong increase, followed by a breakdown after 10% strain. This data is related to the reduced optoelectronic couplings after the phase transition, depicted as dashed line.

Indeed, the ratio shifts towards values below 1, which indicates a phase transition with applied strain. Interestingly, the aspect ratio is larger than 1 for the relaxed state, speaking for a slight off-cubic phase already before any strain is applied. With increasing the strain to 5%, the aspect ratio crosses the cubic phase line. After applying a strain of 10%, the aspect ratio deviates more from the cubic phase line than in the relaxed state. Hence, we see a phase transition from BCT-poor to BCT-rich phase after 10% of applied strain. A similar shift in unit cell symmetry was observed for PbS QD films cooled down from room temperature to 100 K [4]. The comparison to our work suggests that strain has a similar impact on the superlattice deformation as temperature. We compare the *in situ* GISAXS results to photoluminescence measurements at the same strain values. Fig. 7.16 shows the maximum intensity of the photoluminescence emission as a function of strain. The evolution is close to the findings in the literature, showing rising intensity and a breakdown beyond a certain strain threshold [2]. As this breakdown appears after 10%, we identify this threshold to be the cubic-tetragonal phase transition. The unit cell changes from higher to lower density and hence the optoelectronic coupling between nearest neighbors weakens. With these results, we aim to contribute to a more complete picture of CQD superlattice films and their optoelectronic performance.

[1] C. R. Kagan, C. B. Murray, *Nat. Nanotechnol.* **10**, 1013-1026 (2015)

[2] Y. Gong, J. Shen, Y. Zhu, X. Yang, L. Zhang, C. Li, *J. Mater. Chem. C* **8**, 1413 (2020)

[3] W. Chen, H. Tang, Y. Chen, J. E. Heger, N. Li, L. P. Kreuzer, Y. Xie, D. Li, C. Anthony, Z. Pikramenou, K. W. Ng, X. W. Sun, K. Wang P. Müller-Buschbaum, *Nano Energy* **78**, 105254 (2020)

[4] S. W. Winslow, D.-M. Smilgies, J. W. Swan, W. A. Tisdale, *J. Phys. Chem. C* **124**, 13456-13466 (2020)

7.7 *In situ* printing kinetics and active layer morphology of non-fullerene organic solar cells

K. Luo, X. Jiang, S. V. Roth[1], P. Müller-Buschbaum

[1] DESY, Hamburg, Germany

The performance of organic solar cells (OSC) has been improved significantly in recent decades with the progress on synthesis of novel conductive molecules and on photovoltaic device structures. Currently to achieve the upper limit of photoelectric conversion efficiency, a widely used fabricating method of the active layer is spin-coating in inert conditions [1], which limits mass production and future broad application in industry. Compared with spin-coating, the slot-die coating method produces relatively lower efficiency devices but has advantages such as pre-metered thickness and speed control, scalability of coating areas and roll-to-roll compatibility. In order to optimize the performance of slot-die coated OSCs, the knowledge of printing kinetics and the film-formation process still needs further study. In this work, the relation between the roughness of the active layer and the device performance are discussed. Moreover, to learn about the crystallization kinetics of the active layer during the print process, *in situ* GIWAXS measurements were performed at the P03 beamline (DESY, Germany).

The non-fullerene materials selected in this work to fabricate the active layer of the photovoltaic device were the polymer donor D18 and small molecule acceptors IT-4F, ITIC-DCl, and a newly synthesized acceptor M3 [2]. The active layers were printed onto glass substrates out of chloroform, in which all materials have a good solubility and form neat films. To get a closer view of the film surface topography, atomic force microscopy(AFM) measurements were performed, as shown in Fig. 7.17a-c. Fibrous features of the donor-acceptor mixture are clearly seen. The root-mean-square (RMS) roughness values of the blend films D18: IT-4F, D18: ITIC-DCl and D18: M3, are 2.78 nm, 3.17 nm and 1.90 nm respectively. The D18: ITIC-DCl film shows a slightly lower organization. The corresponding devices shown in Fig. 7.17d performed better (PCE = 13.4%) compared to the two other types of active layers (11.4% for D18: IT4F and 10.9% for D18: M3).

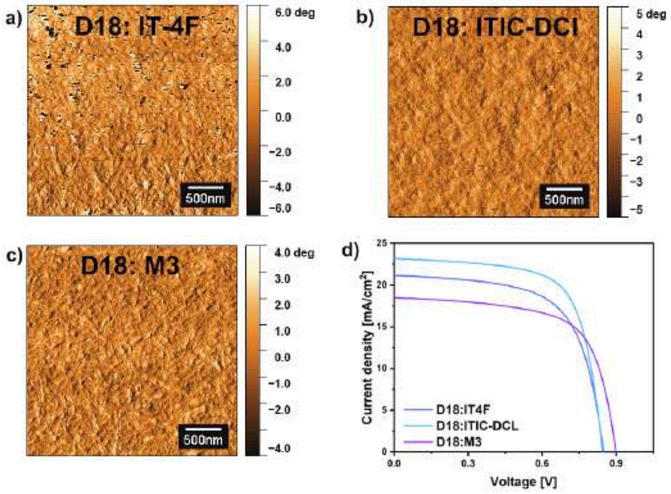

Figure 7.17:
AFM topography of printed blend films a) D18: IT-4F, b) D18: ITIC-DCl and c) D18: M3 and d) the corresponding I-V characteristic of OSC devices fabricated with these three types of active layers.

The 2D GIWAXS data of the final dry active layers of the D18:ITDCL, D18: IT4F, D18:M3, shown in Fig. 7.18a, suggest the presence of a pronounced face-on structure of the active layer in all printed films. To get a deeper understanding of the structure formation of the active layer during printing, the *in situ* out-of-plane cake cuts of the GIWAXS data are shown in Fig. 7.18b.

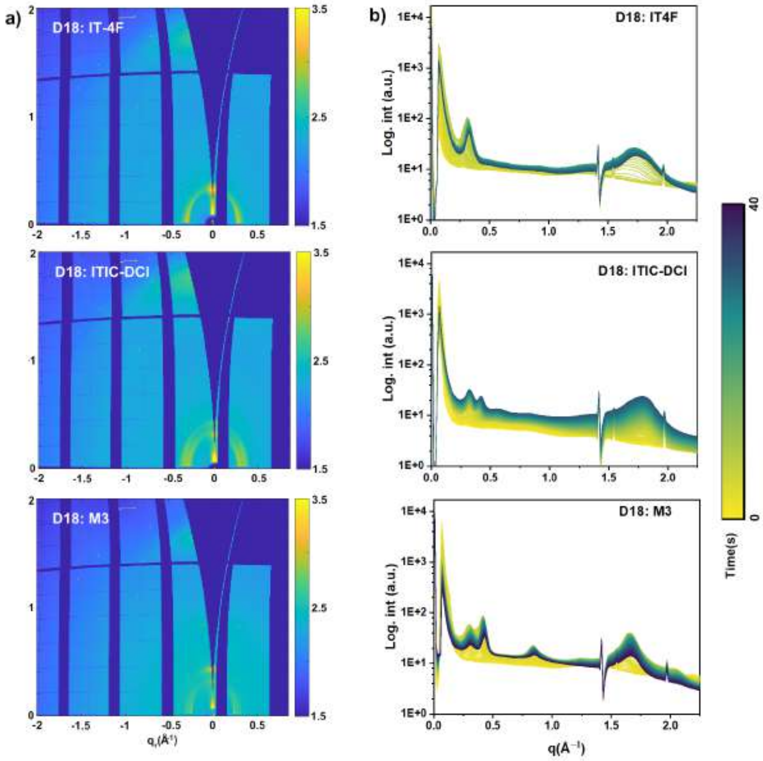

Figure 7.18:
a) 2D GIWAXS data of the active layer blend films D18: IT-4F, D18: ITIC-DCl and D18: M3 at the final dry statess. b) Cake cuts of the *in situ* printing GIWAXS data of the mixtures D18: IT-4F, D18: ITIC-DCl and D18: M3 in the out-of-plane direction.

The underlying kinetics are followed during solvent evaporation, where polymer molecules concentration increase and aggregation occurs. In the 2D GIWAXS data, a strongly pronounced (010) peak in the out-of-plane direction results from the π-π stacking, which was not present at the very beginning of the printing process. This temporal evolution reveals information about the crystallization onset. The cake cuts of reshaped 2D GIWAXS data allow to identify the accurate q-space location of the (010) diffraction peaks. In the case of D18: IT-4F, a peak was observed at q = 1.73 $^{-1}$, for D18: ITIC-DCl at q = 1.79 $^{-1}$ and for D18: M3 at q = 1.68 $^{-1}$. This difference in peak positions indicates that the π-π interaction between the electron donor-acceptor pairs is affected by the structure of the different acceptors. Furthermore, the GIWAXS measurements reveal the predominant crystal orientations, which could be extracted by tube cuts from the 2D GIWAXS data. The diffraction intensity in the in-plane direction represents the face-on structure and in the out-of-plane direction the edge-on structure. The analysis of the structure of active layer is an important step towards further optimization of printing techniques.

[1] Q. Liu, Y. Jiang, K. Jin, J. Qin, J. Xu, W. Li, J. Xiong, J. Liu, Z. Xiao, K. Sun, S. Yang, X. Zhang, L. Ding, *Sci. Bull.* **65**, 272-275 (2020)

[2] Y. Ma, M. Zhang, S. Wan, P. Yin, P. Wang, D. Cai, F. Liu, Q. Zheng, *Joule* **5**, 197-209 (2021)

7.8 Tailoring the optical properties of sputter-deposited gold nanostructures on nanostructured titanium dioxide templates based on *in situ* grazing-incidence small-angle X-ray scattering determined growth laws

S. Liang, W. Chen, S. Yin, S. J. Schaper, R. Guo, J. Drewes[1], N. Carstens[1], T. Strunskus[1], F. Faupel[1], M. Gensch[2], M. Schwartzkopf[2], S. V. Roth[2,3], Y.-J. Cheng[4], P. Müller-Buschbaum

[1] CAU, Kiel, Germany
[2] DESY, Hamburg, Germany
[3] KTH, Stockholm, Sweden
[4] NIMTE, CAS, Ningbo, China

In recent years, gold/titanium dioxide (Au/TiO_2) nanohybrid materials have attracted significant attention due to their enhanced optical, photocatalytic, and photovoltaic performance [1]. In this work, we fabricated Au/TiO_2 hybrid thin films *via* sputter deposition by using porous, reticular, and compact TiO_2 thin-film substrates as templates [2]. Due to the complex surface structures of the TiO_2 templates, it is important and necessary to investigate the kinetics of the sputter-deposited Au growth on the TiO_2 templates to tailor the morphology of the Au/TiO_2 nanohybrid thin films based on a fundamental understanding of the growth process. *In situ* grazing-incidence small-angle X-ray scattering (GISAXS) during sputter deposition has demonstrated to be a powerful tool to probe the growth kinetics and morphologies of as-deposited metallic thin films or nanostructures at interfaces [3]. Therefore, the growth processes of sputter-deposited Au on the different TiO_2 templates are observed in real time with *in situ* GISAXS.

The growth processes of sputter-deposited Au on different TiO_2 templates are analyzed based on the *in situ* GISAXS data. As shown in Fig. 7.19, the horizontal *I*(q_y) line cuts are taken along an integrated q_z region (0.59 nm^{-1} < q_z < 0.63 nm^{-1}) at different effective Au thicknesses. The horizontal line cuts are modeled within the framework of the distorted-wave Born approximation (DWBA) using the local monodisperse approximation and assumption of a 1D paracrystal arrangement of cylindrically shaped scattering objects. For the porous TiO_2 template (Fig. 7.19a), the pseudo-Bragg peak (peak I) and a visible second-order peak (peak II) originate from the well-ordered porous structure of the TiO_2 film. With ongoing sputter deposition, a peak H1 emerges and gradually shifts toward smaller q_y values, indicating the

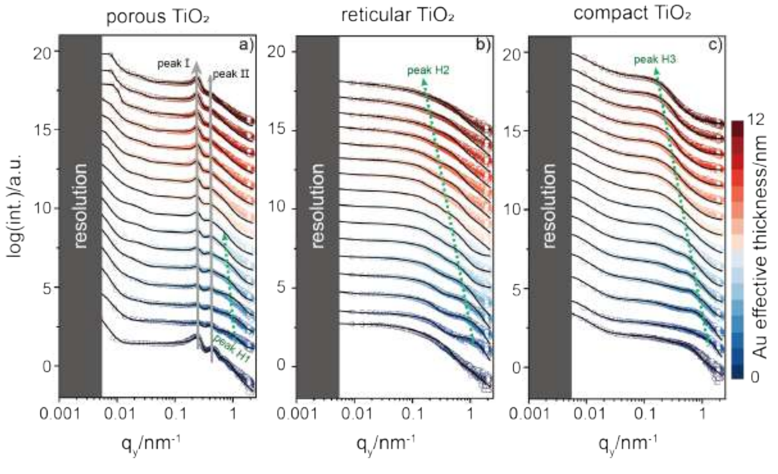

Figure 7.19:
Selected horizontal line cuts from 2D GISAXS data (circles) of Au sputter deposition on a) porous TiO_2, b) reticular TiO_2, and c) compact TiO_2 templates and corresponding model results (black lines).

formation of small Au clusters and the increased interstructural distance of the Au clusters due to the diffusion-mediated coalescence of the clusters and adsorption-mediated cluster growth. For the reticular TiO_2 template (Fig. 7.19b), a different Au growth behavior is observed. The peak H2 emerges at a high q_y value and shifts toward a low q_y value, which is related to the diffusion-mediated coalescence process and adsorption-mediated growth of Au clusters. Compared to the porous TiO_2 template, the reticular TiO_2 template has a larger-scale surface structure landscape, which leads to a weaker templating effect for the Au cluster growth on the nanoscale local areas. In the case of the sputter deposition on the compact TiO_2 template sample (Fig. 7.19c), the peak H3 also appears at a high q_y value. However, the low-q_y shift of peak H3 is faster compared to the corresponding processes on the other two templates. This behavior can be attributed to the absence of dominating lateral nanostructures of the compact template surface, which leads to deposited Au clusters growing uniformly and rapidly interconnecting with each other along the lateral direction [2].

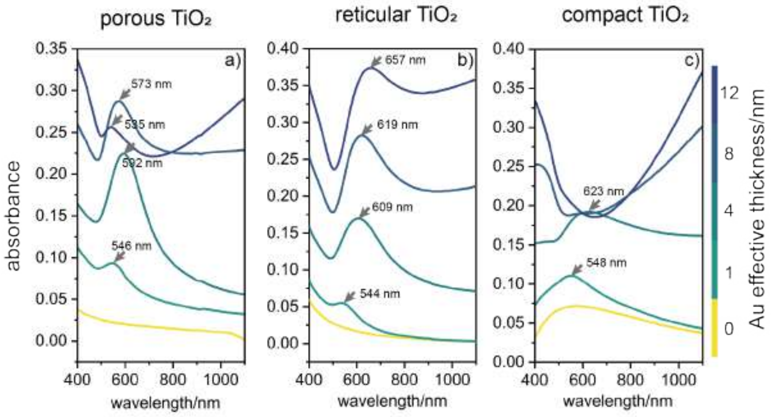

Figure 7.20:
Vis-NIR spectra of sputter-deposited Au/TiO_2 hybrid thin films with different TiO_2 templates: a) porous TiO_2, b) reticular TiO_2, and c) compact TiO_2 templates, with the different Au effective thicknesses of 0, 1, 4, 8, and 12 nm.

The vis-NIR spectra of the selected sputter-deposited Au/TiO_2 hybrid thin films on different TiO_2 templates are measured at the different Au effective thicknesses of 0, 1, 4, 8, and 12 nm, as presented in Fig. 7.20. For the porous and reticular TiO_2 templates, the localized surface plasmon resonance (LSPR) peaks are clearly observed due to the deposited Au nanostructures grown along with the nanostructured TiO_2 templates. With increasing Au effective thickness, the LSPR peaks shift toward red-light region before the Au effective thickness reaches 4 nm, which is ascribed to the size growth and shape variation of the sputter-deposited Au nanoparticles. In the case of the compact TiO_2 template, the LSPR peak around 600 nm disappears when the Au effective thickness is about 8 nm, indicating the disappearance of separated Au clusters and the formation of compact Au regions.

[1] H. Wang, T. You, W. Shi, J. Li, L. Guo, *J. Phys. Chem. C* **116**, 6490 (2012)

[2] S. Liang, W. Chen, S. Yin, S. J. Schaper, R. Guo, J. Drewes, N. Carstens, T. Strunskus, F. Faupel, M. Gensch, M. Schwartzkopf, S. V. Roth, Y.-J. Cheng, P. Müller-Buschbaum, *ACS Appl. Mater. Interfaces* **13**, 14728 (2021)

[3] M. Schwartzkopf, A. Hinz, O. Polonskyi, T. Strunskus, F. C. Löhrer, V. Körstgens, P. Müller-Buschbaum, F. Faupel, S. V. Roth, *ACS Appl. Mater. Interfaces* **9**, 5629 (2017)

7.9 Investigation of the selective wetting of noble metals on PLA-*b*-P3HT

M. Gensch[1], P. Müller-Buschbaum, S. V. Roth[1,2]

[1] DESY, Hamburg, Germany

[2] KTH, Stockholm, Sweden

Metal-polymer thin-films with nanostructure formation either of the metal or the polymer demonstrate great perspectives for optoelectronic applications, e.g. as sensors [1] or organic photovoltaics (OPV) [2]. The nanostructure of both highly influences the performance of these thin-film devices. We use a diblock copolymer thin-film with a conjugated block and apply solvent vapor annealing to the copolymer to form a controlled lamellar structure with a distinct domain spacing of around L_D = (15 ± 1) nm [3]. The nanostructure is realized for a film thickness of t = 137 nm, close to the film thickness which is usually used in OPV applications. The selective decoration of different electrode materials e.g. Au and Ag are investigated on the diblock copolymer PLA-*b*-P3HT with nanostructured morphology. A previous work by Löhrer *et al.* investigated the Au deposition on conjugated polymers and revealed a small difference in the Au growth by changing the polymer properties [4]. The influence of a more reactive metal was shown in our publication about Ag growth on a conjugated diblock copolymer [5]. The copolymer is spin-coated on a silicon wafer and the metal is deposited on the copolymer with a common technique to prepare these nanocomposites of metal/polymer films in the nanometer range, namely by applying a subsequent sputter deposition to create a thin metal film. During sputter deposition, the interfacial morphology of the growing films are investigated by grazing-incidence small-angle X-ray scattering (GISAXS) to obtain information about the lateral arrangement of the metal clusters on the polymer template and the selective decoration on the copolymer domains [5,6]. The GISAXS measurements were accomplished for an X-ray photon energy of 11.8 keV and an incident angle of α_i= 0.4°. The distance from the sample to the detector (SDD) was set to SDD = 2447 mm. A Pilatus 300k detector with a pixel size of 172×172 μm^2 was used. Fig. 7.21 shows GISAXS data of PLA-*b*-P3HT with the

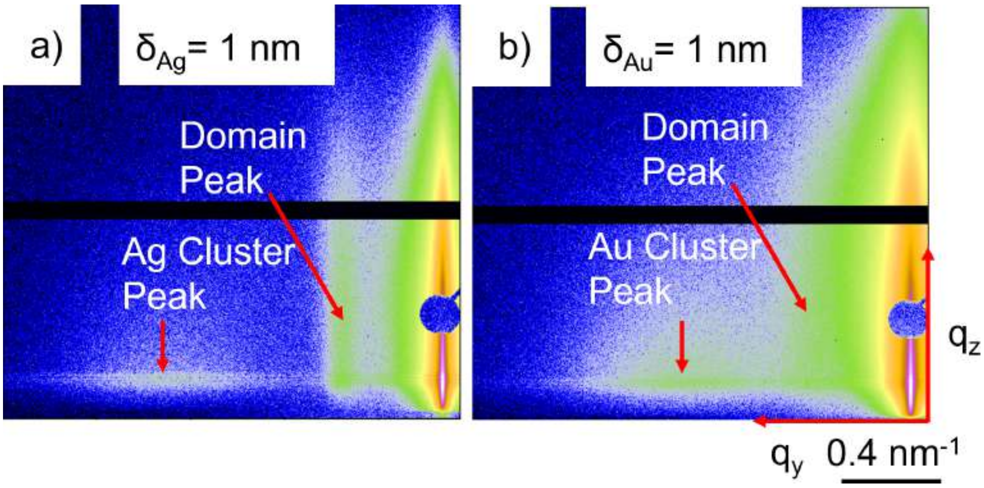

Figure 7.21:
GISAXS data of the PLA-*b*-P3HT copolymer thin film with a) δ_{Ag} = 1 nm and b) δ_{Au} = 1 nm. The domain peak and the cluster peak are marked with arrows. The domain peak with Ag deposition is clearly visible, while the domain peak with Au deposition is more smeared out.

sputter-deposited thickness of $\delta_{Au,Ag}$ = 1 nm. The images show the copolymer domain peak and the metal cluster peaks of Au and Ag. The cluster peaks of Au and Ag are located at different q_y values, which indicate to a bigger cluster size grown for Au compared to a smaller growth of Ag clusters. In Fig. 7.22, the contour plots of the lateral cuts (Yoneda cuts) from the *in situ* GISAXS measurements during sputter deposition on PLA-*b*-P3HT with Au and Ag are compared. The cluster size evolution, illustrated by a red arrow for Au, seems to grow faster to bigger Au clusters compared to Ag on the same copolymer template. The domain peak indicated by the black arrow is visible for a longer time for the Ag contour plot compared to Au and therefore the selective wetting for Ag seems to be much higher. This could be related to the high affinity of Ag to sulfur in the P3HT domain as we reported in a previous publication [5].

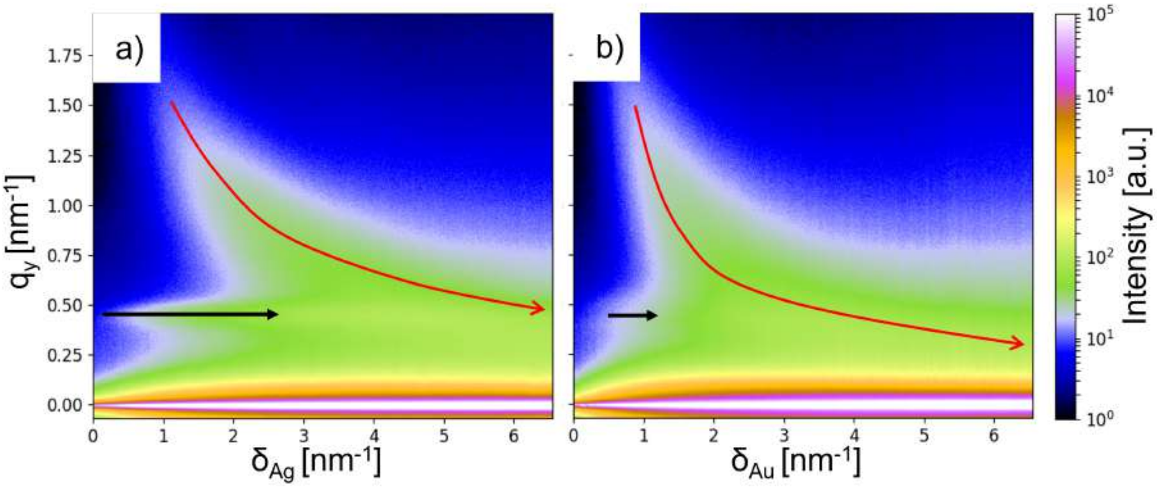

Figure 7.22:
Comparison of the contour plots of the Yoneda cuts from the *in situ* GISAXS data during sputter deposition on PLA-*b*-P3HT as a function of the effective a) Ag and b) Au thickness. The domain peak is shown by a black arrow and the cluster peak is indicated by a red arrow.

[1] F. Faupel, V. Zaporojtchenko, T. Strunskus, M. Elbahri, *Adv. Eng. Mater.* **12**, 1117−1190 (2010)

[2] G. Kaune, M. A. Ruderer, E. Metwalli, W. Wang, S. Couet, K. Schlage, R. Röhlsberger, S. V. Roth, P. Müller-Buschbaum, *ACS Appl. Mater. Interfaces* **1**, 353−360 (2009)

[3] I. Botiz, S. B. Darling, *Macromolecules* **42**, 8211−8217 (2009)

[4] F. C. Löhrer, V. Körstgens, G. Semino, M. Schwartzkopf, A. Hinz, O. Polonskyi, T. Strunskus, F. Faupel, S. V. Roth, P. Müller-Buschbaum, *ACS Appl. Mater. Interfaces* **12**, 1132−1141 (2020)

[5] M. Gensch, M. Schwartzkopf, C. J. Brett, S. J. Schaper, L. P. Kreuzer, N. Li, W. Chen, S. Liang, J. Drewes, O. Polonskyi, T. Strunskus, F. Faupel, P. Müller-Buschbaum, S. V. Roth, *ACS Appl. Nano Mater.* **4**, 4245−4255 (2021)

[6] M. Schwartzkopf, G. Santoro, C. J. Brett, A. Rothkirch, O. Polonskyi, A. Hinz, E. Metwalli, Y. Yao, T. Strunskus, F. Faupel, P. Müller-Buschbaum, S. V. Roth, *ACS Appl. Mater. Interfaces* **7**, 13547−13556 (2015)

7.10 Disintegration of mesoglobules in aqueous PNIPAM solutions following a pressure jump

B.-J. Niebuur, L. Chiappisi[1], A. Schulte[2], C. M. Papadakis

[1] ILL, Grenoble, France
[2] University of Central Florida, Orlando, U.S.A.

Naturally occurring and man-made assemblies of nanostructures from (bio)macromolecules are ubiquitous. The disintegration mechanisms and their kinetics are of importance for applications, such as the separation of polymer blends and the disintegration of microplastics in living systems. Here, we address the fundamental mechanisms that are involved in the disintegration of polymeric nanoparticles [1]. In contrast to particles composed of small molecules or atoms, the disintegration of polymeric particles is more complex, in that not only diffusion, but also disentanglement processes are vital. It was observed that, as solvent diffuses into the polymer grain, a swollen polymer layer forms at the particle surface and grows. From the swollen layer, the polymers disentangle and become solvated. The swelling process is driven by the osmotic pressure of the solvent and by its gel permeability.

Aqueous dispersions of mesoglobules formed by the thermoresponsive polymer poly(*N*-isopropylacrylamide) (PNIPAM) may serve as a model system to investigate the effect of the osmotic pressure of the solvent on the disintegration of polymeric nanoparticles. In aqueous solution, PNIPAM features lower critical solution temperature (LCST) behavior with an LCST of ca. 32 °C. Upon heating through the cloud point, the chains collapse and form mesoglobules, i.e. long-lived aggregates having mesoscopic sizes. The coexistence line of PNIPAM solutions may not only be traversed by a change in temperature, but also by changing pressure. Rapid pressure changes on the millisecond timescale enable the study of the early stages of mesoglobule disintegration. Moreover, varying the target pressure allows to alter the osmotic pressure of the solvent inside the mesoglobules. Kinetic small-angle neutron scattering (SANS) offers the possibility to track particle disintegration with excellent spatial and temporal resolution and over large time and length scales.

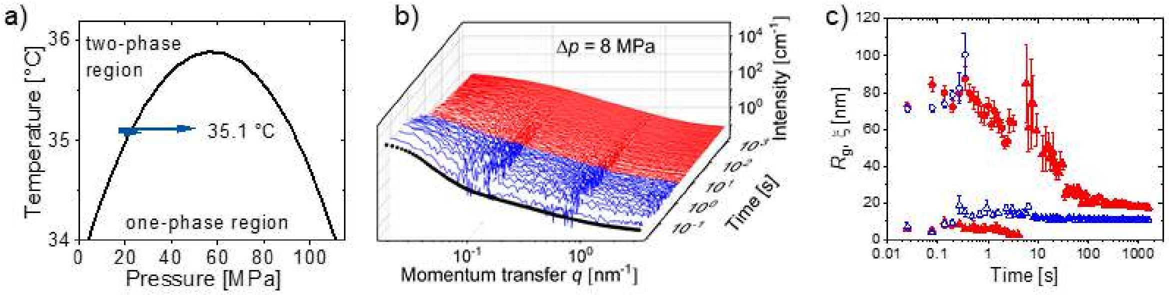

Figure 7.23:
(a) Experimental scheme. Black line: coexistence line. Blue arrows: shallow jump to 25 MPa and deep jump to 48 MPa. (b) SANS curves for the target pressure of 25 MPa in dependence on time. Black: pre-jump curve. Blue and read: early and late times. (c) Resulting R_g of the mesoglobules and correlation length ξ. Closed red symbols: target pressure 25 MPa, open blue symbols: 48 MPa. Circles: R_g, triangles: ξ.

PNIPAM was dissolved in D_2O at a polymer concentration of 3 wt%. Kinetic SANS experiments were performed at the instrument D11 at the Institut Laue-Langevin (ILL), using neutrons of a wavelength of 0.6 nm and sample-detector distances of 1.5, 8.0 and 34.0 m. The isothermal pressure jumps were started at 35.1 °C and 17 MPa in the two-phase region (where mesoglobules are present) and reached across the coexistence line to various target pressures in the one-phase region (where a polymer solution is formed, Fig. 7.23a). The pressure jumps were performed within 0.025 s by rapidly opening a pneumatically driven valve, which also triggered the start of the SANS data acquisition, resulting in a time resolution of 0.05 s (Fig. 7.23b).

In the initial state, a shoulder is observed at momentum transfers $q < 0.1$ nm^{-1}, which is due to scattering from mesoglobules, and a decay at higher q-values, reflecting the inhomogeneities inside. The data are modeled with an Ornstein-Zernike structure factor, describing the local inhomogeneities, and a Guinier-Porod form factor to describe the scattering of the mesoglobules. The radius of gyration of the mesoglobules and the correlation length are found at $R_g = 72$ nm and $\xi = 7$ nm.

After the shallow pressure jump to 25 MPa, the mesoglobule scattering weakens during the first few seconds, and finally, scattering characteristic of a polymer solution is observed (Fig. 7.23b). R_g increases slightly from 72 to 87 nm, pointing to the swelling of the outermost layer of the mesoglobules, in line with theoretical predictions (Fig. 7.23c). After 0.35 s, R_g decreases to 60 nm, which indicates the release of polymers into the solution. After 3.5 s, a single length scale ξ is sufficient to describe the scattering, and it continues to decrease, until it becomes constant at 18 nm after 30 s, i.e., the solution becomes homogeneous, and the released polymers increasingly dominate the scattering. Thus, for the shallow jump, we observe predominantly the release of polymers from this layer (Fig. 7.24a). In contrast, for the deep jump to 48 MPa, R_g increases strongly from the initial value of 76 nm to 105 nm after 0.35 s and increases further above the resolution of the setup. Meanwhile, ξ increases from 4 to 19 nm and remains rather constant afterwards. Thus, the disintegration proceeds via the diffusion of water into the mesoglobules, which makes them swell (Fig. 7.24b). This swelling process continues, until a homogeneous semi-dilute solution is obtained.

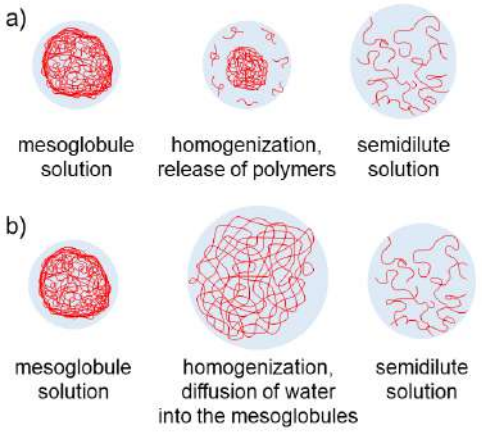

Figure 7.24:
Schematic representation of the pathways of mesoglobule disintegration after a shallow (top) and a deep (bottom) pressure jump.

To conclude, the structural changes during the disintegration of polymeric nanoparticles are investigated with unprecedented temporal resolution (0.05 s) and over a large range of length scales (1-100 nm). These results are of key importance for the tuning of the switching process in applications of responsive polymers for transport and release purposes.

[1] B.-J. Niebuur, L. Chiappisi, F. A. Jung, X. Zhang, A. Schulte, C. M. Papadakis, *RSC Nanoscale* **13**, 13421-13426 (2021)

7.11 Pathways of micelle collapse and disintegration of PMMA-*b*-PNIPAM block copolymers in aqueous solution

P. Álvarez Herrera, C. Henschel[1], L. Chiappisi[2], A. Schulte[3], A. Laschewsky[1] and C. M. Papadakis

[1] Fraunhofer IAP, Potsdam-Golm, Germany
[2] ILL, Grenoble, France
[3] University of Central Florida, Orlando, U.S.A

Block copolymers consisting of a permanently hydrophobic and a thermo-responsive block can self-assemble into different morphologies. Poly(methyl methacrylate)-*b*-poly(N-isopropylacrylamide) (PMMA-*b*-PNIPAM) forms spherical micelles in aqueous solution, characterized by a PMMA core and a hydrated PNIPAM shell. The micellar shell dehydrates, and the collapsed micelles form aggregates when heating above its cloud point T_{cp} at atmospheric pressure [1]. Moreover, the collapse of the micelles and their posterior agglomeration can be caused not only by increasing the temperature, but also by changing the pressure. Pressure is known to affect the hydration and mesoglobule formation of PNIPAM homopolymers. The PNIPAM polymers dehydrate and form small mesoglobules at atmospheric pressure, while they remain partially hydrated and form large aggregates at higher pressures [2]. Although the effect of pressure on the collapse and aggregation of PNIPAM homopolymers has been widely studied, there are not similar studies on amphiphilic block copolymers.

In this study, we investigate the temporal evolution of the micellar structure of PMMA_{23}-*b*-PNIPAM_{480} in aqueous solution after a fast change of pressure. We aim to describe the collapse and aggregation of the micelles after decreasing the pressure from the 1-phase to the 2-phase region at 33 °C. The disintegration of the aggregates and swelling of the micelles is also investigated by changing the pressure in the opposite direction at the same temperature. Beforehand, we determined the phase diagram of PMMA_{23}-*b*-PNIPAM_{480} in aqueous solution by turbidimetry. The micellar structure is characterized by kinetic small-angle neutron scattering (SANS). The rapid pressure change is triggered by opening a pneumatic valve located between the sample and a pressure reservoir, which is pressurized to the desired initial pressure. The opening of the valve activates automatically the acquisition of the data. In total, 85 SANS measurements were taken after the valve opening. The duration of each measurement was increased by a factor of 1.1 starting at 0.05 s. The SANS measurements were done on a 1 wt % solution of PMMA_{23}-*b*-PNIPAM_{480} ($M_n \approx 57$ kg·mol^{-1}) in D_2O at the D11 instrument in ILL Grenoble, France. The neutron wavelength utilized was 0.6 nm, and sample-to-detector distances of 3.0, 8.0 and 34 m were used, covering a scattering vector q range of (0.02 - 3.2 nm^{-1}). The two pressure jumps performed are indicated in the phase diagram of 1 wt % aqueous solution of PMMA_{23}-*b*-PNIPAM_{480} in Fig. 7.25a.

Representative SANS profiles with their respective fits are presented in Fig. 7.25b and Fig. 7.25c. For the jump from the 1-phase to the 2-phase region (Fig. 7.25b), the curve at 0.05 s features a shoulder at $q \sim 0.3$ nm^{-1}, indicating the presence of swollen micelles with strong scattering length density (SLD) contrast between the core and the shell of the micelles. On the contrary, this shoulder shifts to a lower q-value at later times, which is attributed to collapsed micelles with a homogeneous SLD due to the dehydration of the micellar shell, leading to a similar SLD than the PMMA core. The curves of the opposite jump are shown in Fig. 7.25c, describe the presence of collapsed micelles at 0.05 s, while they show hydrated and swollen micelles at later times.

We analyzed the SANS profiles by using the spherical core-shell form factor as model, with an exponential decay of the SLD along the shell. However, a sphere with constant SLD was used as form factor to describe the collapsed micelles in the 2-phase region. The sticky hard-sphere

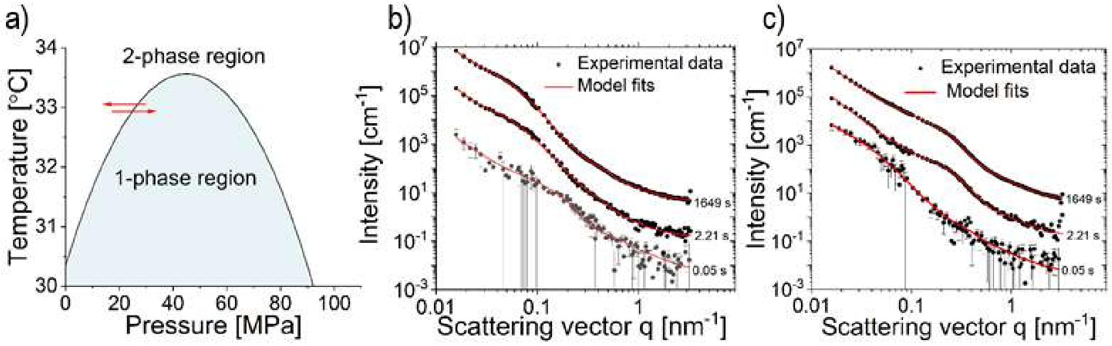

Figure 7.25:
a) Phase diagram of the 1 wt% $PMMA_{23}$-*b*-$PNIPAM_{480}$ solution in D_2O determined by turbidimetry. Pressure jumps are indicated with red arrows. Representative SANS profiles as a function of time for pressure jumps performed between b) 30 → 15 MPa and c) 17 → 35 MPa.

model was used to describe the correlation among the micelles. Fig. 7.26.a shows the micellar structural parameters during the 1-phase to 2-phase jump. The shell thickness decreases abruptly after the rapid increase of pressure. This micelle collapse is characterized by a partial dehydration of the micellar shell. After this rapid collapse, the micelles further rehydrate and interpenetrate with each other as their size increases slightly.

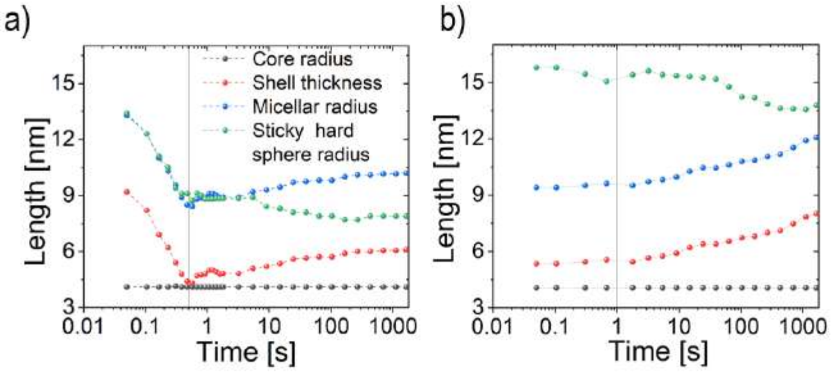

Figure 7.26:
Micellar structural lengths as a function of time after the following pressure jumps: a) 1-phase to 2-phase region and b) 2-phase to 1-phase region.

Contrarily, during the 2-phase and 1-phase jump (Fig. 7.26b), an induction period was identified, in which the micelles do not undergo important changes. After this period, the micellar shell thickness increases continuously, as it partially hydrates. Furthermore, the micelles remain separated from each other, indicating repulsive interactions among them. In summary, we have determined the pathways of the collapse and disintegration of $PMMA_{23}$-*b*-$PNIPAM_{480}$ micelles in aqueous solution by kinetic SANS after a rapid pressure jump. The micellar collapse is characterized by a fast shrinkage of the micellar shell, followed by a slight micellar growth. In contrast, the disintegration of the micellar features a slow micellar growth after a short induction period.

[1] C.-H. Ko, C. Henschel, G. P. Meledam, M. A Schroer, P. Müller-Buschbaum, A. Laschewsky, C. M Papadakis, *Macromolecules* **54**, 384-397 (2021)

[2] B.-J. Niebuur, K.-L. Claude, S. Pinzek, C. Cariker, K. N. Raftopoulos, V. Pipich, M. -S. Appavou, A. Schulte, C. M Papadakis, *ACS. Macro. Lett.* **6**, 1180-1185 (2017)

7.12 Droplet formation by chemically-fueled self-assembly: the role of precursor hydrophobicity

B.-J. Niebuur, H. Hegels, M. Tena-Solsona[1], P. Schwarz[1], J. Boekhoven[1,2],
C. M. Papadakis

[1] Technische Universität München, Department Chemie

[2] Technische Universität München, Institute for Advanced Studies

Transient droplets in an aqueous environment that form and disappear autonomously are ubiquitous in nature, where they control a number of biological functions, e.g., as membrane-less organelles. Such transient, non-equilibrium phase separation may be produced synthetically by an energy-consuming chemical reaction cycle. We investigate a system based on well-soluble precursor molecules based on anionic dicarboxylates, which react in aqueous environment with a chemical fuel, e.g., a carbodiimide, to form an uncharged cyclic anhydride product ("activation"). The latter has a low solubility in water and therefore phase separates into micron-sized droplets. Since the products are unstable in aqueous media, they hydrolyze to yield the original carboxylate precursor ("deactivation"). The latter is slow because it takes place mainly in the aqueous environment phase. Thus, the lower the solubility of the anhydride product, the slower the deactivation and the longer the lifetime of the transient emulsion.

In the present work [1], we chose 2-hexenyl-succinate (C6), 2-octenyl-succinate (C8), and 2-decenyl-succinate (C10) as precursors along with the carbodiimide EDC as the fuel, as in [2] (Fig. 7.27). The corresponding anhydride products differ strongly in their solubility. For each precursor, the fuel concentration is varied in a wide range. Time-resolved dynamic light scattering (DLS) is used to investigate the behavior of the hydrodynamic radius of the droplets and their lifetimes.

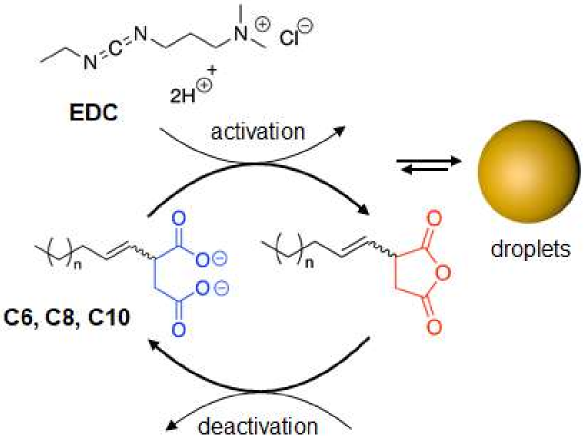

Figure 7.27:
Schematic representation of fuel-driven droplet formation. A chemical reaction cycle drives the transition from the precursor C6 ($n = 2$), C8 ($n = 4$) or C10 ($n = 6$) to the corresponding anhydride, which forms droplets (activation). The anhydrides hydrolyze to the precursor (deactivation). EDC serves as a fuel to drive the activation and is transformed into waste.

Aqueous stock solutions of C6, C8 and C10 were prepared at pH 6 at concentrations of 7.5 or 10 mM. Aqueous stock solutions of 2.0 M EDC were prepared freshly before each experiment. For DLS, a LS Spectrometer from LS Instruments was used. The sample temperature was kept at 25 °C. All measurements were carried out at a scattering angle of 90 °. The duration of the measurements was 10-300 s. The intensity autocorrelation functions were analyzed by fitting stretched exponential functions, and from the decay times, the average hydrodynamic radii R_H were determined using the Stokes-Einstein relation.

In Fig. 7.28, the resulting hydrodynamic radii are shown at the example of C8. The behavior depends strongly on c_EDC: For the lowest value, 2.5 mM, R_H increases slowly from 0.35 μm right after the start of the cycle to 0.6 μm after 20 min, followed by a weak decrease. For $c_\mathrm{EDC} = 10$ mM, R_H keeps increasing until 135 min and reaches a value of 1.0 μm, before it decreases within

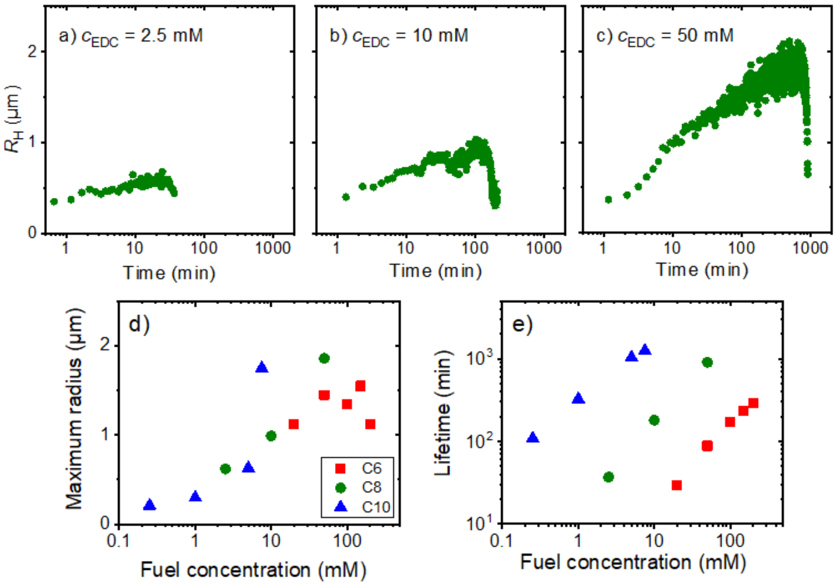

Figure 7.28:
(a-c) Time-dependent hydrodynamic radii of the droplets obtained for the precursor C8 (a-c) at the c_{EDC} values given in the graphs. (d) Maximum hydrodynamic radius and (d) droplet lifetime in dependence on c_{EDC} for C6, C8 and C10.

15 min to 0.4 μm. For $c_{\mathrm{EDC}} = 50$ mM, R_{H} increases up to 2.0 μm, until the droplets disintegrate after 710 min.

To deduce the mechanisms for the formation, growth and the disintegration of the droplets, we compile the maximum hydrodynamic radii as well as the lifetime of the droplets (Fig. 7.28d,e). For C6, the corresponding anhydride product has a relatively high solubility. Thus, a high EDC concentration is needed to induce droplet formation. Large droplet radii are achieved, which are rather independent of c_{EDC}. Due to the fast deactivation of the anhydride, the droplet lifetime is comparatively low. In this system, the droplet lifetime can be tuned in a wide range, with the maximum hydrodynamic radius being nearly unchanged. For C8, increasing c_{EDC} leads to an increase of both R_{H} and of the lifetime. For C10, the largest hydrodynamic radii and lifetimes are achieved, and both increase with c_{EDC}. Even though the maximum value of R_{H} in C10 adopts a similar value as for C8 with equal EDC concentrations, its lifetime is increased by roughly an order of magnitude, i.e., altering the length of the alkenyl chain from 8 to 10 carbon atoms allows to selectively tune the lifetime of the system, while keeping the droplet size unchanged. To summarize, the systems differ strongly in tunability of the droplet size and lifetime, which may help in developing tailor-made systems.

[1] B.-J. Niebuur, H. Hegels, M. Tena-Solsona, P. S. Schwarz, J. Boekhoven, C. M. Papadakis, *J. Phys. Chem. B* **125**, 13542–13551 (2021)

[2] M. Tena-Solsona, J. Janssen, C. Wanzke, F. Schnitter, H. Park, B. Rieß, J. M. Gibbs, C. A. Weber, J. Boekhoven, *ChemSystemsChem* **2**, e2000034 (2020)

8 Development in instrumentation and software

8.1 INSIGHT – methodology of the scattering data analysis tool

L. K. Reb, M. A. Reus, C. Rosemann[1], M. Schwartzkopf[1], S. V. Roth[1], P. Müller-Buschbaum

[1] DESY, Hamburg, Germany

Grazing-incidence X-ray scattering (GIXS) is a powerful analysis method that allows shedding light onto the morphology inside thin films covering length scales from nanometer to micrometer range. While on smaller length scales grazing-incidence wide-angle X-ray scattering probes the crystalline part and allows determining crystal phase, size, orientation, and strain, mesoscopic length scales are investigated using grazing-incidence small-angle X-ray scattering that reveals domain sizes and inter-domain distances and their distributions, respectively. Both methods are applicable for *in situ* or *in operando* studies, where multimodal investigations of kinetic processes, such as crystallization of printed thin films or operation of derived thin-film devices, e.g. solar cells, allow unique insights in real-time assembly processes on the nanoscale. Such studies are designed for revealing the morphology-function relationship in thin-film devices that are progressively used e.g. for future energy materials.

In the last years, developments in computing hardware and software architecture improvements radically increased the availability of computing power for scientific applications. At the same time, progress in X-ray detector resolution and increased frame rates multiplied the amount of data to be processed. This development has raised the necessity to advance data-processing software tools to the next level.

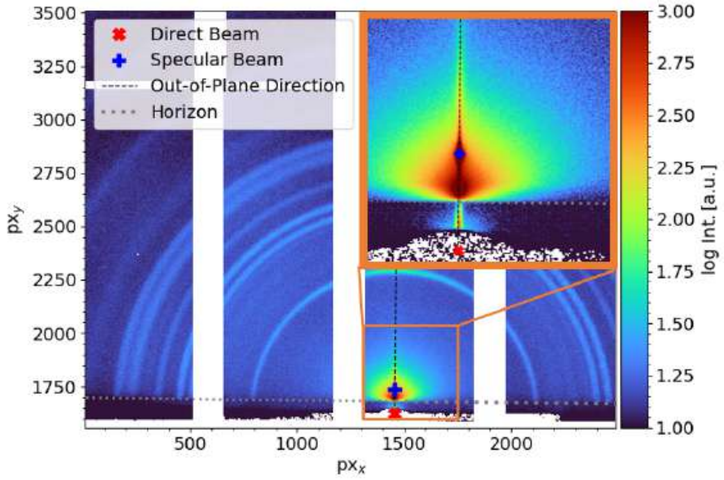

Figure 8.1:
A flat-field corrected high-resolution GISAXS/GIWAXS detector image that includes the central high-intensity small-angle region (highlighted with the orange-framed inset) as well as outer scattering rings of wide-angle signal. With INSIGHT we visually verify the correct choice of the experiment-dependent geometric parameters by controlling the position of the direct beam, specular beam, horizon, and out-of-plane direction. With correct geometry, we reshape the image to reciprocal space for further analysis.

In this work, we present the IN SItu GIXS Heuristic Tool (INSIGHT) [1], an object-oriented python-based performant software tool that shall serve today's scientists for their requirements for the analysis of GIXS experimental data. The focus lies on straightforward data reduction, high degree of flexibility and customizability, and fast and loss-free processing of large scattering datasets. INSIGHT includes the geometrical transformation from detector pixels in real space coordinates into the sample reciprocal space including common intensity corrections while maintaining access to the raw data at any point of the process.

With the example of a GISAXS/GIWAXS (grazing-incidence small/wide-angle X-ray scattering) image, i.e. a single shot containing wide-angle and small-angle scattering information at the same time, we present exemplary 2D and extracted 1D data that can be processed further for gaining insights into the material morphology on the nano- and mesoscale. In Fig. 8.1 we show the raw detector image with some guiding geometrical information that is essential for defining the experimental setup. The direct beam (red) penetrates the substrate and hits the detector below the horizon. Above the horizon, a region of enhanced scattering signal, the Yoneda region, is coupling out of the thin film containing structure information of the film in lateral and vertical directions. The direct beam is reflected when hitting the substrate and gives rives to the specular beam above the Yoneda region.

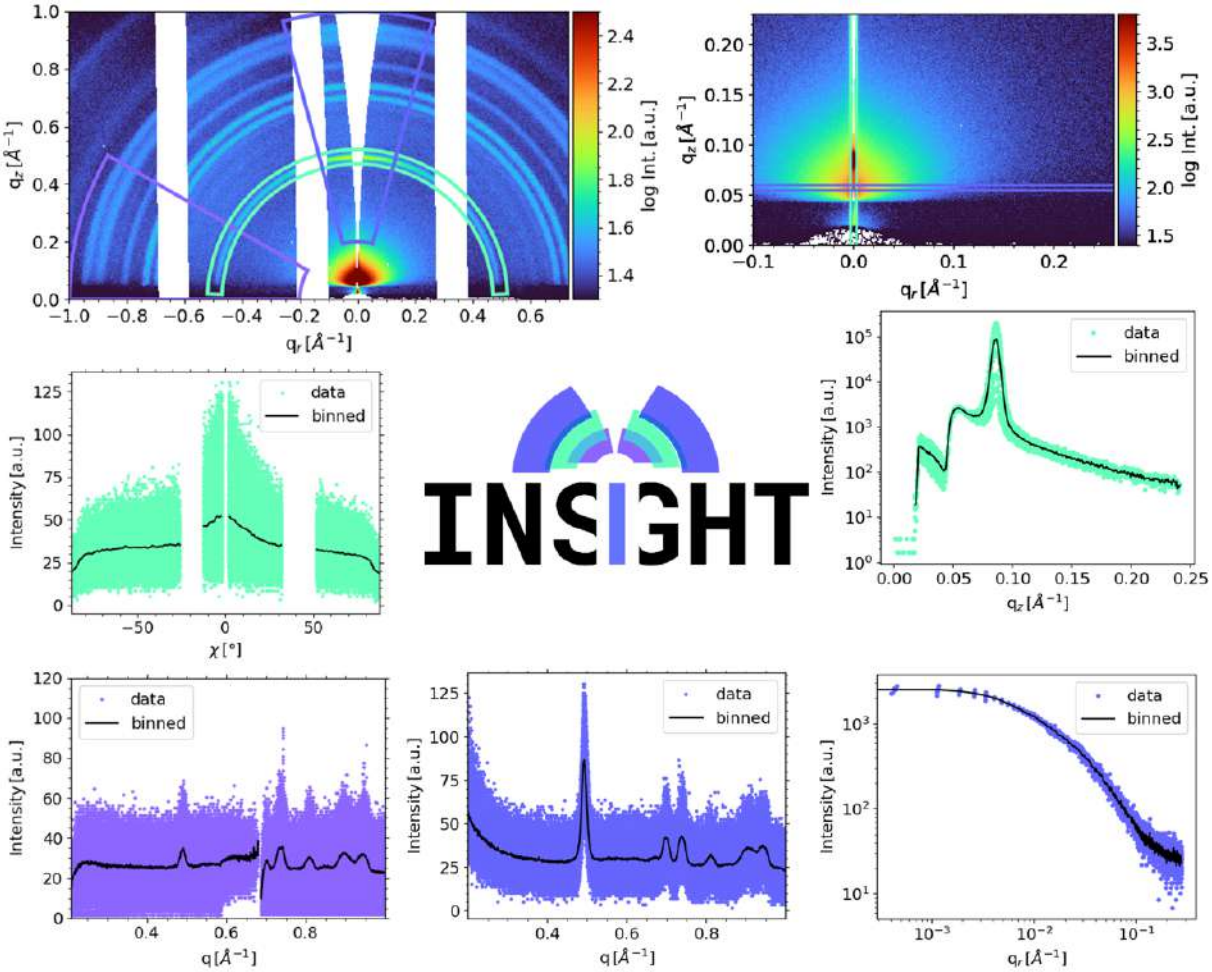

Figure 8.2:
The reshaped image on the upper left is the basis for further analysis. Radially integrated azimuthal cuts (tube-cuts) and azimuthally integrated radial cuts (cake-cuts) help to extract line-cut data for further quantitative analysis (lower left graphs). A zoom into the small-angle region (upper right) allows doing vertical and horizontal line cuts for further analysis (right side middle and lower plot).

This raw image is then further processed; Fig. 8.2 presents an overview of typically employed processing steps. We cut out areas of the 2D reciprocal map respecting the physical origin of the scattered signal, resulting in circular and rectangular shapes. This cut signal is sorted along an axis and then plotted, creating 1D line cuts that contain structural information and can be analyzed quantitatively to uncover the thin-film morphology. This information helps us to advance our knowledge of structure formation and evolution that plays a key role in defining functional properties in soft and condensed matter that are used in thin films. Thus, INSIGHT will help deepening our fundamental knowledge of thin films and their assembling and consequently accelerate developments in the compelling fields of material sciences and nanotechnology.

[1] L. K. Reb, M. A. Reus, C. Rosemann, M. Schwartzkopf, S. V. Roth, P. Müller-Buschbaum, INSIGHT, https://www.groups.ph.tum.de/functmat/forschung/insight/

8.2 Raman spectroscopy set-up at the TOFTOF instrument

A. Alić[1], C. Garvey[1], M. Wolf[1], P. Müller-Buschbaum

[1] MLZ, Garching, Germany

TOFTOF is a time-of-flight spectrometer at MLZ, Garching (Germany), used for QENS (quasi-elastic neutron scattering) and INS (inelastic neutron scattering). TOFTOF can be used to measure non-periodic rotational and long-range motions around 1 meV and periodic vibrations and phonons up to 100 meV. To widen the accessible spectral range to covalent bond vibrations, a Raman spectrometer was recently introduced to the TOFTOF instrument (Fig. 8.3).

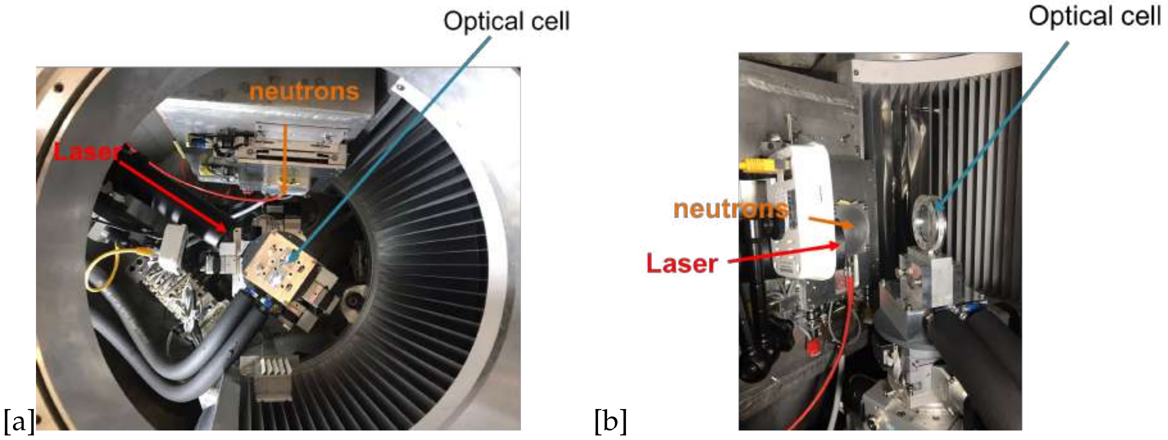

Figure 8.3: a) The Raman setup in TOFTOF instrument seen from above b) Raman setup in TOFTOF instrument seen from the side.

Simultaneous neutron and Raman spectroscopy is very powerful. It allows to measure sample dynamics of different scales at once, while avoiding inconsistencies in the spectra due to different experimental conditions when using the techniques not simultaneously. For hydrogen storage samples, like $Mg(NH_2)_2$ or $LiBH_4$, this means that the hydrogen motion is measured in the environment of neighboring atoms and molecules with quasi-elastic neutron scattering (QENS) and inelastic neutron scattering (INS) and at the same time chemical reactions in the same sample are probed with Raman spectroscopy.
The Raman setup (Horiba Ltd.) that was used (Fig. 8.4) at TOFTOF instrument is composed of:

- Laser and Control Unit (IPS IO785SHOO9OB-IS-TH-L)
- Spectrometer (Horiba iHR 320 and Syncerity CCD Detection System J810050), Camera and Shutter Unit (Horiba SDrive-500)
- Superhead
- Mirror and Lens System
- Sample

Laser source generates the light and this is monochromatized. Photons of specific wavelength go through the gain medium, the light is amplified and then released through an aperture. After the light is amplified by going back and forth through the gain medium, it is transmitted with fiber optic light transmitters to the superhead. The light that goes through the superhead arrives at the sample. At the same time, Raman scattered light is also back-scattered through

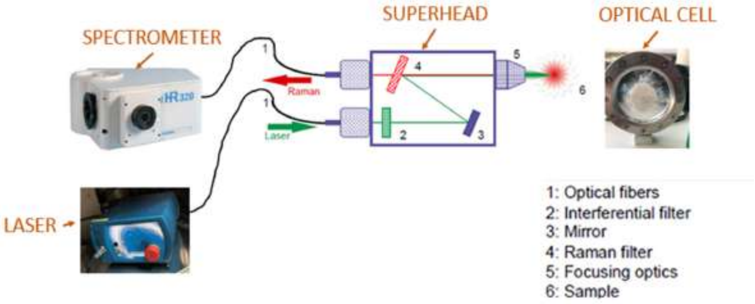

Figure 8.4: Raman setup in the laboratory settings

the superhead to the spectrometer. The purpose of the superhead is to separate the laser light arriving at the sample from the Raman scattered light. Different fibers are used for both Raman and for the laser light. The laser light is guided and focused with some lenses and mirrors onto the sample. The sample, in our case, was put into an optical cell. The sample is located in the alignment box, which shields the environment from the laser.
After the Raman scattered light enters the spectrometer, it is directed by a mirror to the grating where it is dispersed across the exit focal plane. This dispersed light is reflected by a second mirror and guided to a CCD (charge-coupled device) detector, which is mounted at the exit of a spectrometer.
In order to test the setup in laboratory conditions, we measured the molecular vibrations of $LiBH_4$ in powder form. The laser wavelength was 785 nm and the focal length of our spectrometer was 320 mm. We can detect bending and stretching modes [1] shown in Fig. 8.5. The peaks were fitted with Lorentzian functions using Python 3.9.6.

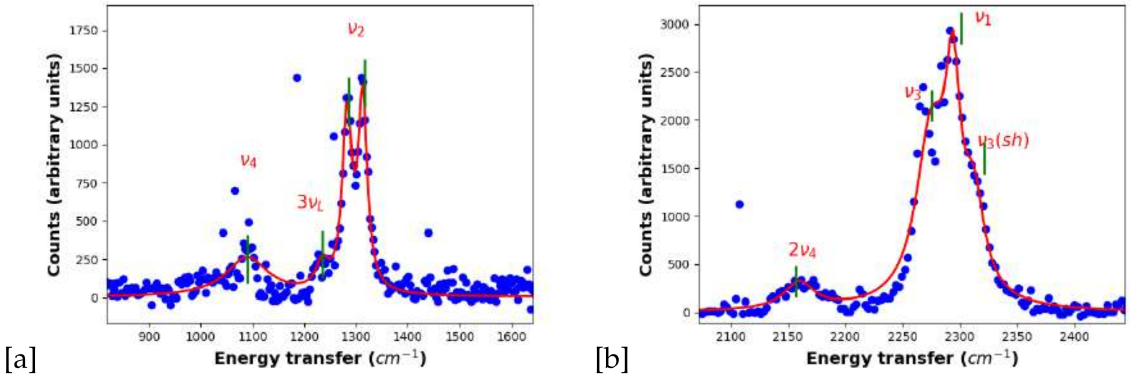

Figure 8.5: Raman spectrum of $LiBH_4$; blue dots - measured data; red line - fitted curve; green markers - position of the peaks according to the literature [1]: (a) bending region and (b) stretching region.

The combined neutron and Raman spectra have still to be acquired since the MLZ was not offering neutrons during the last year. Overall, we successfully demonstrated the Raman spectroscopy set-up operating at the TOFTOF instrument. However, further work will be necessary to increase the stability of the set-up as well as to improve the alignment of the Raman set-up.

[1] S. Gomes, H. Hagemann, K. Yvon, *Journal of Alloys and Compounds* **346**, 206-210 (2002)

8.3 Hydrogel-based electrodes for brain wave detection

G. Erbil, H.-Y. Chiang[1], V. Körstgens, P. Müller-Buschbaum

[1] Cephalgo, Strasbourg, France

Electroencephalography (EEG) is a method to detect the brain signals or the electrical activity of the brain by means of electrodes, which are attached to the scalp [1]. Brain cells communicate all the time with each other via electrical signals. In its conventional method of application (Fig. 8.6), electrodes are made up of tiny wires and small metallic discs are attached to the scalp in order to collect voltage fluctuations resulted from the activity. Typically, the method is non-invasive using wet electrodes based on Ag/AgCl in combination with a conductive gel or dry electrodes. Nowadays also dry electrodes are used with the obvious advantage after application skin and hair does not have to be washed in order to remove gel residues. With each electrode, electrical activity is recorded in the form of a graph to be interpreted by the clinicians. EEG is used for diagnostic purposes, since it can detect changes in the brain activity due to brain disorders. With an arrangement of electrodes, as given in Fig. 8.6, brain activity can be followed and spatially resolved.

Figure 8.6:
An example of how electrodes should be attached for EEG measurements. The yellow circles indicate EEG electrodes on the scalp. The distribution of electrodes allows for a local assessment of brain activity.

Current dry electrodes may have problems maintaining the contact quality between the electrode and the skin. With an impedance instability of the electrode due to a change of applied pressure, the signal quality is harmed [2]. These problems are even more evident when the application of dry electrodes is not supervised in a clinical environment. Any kind of self-attachment of electrodes is challenging as there is no strict protocol in how to place the electrodes on the scalp and the placement will depend on the user. The user might place the electrodes in such a way that the applied pressure is strongly dependent on body movement leading to bad contact quality between the electrodes and the skin for each usage. Therefore, new solutions should be found in order to prevent any resulting artefacts.

In this project, we are aiming at adhesive electrodes based on hydrogels. Composite hydrogels have been recently studied as candidate materials for wearable and implantable devices in order to monitor and collect signals generated by the organs of the human body thanks to their chemical structures and mechanical properties [3]. The advantage of the hydrogels arises from the flexibility of their chemical structure and their tunable mechanical properties, so that they can be modified by adding functional groups in order to give them the desired properties such as conductivity, adhesiveness, self-heal ability. This multifunctionality may allow to overcome current issues of dry electrodes such as impedance instability and contact quality. However, it is challenging to synthesize multifunctional hydrogels, which combine all the functional properties at the same material while demonstrating a reasonable life time without degradation.

The composition and synthesis of the hydrogels is inspired by nature. It is insightful to look at plants and animal how their adhesive properties are tuned in order to adhere and move on distinct surfaces. Especially, this work analyzes adhesive properties of mussels with its outstanding performance in aqueous environments. The principle behind adhesiveness of mussels results from the catechol functional group, which constitutes two neighboring hydroxyl groups on a benzene ring structure. This functional group has a capacity to generate non-covalent interactions and covalent bonds with many surfaces, which leads to strong adhesive properties [4,5]. In this work, the synthetic strategy of the hydrogel basically comprises the polymerization of a self-sustainable, adhesive hydrogel with the inclusion of a conductive filler [6]. The adhesive property was achieved by including tannic acid to the acrylic acid monomer and polymerization was induced in a teflon mold at room temperature conditions. Due to the addition of different conductive fillers, such as silver nanoparticles and carbon nanotubes, a conductive hydrogel is obtained. An example of one of the self-sustaining hydrogel samples of 5 mm length adhered to a metal spatula is shown in Fig. 8.7.

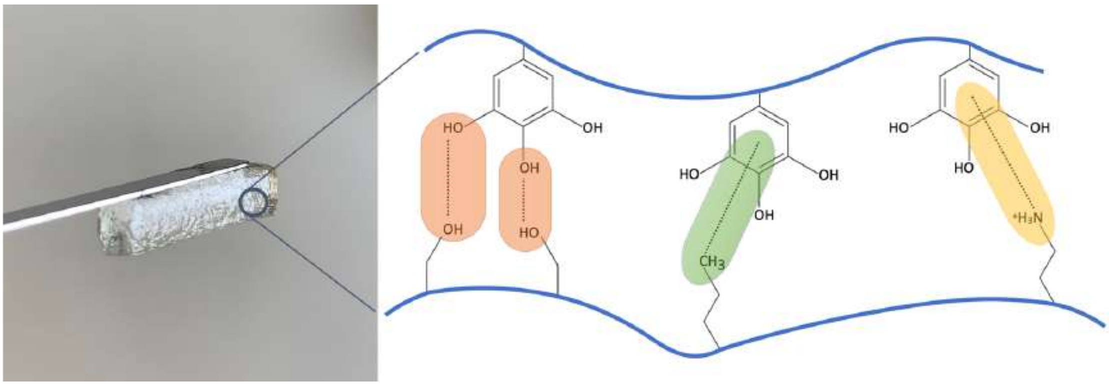

Figure 8.7:
Conductive hydrogel based on tannic acid, polyacrylic acid and silver nanoparticles. The hydrogel structure of about 5 mm length is attached to a metal spatula. Some of the non-covalent interactions discussed for the functional groups of tannic acid are illustrated: hydrogen bonding (orange), hydrophobic interactions (green), and cation-π interaction (yellow). These intermolecular interactions provide cohesion of the gel matrix while interactions with functional groups of the attached surface lead to adhesion.

Tannic acid is a type of polyphenol containing several 1,2,3 hydroxybenzyl groups within its molecular structure. This functional group closely related to the catechol group mentioned above enables a number of non-covalent interactions which are sketched in Fig. 8.7. These interactions play a role in the cohesiveness of the hydrogel as well as in the adhesion to surfaces of different materials. Currently these hydrogel-composite electrodes are optimized in order to achieve high conductivity while showing adhesive properties and maintaining mechanical stability. In addition, a headset comprised of dry electrodes will be tested in an EEG setup in order to monitor brain activity.

[1] P. L. Purdon, A. Sampson, K. J. Pavone, E. N. Brown, *Anesthesiology* **123**, 937-960 (2015)

[2] B. Taji, A. D. C. Chan, S. Shirmohammadi, *IEEE Trans. Instrum. Meas.* **67**, 1900-1912 (2018)

[3] H. Yuk, B. Lu, X. Zhao, *Chem. Soc. Rev.* **48**, 1642-1667

[4] H. Lee, S. M. Dellatore, W. M. Miller, P. B. Messersmith, *Science* **318**, 426-430 (2007)

[5] C. Zhang, B. Wu, Y. Zhou, F. Zhou, W. Liu, Y. Wang, *Chem. Soc. Rev.* **49**, 3605-3637 (2020)

[6] Z. Jia, X. Lv, Y. Hou, K. Wang, F. Ren, D. Xu, Q. Wang, K. Fan, C. Xie, X. Lu, *Bioact. Mater.* **6**, 2676-2687 (2021)

8.4 Bioinspired electrodes for electroencephalography

V. Körstgens, A. Zheng, G. Erbil, H.-Y. Chiang[1], P. Müller-Buschbaum

[1] Cephalgo, Strasbourg, France

The measurement of electric biosignals non-invasively such as measuring brain waves via electroencephalography (EEG) is strongly dependent on the kind of electrodes in contact with the skin. There is a high demand for electrode systems maintaining high signal quality over a long period of time and being comfortable to wear at the same time. With increasing demand in brain-computer interfaces (BCIs) the non-invasive method of EEG is the most adapted and safe solution for the application of a BCI. Traditional wet electrodes require additional skin preparation and high maintenance that prohibit the popularization from end users. In order to find alternative dry electrode technologies it is instructive to observe the solutions nature developed when it comes to establish reversible adhesive contacts between surfaces. Beside the necessary electrical conductivity, electrode materials need to provide an adhesive contact to be able to overcome the physical constraints of motion artefacts. Only if this is given a stable high-quality EEG signal can be obtained.

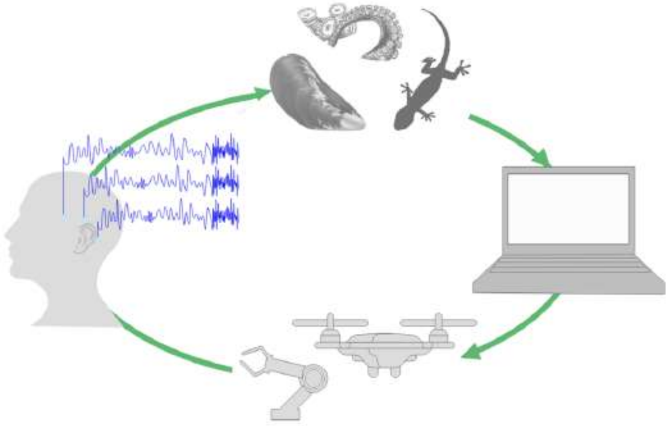

Figure 8.8:
Brain-computer interface with the measurement of brain waves facilitated by bioinspired electrodes. Exemplary inspirations from nature indicated here are mussels adhering by byssal threads, gecko feet with its fine-structured setae, and suction-cup structures as known from octopuses.

In Fig. 8.8 the concept of a BCI based on the measurement of brain waves with bioinspired electrodes is sketched. Some of the inspirations from nature are indicated in Fig. 8.8 including the most prominent inspiration for adhesive technology, the gecko with its tiny hairlike structures of the feet. Further examples are suction cup-like structures as in octopuses or the byssal threads used by mussels to adhere to rocks and other surfaces. One of the routes we followed is the development of an adhesive patch with a pillar structure [1]. Microstructured conductive adhesive patches with a combination of carbon black and graphene sheets dispersed in polydimethylsiloxane (PDMS) are obtained from a microstructured mold.

The pillar structure with a flat-ended mushroom shape shown in Fig. 8.9 has been chosen as an example for the evaluation of the integrity of the adhesive patches, meaning the percentage of successfully reproduced pillars. For this example the pillar radius is 3.5 μm and the pillar density is 6.4 $\cdot 10^5/cm^2$. With different molds, an integrity of the pillar structures close to 100 % has been achieved in our studies. The adhesive properties of these patches have been measured with a home-built setup for the investigations of pressure sensitive adhesives (PSAs). The set-up allows for carefully adapted measurement procedures addressing PSAs and dry adhesives in different sample geometries [2, 3]. Measurements show that the tack achieved of 0.2 to 0.5 N/cm^2 for the dry adhesive patches conforms to the tack observed for adhesive papers known as sticky notes. With a combination of conductive fillers graphene and carbon black powder structured patches with a sheet resistance of about 1000 Ω/sq were achieved. The performance in EEG measurements was tested with a circuit board connected to a computer allowing for the comparison of three different electrodes at the same time.

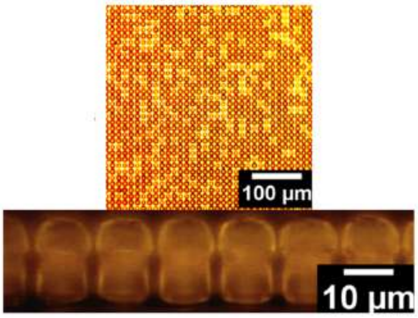

Figure 8.9:
Optical microscopy images before tack measurement for an example PDMS pattern achieved with a mold. The top view showing ≈ 83% of reproduced pillars and side view in higher magnification showing the mushroom tip shape.

Brain waves are detected during a measurement procedure in a sequence of ten eye-blinks, 30 s of focusing the eyes on a black dot, ten eye-blinks and 30 s of relaxing with closed eyes. In this stage the detection of alpha waves is expected. A section of an example measurement is shown in Fig. 8.10 comparing the performance of a structured conductive dry adhesive to a commercial wet electrode with a good replication. Whereas extensive peaks caused by eye blinks are used as seperators, it has to be noted that unintential eye blinks by the subject may also occur in the relaxing phase. This leads to the peaks preceeding the alpha waves in Fig. 8.10.

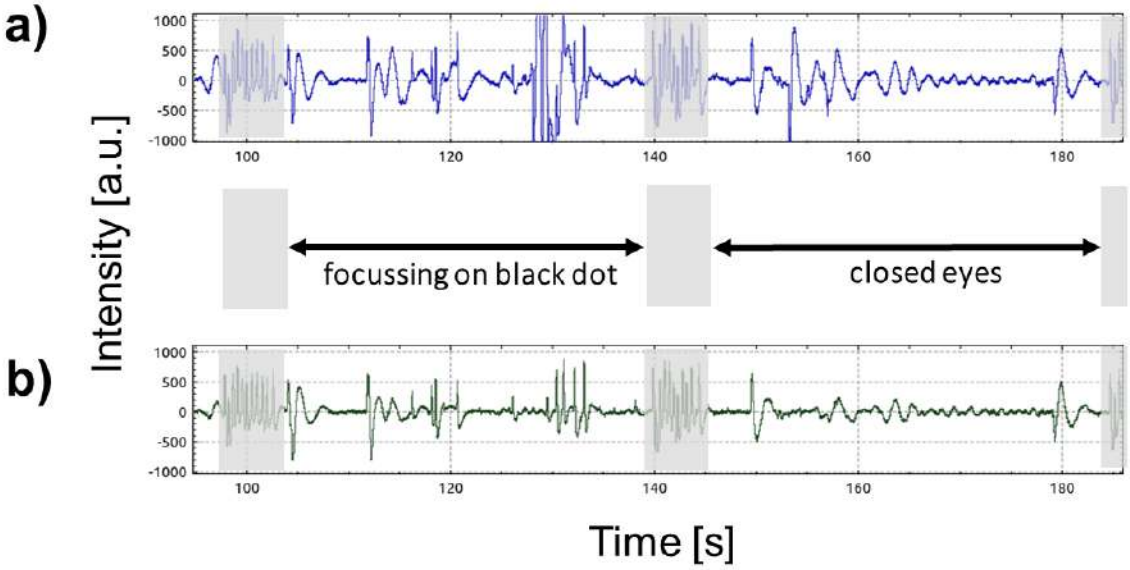

Figure 8.10:
EEG measurement sequence with intermediate ten eye-blinks indicated with gray color: a) structured conductive dry adhesive and b) commercial wet electrode for comparison

In a further bioinspired approach, we look into conductive composite hydrogels. Stable conductive hydrogels inspired by mussel adhesives have been prepared with its EEG performance currently under investigation.

[1] T. Kim, J. Park, J. Sohn, D. Cho, S. Jeon, *ACS Nano* **10**, 4770-4778 (2016)

[2] M. Schindler, M. Koller, P. Müller-Buschbaum, *ACS Appl. Mater. Interfaces* **7**, 12319 (2015)

[3] V. Körstgens, J. Corella Puertas, P. Müller-Buschbaum, *ACS Appl. Polym. Mater.* **2**, 3189 (2020)

8.5 Construction of a thermal vacuum chamber for testing new generation solar cells under space conditions

M. J. Trost, L. V. Spanier, P. Müller-Buschbaum[1]

[1] MLZ, Garching, Germany

New generation solar cells with better power per mass ratio are of great interest for space missions, as they can lead to significant weight and thus cost reductions. However, components needed for space missions must first be tested and verified to ensure their function under these harsh conditions. In previous experiments, not only were organic solar cells shown to be able to withstand well the UV radiation present in a unfiltered AM0 solar radiation in a laboratory environment [1], but organic and perovskite cells have also been launched on a suborbital rocket into space [2]. Following these works, in this project, a small, lab-scale thermal vacuum chamber is created, allowing the investigation of various other novel solar cell technologies in a realistic space environment simulation. In addition, a way to relate previous space experiments to laboratory experiments will be given with the newly established set-up. The current design of the thermal vacuum chamber includes several components which can be seen in Fig. 8.11.

The design of the chamber is based on the standard norms of the European Cooperation for Space Standardization (ECSS) [3,4]. Therefore, pressures of less than $1\text{x}10^{-5}$ hPa must be achieved in the experimental environment. In addition, cosmic background radiation must be taken into account. The cold background of space is simulated by a thermal vessel flushed with liquid nitrogen (LN2) with a highly absorbing surface coating, surrounding the sample environment. To imitate thermal radiation from Earth for low Earth orbit simulations, an electrically heated thermal plate can also be additionally inserted. Heating from solar radiation can either be simulated by means of an AM0 Sun simulator, with an irradiance of 136.7 mW/cm^2, or by electrically heating the entire thermal vessel to the desired temperature. This allows a performance analysis of the solar cells under the most realistic space-like conditions. To recreate the high thermal stresses, most satellites are subjected to continuous cycling between the direct illumination from the Sun and cold environment in Earth's shadow. The LN2 and electric heaters of the thermal vessel can be used to run a thermal cycling program, which is emulating this protocol. This can also incorporate intermittent phases of illumination to better study the effects of photo-degradation. In order to also be able to simulate this scenario and the associated effects, the setup possesses a shutter to cover the solar simulator. All the thermal elements are combined with a temperature control unit, allowing the creation of temperature profiles that can be adapted to reproduce various scenarios. This way, long-term simulations with thermal cycles can be run.

A first design of a thermal vacuum chamber can be seen in Fig. 8.11. It is planned to use a stainless steel housing with various feedthroughs for the electric, LN2, measurement devices, the solar simulator and the vacuum pumps. In addition, the chamber has a simple mechanism to change the solar cells quickly and easily. At the same time, a constant cell position and thus a constant and reproducible experimental setup is guaranteed. The performance of the solar cells is measured by means of a 4-point measurement set-up. As a result, measurement inaccuracies, due to conductor and transition resistances of the measuring cable, can be eliminated from the measurement. However, to obtain reliable results, the illuminated area of the solar cells must be precisely defined. This is ensured by so-called illumination masks, which are usually metal plates that are placed on the cell. But to avoid thermal bridges between the mask and cell which would distort the measurements, the illumination masks are here vapour-deposited directly onto the opposite side of the substrate plate, so that no special adjustments to the cell geometry are needed. That way the thermal vacuum chamber can easily be adapted to other cell geometries.

In a first experiment, the chamber is going to be tested on organic solar cells such as PTQ-2F:BTP-4F (also called PTQ10:BTP-4F). However, due to the design, other types of solar cells (quantum dot, perovskite, hybrid solar cells) with a different structure can also be tested.

Figure 8.11: Current design of the thermal vacuum chamber with the holder for the solar cells to be tested being mounted at the thermal backplane. All three parts are connected via a line guidance system.

In principle, it is even possible to test also other devices, such as batteries, under space-like conditions with this setup. For such tests, only an adapted sample holder is needed. Furthermore, not only can a vacuum be created in this chamber, but it can also be flooded with gas via an additional valve. This is required in order to prevent condensation on the inside of the chamber when it is opened. But also, flooding the chamber with gas allows the imitation of surface conditions on other planets or objects in space. As an example, carbon dioxide could be used to simulate the Marsian surface and thus study the performance of the cells under Mars conditions. Thus, this experimental setup allows the investigation of the performance of solar cells under different ambient conditions, pressures and temperatures. By changing these values during a measurement process, the degradation gradient under changing environmental conditions can also be measured directly.

[1] S. Guo, C. Brandt, T. Andreev, E. Metwalli, W. Wang, J. Perlich, and P. Müller-Buschbaum, *ACS Appl. Mater. Interfaces* **6**, 17902 (2014)

[2] L. K. Reb, M. Böhmer, B. Predeschly, S. Grott, C. L. Weindl, G. I. Ivandekic, R. Guo, C. Dreißigacker, R. Gernhäuser, A. Meyer, and P. Müller-Buschbaum, *Joule* **4**, 1880 (2020)

[3] ECSS Executive Secretariat, ECSS-E-ST-20-08C Rev.1

[4] ECSS Executive Secretariat, ECSS-E-ST-10-03C Rev.1

8.6 New measurement setup to characterize thermoelectric polymer thin films

S. A. Wegener, A. L. Oechsle, P. Müller-Buschbaum

Polymer-based organic thermoelectric materials are attracting an increasing attention due to their advantages over common inorganic thermoelectric materials by being non-toxic, light-weight and potentially cheap in production and device fabrication [1-2]. A big part of this research focuses on thin polymer films with thicknesses from 100 nm to several micrometers. Such small film thicknesses leads to special requirements for the measurement equipment to be used. For example, in most cases, it is impossible to measure the sample without a substrate underneath the thermoelectric thin film. Furthermore, the polymer films are way more sensitive to mechanical stress by pin contacts compared to inorganic materials.

For this reason, we work on the development of a new setup to characterize thermoelectric materials as thin films. The primary purpose is to measure the thermoelectric power factor under adjustable environmental conditions. The so-called thermoelectric power factor is a common performance indicator for thermoelectric materials. It is determined by the conductivity of the sample and its Seebeck coefficient, which describes the ratio between the temperature gradient, applied on a material, and the internally generated thermal voltage.

The intended adjustable environmental conditions include control of ambient temperature and humidity. Additionally, the setup will give the possibility to do grazing-incidence X-ray scattering (GIXS) on the sample simultaneously with the thermoelectric device characterization. This approach allows a detailed *in situ* analysis of occurring processes inside the thermoelectric thin films during operation. The setup consists of three main sections: Substrate holder and contacting, vacuum-providing housing, and substrate with integrated measurement resistors. A image of the setup is seen in Fig. 8.12.

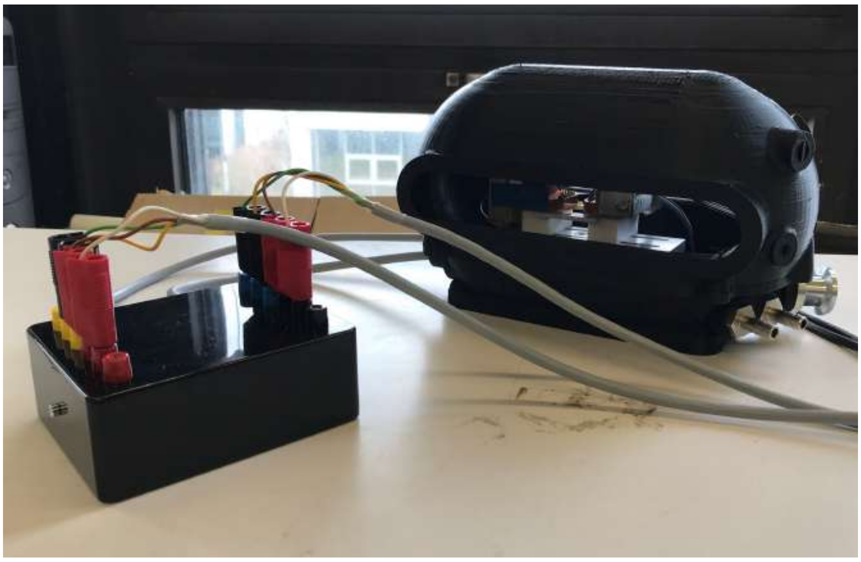

Figure 8.12:
Photograph of the newly developed setup with connection terminal and polylactic acid (PLA) prototype housing.

Especially for kinetic experiments with changing temperature, temperature sensors and polymer films must stay in thermal equilibrium. Therefore, the resistors for the temperature measurement and the contacts for the conductivity measurement will be evaporated directly on the glass substrate via a lift-off process with a photoresist.

Subsequently, the measurement resistors are passivated with an isolating layer. The polymer film can then be deposited on the prepared sample substrate via spin-coating or spray-coating. This process ensures an excellent electrical and thermal connection between the polymer film and the measurement points. Furthermore, as the film is deposited directly on the measurement contacts, the same contacting for all experiments is secured. Additionally, it is also possible to quickly characterize samples with the temperature sensors in the substrate holder. This simplified measurement procedure makes it possible to skip the lift-off process mentioned above and the thermal evaporation of the measurement resistors.

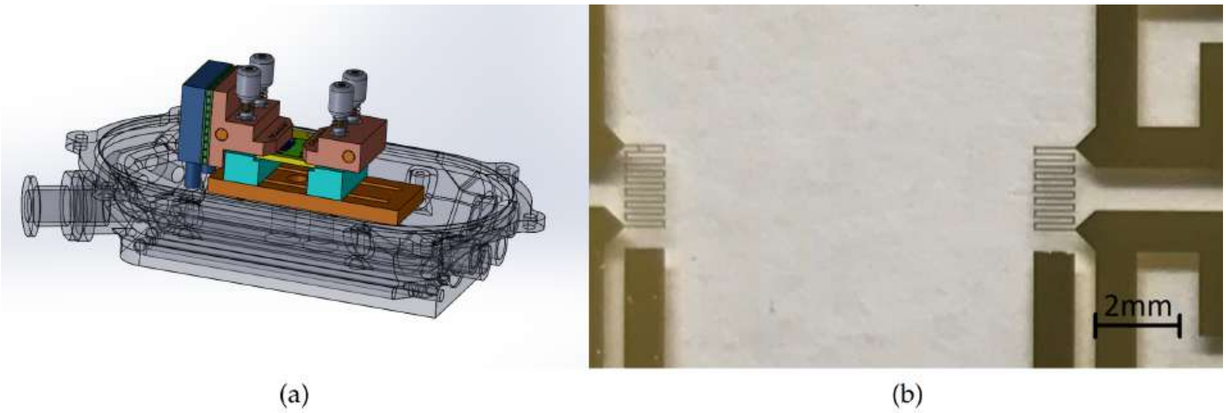

Figure 8.13:
(a) CAD of setup displayed without upper part of the chamber housing; (b) Measurement resistors and electrical contacts on the glass substrate.

The substrate holder provides the cooling and heating of the sample. It allows the application of predefined temperatures and temperature gradients to the sample. Cartridge heaters and a Peltier element allow to realize the heating and cooling. While one side is only heated, the other side can be heated and cooled to reach temperatures below the ambient temperature. The system is controlled via PID temperature controllers that are connected to a computer via a python interface. The electrical contacts that were evaporated on the glass substrate (Fig. 8.13) are connected to an external terminal to allow an easy connection to a source meter and the temperature controller.

The chamber housing is a further development of pre-existing setup that was used to do experiments at different humidities [3]. The chamber was elongated and equipped with several new cable connections for the new setup. It consists of a 3D sintered aluminum housing with integrated cooling circuits. Hence, the temperature of the whole chamber can be more optimally controlled. The humidity is controlled by an external nitrogen supply. Depending on the desired humidity, the initial nitrogen stream can be moistened by flowing throw a gas wash bottle. In the initial phase, the housing is realized as a polylactic acid (PLA) prototype housing as seen in Fig. 8.12. The whole setup is built as modular as possible to enable further improvements and adaption to future experiments.

[1] A. L. Oechsle, J. E. Heger, N. Li, S. Yin, S. Bernstorff, P. Müller-Buschbaum, *Macromol. Rapid Commun.* **42**, 2100397 (2021)

[2] S. Tu, T. Tian, A. L. Oechsle, S. Yin, X. Jiang, W. Cao, N. Li, M. A. Scheel, L. K. Reb, S. Hou, A. S. Bandarenka, M. Schwartzkopf, S. V. Roth, P. Müller-Buschbaum, *Macromol. Symp.* **429**, 132295 (2022)

[3] T. Widmann, L. P. Kreuzer, M. Kühnhammer, A. J. Schmid, L. Wiehemeier, S. Jaksch, H. Frielinghaus, O. Löhmann, H. Schneider, A. Hiess, R. v. Klitzing, T. Hellweg, P. Müller-Buschbaum, *Appl. Sci.* **11**, 4036 (2021)

9 Teaching and outreach

9.1 Lectures, seminars and lab courses

Spring Term 2021

Prof. Dr. Peter Müller-Buschbaum, Dr. Volker Körstgens
Angewandte Physik: Polymerphysik 2
Prof. Dr. Christine M. Papadakis, *Nanostructured Soft Materials 2*
Dr. Michael Leitner, *Materialphysik auf atomarer Skala 2*
Prof. Dr. Peter Müller-Buschbaum, Prof. Dr. Christian Große, *Mess- und Sensortechnologie*
Prof. Dr. Winfried Petry, *Physics with neutrons 2*
Prof. Dr. Christine M. Papadakis, *Materialwissenschaften*
Prof. Dr. Peter Müller-Buschbaum, *Seminar: Current problems in organic photovoltaics*
Prof. Dr. Peter Müller-Buschbaum, Prof. Dr. Christine M. Papadakis,
Bachelor-Seminar: Funktionelle weiche Materialien
Prof. Dr. Bastian Märkisch, Dr. Christoph Morkel, Prof. Dr. Peter Müller-Buschbaum,
Prof. Dr. Christian Pfleiderer, Dr. Christian Franz *Seminar Neutronen in Forschung und Industrie*
Prof. Dr. Peter Müller-Buschbaum, Prof. Dr. Christine M. Papadakis
Seminar: Structure und dynamics of condensed matter
Prof. Dr. Peter Müller-Buschbaum, Prof. Dr. Christine M. Papadakis, *Seminar: Polymers*
Prof. Dr. Peter Müller-Buschbaum, *Führung durch die Forschungs-Neutronenquelle*
Heinz Maier-Leibnitz (FRM II) für Studierende der Physik

Autumn Term 2021/22

Prof. Dr. Peter Müller-Buschbaum, Dr. Volker Körstgens
Angewandte Physik: Polymerphysik 1
Prof. Dr. Christine M. Papadakis, *Einführung in die Festkörperphysik*
Prof. Dr. Christine M. Papadakis, *Nanostructured Soft Materials 1*
Dr. Michael Leitner, *Materialphysik auf atomarer Skala 1*
Prof. Dr. Winfried Petry, *Physics with neutrons 1*
Prof. Dr. Peter Müller-Buschbaum, *Seminar: Current problems in organic photovoltaics*
Prof. Dr. Bastian Märkisch, Dr. Christian Franz, Dr. Jitae Park, Dr. Christoph Morkel,
Prof. Dr. Peter Müller-Buschbaum, *Seminar Neutronen in Forschung und Industrie*
Prof. Dr. Peter Müller-Buschbaum, Prof. Dr. Christine M. Papadakis,
Seminar: Structure und dynamics of condensed matter
Prof. Dr. Peter Müller-Buschbaum, Prof. Dr. Christine M. Papadakis, *Seminar: Polymers*
Prof. Dr. Peter Müller-Buschbaum, *Führung durch die Forschungs-Neutronenquelle*
Heinz Maier-Leibnitz (FRM II) für Studierende der Physik

Lab Courses 2021

Rasterkraftmikroskopie (Fortgeschrittenenpraktikum)
Neutron scattering at FRM II (Fortgeschrittenenpraktikum)
Charakterisierung von Polymeren mittels dynamischer Differenzkalorimetrie (Fortgeschrittenenpraktikum)

9.2 Conferences and public outreach

Technical University of Munich (TUM)/Technical University of Darmstadt (TUD)
Osmolyte and cosolvent effects in stimuli-responsive soft matter systems
25 – 26 February 2021, virtual event

From 25 to 26 February 2021, 42 scientists from Germany, Czech Republik, Slovenia, Italy, U.S.A. and India came together virtually at the conference on osmolyte and cosolvent effects in stimuli-responsive soft matter systems. Aim of the conference was to bring together scientists from experimental, simulation and theoretical domains to discuss the link between experimental observations, and theoretical/simulation models/predictions.

In 15 talk and 8 posters, the effects of cosolvents on thermoresponsive polymers and molecules, block copolymer micelles, hydrogels, microgels and thin films were addressed as well as salt and osmolyte effects on thermoresponsive and zwitterionic polymers and proteins. These phenomena are investigated using a wide range of methods, such as theoretical calculations, computer simulations, scattering and spectroscopy. Lively discussions took place after the excellent talks and at the posters, that were presented in short introductory videos as well.

Sadly, one of the pioneers in the field, Prof. Françoise M. Winnik, passed away few days before the conference. We took the opportunity to commemorate her at the conference.

Swaminath Bharadwaj, Technical University of Darmstadt
Christine M. Papadakis, Technical University of Munich
Nico van der Vegt, Technical University of Darmstadt

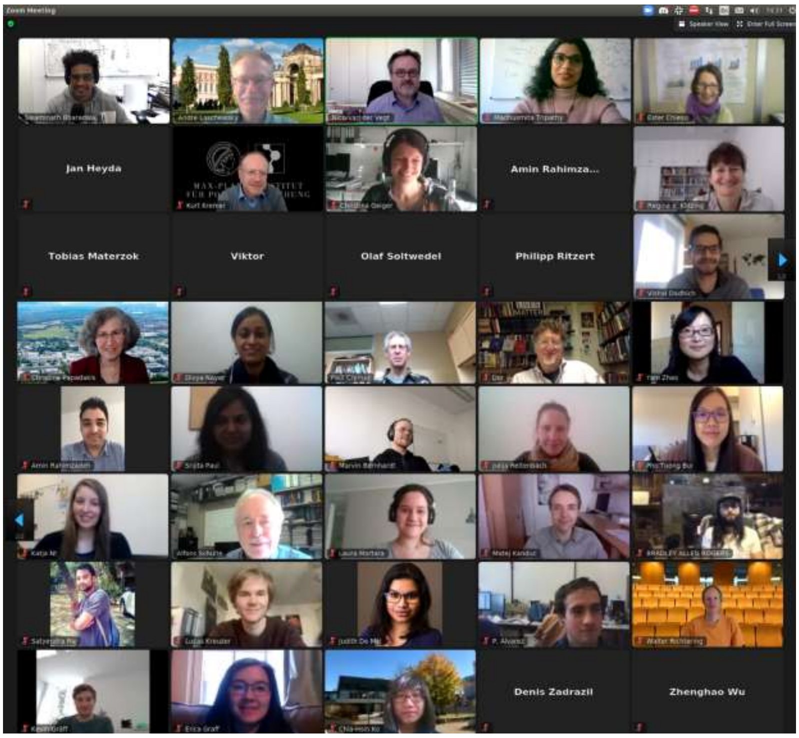

Session "Complex Fluids" at DPG-Frühjahrstagung BP-CPP-DY-SOE of the German Physical Society
22 – 24 March 2021, virtual event

On March 23, 2021, a symposium on the topic "Complex Fluids" was organized within the virtual DPG-Frühjahrstagung (DPG Spring Meeting) BP-CPP-DY-SOE as a joint session of the divisions Chemical and Polymer Physics and Dynamics and Statistical Physics of the German Physical Society. Aim of the symposium was to bring together scientists from experimental, simulation and theoretical domains to give an update of recent developments in the field, in spite of the Covid travel restrictions. Two invited talks, namely by Reidar Lund from Norway on "Polymer micelles with crystalline cores: confinement effects, molecular exchange kinetics and mechanical response" and by Sofia Kantorovich from Austria on the "Dynamic behaviour of anisotropic magnetic particles in suspensions" shed light on these research fields. 10 contributed talks gave an impression about the research that is currently pursued on microgels, magnetogranulometry, magnetically functionalized polymers, polymer grafted nanoparticles, lipid membranes, emulsions under flow, supramolecular polymers and wormlike micelles. As is characteristic for the field, a broad range of methods are employed, such as scattering methods, 3D super-resolution fluorescence microcopy, rheology, as well as new calculation and simulation methods.

Christine M. Papadakis, Technical University of Munich

DPG
ISSN 0420-0195
VERHANDLUNGEN
der Deutschen Physikalischen Gesellschaft

4/2021
Virtuelle DPG-Frühjahrstagung 2021
Virtual DPG Spring Meeting 2021 of the Divisions
Biological Physics
Chemical and Polymer Physics
Dynamics and Statistical Physics
Physics of Socio-Economic Systems

ONLINE

22 – 24 March 2021
bpcppdysoe21.dpg-tagungen.de

Heinz Maier-Leibnitz Zentrum (MLZ)
Girls' Day
22 April 2021, virtual event

The Girls' Day took place on 22 April 2021 as a purely virtual event. This year´s digital format was well received and fully booked. 15 female participants (max. number of participants allowed) were offered a special program: The day began in a livestream with impulse lectures, interviews and discussion rounds with role models from various Girls' Day professions. Afterwards, the participants got an insight into the life of a female scientist at the MLZ, along with presentations via Zoom, a guided tour of the uranium lab, and hands-on experiments and an online escape game.

Heinz Maier-Leibnitz Zentrum (MLZ)
725th WE-Heraeus-Seminar
30 May – 03 June 2021, Tutzing, hybrid format

This seminar has been postponed from June 2020 to May 2021 due to the corona pandemic and took place from 30 May to 03 June 2021 in Tutzing as well as in a virtual format. This WE-Heraeus-Seminar focuses on the technique of magnetic small angle neutron scattering, which is one of the most important methods for magnetic microstructure determination in condensed-matter physics and materials science. It is one of the central aims of this Heraeus seminar to bring groups of researchers closer together on the topic of „Magnetic Small Angle Neutron Scattering – from Nanoscale Magnetism to Long-Range Magnetic Structures“ by providing a stage for intra- and interdisciplinary scientific exchange. Besides, in view of the upcoming European Spallation Source, a further focus will be on future challenges related to neutron instrumentation, sample environment, and neutron data analysis.

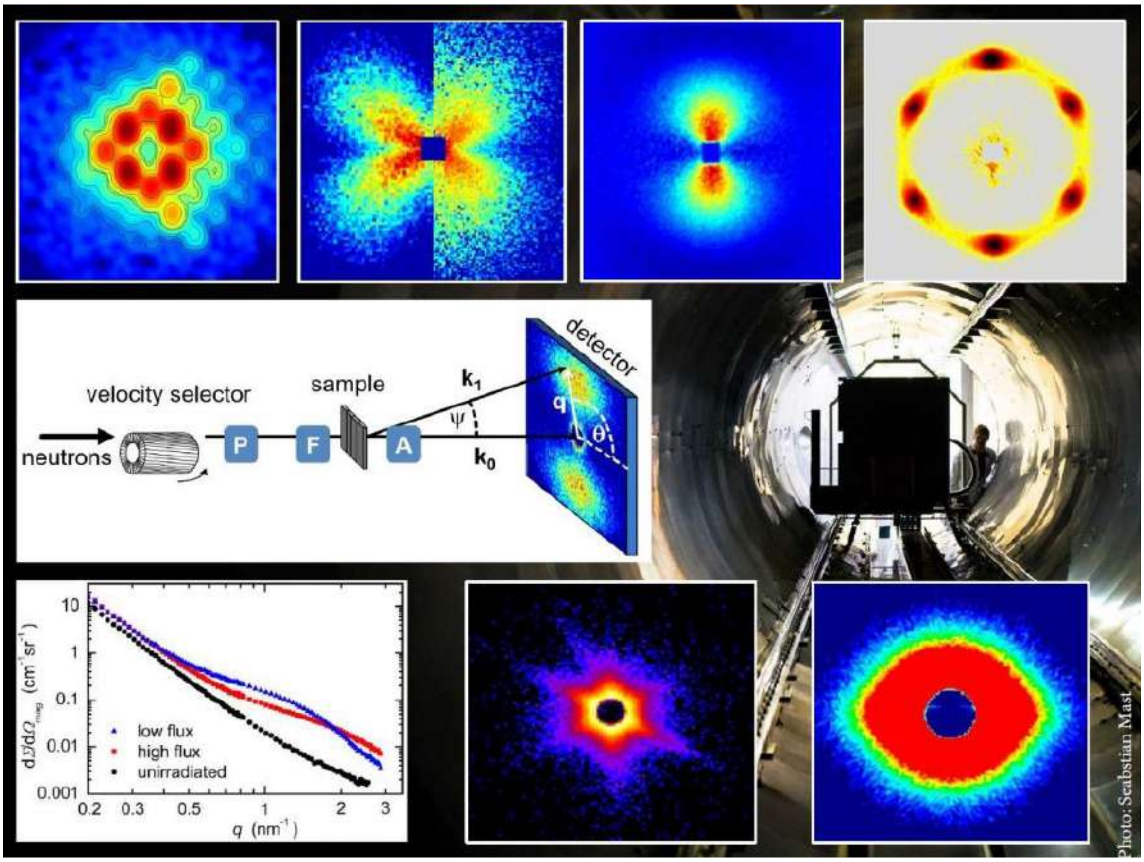

Photo: Seabstian Mast

Heinz Maier-Leibnitz Zentrum (MLZ)
MLZ Conference 2021: Neutrons for Life Sciences
08 – 11 June 2021, virtual event

The MLZ Conference 2021, initially planned for 2020 (due to the Covid-19 pandemic it has been postponed to 2021), took place from 6 to 11 June 2021 in a purely virtual format and intended to bring together experts in the field of life sciences regardless of having used neutron scattering techniques or not. The conference tried to cover all relevant fields of life sciences and aimed to discuss on how to improve neutron instrumentation, access to neutron beam time, sample environments and support labs for future life sciences users.

On the four day conference, topics on protein structure, function and dynamics, drug design and delivery, biological surface and interfaces, neutron and complementary methods in biology, Life Sciences at the PIK reactor as well as neutrons in the fight against virus diseases were discussed. A total of 211 visitors with 66 participants on average in each session from 24 countries attended the 14 sessions (46 talks, 37 posters).

MLZ Conference
Neutrons for Life Sciences
June 8th - 11th, 2021, online event

Life Sciences is a rapidly expanding field in the neutron scattering community. The number of users at the MLZ performing experiments related to Life Sciences is constantly growing. Be it contrast variation for matching out proteins, DNA or lipids or the hunt for catalytically active hydrogen atoms, neutrons play an important role in structure determination of biologically relevant molecules. Using incoherent and coherent neutron scattering, investigations of equilibrium dynamics of biological systems are possible on a wide time scale. The conference covers all relevant fields of Life Sciences and intends to bring together experts in the field regardless whether they have used neutron scattering techniques or not.

- **Protein structure, function and dynamics**
  Peter C. E. Moody
  (Leicester Institute for Structural & Chemical Biology, University of Leicester, UK)
- **Biological membranes, surfaces and interfaces**
  Frank Schreiber
  (Universität Tübingen, Germany)
- **Biological processes**
  Jörg Pieper
  (University of Tartu, Estland)
- **Neutron and complementary methods in biology**
  Andreas Bausch
  (Technische Universität München, Germany)
- **Life Sciences with neutrons in Russia**
  Andrey Konevega
  (Petersburg Nuclear Physics Institute (PNPI), NRC, Russia)
- **Neutrons in the fight against virus diseases**
  Andrey Kovalevsky
  (Oak Ridge National Laboratory, USA)
- **Drug design and delivery**
  Marianna Yanez Arteta
  (AstraZeneca, Schweden)

Important dates for your registration and submission of abstracts

MLZ is a cooperation between:

https://indico.frm2.tum.de/event/230/
mlz-conference@mlz-garching.de

MPI/TUM/LMU
Munich Physics Colloquium: Festive Colloquium for Prof. Dr. Winfried Petry
21 June 2021, virtual event

The Munich Physics Colloquium is a platform for researches in the field of physics. It is jointly organized by the two universities and Max Planck Institutes. The lectures report on current topics in physics and related fields and reflect the interdisciplinary character of modern physics.

On the occasion of Prof. Dr. Petry's 70th birthday, Prof. Dr. Jörg Neugebauer of the Max Planck Institute für Eisenforschung, Düsseldorf, held his presentation entitled "Ab initio descriptors to guide materials design in high-dimensional chemical and structural configuration spaces" on Monday, 21 June 2021, 17:15 h. More than 100 participants attended the virtual colloquium.

Munich School of Engineering (MSE)
11th Energy Colloquium of the Munich School of Engineering:
"Energy Sciences for Europe's Green Deal"
28 – 29 July 2021, Garching, virtual event

Munich School of Engineering
Technical University Munich

11th Energy Colloquium of the Munich School of Engineering
2nd Virtual Edition

Energy Sciences for Europe's Green Deal

July 28 and July 29, 2021

Call for Contributions

After a challenging 2020, this year started with good news: Energy research and policy are playing again a stronger role on an international level. The Green Deal of the EU Commission and the new U.S. policy are reasons for hope and emphasize the importance of technological progress in the energy sector on the way to carbon neutrality. Germany achieved its climate target 2020, mainly driven by a strong power sector with a share of 46% renewable production. However, in other sectors, the effort must be significantly increased.

The 11th energy colloquium of the Munich School of Engineering will present the latest findings of Bavarian energy research. The annual event, a cross-faculty institution, highlights the diversity of research activities on energy-related topics at Bavarian universities. Scientific topics include, but are not limited to, renewable energy sources, energy storage, sustainability in energy supply, sector integration, related simulations and data science. The goal is to connect disciplines, faculties, and universities and nurture knowledge and research, as well as to provide a platform for discussion and exchange.

You are invited to contribute to the 11th Energy Colloquium of the Munich School of Engineering! We encourage doctoral students and young researchers from all energy-related research fields to provide an insight into their research concepts, approaches, methodologies, and results. You can contribute an oral or a poster presentation. The best three contributions in each category will be rewarded. Like last year, the event will be virtual. There will be even more interactions and we will spread the event over two days including the poster session.

More details can be found on **www.mse.tum.de**.

Schedule:	Poster session on July 28 from 1:00 to 6:00 pm Main conference on July 29 from 1:00 to 6:00 pm
Registration:	www.mse.tum.de
Queries:	colloquium@mse.tum.de
Abstract Deadline:	**April 16**
Notification Date:	**April 29**
Publication of Programme:	**June 04**
Poster Deadline:	**July 01**

Heinz Maier-Leibnitz Zentrum (MLZ)
Open Day 2021 at the FRM II
03 October 2021, Garching, MLZ/FRM II

In conjunction with the Mouse Day, the Open Day took place on Sunday, 3rd October 2021, on the premises of the FRM II, 9 AM to 6 PM. On this occasion, more than 200 visitors took the chance to take a look at the reactor pool and learn more about the non-destructive investigation of matter with neutrons. For the first time, the Open Day was also located in the Science Congress Center of the nearby located GALILEO. In the GALILEO, scientists would answer questions about research with neutrons and were given lectures and presented their poster; also films, games, and Lego models of scientific were shown. A total of 60 volunteers helped to make the Open Day 2021 / Mouse Day on 03 October 2021 a successful and informative event.

Heinz Maier-Leibnitz Zentrum (MLZ)
Mouse Day 2021 at the FRM II
03 October 2021, Garching, MLZ/FRM II

On the Mouse Day 2021, families could participate in a special program on the premises of the FRM II. The program lasted 2,5 hours and featured special guided tours and activities especially for children (age: 7-13 years). Scientists of the MLZ were offering tours through the neutron guide hall and the experimental hall in order to explain the various instruments that the scientists of the Heinz Maier-Leibnitz Center (MLZ) use, for example, to investigate the fundamentals of superconductivity or to study the magnetic properties of materials. On the tour, it was also possible to take a look inside the reactor pool.

... am Türöffner-Tag der Maus, 3. Oktober.

Akademie für Lehrerfortbildung Dillingen und TU München
Edgar-Lüscher Lectures "Kernphysik"
06 – 08 October 2021, Dillingen

EDGAR–LÜSCHER–LECTURES DILLINGEN/DONAU 2021
Thema: Kernphysik
Datum: Mittwoch, 6. Oktober bis Freitag, 8. Oktober 2021
Tagungsort: Akademie für Lehrerfortbildung Dillingen
Veranstalter: Akademie für Lehrerfortbildung Dillingen und TU München
wissenschaftliche Leitung: Prof. Dr. Peter Müller-Buschbaum,
Technische Universität München.

Programm

Mittwoch, 06. 10. 2021
15:00 – 15:30 Begrüßung
StR Susanne Dührkoop / Prof. Dr. Peter Müller-Buschbaum (TUM, Physik)

15:30 – 17:00 Einführung in die Kernphysik
Dr. Roman Gernhäuser (TUM, Physik)

18:30 – 20:00 Das Projekt ALICE (A Large Ion Collider Experiment) am CERN
Dr. Stefan Heckel (TUM, Physik)

Donnerstag, 07. 10. 2021
8:30 – 10:00 Die schwache Wechselwirkung
Prof. Dr. Lothar Oberauer (TUM, Physik)

10:00 – 10.30 Kaffeepause

10:30 – 12:00 Struktur exotischer radioaktiver Kerne
Prof. Dr. Thorsten Kröll (TU Darmstadt, Physik)

15:30 – 17:00 Physik jenseits des Standardmodells
Dr. Florian Goertz (MPI Kernphysik, Heidelberg)

18:30 – 20:00 Exotische Kerne
Prof. Dr. Achim Schwenk (TU Darmstadt, Physik)

Freitag, 08. 10. 2021
8:30 – 10:00 Präzisionsmessungen bei niedrigen Energien
Prof. Dr. Bastian Märkisch (TUM, Physik)

10:00 – 10.30 Kaffeepause

10:30 – 12:00 Neutrinooszillationen
Prof. Dr. Dieter Frekers (Universität Münster, Physik)

Ab 12:00 Lehrgangsabschluss
Prof. Dr. Peter Müller-Buschbaum / StR Susanne Dührkoop

P. Müller-Buschbaum
10th SolTech Conference
08 – 11 November 2021, Haus der Bayrischen Wirtschaft, München

SOLAR TECHNOLOGIES
go HYBRID

10th SolTech Conference

November 8 – 11, 2021

Heinz Maier-Leibnitz Zentrum (MLZ)
MLZ User Meeting
07 – 08 December 2021, Garching, virtual event

After the successful virtual MLZ User Meeting 2020 (in combination with the DN2020), the MLZ User Meeting 2021 took also place as a purely virtual format, from 7 to 8 December 2021.
The first day of this virtual meeting was dedicated to specialised workshops organised by the Science Groups. On the second day, the MLZ spokesman Prof. Dr. Martin Müller informed about the current situation at Garching, afterwards there were plenary talks and the poster sessions. Additionally, “Ask the instrument” was offered on both days: Scientists of each instrument were open for all questions.
A total of 374 visitors attended the two days of the event; 30-50 visitors were participating in each session, 100-150 visitors were attending the plenary talks on the second day.

MLZ
USERS2021

9.3 Service to the community

Prof. Dr. Peter Müller-Buschbaum:

- Since 4/2021 spokesperson of Association of Chemical Physics and Polymer Physics (CPP) at Deutsche Physikalische Gesellschaft (DPG)
- Since 1/2021 head of Bavarian research network "Solar Technologies go Hybrid (SolTech)" of the universities Bayreuth, Erlangen-Nürnberg, LMU, TUM, and Würzburg
- Since 1/2019 council member of excellence cluster "ORIGINS"
- 7/2017 until 10/2021 member of the Aptitude Committee of master course Materials Science and Engineering (MSandE) at TUM
- 9/2016 until 10/2021 spokesperson and board member of the Graduate School of "Munich School of Engineering" (MSE) at TUM
- 6/2016 until 10/2021 member of the doctoral committee of "Munich School of Engineering" (MSE) at TUM
- Since 3/2015 member of "Advanced Light Source (ALS) Review Panel"
- Since 6/2014 member of Stanford Synchrotron Radiation Lightsource (SSRL) Review Panel
- Since 9/2012 Associate Editor of journal "ACS Applied Materials & Interfaces" of the American Chemical Society
- Since 3/2012 head of KeyLab "TUM.Solar" at TUM
- Since 2011 member of European Spallation Source (ESS) Scientific Advisory Panel (Reflectivity)
- Since 2011 German representative at the European Polymer Federation (EPF) for polymer physics
- Since 2010 spokesperson of the regenerative energies section (NRG) at the Munich School of Engineering (MSE) of TUM
- Since 2010 member of TUM Energie at TUM
- Since 2010 German representative at the European Synchrotron User Organization (ESUO)
- Since 2008 chairman of "DESY Photon Science User Committee" at the synchrotron radiation laboratory DESY in Hamburg

Prof. Dr. Christine M. Papadakis:

- Since 4/2015 Editor-in-Chief for Colloid & Polymer Science, Springer-Verlag
- Vice women's representative of the Physics Department at TU München

Prof. Dr. Winfried Petry:

- Since 2018 TUM Emeritus of Excellence
- Since 2016 member of the Evaluation Panel for Neutron Research of the Swedish Research Council
- Since 2015 member of the Neutron Scientific Advisory Committee of the National Research Center Kurchatov Institute "Petersburg Nuclear Physics Institute" (PNPI, Gatchina)
- Since 2012 member of the Scientific Advisory Board of NaWi Graz
- Since 2007 member of the Steering Committee of the Laue Langevin Institute and chairman of the instrumentation review panel of the CEA Leon Brillouin Laboratory
- Since 1999 liaison professor of Bayerische Eliteakademie (Bavarian Leadership Academy) and since May 2011 member of the Board of Trustees

10 Publications, talks, posters and funding

10.1 Publications

- S. Akel, M. A. Sharif, R. Al-Esseili, M. A. Al-Wahish, H. A. Hodali, P. Müller-Buschbaum, L. Schmidt-Mende, M. Al-Hussein
  Photovoltaic cells based on ternary P3HT:PCBM:ruthenium(II) complex bearing 8-(diphenylphosphino)quinoline active layer
  J. Coll. Surf. A **622**, 126685 (2021)

- J. Ban, X. Wang, S. Yin, Y. Cheng, L. Ji, P. Müller-Buschbaum, J. Gao, Y. Xia
  Super-small TiO2 nanoparticles homogeneously embedded in mesoporous carbon matrix based on dental methacrylates and KOH activation
  Chemistry Select **6**, 1508-1518 (2021)

- M. Bäumler, S. P. Schwaminger, D. von der Haar-Leistl, S. J. Schaper, P. Müller-Buschbaum, F. E. Wagner, S. Berensmeier
  Characterization of an active ingredient made of nanoscale iron(oxyhydr)oxide for the treatment of hyperphosphatemia
  RSC Advances **11**, 17669-17682 (2021)

- E. Bergendal, P. Gutfreund, G. A. Pilkington, R. A. Campbell, P. Müller-Buschbaum, S. A. Holt, M. W. Rutland
  Tuneable interfacial surfactant aggregates mimic lyototropic phases and facilitate large scale nanopatterning
  Nanoscale **13**, 371-379 (2021)

- C. J. Brett, O. K. Forslund, E. Nocerino, L. P. Kreuzer, T. Widmann, L. Porcar, N. L. Yamada, N. Matsubara, M. Mansson, P. Muller-Buschbaum, L. D. Soderberg, S. V. Roth
  Humidity-induced nanoscale restructuring in PEDOT:PSS and cellulose nanofibrils reinforced biobased organic electronics
  Adv. Electr. Mater. **7**, 2100137(2021)

- C. J. Brett, W. Ohm, B. Fricke, A. E. Alexakis, T. Laarmann, V. Körstgens, P. Müller-Buschbaum, L. D. Söderberg, S. V. Roth
  Nanocellulose-assisted thermally induced growth of silver nanoparticles for optical applications
  ACS Appl. Mater. Interfaces **13**, 27696-27704 (2021)

- D. E. Burkes, I. J. Schwerdt, T. K. Huber, H. Breitkreutz, C. Reiter, W. Petry, J. L. Schulthess, A. M. Casella, A. J. Casella, E. C. Buck, Karl N. Pool, P. J. MacFarlan, M. K. Edwards, F. N. Smith
  Thermal properties of U-Mo alloys irradiated under high fission power density
  J. Nucl. Mater. **547**, 152823 (2021)

- A. Buyruk, D. Blätte, M. Günther, M. A. Scheel, N. F. Hartmann, M. Döblinger, A. Weis, A. Hartschuh, P. Müller-Buschbaum, T. Bein, T. Ameri
  1,10-Phenanthroline as an efficient bifunctional passivating agent for MAPbI3 perovskite solar cells
  ACS Appl. Mater. Interfaces **13**, 32894-32905 (2021)

- W. Cao, S. Yin, M. Plank, A. Chumakov, M. Opel, W. Chen, L. P. Kreuzer, J. E. Heger, M. Gallei, C. J. Brett, M. Schwartzkopf, A. A. Eliseev, E. O. Anokhin, L .A. Trusov, S. V. Roth, P. Müller-Buschbaum
  Spray-deposited anisotropic ferromagnetic hybrid polymer films of PS-b-PMMA and strontium hexaferrite magnetic nanoplatelets
  ACS Appl. Mater. Interfaces **13**, 1592-1602 (2021)

- T. Chemnitz, M. R. Buchner, W. Petry, F. Kraus
  Plasmachemical Synthesis of the binary Hexafluorides of Mo, Os, Ir, Te, and U
  J. Fluorine Chem. **249**, 109862 (2021)

- Q. Chen, C. J. Brett, A. Chumakov, M. Gensch, M. Schwartzkopf, V. Körstgens, L.D. Söderberg, A. Plech, P. Zhang, P. Müller-Buschbaum, S. V. Roth
  Layer-by-layer spray-coating of cellulose nanofibrils and silver nanoparticles for hydrophilic interfaces
  ACS Appl. Nano Mater. **4**, 503-513 (2021)

- W. Chen, R. Guo, H. Tang, K. S. Wienhold, N. Li, Z. Jiang, J. Tang, X. Jiang, L. P. Kreuzer, H. Liu, M. Schwartzkopf, X. W. Sun, S. V. Roth, K. Wang, B. Xu, P. Müller-Buschbaum
  Operando structure degradation study of PbS quantum dot solar cells
  Energy Environ. Sci. **14**, 3420-3429 (2021)

- A. Dey, J. Ye, A. De, E. Debroye, S. K. Ha, E. Bladt, A. S. Kshirsagar, Z. Wang, J. Yin, Y. Wang, L. N. Quan, F. Yan, M. Gao, X. Li, J. Shamsi, T. Debnath, M. Cao, M. A. Scheel, S. Kumar, J. A. Steele, M. Gerhard, L. Chouhan, K. Xu, X.-G. Wu, Y. Li, Y. Zhang, A. Dutta, C. Han, I. Vincon, A. L. Rogach, A. Nag, A. Samanta, B. A. Korgel, C.-J. Shih, D. R. Gamelin, D. H. Son, H. Zeng, H. Zhong, H. Sun, H. V. Demir, I. G. Scheblykin, I. Mora-Seró, J. K. Stolarczyk, J. Z. Zhang, J. Feldmann, J. Hofkens, J. M. Luther, J. Pérez-Prieto, L. Li, L. Manna, M. I. Bodnarchuk, M. V. Kovalenko, M. B. J. Roeffaers, N. Pradhan, O. F. Mohammed, O. M. Bakr, P. Yang, P. Müller-Buschbaum, P. V. Kamat, Q. Bao, Q. Zhang, R. Krahne, R. E. Galian, S. D. Stranks, S. Bals, V. Biju, W. A. Tisdale, Y. Yan, R. L. Z. Hoye, L. Polavarapu
  State of the art and prospects for halide perovskite nanocrystals
  ACS Nano **15**, 10775-10981 (2021)

- M. A. Dyakonova, Y. Li, I. N. Besiri, Z. Di, I. Grillo, C. Tsitsilianis, C. M. Papadakis
  Effect of cosolvent on the rheological properties and self-assembled structures from telechelic polyampholytes
  Colloid Polym. Sci. **299**, 419-428 (2021)

- K. Fang, L. Ma, Y. Cheng, S. Xia, Z. Yang, X. Zuo, L. Ji, J. Gao, P. Müller-Buschbaum, Y. Xia
  Si/Cu/C nanohybrid lithium-ion battery anode with in situ incorporation of non-agglomerated super-small copper nanoparticles based on epoxy resin
  Energy Fuels **35**, 6250-6264 (2021)

- M. Fang, L. Tao, W. Wu, Q. Wei, Y. Xia, P. Li, X. Ran, Q. Zhong, G. Xing, L. Song, P. Müller-Buschbaum, H. Zhang, Y. Chen
  Residual solvent extraction via chemical displacement for efficient and stable perovskite solar cells
  J. Energy. Chem. **61**, 8-14 (2021)

- M. Gensch, M. Schwartzkopf, C. J. Brett, S. J. Schaper, L. P. Kreuzer, N. Li, W. Chen, S. Liang, J. Drewes, O. Polonskyi, T. Strunskus, F. Faupel, P. Müller-Buschbaum, S. V. Roth
  Selective silver nanocluster metallization on conjugated diblock copolymer templates for sensing and photovoltaic applications
  ACS Appl. Nano Mater. **4**, 4245-4255 (2021)

- M. Gensch, M. Schwartzkopf, C. J. Brett, S. J. Schaper, N. Li, W. Chen, S. Liang, J. Drewes, O. Polonskyi, T. Strunskus, F. Faupel, P. Müller-Buschbaum, S. V. Roth
  Correlating optical reflectance with topology of aluminum nanocluster layers growing on partially conjugated diblock copolymer templates
  ACS Appl. Mater. Interfaces **13**, 56663-56673 (2021)

- C. Geiger, J. Reitenbach, C. Henschel, L. P. Kreuzer, T. Widmann, P. Wang, G. Mangiapia, J.-F. Moulin, C. M. Papadakis, A. Laschewsky, P. Müller-Buschbaum
  Ternary nanoswitches realized with multiresponsive PMMA-b-PNIPMAM films in mixed water/acetone vapor atmospheres
  Adv. Eng. Mater. **23**, 2100191 (2021)

- C. Geiger, J. Reitenbach, L. P. Kreuzer, T. Widmann, P. Wang, R. Cubitt, C. Henschel, A. Laschewsky, C. M. Papadakis, P. Müller-Buschbaum
  PMMA-b-PNIPAM thin films display cononsolvency-driven response in mixed water/methanol vapors
  Macromolecules **54**, 3517-3530 (2021)

- H. Gerstenberg, W. Petry
  FRM II (20 MW Germany)
  Book Chapter in: Greenspan, E. (Ed), Encyclopedia of Nuclear Energy, Research Reactor Section, Elsevier,**4**, 113-123 (2021)

- M. Günther, D. Blätte, A. L. Oechsle, S. Sanchez Rivas, A. A. Y. Amin, P. Müller-Buschbaum, T. Bein, T. Ameri
  Increasing photostability of inverted nonfullerene organic solar cells by using fullerene derivatives additives
  ACS Appl. Mater. Interfaces **13**, 19072-19084 (2021)

- R. Guo, D. Han, W. Chen, L. Dai, K. Ji, Q. Xiong, S. Li, L. K. Reb, M. A. Scheel, S. Pratap, N. Li, S. Yin, T. Xiao, S. Liang, A. L. Oechsle, C. L. Weindl, M. Schwartzkopf, H. Ebert, P. Gao, K. Wang, M. Yuan, N. C. Greenham, S. D. Stranks, S. V. Roth, R. H. Friend, P. Müller-Buschbaum
  Degradation mechanisms of perovskite solar cells under vacuum and one atmosphere of nitrogen
  Nature Energy **6**, 977-986 (2021)

- S. Hou, W. Li, S. Watzele, R. M. Kluge, S. Xue, S. Yin, X. Jiang, M. Döblinger, A. Welle, B. Garlyyev, M. Koch, P. Müller-Buschbaum, C. Wöll, A. S. Bandarenka, R. A. Fischer
  Metamorphosis of heterostructured surface-mounted metal-organic frameworks yielding record oxygen evolution mass activities
  Adv. Mater. **33**, 2103218 (2021)

- J. Hu, J. Liu, H. Chen, X. Ran, H. Zhang, P. Li, L. Song, P. Müller-Buschbaum, Y. Xia, Y. Chen
  A bromide-induced highly oriented low-dimensional Ruddlesden–Popper phase for efficient and stable perovskite solar cells
  J. Mater. Chem. **A 9**, 15068-15075 (2021)

- N. Hu, C. Chen, E. Metwalli, L. Bießmann, C. Herold, J. Fu, R. Cubitt, Q. Zhong, P. Müller-Buschbaum
  Hydration and thermal response kinetics of a cross-linked thermoresponsive copolymer film on a hydrophobic PAN substrate coating probed by in-situ neutron reflectivity
  Langmuir **37**, 6819-6829 (2021)

- N. Hu, W. Wang, L. Lei, H. Fan, Y. Tan, H. Yuan, Z. Mao, P. Müller-Buschbaum, Q. Zhong
  A hydrogen evolution system based on hybrid nanogel films with capabilities of spontaneous moisture collection and high light harvesting
  Green Chem. **23**, 8969-8978 (2021)

- Y. Hu, T. Niu, Y. Liu, Y. Zhou, Y. Xia, C. Ran, Z. Wu, L. Song, P. Müller-Buschbaum, Y. Chen, W. Huang
  Flexible perovskite solar cells with high power-per-weight: progress, application, and perspectives
  ACS Energy Lett. **6**, 2917-2943 (2021)

- Y. Huang, T. Xiao, Z. Xie, J. Zheng, Y. Su, W. Chen, K. Liu, M. Tang, P. Müller-Buschbaum, L. Li
  Single-layered reflective metasurface achieving simultaneous spin-selective perfect absorption and efficient wavefront manipulation
  Adv. Optical Mater. **9**, 2001663 (2021)

- Y. Huang, T. Xiao, Z. Xie, J. Zheng, Y. Su, W. Chen, K. Liu, M. Tang, J. Zhu, P. Müller-Buschbaum, L. Li
  Multistate nonvolatile metamirrors with tunable optical chirality
  ACS Appl. Mater. Interfaces **13**, 45890-45897 (2021)

- X. Iltis, D. Drouan, T. Blay, I. Zacharie, C. Sabathier, C. Onofri, C. Steyer, C. Schwarz, B. Baumeister, J. Allenoc, B. Stepnik, W. Petry
  Microstructural characteristics of a fresh U (Mo) monolithic mini-plate: Focus on the Zr coating deposited by PVD
  Nucl. Eng. Technol. **8**, 2629-2639 (2021)

- S. Jaksch, A. Chennevière, S. Désert, T. Kozielewski, H. Feilbach, P. Lavie, R. Hanslik, A. Gussen, S. Butterweck, R. Engels, H. Frielinghaus, S. Förster, P. Müller-Buschbaum
  Technical specification of the small-angle neutron scattering instrument SKADI at the european spallation source
  Applied Sciences **11**, 3620 (2021)

- S. Jaksch, O. Holderer, H. Frielinghaus, A. Koutsioumpas, P. Zolnierczuk, D. W. Hayward, S. Förster, P. Müller-Buschbaum
  Influence of NaCl on the structure and dynamics of phospholipid layers
  Frontiers in Physics **9**, 628219 (2021)

- F. A. Jung, M. Schart, L. Bührend, E. Meidinger, J.-J. Kang, B.-J. Niebuur, S. Ariaee, D. S. Molodenskiy, D. Posselt, H. Amenitsch, C. Tsitsilianis, C. M. Papadakis
  Highly tunable nanostructures in a doubly responsive pentablock terpolymer in solution and in thin films
  Adv. Funct. Mater. **310**, 2102905 (2021)

- J.-J. Kang, K. Shehu, C. Sachse, F. A. Jung, C.-H. Ko, L. C. Barnsley, R. Jordan, C. M. Papadakis
  A molecular brush with thermoresponsive poly(2-ethyl-2-oxazoline) side chains: A structural investigation
  Colloid Polym. Sci. **299**, 193-203 (2021)

- L. Katzenmeier, L. Carstensen, S. J. Schaper, P. Müller-Buschbaum, A. S. Bandarenka
  Characterization and quantification of depletion and accumulation layers in solid-state Li+-conducting electrolytes using in situ spectroscopic ellipsometry
  Adv. Mater. **33**, 2100585 (2021)

- C.-H. Ko, C. Henschel, G. P. Meledam, M. A. Schroer, R.Guo, L. Gaetani, P. Müller-Buschbaum, A. Laschewsky, C. M. Papadakis
  Co-nonsolvency effect in solutions of poly(methyl methacrylate)-b-poly(N-isopropylacrylamide) diblock copolymers in water/methanol mixtures
  Macromolecules **54**, 5825-5837 (2021)

- C.-H. Ko, C. Henschel, G. P. Meledam, M. A. Schroer, P. Müller-Buschbaum, A. Laschewsky, C. M. Papadakis
  Self-assembled micelles from thermoresponsive poly(methyl methacrylate)-b-poly(N-isopropylacrylamide) diblock copolymers in aqueous solution
  Macromolecules **54**, 384-397 (2021)

- V. Kochetov, M. Mühlbauer, A. Schökel, T. Fischer, T. Müller, M. Hofmann, P. Staron, U. Lienert, W. Petry, A. Senyshyn
  Powder diffraction computed tomography: a combined synchrotron and neutron study
  J. Phys.: Condens. Matter **33**, 105901 (2021)

- R. M. Kluge, N. Saxena, P. Müller-Buschbaum
  A solution-processable polymer-based thin-film thermoelectric generator
  Adv. Energy Sustainability Res. **2**, 2000060 (2021)

- L. P. Kreuzer, C. Geiger, T. Widmann, P. Wang, R. Cubitt, V. Hildebrand, A. Laschewsky, C. M. Papadakis, P. Müller-Buschbaum
  Solvation behavior of poly(sulfobetaine)-based diblock copolymer thin films in mixed water/methanol vapors
  Macromolecules **54**, 7147-7159 (2021)

- L. P. Kreuzer, C. Lindenmeir, C. Geiger, T. Widmann, V. Hildebrand, A. Laschewsky, C. M. Papadakis, P. Müller-Buschbaum
  Poly(sulfobetaine) versus poly(N-isopropylmethacrylamide): Co-nonsolvency-type behavior of thin films in water/methanol atmosphere
  Macromolecules **54**, 1548-1556 (2021)

- L. P. Kreuzer, T. Widmann, C. Geiger, P. Wang, A. Vagias, J. E. Heger, M. Haese, V. Hildebrand, A. Laschewsky, C. M. Papadakis, P. Müller-Buschbaum
  Salt-dependent phase transition behavior of doubly thermoresponsive poly(sulfobetaine)-based diblock copolymer thin films
  Langmuir **37**, 9179-9191 (2021)

- M. Kühnhammer, T. Widmann, L. P. Kreuzer, A. J. Schmid, L. Wiehemeier, H. Frielinghaus, S. Jaksch, T. Bögershausen, P. Barron, H. Schneider, A. Hiess, P. Müller-Buschbaum, T. Hellweg, R. von Klitzing, O. Löhmann
  Flexible sample environments for the investigation of soft matter at the European Spallation Source: Part III – The macroscopic foam cell
  Applied Sciences **11**, 5116 (2021)

- L. Lei, W. Wang, Z. Xie, X. Wu, A. K. Yadav, P. Müller-Buschbaum, H. Fan
  A graphitic carbon nitride metal-free visible light photocatalyst with controllable carbon self-doping towards efficient hydrogen evolution
  Sustainable Energy Fuels **5**, 5227-5235 (2021)

- M. M. S. Lencina, C.-H. Ko, F. A. Jung, R. Schweins, M. Rikkou-Kalourkoti, C. S. Patrickios, C. M. Papadakis, C. Tsitsilianis
  Effect of pH on the dynamics and structure of thermoresponsive telechelic polyelectrolyte networks: Impact on hydrogel injectability
  ACS Appl. Polym. Mater. **3**, 819–829 (2021)

- F. Li, Y. Liu, G. Shi, W. Chen, R. Guo, D. Liu, Y. Zhang, Y. Wang, X. Meng, X. Zhang, Y. Lv, W. Deng, Q. Zhang, Y. Shi, Y. Chen, K. Wang, Q. Shen, Z. Liu, P. Müller-Buschbaum, W. Ma
  Matrix manipulation of directly-synthesized PbS quantum dot inks enabled by coordination engineering
  Adv. Funct. Mater. **31**, 2104457 (2021)

- N. Li, R. Guo, W. Chen, V. Körstgens, J. E. Heger, S. Liang, C. J. Brett, M. A. Hossain, J. Zheng, P. S. Deimel, A. Buyruk, F. Allegretti, M. Schwartzkopf, J. G. C. Veinot, G. Schmitz, J. V. Barth, T. Ameri, S. V. Roth, P. Müller-Buschbaum
  Tailoring ordered mesoporous titania films via introducing germanium nanocrystals for enhanced electron transfer photoanodes for photovoltaic applications
  Adv. Funct. Mater. **31**, 2102105 (2021)

- X Li, S. Soria, W. Gan, M. Hofmann, M. Schulz, M. Hoelzel, H. G. Brokmeier, W. Petry
  Multi-scale phase analyses of strain-induced martensite in austempered ductile iron (ADI) using neutron diffraction and transmission techniques
  J. Mater. Sci. **56**, 5296–5306 (2021)

- S. Liang, W. Chen, S. Yin, S. J. Schaper, R. Guo, J. Drewes, N. Carstens, T. Strunskus, M. Gensch, M. Schwartzkopf, F. Faupel, S. V. Roth, Y. Cheng, P. Muller-Buschbaum
  Tailoring the optical properties of sputter-deposited gold nanostructures on nanostructured titanium dioxide templates based on in situ grazing-incidence small-angle x-ray scattering determined growth laws
  ACS Appl. Mater. Interfaces **13**, 14728-14740 (2021)

- S. Liang, Y. Cheng, X. Wang, Z. Xu, L. Ma, H. Xu, Q. Ji, X. Zuo, P. Müller-Buschbaum, Y. Xia
  Impact of CO2 activation on the structure, composition, and performance of Sb/C nanohybrid lithium/sodium-ion battery anodes
  Nanoscale Adv. **3**, 1942-1953 (2021)

- L. Lin, L. Shen, J. Zhang, Y. Xu, Z. Fang, P. Müller-Buschbaum, Q. Zhong
  Ionic hydrogels based wearable sensors to monitor the solar radiation dose for vitamin D production and sunburn prevention
  ACS Appl. Mater. Interfaces **13**, 45995-46002 (2021)

- S.-H. Lin, C. M. Papadakis, J.-J. Kang, J.-M. Lin, S.-h. Hsu
  Injectable phenolic-chitosan self-healing hydrogel with hierarchical micelle architectures and fast adhesiveness
  Chem. Mater. **33**, 3945–3958 (2021)

- Y. Miao, B. Ye, J. Shi, K. Mo, L. Jamison, S. Bhattacharya, A. Oaks, W. Petry, A. M. Yacout
  Microstructure investigations of temperature effect on Al-UMo diffusion couples irradiated by swift Xe ions
  J. Nucl. Mater. **547**, 152757 (2021)

- P. Neibecker, X. Xu, D. Simonne, L. Hollender, F. Porcher, A. Senyshyn, T. Omori, R. Kainuma, W. Petry, M. Leitner
  Atomic and magnetic order along the half to full Heusler transition in Ni1+x MnSb
  Phys. Status Solidi B **2021**, 2100174 (2021)

- B.-J. Niebuur, W. Lohstroh, C.-H. Ko, M.-S. Appavou, A. Schulte, C. M. Papadakis
  Pressure dependence of water dynamics in concentrated aqueous poly(N-isopropylacrylamide) solutions with a methanol cosolvent
  Macromolecules **54**, 4387-4400 (2021)

- B.-J. Niebuur, L. Chiappisi, F. A. Jung, X. Zhang, A. Schulte, C. M. Papadakis
  Nanoscale disintegration kinetics of mesoglobules in aqueous poly(N-isopropylacrylamide) solutions revealed by small-angle neutron scattering and pressure jumps
  RSC Nanoscale **13**, 13421-13426 (2021)

- B.-J. Niebuur, H. Hegels, M. Tena-Solsona, P. S. Schwarz, J. Boekhoven, C. M. Papadakis
  Droplet formation by chemically fueled self-assembly: The role of precursor hydrophobicity
  J. Phys. Chem. B. **125**, 13542–13551 (2021)

- A. L. Oechsle, J. E. Heger, N. Li, S. Yin, S. Bernstorff, P. Müller-Buschbaum
  Correlation of thermoelectric performance, domain morphology and doping level in PEDOT:PSS thin films post-treated with ionic liquids
  Macromol. Rapid Com. **42**, 2100397 (2021)

- A. R. Osi, H. Zhang, J. Chen, Y. Zhou, R. Wang, J. Fu, P. Müller-Buschbaum, Q. Zhong
  Three-dimensional-printable thermo/photo-cross-ed methacrylated chitosan-gelatin hydrogel composites for tissue engineering
  ACS Appl. Mater. Interfaces **13**, 22902-22913 (2021)

- N. Paul, J. Huang, C. Liu, T. Lin, C. Ouyang, Z. Liu, C. Chen, Z. Chen, Z. Weng, M. Schwartzkopf, S. V. Roth, P. Müller-Buschbaum, A. Paul
  Real–time observation of nucleation and growth of Au on CdSe quantum dot templates
  Sci. Rep. **11**, 18777 (2021)

- V. Pipich, T. Starc, J. Buitenhuis, R. Kasher, W. Petry, Y. Oren, D. Schwahn
  Silica Fouling in Reverse Osmosis Systems–Operando Small-Angle Neutron Scattering Studies
  Membranes **11, (6)**, 413 (2021)

- S. Pratap, F. Babbe, N. S. Barchi, Z. Yuan, T. Luong, Z. Haber, T.-B. Song, J. L. Slack, C. V. Stan, N. Tamura, C. M. Sutter-Fella, P. Müller-Buschbaum
  Out-of-equilibrium processes in crystallization of organic-inorganic perovskites during spin coating
  Nat. Commun. **12**, 5624 (2021)

- D. Petz, M. J. Mühlbauer, V. Baran, A. Schökel, V. Kochetov, M. Hofmann, V. Dyadkin, P. Staron, G. Vaughan, U. Lienert, P. Müller-Buschbaum, A. Senyshyn
  Lithium distribution and transfer in high-power 18650-type Li-ion cells at multiple length scales
  Energy Storage Mater. **41**, 546-553 (2021)

- D. Petz, M. J. Mühlbauer, A. Schökel, K. Achterhold, F. Pfeiffer, T. Pirling, M. Hofmann, A. Senyshyn
  Heterogeneity of Graphite Lithiation in State-of-the-Art Cylinder-Type Li-Ion Cells
  Batter. Supercaps. **4**, 327-335 (2021)

- Z. Qian, L. Chen, J. Wang, L. Wang, Y. Xia, X. Ran, P. Li, Q. Zhong, L. Song, P. Müller-Buschbaum, Y. Chen, H. Zhang
  Manipulating SnO2 growth for efficient electron transport in perovskite solar cells
  Adv. Mater. Interf. **8**, 2100128 (2021)

- J. Qiu, Y. Lin, X. Ran, Q. Wei, X. Gao, Y. Xia, P. Müller-Buschbaum, Y. Chen
  Efficient and stable Ruddlesden-Popper layered tin-based perovskite solar cells enabled by ionic liquid bulky spacer
  Sci. China Chem. **64**, 1577-1585 (2021)

- L. K. Reb, M. Böhmer, B. Predeschly, S. Grott, C. Dreißigacker, J. Drescher, A. Meyer, P. Müller-Buschbaum
  An experiment for novel material thin-film solar cell characterization on sounding rocket flights
  Rev. Sci. Instr. **92**, 074501 (2021)

- D. Salvato, J. Shi, H. Breitkreutz, W. Van Renterghem, B. Baumeister, C. Schwarz, A. Leenaers, S. Van den Berghe, C. Detavernier, W. Petry
  U(Mo) grain refinement induced by irradiation with high energy iodine
  J. Nucl. Mater. **548**, 152850 (2021)

- S. J. Schaper, F. C. Löhrer, S. Xia, C. Geiger, M. Schwartzkopf, P. Pandit, J. Rubeck, B. Fricke, S. Frenzke, A. M. Hinz, N. Carstens, O. Polonskyi, T. Strunskus, F. Faupel, S. V. Roth, P. Müller-Buschbaum
  Revealing the growth of copper on polystyrene-block-poly(ethylene oxide) diblock copolymer thin films with in situ GISAXS
  Nanoscale **13**, 10555-10565 (2021)

- S. J. Schaper, E. Metwalli, M. V. Kaeppel, A. Kriele, R. Gilles, K. N. Raftopoulos, P. Müller-Buschbaum
  Morphology – ionic conductivity relationship in polymer-titania hybrid electrolytes for lithium-ion batteries
  ACS Appl. Energy Mater. **4**, 13438-13443 (2021)

- A. J. Schmid, L. Wiehemeier, S. Jaksch, H. Schneider, A. Hiess, T. Bögershausen, T. Widmann, J. Reitenbach, L. P. Kreuzer, M. Kühnhammer, O. Löhmann, G. Brandl, H. Frielinghaus, P. Müller-Buschbaum, R. von Klitzing, T. Hellweg
  Flexible sample environments for the investigation of soft matter at the European Spallation Source: Part I – The in situ SANS/DLS setup
  Applied Sciences **11**, 4089 (2021)

- D. M. Schwaiger, W. Lohstroh, P. Müller-Buschbaum
  The influence of the blend ratio, solvent additive and post-production treatment on the polymer dynamics in PTB7:PCBM blend films
  Macromolecules **54**, 6534-6542 (2021)

- P. S. Schwarz, L. Tebcharani, J. E. Heger, P. Müller-Buschbaum, J. Boekhoven
  Chemically fueled materials with a self-immolative mechanism: transient materials with a fast on/off response
  Chem. Sci. **12**, 9969-9976 (2021)

- M. Schwartzkopf, S.-J. Wöhnert, V. Waclawek, N. Carstens, A. Rothkirch, J. Rubeck, M. Gensch, J. Drewes, O. Polonskyi, T. Strunskus, A. M. Hinz, S. J. Schaper, V. Körstgens, P. Müller-Buschbaum, F. Faupel, S. V. Roth
  Real-time insight into nanostructure evolution during the rapid formation of ultra-thin gold layers on polymers
  Nanoscale Horizon **6**, 132-138 (2021)

- K. Shehu, C. Bojanowski, A. Bergeron, W. Petry, C. Reiter
  First steps to coupled hydraulic and mechanical calculations within a parameter study to define possible core designs for the conversion of FRM II
  EPJ Web of Conferences **247**, 08011 PHYSOR 2020 (2021)

- X. Song, L. Hou, R. Guo, Q. Wei, L. Yang, X. Jiang, S. Tu, A. Zhang, Z. Kan, W. Tang, G. Xing, P. Müller-Buschbaum
  Synergistic interplay between asymmetric backbone conformation, molecular aggregation, and charge-carrier dynamics in fused-ring electron acceptor-based bulk heterojunction solar cells
  ACS Appl. Mater. Interfaces **13**, 2961-2970 (2021)

- R. Stene, B. Scheibe, S. I. Ivlev, A. J. Karttunen, W. Petry, F. Kraus
  Photochemical Synthesis of Tungsten Pentafluoride, WF5
  ZAAC 647, **4**, 218-224 (2021)

- L. Sun, M. Yang, X. Dong, L. Hu, L. Hu, C. Xie, T. Liu, F. Qin, W. Wang, Y. Jiang, M. Wu, W. Cao, F. A. Larrain, C. Fuentes-Hernandez, K. Meng, B. Kippelen, P. Müller-Buschbaum, Y. Zhou
  Efficient electrical doping of organic semiconductors via an orthogonal liquid-liquid contact
  Adv. Funct. Mater. **31**, 2009660 (2021)

- S. Szabó, F. Yang, W. Lohstroh, W. Petry
  Self-diffusion in single component liquid metals: a case study of mercury
  J. Phys.: Condens. Matter **33**, 375101 (2021)

- L. Tao, J. Qiu, B. Sun, X. Wang, X. Ran, L. Song, W. Shi, Q. Zhong, P. Li, H. Zhang, Y. Xia, P. Müller-Buschbaum, Y. Chen
  Stability of mixed-halide wide bandgap perovskite solar cells: Strategies and progress
  J. Energy Chemistry **61**, 395-415 (2021)

- T. Tian, S. Yin, S. Tu, C. L. Weindl, K. S. Wienhold, S. Liang, M. Schwartzkopf, S. V. Roth, P. Müller-Buschbaum
  Morphology transformation pathway of block copolymer-directed co-assembly of ZnO hybrid films monitored in situ during slot-die coating
  Adv Fuct. Mater. **31**, 2105644 (2021)

- A. Vagias, A. Papagiannopoulos, L. P. Kreuzer, D. Giaouzi, S. Busch, S. Pispas, P. Müller-Buschbaum
  Effects of polymer block length asymmetry and temperature on the nanoscale morphology of thermoresponsive double hydrophilic block copolymers in aqueous solutions
  Macromolecules **54**, 7298-7313 (2021)

- X. Wang, A. Funke, Y. Cheng, F. Song, S. Yin, S. Liang, X. Zou, J. Gao, P. Müller-Buschbaum, Y. Xia
  Continuous fast pyrolysis synthesis of TiO2/C nanohybrid lithium-ion battery anode
  Nano Select **2**, 1770-1778 (2021)

- Y. Wang, L. Chao, T. Niu, D. Li, Q. Wei, H. Wu, J. Qiu, H. Lu, C. Ran, Q. Zhong, L. Song, G. Xing, Y. Xia, Y. Chen, P. Müller-Buschbaum, W. Huang
  Efficient and stable perovskite solar cells by fluorinated ionic liquid induced component interaction
  Solar RRL **5**, 2000582 (2021)

- X. Wang, T. Zheng, Y. Cheng, S. Yin, Y. Xia, Q. Ji, Z. Xu, S. Liang, L. Ma, X. Zuo, J.-Q. Meng, J. Zhu, P. Müller-Buschbaum
  SnO2/Sn/carbon nanohybrid lithium-ion battery anode with high reversible capacity and excellent cyclic stability
  Nano Select **2**, 642-653 (2021)

- T. Widmann, L. P. Kreuzer, M. Kühnhammer, A. J. Schmid, L. Wiehemeier, S. Jaksch, H. Frielinghaus, O. Löhmann, H. Schneider, A. Hiess, R. von Klitzing, T. Hellweg, P. Müller-Buschbaum
  Flexible sample environment for the investigation of soft matter at the European Spallation Source: Part II - The GISANS setup
  Applied Sciences **11**, 4036 (2021)

- D. Yang, B. Cao, P. Müller-Buschbaum
  How to choose an interfacial modifier for organic photovoltaics using simple surface energy considerations
  ACS Appl. Mater. Interfaces **13**, 46134-46141 (2021)

- B. Ye, Y. Miao, J. Shi, D. Salvato, K. Mo, L. Jamison, A. Bergeron, G. L. Hofman, A. Leenaers, A. Oaks, A. M. Yacout, S. Van den Berghe, W. Petry, Y. S. Kim
  Temperature effects on interdiffusion of Al and U-Mo under irradiation
  Journal of Nuclear Materials **544**, 152684 (2021)

- S. Yin, W. Cao, Q. Ji, Y. Cheng, L. Song, N. Li, C. L. Weindl, M. Schwartzkopf, S. V. Roth, P. Müller-Buschbaum
  Multidimensional morphology control for PS-b-P4VP templated mesoporous iron (III) oxide thin films
  Adv. Mater. Interf. **8**, 2100141 (2021)

- X. Zhang, L. P. Kreuzer, D. Schwaiger, M. Lu, Z. Mao, R. Cubitt, P. Müller-Buschbaum, Q. Zhong
  Abnormal fast dehydration and rehydration of light- and thermo-dual-responsive copolymer films triggered by UV radiation
  Soft Matter **17**, 2603-2613 (2021)

- X. Zhang, P. Zhang, M. Lu, D. Qi, P. Müller-Buschbaum, Q. Zhong
  Synergistic stain removal achieved by controlling the fractions of light and thermo responsive components in the dual-responsive copolymer immobilized on cotton fabrics by cross-linker
  ACS Appl. Mater. Interfaces **13**, 27372-27381 (2021)

- H. Zheng, D. Li, C. Ran, Q. Zhong, L. Song, Y. Chen, P. Müller-Buschbaum, W. Huang
  Emerging organic/hybrid photovoltaic cells for indoor applications: recent advances and perspectives
  Solar RRL **5**, 2100042 (2021)

- J. Zhou, F. Fang, W. Chen, M. Mei, P. Liu, J. Hao, H. Tang, S. Liang, W. Lei, R. Pan, J. Cheng, P. Müller-Buschbaum, X. W. Sun, W. Cao, K. Zheng, K. Wang
  Luminescent perovskite nanocrystal composites via in situ ligand polymerization towards display application
  J. Mater. Chem. C **9**, 14740-14748 (2021)

10.2 Talks

- C. R. Everett, X. Jiang, M. Reus, H. Zhong, M. Bitsch, M. Plank, M. Gallei, M. Schwartzkopf, S. V. Roth, P. Müller-Buschbaum
  In situ GISAXS analysis of printed hybrid diblock copolymer thin films containing mixed magnetic nanoparticles
  Virtuelle 84. Jahrestagung der DPG und DPG-Tagung der SKM,
  27 September – 01 October 2021

- C. Geiger, J. Reitenbach, L. P. Kreuzer, T. Widmann, P. Wang, R. Cubitt, C. Henschel, A. Laschewsky, C. M. Papadakis, P. Müller-Buschbaum
  Swelling and co-nonsolvency-induced contraction of thin PMMA-b-PNIPAM films in mixed water/methanol vapor
  Osmolyte and Cosolvent Effects in Stimuli-responsive Polymers Virtual Conference,
  25 – 26 February 2021

- C. Geiger, J. Reitenbach, L. P. Kreuzer, T. Widmann, P. Wang, R. Cubitt, C. Henschel, A. Laschewsky, C. M. Papadakis, P. Müller-Buschbaum
  Co-nonsolvency induced response of thin PMMA-b-PNIPAM films in mixed water/methanol vapor
  ACS Virtual Spring Meeting 2021, 05 – 30 April 2021

- C. Geiger, J. Reitenbach, P. Wang, C. Henschel, G. Mangiapia, J.-F. Moulin, A. Laschewsky, C. M. Papadakis, P. Müller-Buschbaum
  Co-nonsolvency behavior of responsive polymers in thin-film/vapor systems
  MLZ User Meeting 2021, 07 – 08 December 2021

- T. Guan, W. Chen, H. Tang, D. Li, S. Liang, C. L. Weindl, Z. Liang, M. Schwartzkopf, S. V. Roth, L. Jiang, P. Müller-Buschbaum
  Decoding the self-assembled plasmonic nano-structure in colloidal quantum dots for photodetectors
  10th International Workshop on Functional Nanocomposites, 07 – 10 September 2021

- R. Guo, D. Han, W. Chen, L. Dai, K. Ji, Q. Xiong S. Li, L. K. Reb, M .A .Scheel, S. Pratap, N. Li, S. Yin, A. L. Oechsle, Tian. Xiao, S .Liang, C. L, Weindl, H. Ebert, N. Greenham, S. Stranks, R. Friend, P. Gao, M. Yuan, M. Schwartzkopf, S. V. Roth, P. Müller-Buschbaum
  Degradation mechanisms of perovskite solar cells under vacuum and one atmosphere of nitrogen
  10th Soltech Conference, 08 – 11 November 2021

- C. Gutiérrez-Bolaños, Lukas V. Spanier, Peter Müller-Buschbaum
  Printed Organic Solar Cells
  MAMASELF Rigi Meeting 2021, 06 – 09 July 2021

- C. Harder, M. Betker, A. Alexakis, E. Erbes, C. J. Brett, A. Chumakov, M. Gensch, B. Sochor, Q. Chen, J. Heger, J. Rubeck, M. Schwartzkopf, D. Söderberg, E. Malmström, P. Müller-Buschbaum, S. V. Roth
  Annealing of polymer colloids on CNF layer
  10th International Workshop on Functional Nanocomposites, 07 – 10 September 2021

- J. E. Heger, W. Chen, S. Yin, C. Geiger, C. J. Brett, W. Ohm, S. V. Roth, P. Müller-Buschbaum
  In situ GIXS investigation of ß-lactoglobulin templated TiO_2 hybrid film formation during spray deposition: An approach to green synthesis of functional materials
  ACS Virtual Spring Meeting 2021, 05 – 16 April 2021

- J. E. Heger, M. Betker, C. Harder, B. Sochor, Y. Zou, C. L. Weindl, M. Schwartzkopf, S. V. Roth, and P. Müller-Buschbaum
  Nanoscale film formation and crystallization of lead-free MBI hybrid perovskite on mesoporous Titania during spray deposition
  10th International Workshop on Functional Nanocomposites, 07 – 10 September 2021

- J. E. Heger, M. Betker, C. Harder, B. Sochor, Y. Zou, C. L. Weindl, M. Schwartzkopf, S. V. Roth, and P. Müller-Buschbaum
  In situ GIXS study on the crystallization and mesoscale film formation of lead-free MBI perovskite on mesoporous titania during spray deposition from a green solvent
  Virtuelle 84. Jahrestagung der DPG und DPG-Tagung der SKM
  27 September – 01 October 2021

- X. Jiang, S. J. Schaper, S. V. Roth, P. Müller-Buschbaum
  In-situ investigation of sputter deposition electrods on different layers based on non-fullerene organic solar cell
  20th SAXS/WAXS/GISAXS Satellite Meeting of
  DESY photon science users' meeting 2021, 19 January 2021

- X. Jiang, P. Chotard, K. Luo, F. Eckmann, S. Tu, M. A. Scheel, M. Schwartzkopf, S. V. Roth, P. Müller-Buschbaum
  Tracking the morphology evolution of active layers for non-fullerene organic solar cells
  16th Coatings Science International 2021, 29 June – 01 July 2021

- F. A. Jung, C. Tsitsilianis, C. M. Papadakis
  Highly tunable nanostructures in a doubly pH-responsive pentablock terpolymer in solution and in thin films
  35th Conference of the European Colloid & Interface Society, Athens, Greece, and online, 05 – 10 September 2021

- V. Körstgens, J. Corella Puertas, P. Müller-Buschbaum
  Tack properties of pressure-sensitive adhesive-coated fiber assemblies
  Virtuelle 84. Jahrestagung der DPG und DPG-Tagung der SKM
  27 September – 01 October 2021

- L. P. Kreuzer, C. Lindenmeir, C. Geiger, T. Widmann, P. Wang, R. Cubitt, V. Hildebrand, A. Laschewsky, C. M. Papadakis, P. Müller-Buschbaum
  Co-nonsolvency-type behavior of polymer thin films in mixed water/methanol vapor
  ACS Virtual Spring Meeting 2021, 05 – 16 April 2021

- N. Li, R. Guo, W. Chen, V. Körstgens, J. E. Heger, S. Liang, C. J. Brett, M. A. Hossain, J. Zheng, P. S. Deimel, A. Buyruk, F. Allegretti, M. Schwartzkopf, J. G. C. Veinot, G. Schmitz, J. V. Barth, T. Ameri, S. V. Roth, P. Müller-Buschbaum
  Tailoring ordered mesoporous titania films via introducing germanium nanocrystals for enhanced electron transfer photoanodes
  ACS Virtual Spring Meeting 2021, 05 – 16 April 2021

- P. Müller-Buschbaum
  In situ and in operando scattering studies on polymer based organic solar cells
  20th SAXS/WAXS/GISAXS Satellite Meeting of
  DESY photon science users' meeting 2021, 19 January 2021

- P. Müller-Buschbaum
  Report of the Users Committee (DPS-UC) - report 2020
  DESY User Meeting, 28 – 29 January 2021

- P. Müller-Buschbaum
  Probing interface transformations in organic solar cells with in-situ and in-operando scattering studies
  ACS Virtual Spring Meeting 2021, 05 – 16 April 2021

- P. Müller-Buschbaum
  Late News: In situ and in operando scattering studies on organic solar cells based on organic semiconductors
  MRS Virtual Spring Meeting, 17 – 23 April 2021

- P. Müller-Buschbaum
  Polymers for photovoltaic applications - challenges and chances for energy harvesting
  US Army Soldier Center, Natick, USA, 22 June 2021

- P. Müller-Buschbaum
  FRM II Status
  Virtual International Facility Directors Meeting at ACNS Conference, 16 July 2021

- P. Müller-Buschbaum
  Polymers for photovoltaic applications - challenges and chances for energy harvesting
  2nd International Conference on Advanced Materials for Energy and Information Technology (AMEIT 2021), Xi'An, China, 30 – 31 August 2021

- P. Müller-Buschbaum
  In-situ study of nanostructure formation during printing of hybrid blend films for solar cell application
  Nanoworkshop 2021, Varese, Italy, 09 September 2021

- P. Müller-Buschbaum
  MLZ – present status and future
  8. Universitätsgruppenleitertreffen des MLZ, Garching, 23 September 2021

- P. Müller-Buschbaum
  Science at the research neutron source Heinz Maier-Leibnitz (FRM II)
  LINXS webinar series, Lund, Sweden, 20 October, 2021

- P. Müller-Buschbaum
  Organic and hybrid nanostructures for applications in solar cells investigated with advanced scattering techniques
  Colloquium, Department of Physics CUHK, 20 October 2021

- P. Müller-Buschbaum
  SolTech Conference opening
  10th SolTech Conference, Munich, 08 - 11 November 2021

- P. Müller-Buschbaum
  Functional materials
  TUM-Tsinghua SIGS Online Research Workshop in the Area of Smart Materials, Shenzhen, China, 16 November 2021

- P. Müller-Buschbaum
  Defect and energy level tuning of printed hybrid perovskite films for photovoltaic applications
  e-conversion Scientific Advisory Board, Munich, 22 November 2021

- P. Müller-Buschbaum
  Next generation solar cells studied with advanced neutron scattering methods
  7th Conference on Neutron Scattering (CNS-2021), Mumbai, India
  25 – 27 November 2021

- P. Müller-Buschbaum
  Switching kinetics of thermo-responsive thin film nanostructures
  International Chemical Congress of Pacific Basin Societies (Pacifichem 21)
  Honolulu, USA, 17 December 2021

- B.-J. Niebuur, L. Chiappisi, F. A. Jung, X. Zhang, A. Schulte, C. M. Papadakis
  Kinetics of mesoglobules formation and disintegration in solutions of thermoresponsive polymers after fast pressure jumps
  ACS Virtual Spring Meeting 2021, 05 – 16 April 2021

- B.-J. Niebuur, V. Pipich, M.-S. Appavou, A. Schulte, C. M. Papadakis
  Poly(N-isopropylacrylamide) mesoglobules under pressure
  Virtual MLZ User Meeting 2021, 07 – 08 December 2021

- C. M. Papadakis
  Kinetics of phase separation and dissolution in solutions of thermoresponsive polymers after fast pressure jumps
  CENS Colloquium, Munich, 15 January 2021

- C. M. Papadakis
  Thin films from multiresponsive pentablock polymers
  IESL Seminar, Institute of Electronic Structure and Laser, FORTH
  Heraklion, Greece, 03 March 2021

- C. M. Papadakis, F. .A. Jung, A. V. Berezkin, D. Posselt, D.-M. Smilgies
  Solvent vapor annealing of diblock copolymer thin films with a mixture of solvents having different selectivities
  APS March Meeting, online, 15 – 19 March 2021

- C. M. Papadakis
  Multiresponsive multiblock polymers
  TUM Virtual Kickoff Meeting ARTEMIS, 11 May 2021

- C. M. Papadakis, B.-J. Niebuur, L. Chiappisi, F. A. Jung, X. Zhang, A. Schulte
  Kinetics of mesoglobule formation and disintegration in solutions of thermoresponsive polymers after fast pressure jumps
  25th Congress and General Assembly of the International Union of Crystallography
  Hybrid event in Prague, Czech Republic, and online, 14 – 21 August 2021

- C. M. Papadakis, F. A. Jung, C. Tsitsilianis
  Tunable self-assembled hydrogels from block copolymers with thermoresponsive and pH-responsive blocks
  Virtuelle 84. Jahrestagung der DPG und DPG-Tagung der SKM
  27 September – 01 October 2021

- W. Petry
  Isotope production for medicine, industry and research by Research Reactors.
  LEU-FOReVER Summer School, 26 – 29 April 2021

- W. Petry
  Neutron Capture produced radioisotopes for diagnostics and therapy –opportunities and challenges
  MLZ Conference, Neutrons for Life Sciences, Garching, 08 – 11 June 2021

- W. Petry
  64 years of cutting-edge research with neutrons in Garching – How science and politics are intertwined
  MLZ Conference, Neutrons for Life Sciences, Garching, 08 – 11 June 2021

- W. Petry
  Neutrons - for what?
  Seminar of Iranic nuclear physicists (virtual), 06 July 2021

- W. Petry
  Neutronen – wie und wozu?
  Bayerische Elite Akademie, Techniktag der BEA, Garching, 13 August 2021

- W. Petry
  Radioisotopes for medicine produced by neutron capture – opportunities and challenges
  GdCh Wissenschaftsforum 2021, Fachgruppe Nuklearchemie, 30 August 2021

- W. Petry
  Kernenergie - vom Winde verweht
  Rotary Club Tegernsee, Seefeld, 21 October 2021

- W. Petry
  Excellent European neutron sources, from past to future
  Conference on Neutron and Synchrotron Radiation
  for Science and Technologies, 13 December 2021

- L. K. Reb, M. Böhmer, B. Predeschly, S. Grott, C. L. Weindl, G. I. Ivandekic, R. Guo, C. Dreißigacker, J. Drescher, R. Gernhäuser, A. Meyer, P. Müller-Buschbaum
  Characterizing organic solar cells in space
  ACS Virtual Spring Meeting 2021, 05 – 16 April 2021

- L. K. Reb, M. Böhmer, B. Predeschly, S. Grott, C. L. Weindl, G. I. Ivandekic, R. Guo, C. Dreißigacker, J. Drescher, R. Gernhäuser, A. Meyer, P. Müller-Buschbaum
  Perovskite solar cells for space application
  MRS Virtual Spring Meeting, 17 – 23 April 2021

- L. K. Reb, M. Böhmer, B. Predeschly, S. Grott, C. L. Weindl, G. I. Ivandekic, R. Guo, C. Dreißigacker, J. Drescher, R. Gernhäuser, A. Meyer, P. Müller-Buschbaum
  Emerging thin-film solar cell technologies reaching space
  11th Energy Colloquium of the Munich School of Engineering, 28 – 29 July 2021

- L. K. Reb, M. Böhmer, B. Predeschly, S. Grott, C. L. Weindl, G. I. Ivandekic, R. Guo, C. Dreißigacker, J. Drescher, R. Gernhäuser, A. Meyer, P. Müller-Buschbaum
  Perovskite and organic solar cells generate power in space
  Virtuelle 84. Jahrestagung der DPG und DPG-Tagung der SKM
  27 September – 01 October 2021

- M. A. Scheel
  In-situ and in-operando scattering studies on polymer based organic solar cells
  20th SAXS/WAXS/GISAXS Satellite Meeting of
  DESY photon science users' meeting 2021, 19 January 2021

- M. A. Scheel
  In situ GIWAXS phase and texture evolution tracking of the formation of 2-step slot-die coated $MAPbI_3$
  ACS Virtual Spring Meeting 2021, 05 – 16 April 2021

- M. A. Scheel
  In situ GIWAXS analysis of $MAPbI_3$ *formation*
  Virtuelle 84. Jahrestagung der DPG und DPG-Tagung der SKM
  27 September – 01 October 2021

- M. A. Scheel
  Perovskite thin-films: From in situ to in space characterization
  10th SolTech Conference, Munich, 08 – 11 November 2021

- D. M. Schwaiger, W. Lohstroh, P. Müller-Buschbaum
  Dynamics in polymer-fullerene blends for photovoltaic applications and the influence of performance enhancing measures
  Virtuelle 84. Jahrestagung der DPG und DPG-Tagung der SKM
  27 September – 01 October 2021

- D. M. Schwaiger, W. Lohstroh, P. Müller-Buschbaum
  Dynamics in polymer-fullerene blends for photovoltaic applications, studied with quasielastic neutron scattering
  Virtual MLZ User Meeting 2021, 07 – 08 December 2021

- A. Vagias, A. Papagiannopoulos, L. P. Kreuzer, D. Giaouzi, S. Busch, S. Pispas, P. Müller-Buschbaum
  Block length asymmetry and temperature effects on the nanoscale morphology of thermoresponsive double hydrophilic block copolymers in aqueous solutions
  ACS Virtual Spring Meeting 2021, 05 – 16 April 2021

- A. Vagias, A. Papagiannopoulos, L. P. Kreuzer, D. Giaouzi, S. Busch, S. Pispas, P. Müller-Buschbaum
  Block length asymmetry and temperature effects on the nanoscale morphology of thermoresponsive double hydrophilic block copolymers in aqueous solutions
  MLZ Conference 2021: Neutrons for Life Sciences, 08 –11 June 2021

- A. Vagias, S. J. Schaper, J. E. Heger, Y. Zou, S. Yin, C. Geiger, M. Schwartzkopf, M. Gensch, A. Laschewsky, S. V. Roth, P. Müller-Buschbaum
  Monitoring nanostructural transformations during gold sputtering
  on zwitterionic thin polymer films
  20th SAXS/WAXS/GISAXS Satellite Meeting of
  DESY photon science users' meeting 2021, 19 January 2021
- C. L. Weindl, C. E. Fajman, M. A. Giebel, T. F. Fässler, P. Müller-Buschbaum
  Amphiphilic diblock copolymer templated Si/Ge/C thin films
  ATUMS: Annual Meeting, 12 November 2021

10.3 Posters

- J. Allwang, Y. Li, S. Da Vela, D. Seliantis, A. Chroni, A. Papagiannopoulos, C. M. Papadakis
  Protein-polysaccharide nanoparticles stabilized by thermal treatment
  Virtuelle 84. Jahrestagung der DPG und DPG-Tagung der SKM,
  27 September – 01 October 2021

- J. Allwang, Y. Li, S. Da Vela, D. Seliantis, A. Chroni, A. Papagiannopoulos, C. M. Papadakis
  Protein-polysaccharide nanoparticles stabilized by thermal treatment
  EMBL Hamburg P12 Virtual User Meeting, 01 – 02 November 2021

- P. Álvarez-Herrera, G. P. Meledam, C.-H. Ko, B. J. Niebuur, S. H. Huang, L. Chiappisi, C. Henschel, A. Laschewsky, A. Schulte, C. M. Papadakis
  Effect of pressure on the micellar structures of PMMA-b-PNIPAM in aqueous solutions
  Virtuelle 84. Jahrestagung der DPG und DPG-Tagung der SKM,
  27 September – 01 October 2021

- F. A. C. Apfelbeck, P. Müller-Buschbaum
  Studies on polymer electrolytes for thin film Lithium-Ion batteries
  11th Energy Colloquium of the Munich School of Engineering, 28 – 29 July 2021

- F. A. C. Apfelbeck, P. Müller-Buschbaum
  Poly((trifluoromethane)sulfonimide Lithium styrene) as solid polymer electrolyte for Lithium-Ion batteries
  Virtuelle 84. Jahrestagung der DPG und DPG-Tagung der SKM,
  27 September – 01 October 2021

- F. A. C. Apfelbeck, P. Müller-Buschbaum
  A capillary battery cell setup for in operando x-ray investigation of solid polymer electrolytes
  MLZ User Meeting 2021, 07 – 08 December 2021

- C. R. Everett, M. Planck, M. Gallei, M. Schwartzkopf, S. V. Roth, P. Müller-Buschbaum
  Growth and morphology of sputtered iron layers on magnetic nanoparticle-containing diblock copolymer films
  DPG Virtual Spring Meeting 2021, 22 – 24 March 2021

- C. Geiger, J. Reitenbach, L. P. Kreuzer, T. Widmann, P. Wang, R. Cubitt, C. Henschel, A. Laschewsky, C. M. Papadakis, P. Müller-Buschbaum
  Co-nonsolvency behavior of responsive polymers in thin film/vapor systems
  Virtuelle 84. Jahrestagung der DPG und DPG-Tagung der SKM,
  27 September – 01 October 2021

- T. Guan, R. Guo, S. Liang, C. L. Weindl, S. V. Roth, L. Jiang, P. Müller-Buschbaum
  Fabrication of plasmonic nanostructures for perovskite solar cells
  DPG Virtual Spring Meeting 2021, 22 – 24 March 2021

- T. Guan, W. Chen, S. Liang, C. L. Weindl, S. V. Roth, L. Jiang, P. Müller-Buschbaum
  Fabrication of plasmonic nanostructures in photovoltaics
  11th Energy Colloquium of the Munich School of Engineering, 28 – 29 July 2021

- T. Guan, W. Chen, H. Tang, D. Li, S. Liang, C. L. Weindl, Z. Liang, M. Schwartzkopf, S. V. Roth, L. Jiang, P. Müller-Buschbaum
  Decoding the self-assembled plasmonic nano-structure in colloidal quantum dots for photodetectors
  MLZ User Meeting 2021, 07 – 08 December 2021

- R. Guo, D. Han, W. Chen, L. Dai, K. Ji, Q. Xiong, S. Li, L. K. Reb, M. A. Scheel, S. Pratap, N. Li, S. Yin, A. L. Oechsle, T. Xiao, S. Liang, C. L, Weindl, H. Ebert, N. Greenham, S. Stranks, R. Friend, P. Gao, M. Yuan, M. Schwartzkopf, S. V. Roth, P. Müller-Buschbaum
  Degradation mechanisms of perovskite solar cells under vacuum and one atmosphere of nitrogen
  11th Energy Colloquium of the Munich School of Engineering, 28 – 29 July 2021

- R. Guo, D. Han, W. Chen, L. Dai, K. Ji, Q. Xiong, S. Li, L. K. Reb, M. A. Scheel, S. Pratap, N. Li, S. Yin, A. L. Oechsle, T. Xiao, S. Liang, C. L. Weindl, H. Ebert, N. Greenham, S. Stranks, R. Friend, P. Gao, M. Yuan, M. Schwartzkopf, S. V. Roth, P. Müller-Buschbaum
  Degradation mechanisms of perovskite solar cells under vacuum and one atmosphere of nitrogen
  e-conversion Conference 2021, 15 – 16 September 2021

- R. Guo, D. Han, W. Chen, L. Dai, K. Ji, Q. Xiong, S. Li, L. K. Reb, M. A. Scheel, S. Pratap, N. Li, S. Yin, A. L. Oechsle, T. Xiao, S. Liang, C. L. Weindl, H. Ebert, N. Greenham, S. Stranks, R. Friend, P. Gao, M. Yuan, M. Schwartzkopf, S. V. Roth, P. Müller-Buschbaum
  Degradation mechanisms of perovskite solar cells under vacuum and one atmosphere of nitrogen
  MLZ User Meeting 2021, 07 – 08 December 2021

- C. Gutiérrez-Bolaños, Lukas V. Spanier, Peter Müller-Buschbaum
  Printed Organic Solar Cells
  11th Energy Colloquium of the Munich School of Engineering, 28 – 29 July 2021

- C. Harder, M. Betker, A. Alexakis, E. Erbes, C. J. Brett, A. Chumakov, M. Gensch, B. Sochor, Q. Chen, J. Rubeck, M. Schwartzkopf, D. Söderberg, E. Malmström, P. Müller-Buschbaum, S. V. Roth
  In-situ spraying of colloids on cellulose nanofibers
  DESY Photon Science Users' Meeting 2021, 27 – 28 January 2021

- C. Harder, M. Betker, A. Alexakis, E. Erbes, C. J. Brett, A. Chumakov, M. Gensch, B. Sochor, Q. Chen, J. Rubeck, M. Schwartzkopf, D. Söderberg, E. Malmström, P. Müller-Buschbaum, S. V. Roth
  In-situ spraying of colloids on cellulose nanofibers
  DPG Virtual Spring Meeting 2021, 22 – 24 March 2021

- C. Harder, M. Betker, A. Alexakis, E. Erbes, C. J. Brett, A. Chumakov, M. Gensch, B. Sochor, Q. Chen, J. Rubeck, M. Schwartzkopf, D. Söderberg, E. Malmström, P. Müller-Buschbaum, S. V.Roth
  Annealing of polymer colloids on CNF
  Bunsentagung, 11 May 2021

- C. Harder, M. Betker, A. Alexakis, E. Erbes, C. J. Brett, A. Chumakov, M. Gensch, B. Sochor, Q. Chen, J. Heger, J. Rubeck, M. Schwartzkopf, D. Söderberg, E. Malmström, P. Müller-Buschbaum, S. V. Roth
  Colloidal layer formation and imbibition of colloidal inks on and in thin cellulose films
  Virtuelle 84. Jahrestagung der DPG und DPG-Tagung der SKM,
  27 September – 01 October 2021

- C. Harder, M. Betker, A. Alexakis, E. Erbes, C. J. Brett, A. Chumakov, M. Gensch, B. Sochor, Q. Chen, J. Heger, J. Rubeck, M. Schwartzkopf, D. Söderberg, E. Malmström, P. Müller-Buschbaum, S. V. Roth
  Morphological properties of polymer colloids on porous CNF layer
  MLZ User Meeting 2021, 07 – 08 December 2021

- J. E. Heger, W. Chen, C. Brett, W. Ohm, S. V. Roth, P. Müller-Buschbaum
  In situ GISAXS/GIWAXS investigation of ß-sheet mediated biotemplating in TiO_2*:ß-lactoglobulin films during spray deposition*
  DESY Photon Science Users' Meeting 2021, 27 – 28 January 2021

- J. E. Heger, W. Chen, S. Yin, C. L. Weindl, C. Geiger, C. J. Brett, W. Ohm, S. V. Roth, P. Müller-Buschbaum
  Observing the role of ß-lactoglobulin in biotemplating TiO_x *during spray deposition with in situ GIXS techniques: A route to green sol-gel chemistry*
  DPG Virtual Spring Meeting 2021, 22 – 24 March 2021

- J. E. Heger, M. Betker, C. Harder, B. Sochor, C. L. Weindl, M. Schwartzkopf, S. V. Roth, P. Müller-Buschbaum
  In situ GIXS observation of spray coating lead-free perovskite on mesoporous titania
  11th Energy Colloquium of the Munich School of Engineering, 28 – 29 July 2021

- J. E. Heger, C. Geiger, T. Widmann, L. P. Kreuzer, S. Yin, A. Koutsioumpas, P. Müller-Buschbaum
  GISANS study on whey protein and titania interfaces: Influence of pH on spray deposited biohybrid film morphology
  MLZ User Meeting, 07 – 08 December 2021

- T. Hölderle, P. Müller-Buschbaum, A. Senyshyn
  Thermal structural stability of lithiated graphites
  MLZ User Meeting 2021, 07 – 08 December 2021

- L. F. Huber, P. Müller-Buschbaum
  Inorganic-organic hybrid nanostructures based on biopolymer templating
  11th Energy Colloquium of the Munich School of Engineering, 28 – 29 July 2021

- L. F. Huber, P. Müller-Buschbaum
  Inorganic-organic hybrid nanostructures based on biopolymer templating
  Virtuelle 84. Jahrestagung der DPG und DPG-Tagung der SKM,
  27 September – 01 October 2021

- X. Jiang, S. Tu, S. V. Roth, P. Müller-Buschbaum
  In-situ sputter deposition of electrodes for non-fullerene organic photovoltaics application
  DPG Virtual Spring Meeting 2021, 22 – 24 March 2021

- X. Jiang, H. Kim, S. V. Roth, P. Müller-Buschbaum
  Internal nanoscale architecture and charge carrier dynamics of wide bandgap non-fullerene bulk heterojunction active layers in organic solar cells
  11th Energy Colloquium of the Munich School of Engineering, 28 July – 29 July 2021

- X. Jiang, S. Tu, S. V. Roth, P. Müller-Buschbaum
  Following the morphology formation of printed non-fullerene active layer for solar cells
  Virtuelle 84. Jahrestagung der DPG und DPG-Tagung der SKM,
  27 September – 01 October 2021

- X. Jiang, S. J. Schaper, S. V. Roth, P. Müller-Buschbaum
  In-situ observation of electrodes formation on the nonfullerene organic solar cells by GISAXS technique
  MLZ User Meeting 2021, 07 – 08 December 2021

- V. Körstgens, L. Diaz Piola, H. Iglev, S. V. Roth, R. Kienberger, P. Müller-Buschbaum
  Active layer printing of hybrid solar cells with in situ GISAXS and GIWAXS
  DESY Photon Science Users' Meeting 2021, Hamburg, 27 – 28 January 2021

- V. Körstgens, J. Corella Puertas, P. Müller-Buschbaum
  Tack properties of pressure-sensitive adhesives: Development of industry-conform measurement techniques
  MLZ User Meeting 2021, 07 – 08 December 2021

- L. P. Kreuzer, C. Lindenmeir, C. Geiger, T. Widmann, V. Hildebrand, A. Laschewsky, C. M. Papadakis, P. Müller-Buschbaum
  Co-nonsolvency-type behavior in poly(sulfobetaine) and poly(N-isopropylacrylamide) thin films
  Virtual Conference on Osmolyte and Cosolvent Effects, 25 – 26 February 2021

- N. Li, R. Guo, W. Chen, V. Körstgens, J. E. Heger, S. Liang, C. J. Brett, M. A. Hossain, J. Zheng, P. S. Deimel, A. Buyruk, F. Allegretti, M. Schwartzkopf, J. G. C. Veinot, G. Schmitz, J. V. Barth, T. Ameri, S. V. Roth, P. Müller-Buschbaum
  Tuning ordered mesoporous titania films via introducing germanium nanocrystals for high-efficient photoanodes
  DESY Photon Science Users' Meeting 2021, 27 – 28 January 2021

- N. Li, R. Guo, W. Chen, V. Körstgens, J. E. Heger, S. Liang, C. J. Brett, M. A. Hossain, J. Zheng, P. S. Deimel, A. Buyruk, F. Allegretti, M. Schwartzkopf, J. G. C. Veinot, G. Schmitz, J. V. Barth, T. Ameri, S. V. Roth, P. Müller-Buschbaum
  Tuning ordered mesoporous titania films via introducing germanium nanocrystals for high-efficient photoanodes
  DPG Virtual Spring Meeting 2021, 22 – 24 March 2021

- N. Li, R. Guo, W. Chen, V. Körstgens, J. E. Heger, S. Liang, C. J. Brett, M. A. Hossain, J. Zheng, P. S. Deimel, A. Buyruk, F. Allegretti, M. Schwartzkopf, J. G. C. Veinot, G. Schmitz, J. V. Barth, T. Ameri, S. V. Roth, P. Müller-Buschbaum
  Tailoring ordered mesoporous titania films by introducing germanium nanocrystals for photoanodes
  11th Energy Colloquium of the Munich School of Engineering, 28 – 29 July 2021

- N. Li, R. Guo, W. Chen, V. Körstgens, J. E. Heger, S. Liang, C. J. Brett, M. A. Hossain, J. Zheng, P. S. Deimel, A. Buyruk, F. Allegretti, M. Schwartzkopf, J. G. C. Veinot, G. Schmitz, J. V. Barth, T. Ameri, S. V. Roth, P. Müller-Buschbaum
  Tuning ordered mesoporous titania films via introducing germanium nanocrystals for high-efficient photoanodes
  MLZ User Meeting 2021, 07 – 08 December 2021

- Y. Li, C.-H. Ko, V. Chrysostomou, D. S. Molodenskiy, S. Pispas, C. M. Papadakis
  Self-assembled micelles from pH-responsive copolymer solutions
  Virtuelle 84. Jahrestagung der DPG und DPG-Tagung der SKM,
  27 September – 01 October 2021

- Y. Li, C.-H. Ko, V. Chrysostomou, D. S. Molodenskiy, S. Pispas, C. M. Papadakis
  Self-assembled micelles from pH-responsive copolymer solutions
  EMBL Hamburg P12 Virtual User Meeting, 01 – 02 November 2021

- Y. Li, Y. Li, J. Heger, J. Zhou, C. Everett, X. Jiang, T. Guan, S. Yin, S. Liang, C. Geiger, C. Jiang, B. Sun, P. Müller-Buschbaum
  Structure of Molybdenum Nitride films as hole-selective contacts of crystalline solar cells determined with X-ray scattering
  MLZ User Meeting 2021, 07 – 08 December 2021

- S. Liang, W. Chen, S. Yin, S. J. Smion, R. Guo, J. Drewes, N. Carstens, T. Strunskus, F. Faupel, M. Gensch, M. Schwartzkopf, S. V. Roth, Y.-J. Cheng, P. Müller-Buschbaum
  Tailoring Optical Properties of Sputter Deposited Au Nanostructures on TiO_2 Templates based on in situ GISAXS Determined Growth Laws
  DPG Virtual Spring Meeting 2021, 22 – 24 March 2021

- S. Liang, Y.-J. Cheng, Y. Xia, P. Müller-Buschbaum
  Impact of CO_2 Activation on Structure, Composition, and Performance of Sb/C Nanohybrid Lithium/Sodium-Ion Battery Anodes
  11th Energy Colloquium of the Munich School of Engineering, 28 – 29 July 2021

- S. Liang, W. Chen, S. Yin, S. J. Smion, R. Guo, J. Drewes, N. Carstens, T. Strunskus, F. Faupel, M. Gensch, M. Schwartzkopf, S. V. Roth, Y.-J. Cheng, P. Müller-Buschbaum
  Tailoring Optical Properties of Sputter Deposited Au Nanostructures on TiO_2 Templates based on in situ GISAXS Determined Growth Laws
  Virtuelle 84. Jahrestagung der DPG und DPG-Tagung der SKM,
  27 September – 01 October 2021

- S. Liang, W. Chen, S. Yin, S. J. Smion, R. Guo, J. Drewes, N. Carstens, T. Strunskus, F. Faupel, M. Gensch, M. Schwartzkopf, S. V. Roth, Y.-J. Cheng, P. Müller-Buschbaum
  Tailoring Optical Properties of Sputter Deposited Au Nanostructures on TiO_2 Templates based on in situ GISAXS Determined Growth Laws
  MLZ User Meeting 2021, 07 – 08 December 2021

- Y. Liang, P. Müller-Buschbaum
  In operando studies of solid polymer electrolyte for thin film Lithium-Ion battery
  11th Energy Colloquium of the Munich School of Engineering, 28 – 29 July 2021

- Y. Liang, P. Müller-Buschbaum
  Influence of Mg on the structure and electrolyte/electrode interface in all-solid state Lithium battery
  Virtuelle 84. Jahrestagung der DPG und DPG-Tagung der SKM,
  27 September – 01 October 2021

- Y. Liang, J. E. Heger, P. Müller-Buschbaum
  Influence of Mg on the structure and electrolyte/electrode interface in all-solid state Lithium battery
  MLZ User Meeting 2021, 07 - 08 December 2021

- C. G. Lindenmeir, A. Vitaloni, L. K. Reb, M. A. Scheel, P. Müller-Buschbaum
  Optimization of printed Perovskite Solar Cells using X-Ray scattering
  MLZ User Meeting 2021, 07 – 08 December 2021

- A. L. Oechsle, J. E. Heger, N. Li, S. Yin, S. Bernstorff, P. Müller-Buschbaum
  Conductivity stability of EMIM-DCA post-treated semi-conducting PEDOT:PSS polymer thin films under elevated temperatures
  DPG Virtual Spring Meeting 2021, 22 – 24 March 2021

- A. L. Oechsle, J. E. Heger, N. Li, S. Yin, S. Bernstorff, P. Müller-Buschbaum
  Conductivity stability of EMIM DCA post-treated semi-conducting PEDOT:PSS polymer thin films under elevated temperatures
  11th Energy Colloquium of the Munich School of Engineering, 28 – 29 July 2021

- A. L. Oechsle, J. E. Heger, N. Li, S. Yin, S. Bernstorff, P. Müller-Buschbaum
  Thermal degradation of EMIM DCA post-treated PEDOT:PSS thermoelectric thin films, investigated via in-situ GISAXS
  Virtuelle 84. Jahrestagung der DPG und DPG-Tagung der SKM,
  27 September – 01 October 2021

- G. Pan, S. Yin, N. Li, T. Guan, S. Liang, Y. Zou, P. Müller-Buschbaum
  Morphology control of Titanium thin films in a low temperature process
  MLZ User Meeting 2021, 07 – 08 December 2021

- D. Petz, V. Baran, M. J. Mühlbauer, A. Schökel, C. Paulmann, P. Müller-Buschbaum, A. Senyshyn
  Lithium distribution in stripes of negative electrodes extracted from cylinder-type Li-ion batteries
  DESY Photon Science Users' Meeting 2021, 27 – 28 January 2021

- D. Petz, V. Baran, M. J. Mühlbauer, A. Schökel, M. Hofmann, P. Müller-Buschbaum, A. Senyshyn
  Dynamics of the lithium distribution in commercial $LiFePO_4|C$ *cylinder-type Li-ion batteries under charge/discharge*
  DGK Conference 2021, 15 – 18 March 2021

- D. Petz, M J. Mühlbauer, V. Baran, M. Hofmann, P. Müller-Buschbaum, A. Senyshyn
  Lithium and electrolyte distribution in 18650-type lithium-ion batteries
  239th ECS Meeting 2021, 30 May – 03 June 2021

- D. Petz, P. Müller-Buschbaum, A. Senyshyn
  Non-destructive quantification of lithium and electrolyte losses in Li-ion batteries
  11th Energy Colloquium of the Munich School of Engineering, 28 – 29 July 2021

- D. Petz, P. Müller-Buschbaum, A. Senyshyn
  Spatially-resolved lithium and electrolyte distribution in cylindrical 18650-type lithium-ion batteries
  Virtuelle 84. Jahrestagung der DPG und DPG-Tagung der SKM,
  27 September – 01 October 2021

- D. Petz, P. Müller-Buschbaum, A. Senyshyn
  Dynamics of lithium-distribution in 18650-type lithium-ion batteries during electrochemical cycling
  MLZ User Meeting 2021, 07 – 08 December 2021
- T. A. Pham, R. Gilles and P. Müller-Buschbaum
  Solid polymers for high energy cathode materials
  11th Energy Colloquium of the Munich School of Engineering, 28 – 29 July 2021
- T. A. Pham, R. Gilles and P. Müller-Buschbaum
  Poly(propylene carbonate) as a solid polymer electrolyte
  Virtuelle 84. Jahrestagung der DPG und DPG-Tagung der SKM,
  27 September – 01 October 2021
- T. A. Pham, L. Wells, S. Seidlmayer, G. Ceccio, A. Cannavo, J. Vacik, P. Müller-Buschbaum, E. Figgemeier and R. Gilles
  X-ray diffraction studies on the lithiation of LiAl electrodes for Li Ion batteries
  MLZ User Meeting 2021, 07 – 08 December 2021
- I. Pivarníková, R. Gilles, P. Müller-Buschbaum
  Sol-gel based tailored Lithium-Ion battery electrodes
  11th Energy Colloquium of the Munich School of Engineering, 28 – 29 July 2021
- I. Pivarníková, R. Gilles, P. Müller-Buschbaum
  Sol-gel based tailored Lithium-Ion battery electrodes
  Virtuelle 84. Jahrestagung der DPG und DPG-Tagung der SKM,
  27 September – 01 October 2021
- I. Pivarníková, S. Seidlmayer, M. Finsterbusch, G. Dück, S. Naqash, N. Jalarvo, P. Müller-Buschbaum, R. Gilles
  Na-ion diffusion in NASICON solid electrolyte material studied by quasi-elastic neutron scattering
  MLZ User Meeting 2021, 07 – 08 December 2021
- L. K. Reb, M. A. Reus, M. Schwartzkopf, S. V. Roth, P. Müller-Buschbaum
  GIWAXS in-situ analysis of MAPI perovskite annealing
  DESY Photon Science Users' Meeting 2021, 27 – 28 January 2021
- L. K. Reb, M. Böhmer, B. Predeschly, S. Grott, C. L. Weindl, G. I. Ivandekic, R. Guo, C. Dreißigacker, J. Drescher, R. Gernhäuser, A Meyer, P. Müller-Buschbaum
  A further step towards space: Perovskite and organic solar cells on a rocket flight
  DPG Virtual Spring Meeting 2021, 22 – 24 March 2021
- L. K. Reb, A. Vitaloni, M. Reus, P. Müller-Buschbaum
  Tuning composition and morphology of printed perovskite films for photovoltaic applications
  ATUMS Annual Meeting, 12 November 2021
- L. K. Reb, M. A. Reus, M. Schwartzkopf, C. Rosemann, S. V. Roth, P. Müller-Buschbaum
  The in-situ GIWAXS heuristic tool for efficient reduction of high-quality big data
  MLZ User Meeting 2021, 07 – 08 December 2021

- J. Reitenbach, C. Geiger, L. P. Kreuzer, T. Widmann, P. Wang, G. Mangiapia, C. Henschel, A. Laschewsky, C. M. Papadakis, P. Müller-Buschbaum
  Co-nonsolvency-induced collapse transition in thin PMMA-b-PNIPMAM films
  Virtual Conference on Osmolyte and Cosolvent Effects, 25 – 26 February 2021

- J. Reitenbach, C. Geiger, L. P. Kreuzer, T. Widmann, P. Wang, G. Mangiapia, C. Henschel, A. Laschewsky, C. M. Papadakis, P. Müller-Buschbaum
  Co-nonsolvency-induced collapse transition in thin PMMA-b-PNIPMAM films
  ACS Spring Meeting 2021, 05 – 16 April 2021

- J. Reitenbach, C. Geiger, P. Wang, R. Cubitt, D. Schanzenbach, A. Laschewsky, C. M. Papadakis, P. Müller-Buschbaum
  Investigation of the effect of magnesium salts with Chaotropic Anions on the swelling behavior of PNIPMAM thin films
  Virtuelle 84. Jahrestagung der DPG und DPG-Tagung der SKM,
  27 September – 01 October 2021

- J. Reitenbach, C. Geiger, P. Wang, R. Cubitt, D. Schanzenbach, A. Laschewsky, C. M. Papadakis, P. Müller-Buschbaum
  Influence of Hofmeister salts on the swelling behavior of PNIPMAM thin films
  MLZ User Meeting 2021, 07 – 08 December 2021

- D. M. Schwaiger, W. Lohstroh, P. Müller-Buschbaum
  Dynamics in polymer-fullerene blends for photovoltaic applications
  DPG Virtual Spring Meeting 2021, 22 – 24 March 2021

- D. M. Schwaiger, W. Lohstroh, P. Müller-Buschbaum
  Dynamics in polymer-fullerene blends for photovoltaic applications
  ACS Spring Meeting, 05 – 16 April 2021

- D. M. Schwaiger, W. Lohstroh, P. Müller-Buschbaum
  Dynamics in polymer-fullerene blends for photovoltaic applications
  QENS/WINS 2021, 17 – 21 May 2021

- L. V. Spanier, M. Nuber, S. Roth, X. Jiang, H. Iglev, R. Kienberger, P. Müller-Buschbaum
  Influence of solvent composition on optical and morphological properties of PTQ10:BTP-4F bulk heterojunctions
  DPG Virtual Spring Meeting 2021, 22 – 24 March 2021

- L. V. Spanier, R. Guo, J. E. Heger, Y. Zou, M. Nuber, M. Schwartzkopf, D. Toth, R. Houssaini, H. Iglev, R. Kienberger, A. Hartschuh, S. V. Roth, P. Müller-Buschbaum
  Influence of solvent composition on optical and morphological properties of PTQ10:BTP-4F bulk heterojunctions
  11th Energy Colloquium of the Munich School of Engineering, 28 – 29 July 2021

- L. V. Spanier, R. Guo, J. E. Heger, Y. Zou, M. Nuber, M. Schwartzkopf, D. Toth, R. Houssaini, H. Iglev, R. Kienberger, A. Hartschuh, S. V. Roth, P. Müller-Buschbaum
  Influence of non-halogenated solvents on the morphology and stability of PTQ10:BTP-4F organic solar cells
  e-conversion Meeting 2021, 15 – 16 September 2021

- L. V. Spanier, R. Guo, J. E. Heger, Y. Zou, M. Nuber, M. Schwartzkopf, D. Toth, R. Houssaini, H. Iglev, R. Kienberger, A. Hartschuh, S. V. Roth, P. Müller-Buschbaum
  Influence of non-halogenated solvents on the morphology and stability of PTQ10:BTP-4F organic solar cells
  Virtuelle 84. Jahrestagung der DPG und DPG-Tagung der SKM,
  27 September – 01 October 2021

- L. V. Spanier, R. Guo, J. E. Heger, Y. Zou, M. Nuber, M. Schwartzkopf, D. Toth, R. Houssaini, H. Iglev, R. Kienberger, A. Hartschuh, S. V. Roth, P. Müller-Buschbaum
  Gracing incidence scattering as a method to understand the influence of non-halogenated solvents on the morphology of organic solar cells
  MLZ User Meeting 2021, 07 – 08 December 2021

- K. Sun, P. Müller-Buschbaum
  In-situ study of compositional engineering for Perovskite solar cells
  11th Energy Colloquium of the Munich School of Engineering, 28 – 29 July 2021

- K. Sun, P. Müller-Buschbaum
  In-operando study of humidity on the performance of perovskite solar cells
  Virtuelle 84. Jahrestagung der DPG und DPG-Tagung der SKM,
  27 September – 01 October 2021

- K. Sun, J. E. Heger, M. A. Reus, X. Jiang, L. Spanier, S. Bernstorff, P. Müller-Buschbaum
  Operando study of humidity on the performance of perovskite solar cells
  MLZ User Meeting 2021, 07 – 08 December 2021

- T. Tian, S. Yin, K. S. Wienhold, C. L. Weindl, M. Schwartzkopf, S. V. Roth, P. Müller-Buschbaum
  In situ investigation of printed mesoporous ZnO films templated by diblock copolymer
  DPG Virtual Spring Meeting 2021, 22 – 24 March 2021

- T. Tian, S. Yin, K. S. Wienhold, C. L. Weindl, M. Schwartzkopf, S. V. Roth, P. Müller-Buschbaum
  In situ investigation of printed mesoporous ZnO films templated by diblock copolymer
  11th Energy Colloquium of the Munich School of Engineering, 28 – 29 July 2021

- T. Tian, S. Yin, K. S. Wienhold, C. L. Weindl, M. Schwartzkopf, S. V. Roth, P. Müller-Buschbaum
  In situ investigation of printed mesoporous ZnO films templated by diblock copolymer
  MLZ User Meeting 2021, 07 – 08 December 2021

- S. Tu, T. Tian, A. L. Oechsle, S. Yin, W. Cao, N. Li, M. Reus, M. Schwartzkopf, S. V. Roth, P. Müller-Buschbaum
  Feasible tuning of microstacking structure and oxidation level in PEDOT: PSS films via sequential post-treatment
  DPG Virtual Spring Meeting 2021, 22 – 24 March 2021

- S. Tu, T. Tian, A. L. Oechsle, S. Yin, W. Cao, N. Li, M. Reus, M. Schwartzkopf, S. V. Roth, P. Müller-Buschbaum
  Feasible tuning of microstacking structure and oxidation level in PEDOT: PSS films via sequential post-treatment
  11th Energy Colloquium of the Munich School of Engineering, 28 – 29 July 2021

- S. Tu, T. Tian, A. L. Oechsle, S. Yin, W. Cao, N. Li, M. Reus, L. K. Reb, S. Hou, A. S. Bandarenka, M. Schwartzkopf, S. V. Roth, P. Müller-Buschbaum
  Improvement of TE properties of PEDOT:PSS films via DMSO addition and DMSO/salt post-treatment resolved from a fundamental view
  MLZ User Meeting 2021, 07 – 08 December 2021

- A. Vagias, S. J. Schaper, J. E. Heger, Y. Zou, S. Yin, C. Geiger, M. Schwartzkopf, M. Gensch, A. Laschewsky, S. V. Roth, P. Müller-Buschbaum
  Oxygen plasma effects on the nanoscale morphology of polyzwitterion-gold interfaces during gold sputtering
  DPG Virtual Spring Meeting 2021, 22 – 24 March 2021

- A. Vagias, S. J. Schaper, W. Chen, S. Liang, C. Geiger, N. Li, L. P. Kreuzer, M. Gensch, P. Pandit, M. Schwartzkopf, S. V. Roth, J. Drewes, N. Carstens, T. Strunskus, F. Faupel, A. Laschewsky, P. Müller-Buschbaum
  Monitoring gold cluster growth/formation on zwitterionic thin block copolymer coatings as functional interlayers
  11th Energy Colloquium of the Munich School of Engineering, 28 – 29 July 2021

- A. Vagias, A. Papagiannopoulos, L. P. Kreuzer, D. Giaouzi, S. Busch, S. Pispas, P. Müller-Buschbaum
  Polymer block length and temperature effects on the nanoscale morphology of thermoresponsive double hydrophilic block copolymers
  MLZ User Meeting, 07 – 08 December 2021

- A. Vitaloni, L. K. Reb, P. Müller-Buschbaum
  Slot-die coating of perovskite solar cells: A technique for upscaling
  11th Energy Colloquium of the Munich School of Engineering, 28 – 29 July 2021

- A. Vitaloni, L. K. Reb, P. Müller-Buschbaum
  Upscaling perovskite: Optoelectronics and morphology of slot-die coated solar cells
  Virtuelle 84. Jahrestagung der DPG und DPG-Tagung der SKM,
  27 September – 01 October 2021

- A. Vitaloni, L. K. Reb, M. A. Reus, R. Guo, J. E. Heger, M. Schwartzkopf, S. V. Roth, P. Müller-Buschbaum
  Upscaling perovskite: Optoelectronics and morphology of slot-die coated solar cells
  MLZ User Meeting 2021, 07 – 08 December 2021

- P. Wang, L. P. Kreuzer, C. Geiger, T. Widmann, S. Liang, A. Laschewsky, C. M. Papadakis, R. Cubitt, P. Müller-Buschbaum
  Investigation of Cononsolvency Phase Transition of Poly(sulfobetaine)-based Diblock Copolymer Thin Films
  Virtual Conference on Osmolyte and Cosolvent Effects, 25 – 26 February 2021

- P. Wang, L. P. Kreuzer, C. Geiger, T. Widmann, S. Liang, A. Laschewsky, C. M. Papadakis, R. Cubitt, P. Müller-Buschbaum
  Investigation of Cononsolvency Phase Transition of Poly(sulfobetaine)-based Diblock Copolymer Thin Films
  DPG Virtual Spring Meeting 2021, 22 – 24 March 2021

- P. Wang, L. P. Kreuzer, C. Geiger, T. Widmann, S. Liang, A. Laschewsky, C. M. Papadakis, R. Cubitt, P. Müller-Buschbaum
  Co-Nonsolvency Transition of PNIPMAM-based Block Copolymer Thin Films in Water/Acetone Mixtures
  ACS Spring Meeting 2021, 05 – 16 April 2021

- P. Wang, L. P. Kreuzer, C. Geiger, T. Widmann, S. Liang, A. Laschewsky, C. M. Papadakis, R. Cubitt, P. Müller-Buschbaum
  Co-nonsolvency Triggered thin Films Contraction of Poly(sulfobetaine) based Diblock Copolymer Thin Films in Water/Acetone Atmosphere
  MLZ User Meeting 2021, 07 – 08 December 2021

- S. Wegener, A. L. Oechsle, P. Müller-Buschbaum
  Measurement setup to characterize thermoelectric polymer thin films
  11th Energy Colloquium of the Munich School of Engineering, 28 – 29 July 2021

- S. Wegener, A L. Oechsle, P. Müller-Buschbaum
  New measurement setup to characterize thermoelectric polymer thin films
  Virtuelle 84. Jahrestagung der DPG und DPG-Tagung der SKM,
  27 September – 01 October 2021

- C. L. Weindl, C. Fajman, M. A. Giebel, T. F. Fässler, P. Müller-Buschbaum
  Germanium-based nanostructure synthesis guided by amphiphilic diblock copolymer templating
  DESY Photon Science Users' Meeting 2021, 28 – 29 January 2021

- C. L. Weindl, C. Fajman, M. A. Giebel, T. F. Fässler, P. Müller-Buschbaum
  Investigation of polymer templated Silicon-Germanium hybrid materials
  DPG Virtual Spring Meeting 2021, 22 – 24 March 2021

- C. L. Weindl, C. Fajman, M. A. Giebel, T. F. Fässler, P. Müller-Buschbaum
  Sol-gel derived germanium-based nanostructures
  11th Energy Colloquium of the Munich School of Engineering, 28 – 29 July 2021

- C. L. Weindl, C. Fajman, M. A. Giebel, T. F. Fässler, P. Müller-Buschbaum
  The influence of toluene in a Si/Ge sol-gel approach
  Virtuelle 84. Jahrestagung der DPG und DPG-Tagung der SKM,
  27 September – 01 October 2021

- C. L. Weindl, C. Fajman, M. A. Giebel, T. F. Fässler, P. Müller-Buschbaum
  The influence of toluene in a Si/Ge sol-gel approach
  MLZ User Meeting 2021, 07 – 08 December 2021

- A. F. Weinzierl, M. A. Scheel, L. K. Reb, P. Müller-Buschbaum
  Fabrication and characterisaton of slot-die coated Formamidinium-Cesium lead iodide perovskite solar cells
  Virtuelle 84. Jahrestagung der DPG und DPG-Tagung der SKM,
  27 September – 01 October 2021

- T. Xiao, W. Chen, W. Cao, S. Wöhnert, S. V. Roth, P. Müller-Buschbaum
  Hybrid energy harvester based on triboelectric nanogenerator and solar cells
  DPG Virtual Spring Meeting 2021, 22 – 24 March 2021

- T. Xiao, W. Chen, W. Cao, S. Wöhnert, S. V. Roth, P. Müller-Buschbaum
  Hybrid energy harvester based on triboelectric nanogenerator and solar cells
  11th Energy Colloquium of the Munich School of Engineering, 28 – 29 July 2021
- T. Xiao, W. Chen, W. Cao, S. Wöhnert, S. V. Roth, P. Müller-Buschbaum
  Hybrid energy harvester based on triboelectric nanogenerator and solar cells
  MLZ User Meeting 2021, 07 – 08 December 2021
- Z. Xu, Y. Gao, Y. Cheng, P. Müller-Buschbaum
  Design, fabrication and nano-scale characterization of novel SEI layers
  MLZ User Meeting 2021, 07 – 08 December 2021
- B. Yazdanshenas, B. J. Niebuur, D. Schanzenbach, A. Laschewsky, M. Zamponi, D. Noferini, A. Schulte, C. M. Papadakis
  Water dynamics in a concentrated aqueous solution of perdeuterated poly(N-isopropylacrylamide) across the cloud point
  DPG Virtual Spring Meeting 2021, 22 – 24 March 2021
- B. Yazdanshenas, C. Spies, K. Shehu, C. Sachse, S. Da Vela, R. Jordan, C. M. Papadakis
  A thermoresponsive poly(2-oxazoline)-based molecular brush in aqueous solution: effect of a cosolvent
  Virtuelle 84. Jahrestagung der DPG und DPG-Tagung der SKM, 27 September – 01 October 2021
- B. Yazdanshenas, C. Spies, K. Shehu, C. Sachse, S. Da Vela, R. Jordan, C. M. Papadakis
  A thermoresponsive poly(2-oxazoline)-based molecular brush in aqueous solution: effect of a cosolvent
  EMBL Hamburg P12 Virtual User Meeting, 01 – 02 November 2021
- S. Yin, W. Cao, M. Schwartzkopf, S. V. Roth, P. Müller Buschbaum
  Morphology control of PS-b-P4VP templated monolayer mesoporous Fe_2O_3 *thin films*
  DPG Virtual Spring Meeting 2021, 22 – 24 March 2021
- S. Yin, W. Cao, M. Schwartzkopf, S. V. Roth, P. Müller Buschbaum
  Morphology control of PS-b-P4VP templated monolayer mesoporous Fe_2O_3 *thin films*
  11th Energy Colloquium of the Munich School of Engineering, 28 – 29 July 2021
- S. Yin, W. Cao, M. Schwartzkopf, S. V. Roth, P. Müller Buschbaum
  Morphology control of PS-b-P4VP templated monolayer mesoporous Fe_2O_3 *thin films*
  Virtuelle 84. Jahrestagung der DPG und DPG-Tagung der SKM, 27 September – 01 October 2021
- S. Yin, W. Cao, M. Schwartzkopf, S. V. Roth, P. Müller Buschbaum
  Morphology control of PS-b-P4VP templated monolayer mesoporous Fe_2O_3 *thin films*
  MLZ User Meeting 2021, 07 – 08 December 2021
- H. Zhong, W. Chen, M. A. Scheel, C. R. Everett, X. Jiang, M. Schwartzkopf, S. V. Roth, P. Müller-Buschbaum
  Film morphology of printed CQDs ink for solar cell application
  11th Energy Colloquium of the Munich School of Engineering, 28 – 29 July 2021

- H. Zhong, W. Chen, M. A. Scheel, L. Spanier, C. R. Everett, X. Jiang, S. Yin, M. S. Hörtel, J. Zhang, B. B. O. Seibertz, M. Schwartzkopf, S. V. Roth, P. Müller-Buschbaum
  PbS quantum dot solar cells with an IZO buffer layer at quantum dot/ZnO interface
  Virtuelle 84. Jahrestagung der DPG und DPG-Tagung der SKM,
  27 September – 01 October 2021

- H. Zhong, W. Chen, M. A. Scheel, L. Spanier, C. R. Everett, X. Jiang, S. Yin, M. S. Hörtel, J. Zhang, B. B. O. Seibertz, M. Schwartzkopf, S. V. Roth, P. Müller-Buschbaum
  PbS quantum dot solar cells with an IZO buffer layer at quantum dot/ZnO interface
  MLZ User Meeting 2021, 07 – 08 December 2021

- J. Zhou, X. Jiang, X. Dong, L. Cai, Y. Li, M. Schwartzkopf, S. V. Roth, M. Fung, P. Müller-Buschbaum
  Analysis of quasi-2D perovskite crystallization induced by small molecules
  MLZ User Meeting 2021, 07 – 08 December 2021

- Y. Zou, M. Scheel, T. Xiao, S. Pratap, B. Ali, S. Yin, C. Mu, T. Ameri, M. Schwartzkopf, S. V. Roth, P. Müller-Buschbaum
  The role of CsBr in crystal orientation and optoelectronic properties of $MAPbI_3$*-based devices*
  DPG Virtual Spring Meeting 2021, 22 – 24 March 2021

- Y. Zou, M. Scheel, T. Xiao, S. Pratap, B. Ali, S. Yin, C. Mu, T. Ameri, M. Schwartzkopf, S. V. Roth, P. Müller-Buschbaum
  The influence of CsBr on crystal orientation and optoelectronic properties of MAPbI3-based solar cells
  11th Energy Colloquium of the Munich School of Engineering, 28 – 29 July 2021

- Y. Zou, M. Scheel, T. Xiao, S. Pratap, B. Ali, S. Yin, C. Mu, T. Ameri, M. Schwartzkopf, S. V. Roth, P. Müller-Buschbaum
  The influence of CsBr on crystal orientation and optoelectronic properties of MAPbI3-based solar cells
  Virtuelle 84. Jahrestagung der DPG und DPG-Tagung der SKM,
  27 September – 01 October 2021

- Y. Zou, M. Scheel, T. Xiao, S. Pratap, B. Ali, S. Yin, C. Mu, T. Ameri, M. Schwartzkopf, S. V. Roth, P. Müller-Buschbaum
  The influence of CsBr on crystal orientation and optoelectronic properties of MAPbI3-based solar cells
  MLZ User Meeting 2021, 07 – 08 December 2021

10.4 Invited talks (online)

- Dr. Carolin M. Sutter-Fella, Lawrence Berkeley National Laboratory, USA
  Watching and understanding the formation of functional materials: A case study on halide perovskites
  13 January 2021

- Prof. Dr. Maria Vamvakaki, University of Crete, Greece
  Dual-functional bactericidal polymer films with persistent antimicrobial functionality
  27 January 2021

- Zhuijun Xu
  New Niobium-Titanium oxide for Lithium-ion battery anode: synthesis and mechanism understanding
  05 February 2021

- Janik Scharf, TUM
  Investigation of the effect of pyrolysis temperature and duration on fuel cell performance and composition of the FeNC catalysts
  15 February 2021

- Rainer Götz, TUM
  EPR spectroscopy for solid electrolytes and a proof-of-concept in-situ cells
  18 March 2021

- Dr. Martin A. Schroer, University of Duisburg-Essen
  Studying pressure-induced structural changes in biological, soft matter & nanoparticle systems
  17 November 2021

10.5 Funding

Deutsche Forschungsgemeinschaft:

- *In-situ Untersuchungen zu Kondensation, Nukleation und Wachstum von Metallfilmen und Nanostrukturen auf organischen Oberflächen während Sputterbeschichtung*
  Grant Number: MU 1487/18-2
  Project Leader: Prof. Dr. Peter Müller-Buschbaum

- *Rheologie und Grenzflächenstrukturen von Protein- und Partikelstabilisierten Schäumen - ein Multiskalenansatz*
  Grant Number: MU 1487/32-1
  Project Leader: Prof. Dr. Peter Müller-Buschbaum

- *Oberflächenmodifikation von Lithium-Batterie-Anoden mit multifunktionalen Block-Copolymeren*
  Grant Number: MU 1487/38-1
  Project Leader: Prof. Dr. Peter Müller-Buschbaum

- *In-Situ Untersuchungen von Keimbildungs- und Wachstumsprozessen*
  Grant Number: MU 1487/39-1
  Project Leader: Prof. Dr. Peter Müller-Buschbaum

- *Cononsolvency-induzierte Selbstorganisation thermoresponsiver Blockcopolymere in Lösung und im dünnen Film*
  Grant Number: MU 1487/29-1, Project Leader: Prof. Dr. Peter Müller-Buschbaum
  Grant Number: PA 771/20-1, Project Leader: Prof. Dr. Christine M. Papadakis

- *Dünne Filme aus pH und thermoresponsiven Triblockcopolymeren: von der Netzwerkdynamik zum defektfreien Film*
  Grant Number: PA 771/19-1
  Project Leader: Prof. Dr. Christine M. Papadakis

- *Kinetik der Aggregation in thermoresponsiven Polymerlösungen bei Drucksprüngen*
  Grant Number: PA 771/22-1, Project Leader: Prof. Dr. Christine M. Papadakis

- *Molekulare Bürsten mit amphiphilen thermoresponsiven Seitenketten - von der Synthese über Lösungen zu selbstassemblierten Gelen*
  Grant Number: PA 771/27-1, Project Leader: Prof. Dr. Christine M. Papadakis

- Teilprojekt *Inorganic-organic hybrid photovoltaic solar cells using novel hybrid materials* im GRK 2022: University of Alberta / Technische Universität München Internationale Graduiertenschule für Funktionelle Hybridmaterialien (ATUMS) der DFG
  IRTG-2022
  Project Leader: Prof. Dr. Peter Müller-Buschbaum

Bundesministerium für Bildung und Forschung:

- *FlexiProb: Flexible Probenumgebungen für die Untersuchung weicher Materie zur Implementierung an der ESS*
  Teilprojekt: 3
  Project Leader: Prof. Dr. Peter Müller-Buschbaum

Bayerisches Staatsministerium für Wissenschaft und Kunst:

- Im Rahmen der Munich School of Engineering (MSE):
  Solar Technologies Go Hybrid (SolTech) - Forschungsnetzwerk TUM.solar
  Project Leader: Prof. Dr. Peter Müller-Buschbaum

- Im Rahmen der Munich School of Engineering (MSE): Netzwerk Regenerative Energien
  Aufbau eines interdisziplinären Netzwerks aus Lehrstühlen der Technischen Universität München und anderen Forschungseinrichtungen zur Förderung der Forschungsaktivitäten im Bereich der regenerativen Energien
  Project Leader: Prof. Dr. Peter Müller-Buschbaum

Others:

- Im Rahmen des Exzellenzclusters e-conversion

  e-conversion
  Principal Investigator: Prof. Dr. Peter Müller-Buschbaum

  Impact of morphology on the polaron dynamics in polymer: nonfullerene blends for photovoltaic applications
  Principal Investigators: Prof. Dr. Peter Müller-Buschbaum, Prof. Dr. Reinhard Kienberger

  Defect and energy level tuning of printed hybrid perovskite films for photovoltaic applications
  Principal Investigators: Prof. Dr. Peter Müller-Buschbaum, Dr. Johanna Eichhorn

- Im Rahmen des Deutschen Akademischen Austauschdienstes (DAAD):
  Programm Projektbezogener Personenaustausch Griechenland 2020 - 2022
  Protein/polysaccharide nanoparticles by biocompatible protocols for the encapsulation of natural pharmaceutical compounds (BioEncaps)
  Project Leader: Prof. Dr. Christine M. Papadakis

11 The chair

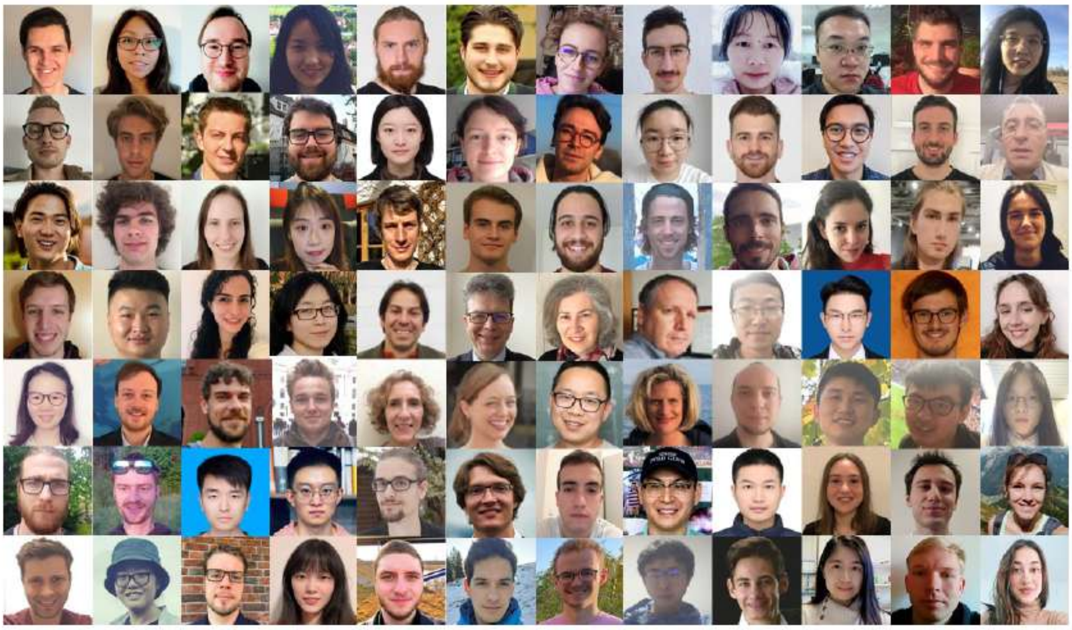

11.1 Staff

Chair:

Prof. Dr. Peter Müller-Buschbaum

Professor:

Prof. Dr. Christine M. Papadakis

Emerited Professor:

Prof. Dr. Winfried Petry

Fellows:

Dr. Wei Chen
Dr. Florian A. Jung
Dr. Volker Körstgens
Dr. Michael Leitner
Dr. Yajuan Li
Dr. Wiebke Lohstroh
Dr. Jürgen Neuhaus
Dr. Neelima Paul
Dr. Apostolos Vagias
Dr. Jun-Gui Zhou

PhD Students:

Pablo Andrés Álvarez Herrera
Fabian Alexander Christian Apfelbeck
Bruno Baumeister
Yusuf Bulut
Wei Cao
Christopher Reck Everett
Sandra Geara
Christina Geiger
Marc Gensch
Sebastian Grott
Tianfu Guan
Renjun Guo
Constantin Harder
Julian Eliah Heger
Alexander Ewin Heldmann
Linus Huber
Xinyu Jiang
Jia-Jhen Kang
Chia-Hsin Ko
Lucas Philipp Kreuzer
Nian Li
Yanan Li
Zerui Li
Suzhe Liang
Yuxin Liang
Franziska Carina Löhrer
Julia Mausz
Anna Lena Oechsle
Guangjiu Pan
Dominik Petz
Thien An Pham
Ivana Pivarníková
Shambhavi Pratap
Lennart Reb
Julija Reitenbach
Simon Jakob Schaper
Manuel Andree Scheel
Ronja Schoenecker
Dominik Schwaiger
Christian Schwarz
Kaltrina Shehu
Jingyi Shi
Lukas Viktor Spanier
Kun Sun
Ting Tian
Suo Tu
Peixi Wang
Christian Ludwig Weindl
Tobias Widmann
Kerstin Sabrina Wienhold
Bonete Wiese
Tianxiao Xiao
Zhuijun Xu
Bahar Yazdanshenas
Shanshan Yin
Tianle Zheng
Huaying Zhong
Yuqin Zou
Ulrike Zweck

Master Students:

Amina Alić
Johannes Allwang
Thomas Baier
Debamitra Chakraborty
Sebastian Coen
Marta Di Girolamo
Gökay Erbil
Carolina Bolanõs Gutierrez
Linus Huber
Ahmed Krifa
Morgan Le Dû
Christoph Lindenmeir
Kexun Luo
Hsu-Thazin Myint
Aikaterina Panagiotou
Tobias Schöner
Oleg Shindelov
Magdalini Spyranti
Markus Trost
Andrea Vitaloni
Rui Wang
Simon Wegener
Alexander Weinzierl
Feifei Zheng

Bachelor Students:

Lukas Dörringer
Mateo Gabriel Flohr Reija
Luke Richard Jatho
Jonas Fabian Keil
Lukas Kohlmaier
Johannes Kowalewics
Andreas Lukas
Florian Karl Peter Maly
Herman Muzychko
Raphael Prandtl
Dominic Rapf
Samuel Reiser
Lukas Schrödinger
Bianca Seyschab
Christoph Spies
Andreas Steinhart
Erik Walz
Andreas Wirler
Sophia Werny

Student Assistants:

Johannes Allwang
Pia Sapelza
Fotoula Kounelaki

Guest Students:

Fotoula Kounelaki

Technical/Administrative Staff:

Reinhold Funer
Andreas Huber
Josef Kaplonski
Carola Kappauf
Marion Waletzki

11.2 Graduations

- **Accomplished PhD Theses**

  Wei Cao
  Magnetic hybrid films based on ultrahigh molecular weight diblock copolymers

  Tobias Chemnitz
  Development of a dry-chemical extraction process for 99Mo and plasma-aided synthesis of transition metal hexafluorides

  Sandra Geara
  SPH simulation of free surface flows application to a centrifugal atomization process for UMo powder synthesis

  Jia-Jhen Kang
  Structural investigation on molecular brushes

  Chia-Hsin Ko
  Novel thermoresponsive homopolymers and amphiphilic diblock copolymers

  Lucas Philipp Kreuzer
  Dual thermo-responsive diblock copolymer thin films

  Nian Li
  Tailoring titania nanostructures for application in solar cells

  Franziska Carina Löhrer
  Relating morphology and function in low-bandgap polymer-based solar cells

  Shambhavi Pratap
  Hybrid perovskites: Colloidal precursors to thin films

  Jingyi Shi
  Qualification of U-Mo fuel for research reactors: Characterisation of the interfaces between U-Mo kernel, diffusion barrier and Al matrix under heavy ion irradiation

  Kerstin Sabrina Wienhold
  Printed organic solar cells

- **Accomplished Master Theses**

  Amina Alić
  In-situ raman and neutron spectroscopy of hydrogen storage materials

  Morgan Le Dû
  Soft robotics based on thermos-responsive polymer films

  Aikaterina Panagiotou
  Stability and performance study of non-fullerene organic solar cells

  Oleg Shindelov
  Structural and morphological investigations of slot-die coated perovskite layers for photovoltaics

  Rui Wang
  2D-quasi-2D-3D hierarchy structure for lead tin mixed perovskite solar cells with enhanced efficiency and stability

  Feifei Zheng
  Thermoresponsive polymers under pressure

- **Accomplished Bachelor Theses**

  Lukas Dörringer
  Photochromic and electrically conductive nanocellulose-based mulitlayer fillms

  Mateo Gabriel Flohr Reija
  Characterization of printed hybrid solar cells

  Jonas Fabian Keil
  Polymer blend electrolytes for Lithium ion batteries

  Lukas Kohlmaier
  High efficiency organic solar cells

  Johannes Kowalewicz
  Spray processing of green hybrid solar cells based on water-soluble donor materials

  Andreas Lukas
  High efficiency organic solar cells

  Florian Maly
  Design of a setup for measuring the electrical conductivity of thin films at variable humidity levels, combinable with neutron reflectometry measurements

  Herman Muzychko
  Printed ZnO nanostructures

  Raphael Prandtl
  Conductive paper

  Dominic Rapf
  Green photovoltaics with printed water-based active layers

  Samuel Reiser
  Role of hole transport layer in the stabilization of perovskite solar cells

  Lukas Schrödinger
  Self-assembled micelles from amphiphilic triblock terpolymers

  Bianca Seyschab
  Low-temperature fabrication of titania films for dye-sensitized solar cells

  Christoph Spies
  Effect of a cosolvent on a thermoresponsive molecular brush

  Andreas Steinhart
  Thermal degradation of PEDOT:PSS

  Erik Walz
  Texture evaluation with neutron diffraction: intensity correction for complex shaped and additive manufactured parts

  Sophia Werny
  Printing perovskite thin films for next-generation solar cells

  Andreas Wirler
  Morphology characterization of printed CsPbBr3 nanocrystals for PV applications